POLITECNICO DI MILANO

UNIVERSITY OF BASEL

Double Doctoral degree – Cotutelle de thèse

Organs-on-Chip as advanced models of osteoarthritis and mechanically active body districts

Final dissertation

To be awarded the degree of *Dottorato di ricerca in Bioingegneria*
at
the department of Electronics, informatics and bioengineering
of Politecnico di Milano
and the degree of *Dr. sc. med. Biomedizinische Technik*
at
the Faculty of Medicine
of the University of Basel

by

Andrea Mainardi

From Abbiategrasso (MI), Italy

2021, Basel

Backside of title page

Approved by the Faculty of Medicine of the University of Basel

On application of

Prof. Ivan Martin (First Supervisor)

Prof. Andrea Barbero (Second supervisor)

Prof. Marco Rasponi (First supervisor Politecnico di Milano)

Prof. Daniel Kelly (External supervisor)

Prof. Mauro Alini (Further external expert)

Members of the PhD committee

Basel, 1st November 2021
(Date of the acceptance of the Faculty)

……..
Dean
(Prof. Dr. Primo Leo Schär)

Table of contents

Extended summary

The development of a new drug is estimated to require $ 2.8 billion [1, 2] and a time comprised between 10 and 15 years [3]. Moreover, only 10% of compounds considered in phase I clinical trials reach the market [3]. This inefficiency correlates with the lack of predictive preclinical disease models [4].

Classic 2D plasticware-based models were demonstrated to be over-simplified and ineffective drug response predictors [4]. Conversely, costly and time expensive animal models, beside presenting ethical concerns, cannot be adopted in the initial, high throughput, phases of chemical entities screenings [5].

Organs-on-chip (OoC) are microfluidic based devices aiming at recapitulating organ and tissue level functions *in vitro* [6]. Allowing an increased control over the experimental environment, OoCs are gaining increasing consensus as disease modelling tools. The ability to model diseases affecting mechanically active body districts, such as the musculoskeletal apparatus or the myocardium remains however an open challenge. This aspect becomes particularly relevant when proper disease mimicry requires the incorporation of multiple tissues. Moreover, most OoCs are currently limited to single chamber devices thus impairing their applicability as high throughput screening tools [7].

Case in point, osteoarthritis (OA) is a degenerative disease mainly affecting load bearing joints such as knees and hips. Exact estimates of OA prevalence vary depending on the considered definition of OA, the joint of interest, and the studied population [8]. Knee osteoarthritis was deemed to effect roughly 10% of men and 13% of women over the age of 60 [9]. Despite this, a successful OA treatment is currently missing [10] being existing therapeutic choices palliatives aimed at relieving symptoms rather than reversing the degenerative processes.

OA is recognized as a multifactorial and complex disorder affecting the joint as a whole. OA pathological alterations include hyaline cartilage focal damage and degradation; chondrocyte assumption of a hypertrophic phenotype; vascular invasion, expansion towards the upper layers, and increase of the mineral content of calcified cartilage; and sclerosis and hypomineralization of subchondral bone. Indeed, the whole osteochondral unit (OCU) is affected [11, 12].

While no consensus is present regarding OA origin, a clear correlation between the pathology and mechanical risk factors such as trauma, joint misalignment and obesity has been demonstrated [13][14].

The lack of disease modifying anti-OA drugs was associated to the absence of relevant preclinical OA models [15]. The generation of representative OA models is however challenging given the difficulty of representing the multitude of tissues involved as well as the natural mechanically active joint environment.

In this framework, the present PhD work aimed at exploiting OoCs principles and microfabrication techniques together with tissue engineering, to develop disease relevant models of mechanically active tissues with a particular focus on OA.
The final aim was broke-down into five subsections, each aimed at delivering a specific technological or biological advancement.

i) Initially, a mechanically active OoC platform capable of providing three dimensional (3D) constructs with physiological (i.e. 10%) or hyperphysiological (i.e. 30%) compressive levels was designed, functionally validated, and exploited to achieve (i) a healthy cartilage on chip model (CoC) positive for the deposition of cartilage extracellular matrix constituents (e.g. collagen type II and aggrecan) and to (ii) induce OA traits in the CoC through the sole application of hyperphysiological compression. Specifically, it was feasible to recapitulate the imbalance of catabolic and anabolic processes, the increased inflammatory state, and the hypertrophic phenotype characterizing cartilage in OA. The model was also exploited to evaluate the response to known and innovative anti OA compounds.

ii) The adoption of OoCs as possible testing systems in drug screening campaigns depends on the achievement of a satisfactory experimental throughput. A platform capable of subjecting multiple independent 3D constructs to cyclical mechanical stimulation was engineered and functionally validated. Appropriately designed valves positioned between the different culture chambers allowed to inject multiple compartments with a single operation while assuring their independence during the culture period. As a proof of concept, the device was adopted to apply cyclical strain to cardiomyocytes and fibroblasts co-cultures recapitulating some traits of cardiac fibrosis. The device was then modified to make it suitable for the study of OA, shifting its mechanical stimulation from the stretching to the compression of hosted tissues.

iii) Cartilage and bone are examples of tissues with a hierarchical organization. During OA the whole OCU is affected leading to altered tissues mechanical properties.
A direct assessment of the mechanical, compositional and morphological alterations characterizing the different OCU tissues of OA patients was performed focusing on a dimensional scale relevant for developing future complex OA models based on the OoC technology.
Specifically, indentation type atomic force microscopy (IT-AFM) was adopted to study OCU tissues mechanical properties at a sub-micrometre scale and differentiating between hyaline cartilage zones, and calcified cartilage and subchondral layers. The technique was then translated to the determination of the mechanical properties of cartilaginous microconstructs.

iv) While the whole OCU is affected by OA, most *in vitro* models are limited to the study of cartilage. Modelling physiologically relevant mechanical stimulation in other OCU layers remains a challenge.
To fill this gap, a new OoC platform enabling the provision of well-defined and discrete levels of mechanical compression to directly interfaced superimposed 3D microconstructs was designed. Specifically, a new microfluidic concept (namely Vertical Capillary burst Valve, VBV) was introduced, consenting the vertical superimposition of two 3D cell-laden hydrogels and the spatially precise modulation of the strain field experienced by the two tissues. The device was validated demonstrating that different layers of cartilaginous constructs can be subjected to various levels of compression resulting in distinct mechanotransduction signalling. The platform was then exploited to demonstrate that local perturbations in the composition of acellular subchondral layers resulted in modulations of the loading response of cartilage-like constructs.

v) Finally, the culture conditions to obtain cellular microconstructs recapitulating multiple OCU layers were investigated. Specifically, primary human articular chondrocytes (hACs) and mesenchymal stromal cells (MSCs) were differentiated, respectively, in hyaline cartilage and calcified cartilage. A biphasic microconstruct integrating the two tissues was then achieved through a specifically designed OoC platform allowing a direct interface between two adjacent cell-laden hydrogels. The model was further integrated with a vascular compartment, used to preliminary assess how endothelial cells influence MSCs differentiation. Finally, providing spatially discrete mechanical compression to the obtained biphasic constructs, a preliminary evaluation of the effect of loading was performed.

References

1. Wouters OJ, McKee M, Luyten J (2020) Estimated Research and Development Investment Needed to Bring a New Medicine to Market, 2009-2018. JAMA 323:844–853. https://doi.org/10.1001/JAMA.2020.1166
2. Dierynck B, Joos P (2020) Research and Development Costs of New Drugs. JAMA 324:516–517. https://doi.org/10.1001/JAMA.2020.8642
3. Takebe T, Imai R, Ono S (2018) The Current Status of Drug Discovery and Development as Originated in United States Academia: The Influence of Industrial and Academic Collaboration on Drug Discovery and Development. Clin Transl Sci 11:597–606. https://doi.org/10.1111/cts.12577
4. Horvath P, Aulner N, Bickle M, et al (2016) Screening out irrelevant cell-based models of disease. Nat Rev Drug Discov 15:751–769. https://doi.org/10.1038/nrd.2016.175
5. Probst C, Schneider S, Loskill P (2018) High-throughput organ-on-a-chip systems: Current status and remaining challenges. Curr. Opin. Biomed. Eng. 6:33–41
6. Bhatia SN, Ingber DE (2014) Microfluidic organs-on-chips. Nat Biotechnol 2014 328 32:760–772. https://doi.org/10.1038/nbt.2989
7. Schneider O, Zeifang L, Fuchs S, et al (2019) User-Friendly and Parallelized Generation of Human Induced Pluripotent Stem Cell-Derived Microtissues in a Centrifugal Heart-on-a-Chip. Tissue Eng Part A 25:786–798. https://doi.org/10.1089/ten.tea.2019.0002
8. Vina ER, Kwoh CK (2018) Epidemiology of Osteoarthritis: Literature Update. Curr Opin Rheumatol 30:160. https://doi.org/10.1097/BOR.0000000000000479
9. Zhang Y, Jordan JM (2010) Epidemiology of Osteoarthritis. Clin Geriatr Med 26:355. https://doi.org/10.1016/J.CGER.2010.03.001
10. Kloppenburg M, Berenbaum F (2020) Osteoarthritis year in review 2019: epidemiology and therapy. Osteoarthr Cartil 28:242–248. https://doi.org/10.1016/j.joca.2020.01.002
11. Loeser RF, Goldring SR, Scanzello CR, Goldring MB (2012) Osteoarthritis: A Disease of the Joint as an Organ. Arthritis Rheum 64:1697. https://doi.org/10.1002/ART.34453
12. Goldring SR, Goldring MB (2016) Changes in the osteochondral unit during osteoarthritis: structure, function and cartilage–bone crosstalk. Nat Rev Rheumatol 12:632–644. https://doi.org/10.1038/nrrheum.2016.148
13. He Y, Li Z, Alexander PG, et al (2020) Pathogenesis of Osteoarthritis: Risk Factors, Regulatory Pathways in Chondrocytes, and Experimental Models. Biol 2020, Vol 9, Page 194 9:194. https://doi.org/10.3390/BIOLOGY9080194
14. Andriacchi TP, Mündermann A (2006) The role of ambulatory mechanics in the initiation and progression of knee osteoarthritis. Curr Opin Rheumatol 18:514–518. https://doi.org/10.1097/01.BOR.0000240365.16842.4E
15. CI J, DJ A, DN C (2016) In vitro models for the study of osteoarthritis. Vet J 209:40–49. https://doi.org/10.1016/J.TVJL.2015.07.011

Sommario

Il costo per lo sviluppo di un singolo nuovo farmaco è oggi stimato intorno ai 2.8 miliardi di dollari [1, 2] con tempi compresi fra i 10 ed i 15 anni [3]. Inoltre, solo il 10 % dei farmaci che entrano nei test clinici di fase I raggiunge effettivamente il mercato [3]. Questa inefficienza è correlata alla mancanza, in fase preclinica, di modelli patologici predittivi [4].

I modelli 2D basati su culture cellulari in piastra sono infatti over-semplicistici ed inefficaci nel predire l'effetto terapeutico dei farmaci *in vivo* [4]. D'altra parte, i modelli animali, oltre a presentare problematiche etiche, sono costosi e richiedono lunghe tempistiche sperimentali, spesso non compatibili con le fasi iniziali dei test farmacologici, le quali necessitano di un throughput elevato [5].

Gli organi-su-chip (OoC) sono dispositivi microfluidici per colture cellulari avanzate che mirano a ricapitolare *in vitro* le unità funzionali degli organi nativi [6]. Permettendo uno stretto controllo delle condizioni sperimentali, gli OoC stanno acquisendo un crescente consenso come modelli per lo studio di varie patologie. Rappresentare *in vitro* patologie che colpiscono distretti corporei caratterizzati da un ambiente meccanico attivo, come il sistema muscoloscheletrico o il muscolo cardiaco, rimane tuttavia una sfida aperta. Questo aspetto risulta particolarmente problematico quando è richiesto lo studio simultaneo di più tessuti interconnessi a formare distretti funzionali (come nel caso delle articolazioni). Inoltre, la maggior parte delle soluzioni basate sulla tecnologia degli OoC è costituita da dispositivi contenenti una singola camera di cultura e questo limita il loro possibile utilizzo come strumenti per test a throughput elevato [7].

L'osteoartrosi (OA), patologia degenerativa che colpisce soprattutto articolazioni soggette a carico meccanico come ginocchia ed articolazione acetabolo-femorale, è un esempio paradigmatico. Le stime sulla sua prevalenza variano a seconda della definizione di OA, dell'articolazione interessata o della popolazione campione [8]. L'osteoartrosi al ginocchio, per esempio, colpisce circa il 10% degli uomini ed il 13 % delle donne sopra l'età di 60 anni [9]. A dispetto dell'ampia diffusione tuttavia, una terapia efficacie non è ancora disponibile [10] e le attuali opzioni terapeutiche sono limitate a palliativi volti a diminuire i sintomi piuttosto che a invertire i processi degenerativi.

L' OA è riconosciuta come una complessa patologia multifattoriale che interessa l'intera articolazione. Le alterazioni patologiche includono danni focali e degenerazione della cartilagine ialina con l'assunzione di un fenotipo ipertrofico da parte dei condrociti (i.e. la popolazione cellulare residente); invasione vascolare, espansione, ed aumento del contenuto minerale della cartilagine calcificata; e sclerosi ed ipo-mineralizzazione dell'osso sub-condrale. Di fatto, l'intera unita osteocondrale (OCU) viene colpita [11, 12]. Mentre un pieno consenso riguardo alle cause dell'OA non è stato raggiunto, vi sono evidenze che indicano una correlazione fra l'insorgere della patologia e fattori che comportano alterazioni della meccano-biologia articolare quali traumi pregressi, disallineamento articolare, ed obesità [13][14].

L’assenza di trattamenti farmacologici è stata associata alla mancanza di modelli predittivi da utilizzare in fase preclinica [15]. La generazione di modelli rilevanti di OA è infatti ostacolata dalla necessità di rappresentare sia la moltitudine dei tessuti affetti che l’ambiente meccanicamente attivo che contraddistingue le articolazioni.

All’interno di questo contesto, il presente lavoro di dottorato è stato focalizzato sull’utilizzo delle tecnologie degli OoC, della microfabbricazione, e dell’ingegneria tissutale, per lo sviluppo di modelli rilevanti di patologie che interessano distretti corporei meccanicamente attivi, incentrandosi sull’OA come applicazione principale.
L’obiettivo finale è stato suddiviso in cinque sottosezioni, ciascuna voluta a raggiungere uno specifico avanzamento tecnologico o biologico.

i) Inizialmente, è stato progettato un dispositivo OoC capace di sottoporre costrutti tridimensionali (3D) a livelli fisiologici (i.e. 10%) o iperfisiologici (i.e. 30%) di compressione meccanica. Tale dispositivo è stato validato ed utilizzato (i) per ottenere un modello di cartilagine su chip ricco in costituenti della matrice extracellulare nativa (p.e. collagene di tipo II ed aggrecano) e (ii) per indurre nello stesso modello alcuni dei tratti tipici dell’OA unicamente attraverso una compressione iperfisiologica. Nel dettaglio, è stato possibile ricapitolare lo sbilanciamento tra i processi catabolici ed anabolici, lo stato infiammatorio, ed il fenotipo ipertrofico che caratterizzano la cartilagine nell’OA. Il modello è anche stato utilizzato per valutare la risposta a diversi composti anti-OA fra cui farmaceutici sperimentali.

ii) L’utilizzo degli OoC come strumenti per svolgere test farmacologici preclinici dipende dall’ottenimento di un throughput sperimentale sufficiente. Per rispondere a questo fabbisogno è stato sviluppato un dispositivo OoC capace di esporre costrutti cellulari multipli e indipendenti ad una stimolazione meccanica. In particolare, l’introduzione di un sistema di valvole poste fra le diverse camere di cultura (e quindi fra i costrutti) permette di riempire tutte le camere con una sola operazione di semina, assicurando al contempo la loro indipendenza durante il periodo di cultura. Come caso di studio, il dispositivo è stato utilizzato per valutare l’effetto di uno stretching ciclico su co-culture di fibroblasti e cardiomiociti replicando alcuni tratti tipici della fibrosi cardiaca. Il dispositivo è stato poi modificato perché potesse essere applicato allo studio dell’OA, tramutando la tipologia di stimolazione meccanica applicata ai costrutti nel dispositivo dallo stretching alla compressione.

iii) Cartilagine ed osso sono esempi di tessuti con un’organizzazione gerarchica. L’OA colpisce l’intera OCU causando alterazioni nelle proprietà meccaniche dei singoli tessuti. Una valutazione diretta delle alterazioni meccaniche, di composizione, e strutturali dei vari tessuti dell’OCU isolati da pazienti affetti da

OA è stata eseguita, concentrandosi su una scala dimensionale rilevante per sviluppare futuri modelli complessi di OA basati sulle tecnologie OoC. Nello specifico, la tecnica dell'IT-AFM (i.e. indentation type atomic force microscopy) è stata utilizzata per evidenziare come, in seguito ai processi degenerativi dell'OA, le proprietà meccaniche dei vari tessuti dell'OCU varino ad una scala sub-micrometrica, con differenze settoriali fra cartilagine ialina, cartilagine calcificata ed osso sub-condrale. La tecnica è stata poi usata per determinare le proprietà meccaniche di costrutti cartilaginei ottenuti in una piattaforma microfluidica.

iv) Nonostante l'OA colpisca l'intera OCU, la maggior parte dei modelli *in vitro* esistenti considera solo il tessuto cartilagineo. L'introduzione di modelli meccanicamente attivi che rappresentino l'intera OCU è ancora una sfida aperta.
Per colmare questa lacuna è stata introdotta una nuova piattaforma OoC che permette di sottoporre costrutti bifasici complessi a livelli discreti di compressione meccanica. Nello specifico, uno nuovo concetto microfluidico, denominato "Vertical capillary Burst Valve", è stato introdotto, consentendo (i) la sovrapposizione spaziale di due micro costrutti cellulari ed (ii) il controllo posizionale sul campo di deformazione a cui i costrutti sono sottoposti nel dispositivo. Il dispositivo è stato poi validato dimostrando come due costrutti cartilaginei seminati nei due compartimenti del dispositivo siano effettivamente sottoposti a livelli di stimolazione meccanica diversi, risultando in una diversa attivazione dei rispettivi meccanismi di meccanotransduzione. La piattaforma è stata infine utilizzata per dimostrare come variazioni locali nelle proprietà dello strato sub-condrale della OCU influenzino la risposta dei costrutti cartilaginei alla stimolazione meccanica.

v) Da ultimo sono state investigate le condizioni per ottenere micro-costrutti cellulari compositi, rappresentativi di diversi tessuti dell'OCU. Condrociti articolari primari e cellule mesenchimali stromali (MSCs) sono stati usati per ottenere, rispettivamente, micro-costrutti con le caratteristiche di cartilagine ialina a calcificata. Tramite un dispositivo disegnato opportunamente per permettere una interfaccia diretta fra due compartimenti cellulari è poi stato ottenuto un costrutto bifasico comprensivo di entrambi i tessuti. Il modello è stato completato con l'introduzione di una componente vascolare per valutare, in modo preliminare, come le cellule endoteliali influenzino la differenziazione delle MSCs. Da ultimo è stata eseguita una prima valutazione dell'effetto della stimolazione meccanica (iperfisiologica) su questi costrutti complessi.

Referenze

1. Wouters OJ, McKee M, Luyten J (2020) Estimated Research and Development Investment Needed to Bring a New Medicine to Market, 2009-2018. JAMA 323:844–853. https://doi.org/10.1001/JAMA.2020.1166
2. Dierynck B, Joos P (2020) Research and Development Costs of New Drugs. JAMA 324:516–517. https://doi.org/10.1001/JAMA.2020.8642
3. Takebe T, Imai R, Ono S (2018) The Current Status of Drug Discovery and Development as Originated in United States Academia: The Influence of Industrial and Academic Collaboration on Drug Discovery and Development. Clin Transl Sci 11:597–606. https://doi.org/10.1111/cts.12577
4. Horvath P, Aulner N, Bickle M, et al (2016) Screening out irrelevant cell-based models of disease. Nat Rev Drug Discov 15:751–769. https://doi.org/10.1038/nrd.2016.175
5. Probst C, Schneider S, Loskill P (2018) High-throughput organ-on-a-chip systems: Current status and remaining challenges. Curr. Opin. Biomed. Eng. 6:33–41
6. Bhatia SN, Ingber DE (2014) Microfluidic organs-on-chips. Nat Biotechnol 2014 328 32:760–772. https://doi.org/10.1038/nbt.2989
7. Schneider O, Zeifang L, Fuchs S, et al (2019) User-Friendly and Parallelized Generation of Human Induced Pluripotent Stem Cell-Derived Microtissues in a Centrifugal Heart-on-a-Chip. Tissue Eng Part A 25:786–798. https://doi.org/10.1089/ten.tea.2019.0002
8. Vina ER, Kwoh CK (2018) Epidemiology of Osteoarthritis: Literature Update. Curr Opin Rheumatol 30:160. https://doi.org/10.1097/BOR.0000000000000479
9. Zhang Y, Jordan JM (2010) Epidemiology of Osteoarthritis. Clin Geriatr Med 26:355. https://doi.org/10.1016/J.CGER.2010.03.001
10. Kloppenburg M, Berenbaum F (2020) Osteoarthritis year in review 2019: epidemiology and therapy. Osteoarthr Cartil 28:242–248. https://doi.org/10.1016/j.joca.2020.01.002
11. Loeser RF, Goldring SR, Scanzello CR, Goldring MB (2012) Osteoarthritis: A Disease of the Joint as an Organ. Arthritis Rheum 64:1697. https://doi.org/10.1002/ART.34453
12. Goldring SR, Goldring MB (2016) Changes in the osteochondral unit during osteoarthritis: structure, function and cartilage–bone crosstalk. Nat Rev Rheumatol 12:632–644. https://doi.org/10.1038/nrrheum.2016.148
13. He Y, Li Z, Alexander PG, et al (2020) Pathogenesis of Osteoarthritis: Risk Factors, Regulatory Pathways in Chondrocytes, and Experimental Models. Biol 2020, Vol 9, Page 194 9:194. https://doi.org/10.3390/BIOLOGY9080194
14. Andriacchi TP, Mündermann A (2006) The role of ambulatory mechanics in the initiation and progression of knee osteoarthritis. Curr Opin Rheumatol 18:514–518. https://doi.org/10.1097/01.BOR.0000240365.16842.4E
15. CI J, DJ A, DN C (2016) In vitro models for the study of osteoarthritis. Vet J 209:40–49. https://doi.org/10.1016/J.TVJL.2015.07.011

Zusammenfassung

Die Kosten für die Entwicklung eines neuen Medikaments belaufen sich schätzungsweise auf 2,8 Milliarden US-Dollar [1, 2] und bis zur Markteinführung dauert es derzeit 10 bis 15 Jahre [3]. Darüber hinaus gelangen nur 10 % der in klinischen Phase-I-Studien untersuchten Wirkstoffe auf den Markt [3]. Unter anderem, diese Ineffizienz hängt mit dem Fehlen von vorhersagekräftigen präklinischen Krankheitsmodellen zusammen [4].

Es wurde gezeigt, dass die klassischen 2D-Zellkulturmodelle zu stark vereinfacht sind und daher eine unzureichende Vorhersagekraft über die Ansprechbarkeit von zukünftigen Arzneimitteln haben [4]. Umgekehrt können kostspielige und zeitaufwendige Tiermodelle, abgesehen von ethischen Bedenken, nicht in anfänglichen Hochdurchsatz-Screenings von chemischen Stoffen eingesetzt werden [5].

Organs-on-Chip (OoCs) sind mikrofluidische Geräte, die darauf abzielen, in vitro Funktionen auf Organ- und Gewebeebene zu rekapitulieren [6]. OoCs ermöglichen eine verbesserte Kontrolle über die experimentelle Umgebung und gewinnen zunehmend an Zustimmung als Werkzeuge zur Modellierung von Krankheiten. Die Modellierung von Erkrankungen, die mechanisch aktive Körperbezirke, wie den Bewegungsapparat oder das Myokard betreffen, bleibt jedoch eine Herausforderung. Dieser Aspekt wird insbesondere relevant, wenn ein konkretes Krankheitsmodell mehrere Gewebe in dieselbe Plattform einbeziehen soll. Darüber hinaus sind die meisten OoCs auf Einzelgeräte beschränkt, was ihre Anwendbarkeit als Screening-Tools mit hohem Durchsatz einschränkt [7].

Osteoarthritis (OA) ist eine degenerative Erkrankung, die hauptsächlich lasttragende Gelenke wie Knie und Hüfte betrifft. Genaue Schätzungen der OA-Prävalenz variieren in Abhängigkeit von der betrachteten Definition von OA, dem betroffenen Gelenk und der untersuchten Population [8]. Es wird angenommen, dass etwa 10 % der Männer und 13 % der Frauen über 60 Jahren von einer Kniearthrose betroffen sind [9]. Eine erfolgreiche OA-Therapie fehlt jedoch noch [10], wobei die zurzeit bestehenden therapeutischen Optionen einen palliativen Ansatz bieten, die darauf abzielen, Symptome zu lindern, anstatt die degenerativen Prozesse rückgängig zu machen.

OA wird als multifaktorielle und komplexe Erkrankung anerkannt, die das gesamte Gelenk betrifft. Die Krankheit charakterisiert sich durch folgenden pathologische Veränderungen: fokale Schäden des hyalinen Knorpels, sowie dessen Übergang in einen hypertrophen Phänotypen, Gefäßinvasion in Richtung der oberen Schichten und Erhöhung des Mineralgehalts von kalzifiziertem Knorpel, sowie Sklerosierung und Hypomineralisation des subchondralen Knochens. Tatsächlich ist die gesamte osteochondrale Einheit (OCU) betroffen [11, 12].

Obwohl kein Konsens über den Ursprung von OA besteht, wurde ein klarer Zusammenhang zwischen der Pathologie und mechanischen Risikofaktoren wie Traumata, Gelenkfehlstellungen oder Adipositas gezeigt [13][14].
Das Fehlen von krankheitsmodifizierenden OA-Medikamenten wurde mit dem Fehlen relevanter präklinischer OA-Modelle in Zusammenhang gebracht [15]. Die Entwicklung eines repräsentativen OA-Modells wird jedoch durch die Vielzahl der beteiligten Gewebe und die mechanisch aktive Umgebung erschwert.

In diesem Rahmen zielte die vorliegende Doktorarbeit darauf ab, OoC-Prinzipien und Mikrofabrikationstechniken zusammen mit Tissue-Engineering-Kompetenzen zu nutzen, um krankheitsrelevante Modelle mechanisch aktiver Gewebe zu entwickeln, mit besonderem Fokus auf OA.
Das Endziel wurde in verschiedene Unterabschnitte gegliedert, die jeweils darauf abzielten, einen spezifischen technologischen oder biologischen Fortschritt zu erzielen.

i) Zunächst wurde eine mechanisch aktive OoC-Plattform entwickelt, die dreidimensionale (3D) Konstrukte mit physiologischem (i.e. 10%) oder hyperphysiologischem (i.e. 30%) Kompressionsniveau bereitstellt. Diese wurde funktional validiert und genutzt, um (i) ein gesundes Knorpel-on-Chip-Modell zu erreichen (CoC), der sich durch die Ablagerung von extrazellulären Bestandteilen der Knorpelmatrix auszeichnet (e.g. Typ II Kollagen und Aggrecan) und (ii) OA-Merkmale im CoC durch die alleinige Anwendung einer hyperphysiologischen Kompression zu induzieren. Insbesondere war es möglich, das Ungleichgewicht von katabolen und anabolen Prozessen, die Zunahme der Entzündungsparameter und den hypertrophen Phänotyp, die den osteoarthrotischen Knorpel charakterisieren, zu rekapitulieren. Das Modell wurde auch genutzt, um die Reaktion auf bekannte und innovative OA-Medikamente zu bewerten.

ii) Die Anwendbarkeit von OoCs als mögliches Testsystem in Screeningskampagnen für Arzneimittel hängt von der Erreichung eines zufriedenstellenden experimentellen Durchsatzes ab. Eine Plattform, die mehrere unabhängige 3D-Konstrukte einer zyklischen mechanischen Stimulation aussetzen kann, wurde entworfen und funktional validiert. Entsprechend konstruierte Ventile zwischen den verschiedenen Kulturkammern ermöglichten die Injektion mehrerer Kompartimente in einem einzigen Arbeitsgang, wobei ihre Unabhängigkeit während der Kultivierungsperiode sichergestellt wurde. Als Machbarkeitsnachweis wurde dieses Gerät eingeführt, um die Wirkung zyklischer Belastungen auf Kardiomyozyten und Fibroblasten in Ko-Kultur zu bewerten, wobei einige Merkmale der Herzfibrose rekapituliert werden konnten. Das Gerät wurde modifiziert, um es für die Untersuchung von OA geeignet zu machen, indem seine mechanische Stimulation von der Dehnung auf die Kompression des beinhalteten Gewebes umgestellt wurde.

iii) Knorpel und Knochen sind Beispiele für Gewebe mit einer hierarchischen Organisation. Bei OA ist die gesamte OCU betroffen, was zu veränderten mechanischen Eigenschaften des Gewebes führt. Mit dem Ziel, OoC basierte Modelle zukünftig zur Untersuchung von Veränderungen zu verwenden, die durch einen zugegebenen OA-imitierenden Stimulus (z. B. Belastung oder die Verabreichung von entzündlichen Zytokinen) hervorgerufen werden, wurden mechanische, kompositorische und morphologische Veränderungen der OCU von OA Patienten in einem mikrofluidisch relevanten Maßstab erforscht. Insbesondere wurde die Rasterkraftmikroskopie vom Eindrucktyp (IT-AFM) angewendet, um die Variation der mechanischen Eigenschaften im Submikrometerbereich zu bestimmen und zwischen hyalinem Knorpel, kalzifiziertem Knorpel und subchondralen Schichten zu unterscheiden. Die Technik wurde dann auf die Bestimmung der mechanischen Eigenschaften von knorpeligen Mikrokonstrukten übertragen.

iv) Obwohl die gesamte OCU von OA betroffen ist, beschränken sich die meisten In-vitro-Modelle auf die Untersuchung von Knorpel, während der Einfluss von physiologisch relevanten mechanischen Stimulationen auf anderen OCU-Schichten nicht berücksichtigt wird.
Um diese Lücke zu schließen, wurde eine neue OoC-Plattform entwickelt, die die Bereitstellung gut definierter und räumlich getrennter mechanischer Kompressionsstufen für direkt verbundene überlagerte 3D-Mikrokonstrukte ermöglicht. Insbesondere wurde ein neues mikrofluidisches Konzept (nämlich Vertical Capillary Burst Valve, VBV) eingeführt, dass die vertikale Überlagerung von zwei 3D-Zell-beladenen Hydrogelen und die räumlich präzise Modulation des von den beiden Geweben erfahrenen Dehnungsfeldes ermöglicht. Das Gerät wurde validiert und zeigte, dass verschiedene Schichten von Knorpelkonstrukten unterschiedlichen Kompressionsstärken ausgesetzt werden können, was zu entsprechenden Mechanotransduktionssignalen führt. Die Plattform wurde dann genutzt, um zu zeigen, dass Störungen in der Zusammensetzung azellulärer subchondraler Schichten zu Reaktionen auf die Belastungsmodulation von knorpelähnlichen Konstrukten führten.

v) Schließlich wurden die Bedingungen untersucht, um zelluläre Mikrokonstrukte zu erhalten, die mehrere OCU-Schichten rekapitulieren. Insbesondere wurden primäre humane artikuläre Chondrozyten (hACs) bzw. MSCs in hyalinen Knorpel und kalzifizierten Knorpel differenziert. Ein zweiphasiges Mikrokonstrukt, dass die beiden Gewebe integriert, wurde dann durch eine speziell entwickelte OoC-Plattform erreicht, die eine direkte Schnittstelle zwischen zwei benachbarten zellbeladenen Hydrogelen ermöglicht. Das Modell wurde außerdem in ein Gefäßkompartiment integriert, das vorläufig untersuchte, wie Endothelzellen die Differenzierung von MSCs beeinflussen. Schließlich wurde eine vorläufige Bewertung der Wirkung der Belastung durchgeführt, indem den erhaltenen zweiphasigen Konstrukten eine räumlich getrennte mechanische Kompression verliehen wurde.

Verweise

1. Wouters OJ, McKee M, Luyten J (2020) Estimated Research and Development Investment Needed to Bring a New Medicine to Market, 2009-2018. JAMA 323:844–853. https://doi.org/10.1001/JAMA.2020.1166
2. Dierynck B, Joos P (2020) Research and Development Costs of New Drugs. JAMA 324:516–517. https://doi.org/10.1001/JAMA.2020.8642
3. Takebe T, Imai R, Ono S (2018) The Current Status of Drug Discovery and Development as Originated in United States Academia: The Influence of Industrial and Academic Collaboration on Drug Discovery and Development. Clin Transl Sci 11:597–606. https://doi.org/10.1111/cts.12577
4. Horvath P, Aulner N, Bickle M, et al (2016) Screening out irrelevant cell-based models of disease. Nat Rev Drug Discov 15:751–769. https://doi.org/10.1038/nrd.2016.175
5. Probst C, Schneider S, Loskill P (2018) High-throughput organ-on-a-chip systems: Current status and remaining challenges. Curr. Opin. Biomed. Eng. 6:33–41
6. Bhatia SN, Ingber DE (2014) Microfluidic organs-on-chips. Nat Biotechnol 2014 328 32:760–772. https://doi.org/10.1038/nbt.2989
7. Schneider O, Zeifang L, Fuchs S, et al (2019) User-Friendly and Parallelized Generation of Human Induced Pluripotent Stem Cell-Derived Microtissues in a Centrifugal Heart-on-a-Chip. Tissue Eng Part A 25:786–798. https://doi.org/10.1089/ten.tea.2019.0002
8. Vina ER, Kwoh CK (2018) Epidemiology of Osteoarthritis: Literature Update. Curr Opin Rheumatol 30:160. https://doi.org/10.1097/BOR.0000000000000479
9. Zhang Y, Jordan JM (2010) Epidemiology of Osteoarthritis. Clin Geriatr Med 26:355. https://doi.org/10.1016/J.CGER.2010.03.001
10. Kloppenburg M, Berenbaum F (2020) Osteoarthritis year in review 2019: epidemiology and therapy. Osteoarthr Cartil 28:242–248. https://doi.org/10.1016/j.joca.2020.01.002
11. Loeser RF, Goldring SR, Scanzello CR, Goldring MB (2012) Osteoarthritis: A Disease of the Joint as an Organ. Arthritis Rheum 64:1697. https://doi.org/10.1002/ART.34453
12. Goldring SR, Goldring MB (2016) Changes in the osteochondral unit during osteoarthritis: structure, function and cartilage–bone crosstalk. Nat Rev Rheumatol 12:632–644. https://doi.org/10.1038/nrrheum.2016.148
13. He Y, Li Z, Alexander PG, et al (2020) Pathogenesis of Osteoarthritis: Risk Factors, Regulatory Pathways in Chondrocytes, and Experimental Models. Biol 2020, Vol 9, Page 194 9:194. https://doi.org/10.3390/BIOLOGY9080194
14. Andriacchi TP, Mündermann A (2006) The role of ambulatory mechanics in the initiation and progression of knee osteoarthritis. Curr Opin Rheumatol 18:514–518. https://doi.org/10.1097/01.BOR.0000240365.16842.4E
15. CI J, DJ A, DN C (2016) In vitro models for the study of osteoarthritis. Vet J 209:40–49. https://doi.org/10.1016/J.TVJL.2015.07.011

1 *Osteoarthritis as a paradigmatic disease modelling challenge: from mechanical stimulation to experimental throughput*

1.1 Assessing the relevance of cell-based disease models: current issues in drug development

Developed in the 1960s, the paradigm for pharmaceutical innovation, comprehensive of *in vitro* experimentation, *in vivo* animal testing, and clinical trials, has remained unchanged for more than 50 years. The success of approval of a new drug from phase I clinical trials is estimated to be around 10%, with an average time to market higher than 10 years for some disease categories [1]. Associated costs ranged between 92 and 883.6 million $ between the 1980s and the 2010s [2], with figures rising to an upper limit of $ 2.8 billion in recent years [3, 4].

Drugs high inefficiency in reaching clinical usage correlates with the perpetuated adoption, in the early phases of research and development (R&D) processes (i.e. high throughput screenings, HTS), of non-relevant disease models uncapable of representing tissues specific functions and predict drugs behaviour in patients [5, 6].

Classic disease models are mostly based on rigid 2-dimensional (2D), unphysiological plasticware substrates and fail to represent features such as tissues organisation in complex 3-dimensional (3D) structures, inter and intra tissue communication, drugs tissue penetration, as well as the multitude of stimuli to which tissues are subjected *in vivo* from chemical gradients to mechanical and electrical cues. As a result, compound failure is detected late during drug development campaigns, increasing related time and costs [7].

In recent decades, the advent of more advanced culture systems based on scaffolds, hydrogels, and micro-structured self-assembled cells (i.e. organoids) allowed to successfully recapitulate the 3D organization and basic functionality of multiple organs [8]. Introducing signals such as mechanical stimuli, fluid motion, and shear stresses, necessary to mimic the native biological environment, requires however the adoption of bioreactors (i.e. devices in which biological and/or biochemical processes develop under closely monitored and tightly controlled environmental and operating conditions) [9].

These systems hold great potentialities for both basic research and translational tissue engineering applications [10]. Given their operational difficulty, bulk, and associated high costs, bioreactors are nonetheless not indicated for the early phases of R&D processes where a higher throughput, and a limited quantitative of reagents and cellular components are available.

As a result, the struggle in developing disease relevant models and identifying promising drug candidates is aggravated when dealing with pathologies of mechanically active corporeal districts (such as

osteoarthritis or cardiac diseases) where mechanical cues have a paramount role both in homeostasis [11] and pathological evolution [12].

The present situation calls therefore for new disease and tissue models capable of recapitulating the cellular microenvironment (comprehensive both of physicochemical properties such as temperature, pH, and chemical gradients of nutrients, metabolites, hormones, growth factors, and cytokines), but also cell-cell and cell-matrix interactions, and physical (e.g. strain, mechanical forces, fluid flow and shear stresses), and electrical (e.g. ions currents, action potentials) stimuli, within cost effective, easily usable, and high throughput setups.

1.2 Microfluidics as a tool for disease modelling and drug screening: Organs-on-chip

Organs-on-chip (OoCs) are microengineered biomimetic devices that aim at recapitulating organ and tissue level functions *in vitro* [13]. Their design and implementation are based on microfluidics: a set of technologies that enables the control of small quantities of fluids (10^{-9} to 10^{-18} litres) using channels with characteristic dimensions ranging from ten to hundreds of microns [14]. Beside permitting to minimise required cells and reagents amounts, the reduction in scale leads to an increased surface to volume ratio resulting in the predominance of surface forces (e.g. surface tension) over volumetric ones (e.g. gravity). As a consequence, the interfaces for mass and energy transfer phenomena are maximized, reactions efficiency is increased, and reaction dynamics augmented. Moreover, fluid flow is characterized by high laminarity and chemical transport phenomena are exclusively diffusion mediated, yielding to an unprecedented control over local environment parameters at a cellular relevant scale.

Inspired by electronics, pioneering work in microfluidics adopted materials such as silicon or glass, obtaining 3D structures through photolithography and etching [15]. In the 1990s the group of Whitesides introduced soft lithography: a set of procedures to achieve polymer based devices exploiting microstructured master moulds obtained by photolithography through replica moulding [16]. The switch to polymeric materials, and mainly to polydimethylsiloxane (PDMS), allowed for the production of cell compatible structures that were exploited to recapitulate *in vitro* the organization and the function of different tissues. PDMS is an elastomeric rubber constituted by a siloxane backbone connected by organic methyl groups. It is permeable to gasses, and exhibits low autofluorescence and high optical transparency in the range between 240 and 1100 nm making it particularly suitable for cell culture applications and allowing direct on-chip imaging [17].

Leveraging on the advantages of polymeric based microfabrication, OoCs allow the recapitulation of organs 3D microarchitecture, functional tissue–tissue interfaces, and complex organ-specific mechanical and biochemical microenvironments [7] incorporating features such as chemical gradient generators [18],

electrical signal sensors [19], and mechanical actuators [20]. Proposed OoCs included both 2D epithelia [21] and 3D cellular microconstructs ranging from gut [22], kidney, liver [23], lung [21], and heart [20] models to multi organ systems [23].

Less attention was however dedicated to musculoskeletal diseases where the involvement of multiple 3D tissues and the mechanically active environment need to be considered at the same time. Moreover, OoC devices are often still based on single chamber units limiting their experimental throughput and, ultimately their usability as drug screening tools.

1.3 Osteoarthritis: prevalence, diffusion and current therapies

Osteoarthritis (OA), is a highly prevalent multifactorial joint disorder and a major cause of pain and disability worldwide [24]. Clinical manifestation include pain, joint disfunction and articular deformity. Exact estimates of OA prevalence vary depending on the considered definition of OA, the joint of interest, and the studied population [25]. Radiographically established OA was valued to affect 37% of the over 60 population in the United States [26, 27] estimates that display upward tendencies given the increasingly aging population [28]. Knee osteoarthritis was deemed to effect roughly 10% of men and 13% of women over the age of 60 [29] with reports indicating, however, that more that 50% of people with knee OA are younger than 65 [25].

Cartilage fibrillation and breakdown are the most prominent pathological features, but OA has now been recognized as a whole joint disorder leading also to subchondral bone alterations (with reactive bone hyperplasia at the joint margins and formation of bone spurs, i.e. osteophytes), expansion of calcified cartilage and its vascular invasion, synovial distension and inflammation, ligamentous laxity and, in the knees, meniscus degeneration, and hypertrophy of the joint capsule [30, 31]. OA related tissues alteration in knee joints are depicted in Fig. 1.

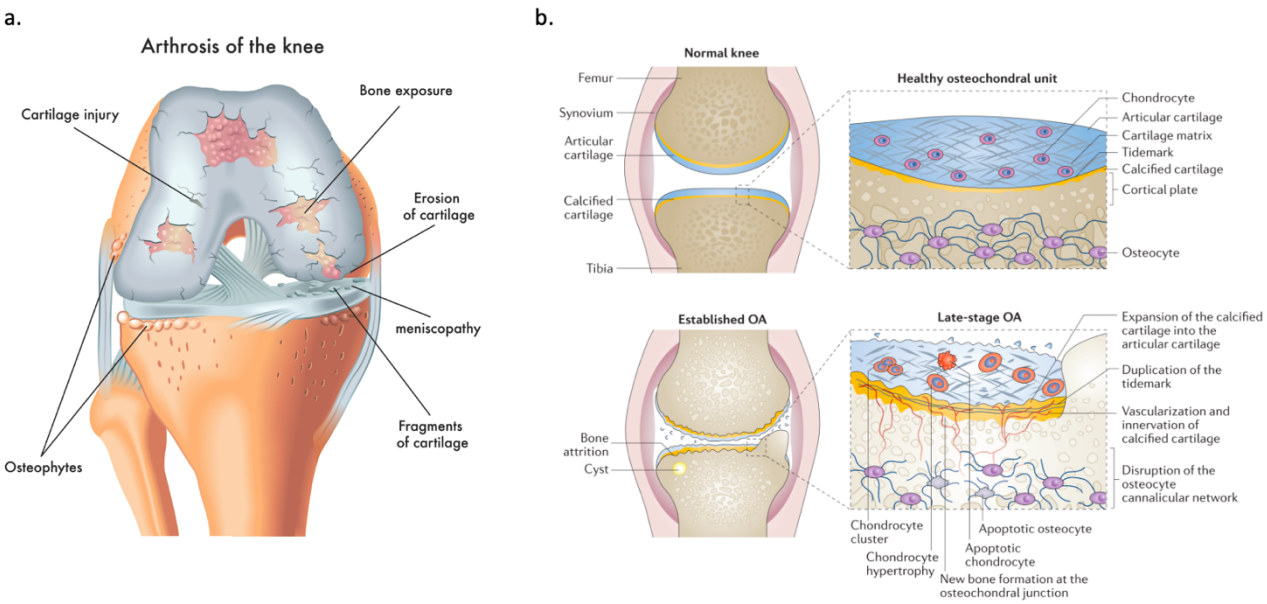

Figure 1: ***Pathological alterations in the osteoarthritic knee joint****.* ***a****, Schematization of macroscale effects of knee OA. Areas of cartilage erosion and degradation, and osteophytes are highlighted* ***b****, OA related alterations in the osteochondral unit, image adapted from* [32].

Despite recent advancements, the exact pathogenic mechanisms of OA remain unknown [33]; altered joint kinematics, obesity, joint injury, immune-mediate responses, genetics, and age are all risk factors that result in the inability of the articular surface to serve its function of absorbing and distributing the mechanical load through the joint [33].

The multifactorial origin and its multi tissue involvement render the research for a disease modifying OA drug (DMOAD) particularly cumbersome. Existing therapeutic options based on administration of non-steroidal anti-inflammatory drugs (NSAIDs), intraarticular corticosteroid injections, and weak opioids [24] are, in fact, palliatives limited at easing the symptoms, namely pain and stiffness [24]. As a result, the underlying disease progresses and joint prosthetization remains the only treatment option for end stage disease manifestations.

Although different DMOADs are under investigation, promising compounds have had, so far, a poor clinical translation. This failure correlates with the lack of predictivity of presently available disease models that neglect to accurately forecast compounds effects *in vivo* and do not allow a clear dissection of the pathological onset causes which could serve as promising therapeutic targets.

1.4 Osteoarthritis tissues modifications and molecular mechanisms

As introduced, OA alters all joint tissues, the main effected compartments being the osteochondral unit (OCU) and the synovial membrane. Joint tissues' structure and their OA pathological alterations are here described. The structure of the osteochondral unit is also depicted in Fig. 2.

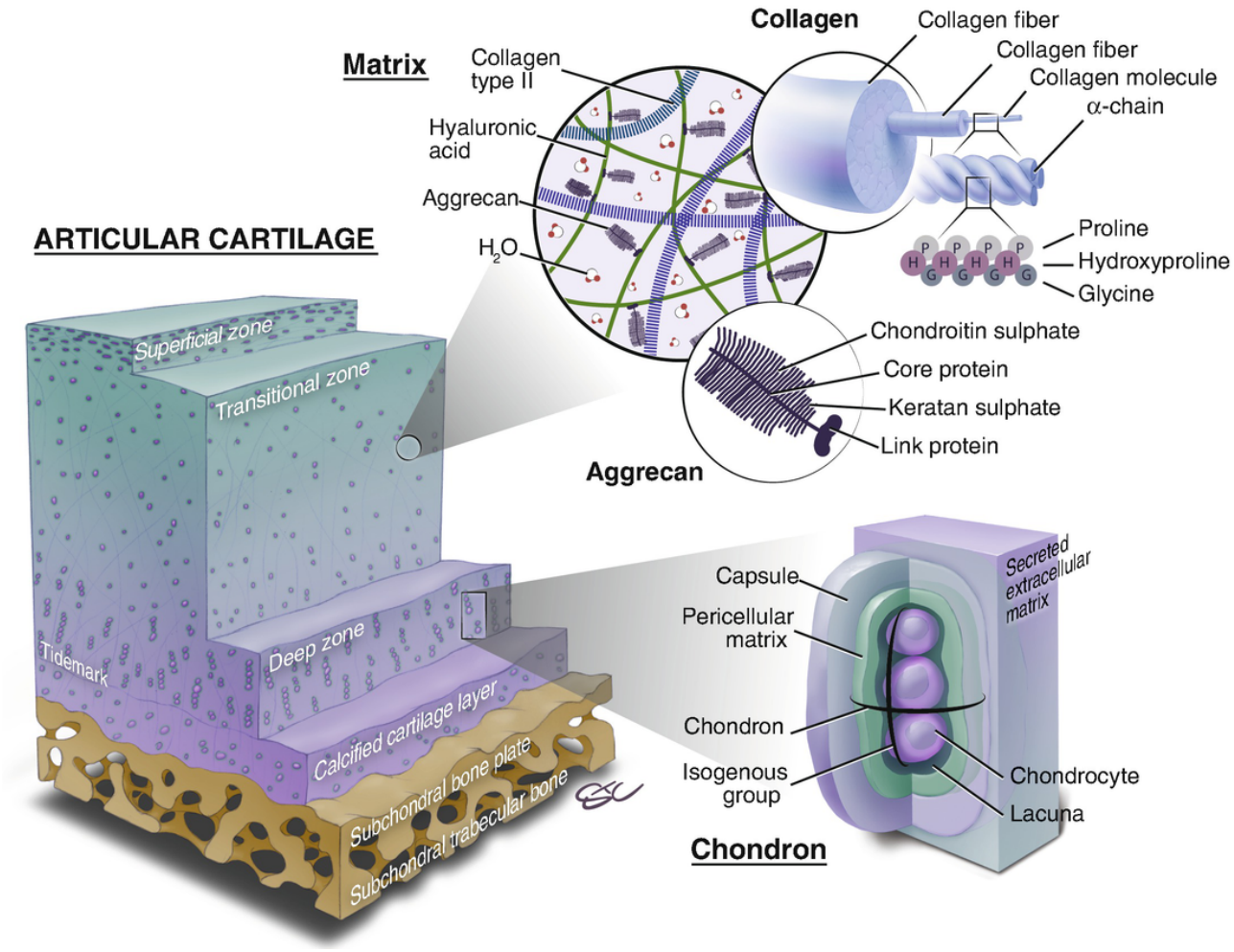

Figure 2: ***Structure of the osteochondral unit as reported in*** [34]. *The multi-layered architecture of hyaline cartilage, divided in morphologically distinct zones, and its interdigitation with calcified cartilage and subchondral bone are highlighted. Insets of cartilage extracellular matrix constituents at a molecular level are depicted.*

Articular Cartilage

Hyaline articular cartilage, that provides a smooth lubricated surface for joint articulation while distributing movement associated loads [35], is an avascular and aneural tissue constituted by a highly hydrated (water constitutes roughly 70% of the tissue volume [31]) extracellular matrix (ECM) rich in fibrillar collagens (mainly Collagen type II, Collagen type I on the articular surface, and smaller quantities collagen type VI, IX and XI), and proteoglycans (mainly aggrecan (ACAN), a glycosaminoglycan rich protein structure). Chondrocytes, the only sparse resident population, (accounting for only 1% of the cartilaginous tissues) are responsible for its homeostasis. The tissue is divided in different zones, namely (from the articular surface) superficial zone, intermediate and transitional zone, and deep zone, according to chondrocytes morphology and collagen structure and orientation [36].

In cartilage, OA causes an imbalance of catabolic and anabolic processes leading to an increased release of degrading enzyme such as matrix metalloproteinases (MMPs) (e.g. ADAMTS5, MMP9, MMP13), ECM

degradation, and tissue inflammation (mediated by IL6, IL8, and TNF-α). Cartilage also undergoes a developmental like process leading to chondrocytes hypertrophy, release of pro angiogenic factors, and bone morphogenic protein (BMP) and wingless and int-1 (Wnt) pathways dysregulation. Moreover, damage associated molecular patterns (DAMPS) trigger inflammatory responses [26].

Calcified cartilage

Calcified cartilage (CC) is a mineralized cartilaginous region that provides the attachment of cartilage to bone, allows the transmission of forces across the joint, and limits molecules diffusion from subchondral bone to hyaline cartilage [37]. CC, characterized by hypertrophic chondrocytes, is divided from articular cartilage by the tidemark [38], a thin wavy line appearing in histological sections and resulting from the barrier provided by CC to the transition of chondrocytes apoptotic bodies, phospholipids, alkaline phosphatase, adenosine triphosphatase, and DNA [38].

During OA, the CC advances into the overlaying hyaline articular cartilage, the tidemark duplicates, and the tissue is subjected to a vascular invasion hypothesized to be mediated by vascular endothelial growth factor A (VEGFA) [31]. CC was also reported to undergo hyper-mineralization as a consequence of OA [39].

Synovial membrane

The Synovial membrane (SM) is a thin adventitious layer lining non articulating surfaces of diarthrodial joints.

The healthy SM is constituted by one to three layers of specialized columnar synovial fibroblasts inter dispersed with synovial resident macrophages [40].

During OA the SM undergoes hyperplasia, fibrosis, and stroma neovascularization. The number of cells producing the inflammatory signals tumour necrosis factor alpha (TNFα) and interleukin 1 Beta (IL1β) significantly increases together with the expression of VEGF [41]. Furthermore, specific OA synovium cellular subpopulations exacerbate cartilage breakdown releasing a large variety of inflammatory mediators (e.g. IL6, IL1β, IL1α, EDN1, OSM, CXCL12, IL15, IL18, adipokines) [26, 42]

Subchondral bone

Subchondral bone (SB) is the portion of bone immediately underlying CC, and can be divided in subchondral bone plate and subchondral trabecular bone [34]. In OA, SB is subjected to formation of bone cysts, increase of subchondral plate thickness, trabecular mass changes, faster collagen turnover and hypomineralization.

Moreover, OA leads to bone marrow lesions characterized by fat necrosis, localized bone marrow fibrosis, and vascular changes associated with microfractures of the trabecular bone at various stages of healing [31]. While the molecular mechanisms driving bone sclerosis have not yet been completely uncovered, animal models of OA seemed to indicate that a pre-osteoclast-mediated increased production of platelet derived growth factor BB (PDGF-BB) drives angiogenesis dysregulation and alteration of bone cartilage cross-talks [43].

Mice models of OA also indicated dysregulation of the Wnt pathway as well as alteration of the tissue growth factor-beta (TGF-β) – BMP signalling in osteoblasts [44, 45]. Finally, in OA, osteocytes were reported to release membrane-derived lipids, chemokines, and VEGFA, as well as the receptor activator of the nuclear factor *k*appa-light-chain-enhancer of activated B cell (NFκB) ligand [32].

1.5 Modelling osteoarthritis, state of the art

Different *in vitro* and *in vivo* models of OA have been adopted to detect factors involved in OA pathogenesis and to evaluate potential treatment modalities [33, 46]. Animal models are commonly used owing to their capacity to reflect the natural occurring whole joint disease, recapitulating transient and long-term alterations in tissue structure and joint organization. Typical examples (mostly based on small animals like mice, rats, and rabbits) include age related models [47], joint instability models (e.g. obtained through anterior cruciate ligament transection ACLT or destabilization of the medial meniscus DMM) [48, 49], obesity models, and transgenic animal models [33][47]. Exploitation of knock-in or -out mouse strains for the mechanistic identification of target genes downstream networks, in particular, has significantly enhanced our understanding of the machinery underlying OA pathogenesis [50].

Animal models present however inherent differences in joint loading state and size, beside genetic dissimilarities, with respect to humans [50]. Such factors contribute to a limited translational power in accurately predicting the successful clinical introduction potential of OA drug candidates. Additionally, the associated high costs and time consumption, and the increasing tendency to refine, reduce and replace the use of animal models in preclinical studies (i.e. the adhesion to the 3R principles), together with the ease of manipulation of *in vitro* systems, render OA *in vitro* modelling highly desirable [46].

In vitro modes of OA can be broadly categorized in cytokine-based models and load based models [46]. During OA, synoviocytes, mononuclear cells, and chondrocytes may increase expression of catabolic proteins following stimuli such as cytokine or chemokine exposure which are present in the joint following synovial inflammation [51]. Pro-inflammatory cytokines are therefore the natural candidates for the induction of OA mimicking biological changes, allowing the determination of both concentration and temporal exposure effects. Cartilage degradation being typically recognized as OA predominant feature,

most models of OA are based exclusively on the supplementation of high levels of pro inflammatory compounds to chondrocytes, chiefly IL-1β and TNFα, but also IL6 and IL8. OA models where cytokines are the primary method for pathological traits induction are common, generally well understood, inexpensive and easily manipulated. Setups include chondrocytes monolayers, cartilage explants, and 3D engineered constructs [52–54]. Chondrocytes have however been demonstrated to dedifferentiate in 2D with an early shift towards a fibroblastic phenotype [55] while, conversely , explants imply a low sample numerosity. Furthermore, the outcome of biochemical studies involving cartilage explants has been demonstrated to be highly susceptible to the choice of sampling sites due to topological variations in the biochemical composition of cartilage and the metabolism of resident chondrocytes [56, 57]. 3D cytokine models are based either on high cell density micro-masses cultures (i.e. pellets) or on the encapsulation of primary chondrocytes or stem cells in biomaterial scaffolds. 3D cultures were demonstrated to better recapitulate OA phenotype *in vitro* with respect to 2D models [58]. The deposition of a cartilaginous like matrix, moreover, was correlated to a diminished release of degrative enzymes (e.g. MMP1 and MMP13) following cytokine administration, highlighting the presence of matrix dependent effects [59]. Adopted cytokine concentrations are nevertheless often aimed at obtaining a downstream effect rather than being representative of the low grade inflammatory state of OA patients synovial fluid [46].

While OA was characterized as affecting the whole osteochondral unit, only a few cytokines based models concentrated on the bone compartment. Exposure of osteoblasts to IL-1β demonstrated a link with an increase in degradative enzymes activity (e.g.MMP3 and MMP13) but the adopted models were limited to cellular monolayers and made use exclusively of animal cells or cell lines [60, 61].

Load based OA models were developed given the positive correlation between OA and mechanical risk factors. Loading was proven to be beneficial or detrimental to extracellular matrix homeostasis in a magnitude dependent manner. Mild mechanical stimulation acts as a potent inhibitor of IL-1β and TNFα mediated upregulation of inflammatory related gene transcription [62, 63]. Contrariwise, overloading can stimulate stress pathways leading to cytoskeleton disruption, activation of the pro-inflammatory gene transcription inducing the NF-κB signalling cascade [62], and release of inflammatory cytokines. The process is mediated by nitric oxide (NO), Prostaglandin E2 (PGE2) and reactive oxygen species [46].

Load based models, strain or stress controlled, have mainly been based on cartilage explants or on the loading of chondrocytes embedded in artificial matrices. Both static and cyclical loading was applied to cartilage explant correlating mechanical overload to a decrease in collagen type II (COL2A1) and ACAN deposition, and to an increase in the release of degradative enzymes (e.g. MMP3, MMP9 and MMP13). Applied strains ranged however from 25% to 50%, being hence superior even to pathological loading experienced by chondrocytes *in vivo,* and reflecting the necessity to obtain effects within a short time-frame [46]. Explant stress-controlled models on the other hand are affected by tissue properties variability.

Alternatively, load based models have been based on chondrocytes incorporated in artificial matrices, mainly agarose-based hydrogels, and stimulated through the use of bioreactors. Bioreactors based models of OA cartilage allowed to correlate cyclic loading (1KPa, 1 Hz) to activation of Erk1/2 and c-Jun N-terminal Kinase (JNK) resulting in MMP3 and 13 mRNA expression upregulation, and MMP13 mediated ECM degradation followed by an active anabolic process [64]. While this approach allows higher reproducibility and control over the loading parameters, removing cells from their native environment alters the ECM mediated signalling network [46].

As for bone loading models, loading was demonstrated to increase collagen type I (COL1A1) and PGE2 expression after stimulation in collagen gels seeded with osteocytes and layered with osteoblast [64], but limited data are reported in the literature.

Finally, a few cases of model comprehensive of a cartilaginous and a bone compartment were reported [59, 65]. As an example, alginate-embedded chondrocytes were observed to become more hypertrophic if co-cultured with mechanically stretched osteoblasts [62]. The majority of the studies, however, introduced models based on non-contact co-culture systems (such as transwells), while in the OCU cartilage and bone are directly superimposed and organized in a complex 3D architecture.

Generally, therefore, although considerable advances have been made in the development of OA cell culture models, the relevance of *in vitro* representations needs to be assessed with caution as demonstrated by the poor capacity of predicting drug responses in clinically relevant settings [6].

With the aim of mimicking OA *in vitro*, consequently, models should include 3D constructs rich in ECM components and possibly consisting of multiple tissues (e.g. cartilage and subchondral bone), and provide them with appropriate stimuli to recapitulate mechanotransduction related signalling.

Engineering of a single model with the enumerated features remains however a challenge. Moreover, the achievement of models where multiple concurrent factors are represented at a cellular relevant scale contrasts with the ultimate goal of developing models for the early phases of drug discovery and development campaigns where ease of use and experimental throughput (intrinsically limited by models complexity) are of paramount importance.

Microengineered OoC models enable the control of the cellular microenvironment with high spatiotemporal precision and the presentation of a variety of extracellular cues (e.g. mechanical stimuli) to cells cultured in a physiologically relevant context [7]. Moreover, they offer the possibility of having high number of replicates and limited time and money expenditures. A microengineered model of OA could serve as a promising tool for industry-compatible *in vitro* drug screening campaigns.

1.6 Organs-on-chip for cartilage bone and osteoarthritis modelling

OoCs were adopted for the realization of multicompartmental cellular structures [66] and mechanically active devices [20]. Microfluidic technologies are, hence, characterized as the ideal candidate for the development of OA models. Here are briefly described devices that broadly aimed at representing cartilage, bone or the osteochondral unit. Fig. 3 illustrates some examples of relevant platforms.

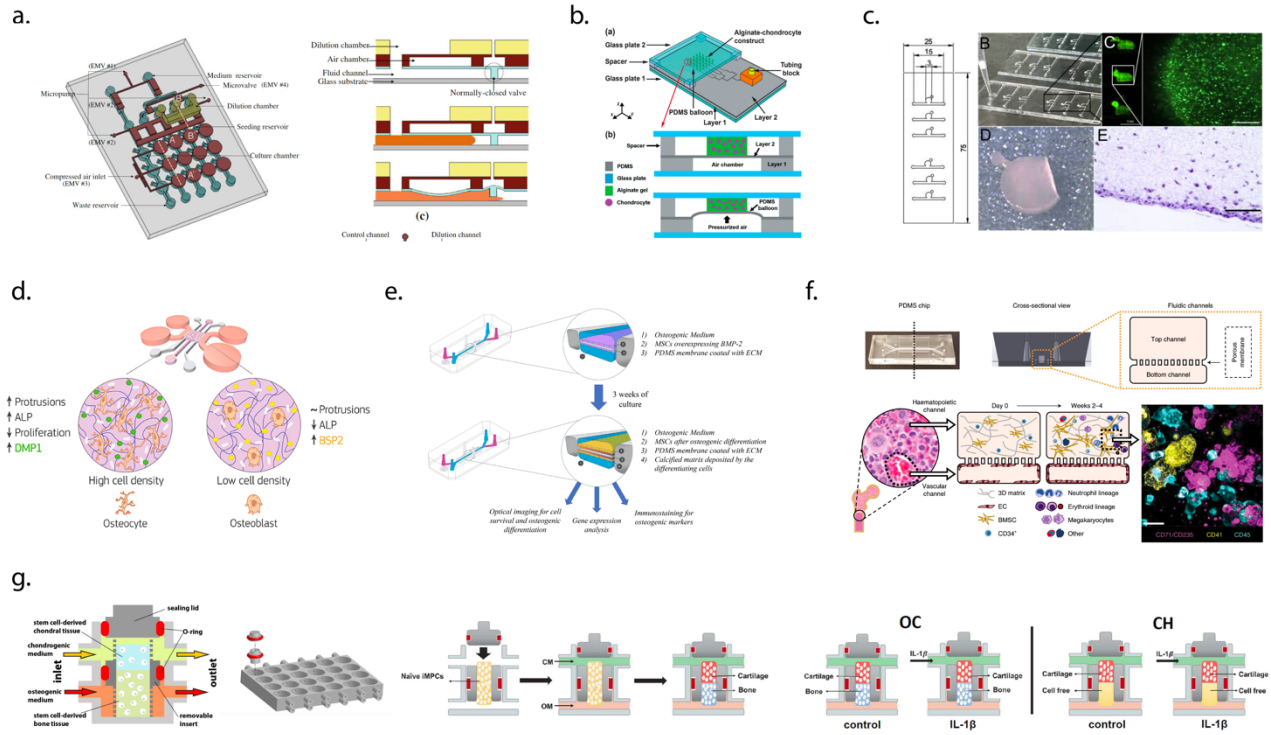

Figure 3: ***Microengineered platforms used to study models of cartilage, bone and osteochondral unit****.* ***a,***[67]. ***b,***[68]. ***c,***[69]. ***d,***[70]. ***g,***[71] *and* [72]. *Proposed devices included mechanical actuator systems, channels for the supplementation of chemical cues, compartments for tissues co-culture, and systems to achieve growth factors gradients.*

Wu et al. [67] reported a methodology to mechanically stimulate bone marrow derived Mesenchymal Stromal Cells (MSCs). The platform (Fig. 3a) was comprehensive of a dilution module and pneumatically modulated module for the application of shear stresses to 2D MSCs layers. While MSCs have been demonstrated to have trilinear differentiation capacity, Wu et al. aimed at adipogenic differentiation. A first example of mechanical stimulation of chondrocytes in an OoC platform was provided by Moraes et al. [73] and then by Leet al. [68] who proposed a device that allows unconfined compression of 3D cylindrical constructs laden with chondrocytes (Fig. 3b). More recently, Rosser et al. [69] reported the transient upregulation of MMP1, MMP3, MMP13 and ADAMTS5 following exposure to IL-1β and TNFα of chondrocytes constructs in a microfluidic device [69] (Fig. 3c). Presented models were however based on the adoption of animal derived cells and the achievement of a cartilage like ECM was not demonstrated.

As regards bone on chip models, a variety of devices have been proposed with the aim of investigating bone cells functions, bone regeneration and tissue engineering possibilities, and for the study of bone vasculature and innervation and that of cancer metastasis to bone [74] (Fig. 3d, e, f). Nasello et al. investigated the effects of osteoblasts seeding density on cellular differentiation [70], while Sheyn et al. [75] demonstrated the outcomes of fluid induced shear stress on MSCs osteogenic differentiation in monolayer. The systems were however limited by the use of 2D cell cultures or by short culture times. More advanced studies on bone on chip were dedicated specifically to the study of bone marrow. A human bone-marrow-on-a-chip was demonstrated to support the differentiation and maturation of multiple blood cell lineages recapitulating myeloerythroid toxicity after clinically relevant exposures to chemotherapeutic drugs and ionizing radiation [76].

A first model of osteochondral unit on chip was developed by Lin et al [71]. The authors reported the achievement of an MSCs derived osteochondral like construct in a perfusion-based bioreactors. The same platform was exploited to obtain osteochondral constructs from induced pluripotent stem cells (iPSCs) [72].

1.7 Funding technologies: Organs-on-chip models allowing tissues compartmentalization, mechanical actuation and higher throughput

As discussed, relevant OA models would require the adoption of multiple tissues and a mechanically active environment (Fig. 4).

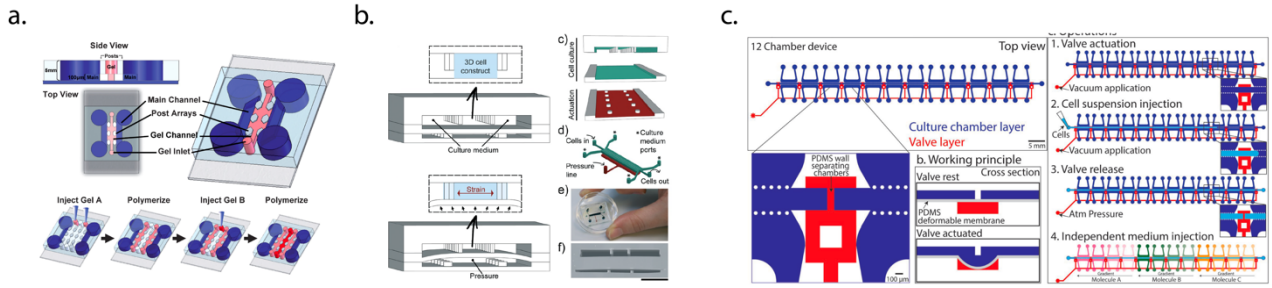

Figure 4: ***Organs-on-chip models featuring innovative technological concepts****. Exemplificative platforms showing how to achieve multiple directly interfaced tissues**(a)** and defined mechanical stimulation of 3D construct **(b)**. While these methodologies were adopted respectively to study cancer metastatic processes* [66] *and cardia physiology* [20]*, it would be possible possibly to translate the presented concepts to the study of OA. An example of a multi-chamber device increasing the possible throughput of OoC models is also depicted **(c)*** [77].

While these features were never reported for *in vitro* models directly aimed at studying joint tissues or OA, technologies which could be adapted for the purpose were introduced with different biological aims. Huang et al. devised a system to pattern multiple discrete but directly contacting 3D constructs [66] which was originally destined at studying breast cancer metastatic behaviour. Marsano et al. [20] introduced a device with a pneumatic compartment allowing defined level of cyclical stretching to be applied to cardiac microconstructs. Both of these concepts could be adapted for the achievement of biological aspects relevant

to OA, that is to say the involvement of multiple tissues and the mechanically active joint environment. Finally, while most OoC models are limited to single unit devices, Visone et. al [77] introduced a methodology to incorporate multiple independent chambers in the same device while minimising the required handling operations.

1.8 Motivation and outline of the thesis

The advent of OoC devices has allowed the development of relevant organ and disease models ranging from gut [22] and lungs [21] to bone marrow [76]. Yet, models of mechanically active musculoskeletal districts are still rare given the intrinsic complexity of providing physiologically significant physical stimuli to 3D tissues.

Case in point, a satisfactory *in vitro* model of OA is still absent. Given its characterization as a whole joint disease and the association between OA and mechanical risk factors, a clinically relevant OA *in vitro* model should (i) incorporate multiple tissues such as cartilage and subchondral layers, and (ii) recapitulate the aberrant strains which are associated with an impaired joint mechanics. The development of a model with these requirement remains however a challenge and this deficiency correlates with the lack of satisfactory disease modifying OA treatments.

Moreover, while providing a finely controlled cellular microenvironment, most OoCs are still based on single-unit platforms precluding their exploitation as high throughput tools in drug discovery campaigns. This tendency seems exacerbated when technologically demanding active mechanical cues are necessary.

In the present PhD project microfabrication techniques and OoCs technologies were exploited to develop advanced disease models of mechanically active body districts focusing primarily on osteoarthritis, and aiming at platforms coupling a clinically relevant recapitulation of the *in vivo milieu* with a sufficient experimental throughput.

Performed activities were inserted in the context of an international collaboration between Politecnico di Milano and the University of Basel-University hospital of Basel in the framework of a double PhD program. In details, the final aim was subdivided into five conceptual blocks which are presented separately in the chapters of this dissertation. Each chapter focuses on a specific platform and/or technique developed *ad hoc* to deepen the present knowledge on OA or to provide a specific technological advancement.

In Chapter 2 the hypothesis that a model of OA cartilage could be achieved in an OoC device was addressed. A mechanically active microfluidic device was exploited to generate a healthy cartilage on chip model. The correlation between OA and mechanical risk factors was then studied inducing OA traits through the sole application of hyperphysiological loading. The platform was tested in the evaluation of construct responses to known and innovative anti OA compounds assessing its potentiality as a drug screening tool.

In Chapter 3 was affronted the issue of an increased throughput for mechanically active devices. A modified version of the model presented in Chapter 2 was designed to comprise multiple independent chambers. As a proof of concept, the device was exploited in the development of a model of cardiac fibrosis on chip

studying the effect of co-culturing cardiomyocytes and fibroblast in the assumption of a hypertrophic phenotype. The platform was then modified for its application in cartilage compression.

In Chapter 4 a direct assessment of the alterations happening in the osteochondral unit of OA patients undergoing total or uni-condyle knee arthroplasty was performed. Modifications in terms of tissues composition, morphology and mechanical properties were investigated. A workflow to couple assessments of samples OA grade based on quantitative macroscale morphological parameters with microscale mechanical properties was established. Specifically, indentation type atomic force microscopy was adopted to assess OA related variations in the elastic modulus of the different tissues constituting the osteochondral unit focusing on a dimensional scale relevant for developing future complex OA models based on the OoC technology

In Chapter 5 a new microfluidic concept allowing the mechanical stimulation of complex bilayer 3D construct was proposed. The platform was validated demonstrating that well-differentiated and discrete compression levels reminiscent of the OCU deformation *in vivo* can be applied to cartilaginous microconstructs thus modulating their mechanotransduction signalling activation. The model was moreover exploited in a proof-of-concept demonstration that alterations in the local mechanical properties of subchondral layers modulate chondrocytes response to loading.

In Chapter 6 previously developed techniques and platforms, united with a purposely developed differentiation protocol, were exploited for the generation of an OoC based model of OCU comprehensive of a cartilaginous microconstruct and a mineralized calcified layer or a vascularized subchondral layer. A preliminary assessment of the induction of OA traits in this complex osteochondral OA model was also provided.

In the last chapter a general discussion of the PhD dissertation and conclusive remarks are provided.

1.9 References

1. Takebe T, Imai R, Ono S (2018) The Current Status of Drug Discovery and Development as Originated in United States Academia: The Influence of Industrial and Academic Collaboration on Drug Discovery and Development. Clin Transl Sci 11:597–606. https://doi.org/10.1111/cts.12577
2. Morgan S, Grootendorst P, Lexchin J, et al (2011) The cost of drug development: A systematic review. Health Policy (New York) 100:4–17. https://doi.org/10.1016/J.HEALTHPOL.2010.12.002
3. Wouters OJ, McKee M, Luyten J (2020) Estimated Research and Development Investment Needed to Bring a New Medicine to Market, 2009-2018. JAMA 323:844–853. https://doi.org/10.1001/JAMA.2020.1166
4. Dierynck B, Joos P (2020) Research and Development Costs of New Drugs. JAMA 324:516–517. https://doi.org/10.1001/JAMA.2020.8642
5. Probst C, Schneider S, Loskill P (2018) High-throughput organ-on-a-chip systems: Current status and remaining challenges. Curr. Opin. Biomed. Eng. 6:33–41
6. Horvath P, Aulner N, Bickle M, et al (2016) Screening out irrelevant cell-based models of disease. Nat Rev Drug Discov 15:751–769. https://doi.org/10.1038/nrd.2016.175
7. Esch EW, Bahinski A, Huh D (2015) Organs-on-chips at the frontiers of drug discovery. Nat Rev Drug Discov 2015 144 14:248–260. https://doi.org/10.1038/nrd4539
8. Lancaster MA, Knoblich JA (2014) Organogenesisin a dish: Modeling development and disease using organoid technologies. Science (80-) 345:. https://doi.org/10.1126/SCIENCE.1247125
9. Martin I, Wendt D, Heberer M (2004) The role of bioreactors in tissue engineering. Trends Biotechnol 22:80–86. https://doi.org/10.1016/J.TIBTECH.2003.12.001
10. Pörtner R, Nagel-Heyer S, Goepfert C, et al (2005) Bioreactor design for tissue engineering. J Biosci Bioeng 100:235–245. https://doi.org/10.1263/JBB.100.235
11. Hoshijima M (2006) Mechanical stress-strain sensors embedded in cardiac cytoskeleton: Z disk, titin, and associated structures. https://doi.org/101152/ajpheart008162005 290:1313–1325. https://doi.org/10.1152/AJPHEART.00816.2005
12. Andriacchi TP, Mündermann A (2006) The role of ambulatory mechanics in the initiation and progression of knee osteoarthritis. Curr Opin Rheumatol 18:514–518. https://doi.org/10.1097/01.BOR.0000240365.16842.4E
13. Huh D, Kim HJ, Fraser JP, et al (2013) Microfabrication of human organs-on-chips. Nat Protoc 8:2135–2157. https://doi.org/10.1038/nprot.2013.137
14. Whitesides GM (2006) The origins and the future of microfluidics. Nat 2006 4427101 442:368–373. https://doi.org/10.1038/nature05058
15. Karl Fluri †, Glen Fitzpatrick ‡, Nghia Chiem † and, D. Jed Harrison* † (1996) Integrated Capillary Electrophoresis Devices with an Efficient Postcolumn Reactor in Planar Quartz and Glass Chips. Anal Chem 68:4285–4290. https://doi.org/10.1021/AC9604090
16. Xia Y, Whitesides GM (1998) SOFT LITHOGRAPHY. Annu Rev Mater Sci 28:153–84
17. and JCM, Whitesides* GM (2002) Poly(dimethylsiloxane) as a Material for Fabricating Microfluidic Devices. Acc Chem Res 35:491–499. https://doi.org/10.1021/AR010110Q
18. Occhetta P, Centola M, Tonnarelli B, et al (2015) High-Throughput Microfluidic Platform for 3D Cultures of Mesenchymal Stem Cells, Towards Engineering Developmental Processes. Sci Reports 2015 51 5:1–12. https://doi.org/10.1038/srep10288
19. (2021) Micro-electrode channel guide (μECG) technology: an online method for continuous electrical recording in a human beating heart-on-chip. https://doi.org/10.1088/1758-5090/abe4c4
20. Marsano A, Conficconi C, Lemme M, et al (2016) Beating heart on a chip: a novel microfluidic platform to generate functional 3D cardiac microtissues. Lab Chip 16:599–610
21. Huh D, Matthews BD, Mammoto A, et al (2010) Reconstituting organ-level lung functions on a chip. Science (80-) 328:1662–1668. https://doi.org/10.1126/science.1188302
22. HJ K, DE I (2013) Gut-on-a-Chip microenvironment induces human intestinal cells to undergo villus differentiation. Integr Biol (Camb) 5:1130–1140. https://doi.org/10.1039/C3IB40126J
23. Herland A, Maoz BM, Das D, et al (2020) Quantitative prediction of human pharmacokinetic responses to drugs via fluidically coupled vascularized organ chips. Nat Biomed Eng 1–16. https://doi.org/10.1038/s41551-019-0498-9
24. Kloppenburg M, Berenbaum F (2020) Osteoarthritis year in review 2019: epidemiology and therapy. Osteoarthr Cartil 28:242–248. https://doi.org/10.1016/j.joca.2020.01.002
25. Vina ER, Kwoh CK (2018) Epidemiology of Osteoarthritis: Literature Update. Curr Opin Rheumatol 30:160. https://doi.org/10.1097/BOR.0000000000000479
26. Robinson WH, Lepus CM, Wang Q, et al (2016) Low-grade inflammation as a key mediator of the pathogenesis of osteoarthritis. Nat Rev Rheumatol 12:580–592. https://doi.org/10.1038/nrrheum.2016.136
27. Helmick CG, Felson DT, Lawrence RC, et al (2008) Estimates of the prevalence of arthritis and other rheumatic conditions in the United States: Part I. Arthritis Rheum 58:15–25. https://doi.org/10.1002/ART.23177
28. Wittenauer R, Smith L, Aden K (2013) Background Paper 6.12 Osteoarthritis
29. Zhang Y, Jordan JM (2010) Epidemiology of Osteoarthritis. Clin Geriatr Med 26:355. https://doi.org/10.1016/J.CGER.2010.03.001
30. Loeser RF, Goldring SR, Scanzello CR, Goldring MB (2012) Osteoarthritis: A Disease of the Joint as an Organ. Arthritis Rheum 64:1697. https://doi.org/10.1002/ART.34453
31. Goldring SR, Goldring MB (2016) Changes in the osteochondral unit during osteoarthritis: structure, function and cartilage–bone crosstalk. Nat Rev Rheumatol 12:632–644. https://doi.org/10.1038/nrrheum.2016.148
32. Goldring SR, Goldring MB (2016) Changes in the osteochondral unit during osteoarthritis: Structure, function and cartilage bone crosstalk. Nat. Rev. Rheumatol. 12:632–644
33. He Y, Li Z, Alexander PG, et al (2020) Pathogenesis of Osteoarthritis: Risk Factors, Regulatory Pathways in Chondrocytes, and Experimental Models. Biol 2020, Vol 9, Page 194 9:194. https://doi.org/10.3390/BIOLOGY9080194
34. Baumann CA, Hinckel BB, Bozynski CC, Farr J (2019) Articular Cartilage: Structure and Restoration. Jt Preserv Knee A Clin Caseb 3–24. https://doi.org/10.1007/978-3-030-01491-9_1
35. Sanchez-Adams J, Leddy HA, McNulty AL, et al (2014) The Mechanobiology of Articular Cartilage: Bearing the Burden of Osteoarthritis. Curr Rheumatol Rep 16:451. https://doi.org/10.1007/S11926-014-0451-6

36. Poole AR, Pidoux I, Reiner A, Rosenberg L (1982) An immunoelectron microscope study of the organization of proteoglycan monomer, link protein, and collagen in the matrix of articular cartilage. J Cell Biol 93:921. https://doi.org/10.1083/JCB.93.3.921
37. Oegema TR, Carpenter RJ, Hofmeister F, Thompson RC (1997) The interaction of the zone of calcified cartilage and subchondral bone in osteoarthritis. Microsc Res Tech 37:324–332. https://doi.org/10.1002/(SICI)1097-0029(19970515)37:4<324::AID-JEMT7>3.0.CO;2-K
38. Simkin PA (2012) Consider the Tidemark. J Rheumatol Rheumatol J March 39:890–892. https://doi.org/10.3899/jrheum.110942
39. Ferguson VL, Bushby AJ, Boyde A (2003) Nanomechanical properties and mineral concentration in articular calcified cartilage and subchondral bone. J Anat 203:191–202. https://doi.org/10.1046/j.1469-7580.2003.00193.x
40. C O, E V-S, DL B, et al (2017) Synovial tissue research: a state-of-the-art review. Nat Rev Rheumatol 13:463–475. https://doi.org/10.1038/NRRHEUM.2017.115
41. MJ B, DJ V, O F, et al (2005) Synovial tissue inflammation in early and late osteoarthritis. Ann Rheum Dis 64:1263–1267. https://doi.org/10.1136/ARD.2004.025270
42. Chou C-H, Jain V, Gibson J, et al (123AD) Synovial cell cross-talk with cartilage plays a major role in the pathogenesis of osteoarthritis. https://doi.org/10.1038/s41598-020-67730-y
43. W S, G L, X L, et al (2020) Angiogenesis stimulated by elevated PDGF-BB in subchondral bone contributes to osteoarthritis development. JCI insight 5:. https://doi.org/10.1172/JCI.INSIGHT.135446
44. Wu M, Chen G, Li Y-P (2016) TGF-β and BMP signaling in osteoblast, skeletal development, and bone formation, homeostasis and disease. Bone Res 2016 41 4:1–21. https://doi.org/10.1038/boneres.2016.9
45. Y W, X F, L X, F T (2019) Wnt signaling: a promising target for osteoarthritis therapy. Cell Commun Signal 17:. https://doi.org/10.1186/S12964-019-0411-X
46. CI J, DJ A, DN C (2016) In vitro models for the study of osteoarthritis. Vet J 209:40–49. https://doi.org/10.1016/J.TVJL.2015.07.011
47. O'conor CJ, Ramalingam S, Zelenski NA, et al (2016) Cartilage-Specific Knockout of the Mechanosensory Ion Channel TRPV4 Decreases Age-Related Osteoarthritis. https://doi.org/10.1038/srep29053
48. Appleyard RC, Ghosh P, Swain M V. (1999) Biomechanical, histological and immunohistological studies of patellar cartilage in an ovine model of osteoarthritis induced by lateral meniscectomy. Osteoarthr Cartil 7:281–294. https://doi.org/10.1053/JOCA.1998.0202
49. DL B, A K, S L, et al (2004) Ex vivo characterization of articular cartilage and bone lesions in a rabbit ACL transection model of osteoarthritis using MRI and micro-CT. Osteoarthr Cartil 12:986–996. https://doi.org/10.1016/J.JOCA.2004.08.010
50. Little CB, Hunter DJ (2013) Post-traumatic osteoarthritis: from mouse models to clinical trials. Nat Rev Rheumatol 2013 98 9:485–497. https://doi.org/10.1038/nrrheum.2013.72
51. Sohn DH, Sokolove J, Sharpe O, et al (2012) Plasma proteins present in osteoarthritic synovial fluid can stimulate cytokine production via Toll-like receptor 4. Arthritis Res Ther 2012 141 14:1–13. https://doi.org/10.1186/AR3555
52. B B, PM G, J H, et al (2002) Relative messenger RNA expression profiling of collagenases and aggrecanases in human articular chondrocytes in vivo and in vitro. Arthritis Rheum 46:2648–2657. https://doi.org/10.1002/ART.10531
53. AM R, C S-R, A D, et al (1993) Transcriptional modulation of cartilage-specific collagen gene expression by interferon gamma and tumour necrosis factor alpha in cultured human chondrocytes. Biochem J 294 (Pt 3:761–769. https://doi.org/10.1042/BJ2940761
54. Goldring MB, Fukuo K, Birkhead JR, et al (1994) Transcriptional suppression by interleukin-1 and interferon-γ of type II collagen gene expression in human chondrocytes. J Cell Biochem 54:85–99. https://doi.org/10.1002/JCB.240540110
55. VON DER MARK K, GAUSS V, VON DER MARK H, MÜLLER P (1977) Relationship between cell shape and type of collagen synthesised as chondrocytes lose their cartilage phenotype in culture. Nat 1977 2675611 267:531–532. https://doi.org/10.1038/267531a0
56. Brama PAJ, Tekoppele JM, Bank RA, et al (2000) Topographical mapping of biochemical properties of articular cartilage in the equine fetlock joint. Equine Vet J 32:19–26. https://doi.org/10.2746/042516400777612062
57. BA R, CL M, SR C, TW B (2006) Topographical variation in glycosaminoglycan content in human articular cartilage. J Bone Joint Surg Br 88:1670–1674. https://doi.org/10.1302/0301-620X.88B12.18132
58. Yeung P, Cheng KH, Yan CH, Chan BP (2019) Collagen microsphere based 3D culture system for human osteoarthritis chondrocytes (hOACs). Sci Reports 2019 91 9:1–14. https://doi.org/10.1038/s41598-019-47946-3
59. S F, C C, B G, et al (2011) Engineered cartilage maturation regulates cytokine production and interleukin-1β response. Clin Orthop Relat Res 469:2773–2784. https://doi.org/10.1007/S11999-011-1826-X
60. E P, S P, Z M, et al (2012) A potential role of chondroitin sulfate on bone in osteoarthritis: inhibition of prostaglandin E_2 and matrix metalloproteinases synthesis in interleukin-1β-stimulated osteoblasts. Osteoarthr Cartil 20:127–135. https://doi.org/10.1016/J.JOCA.2011.12.002
61. Damoulis PD, Hauschka P V. (1994) Cytokines induce nitric oxide production in mouse osteoblasts. Biochem Biophys Res Commun 201:924–931. https://doi.org/10.1006/BBRC.1994.1790
62. S A, J D, P L, et al (2004) Role of NF-kappaB transcription factors in antiinflammatory and proinflammatory actions of mechanical signals. Arthritis Rheum 50:3541–3548. https://doi.org/10.1002/ART.20601
63. Long P, Gassner R, Agarwal S (2001) Tumor Necrosis Factor-Dependent Proinflammatory Gene Induction Is Inhibited by Cyclic Tensile Strain in Articular Chondrocytes In Vitro. ARTHRITIS Rheum 44:2311–2319. https://doi.org/10.1002/1529-0131
64. De Croos JNA, Dhaliwal SS, Grynpas MD, et al (2006) Cyclic compressive mechanical stimulation induces sequential catabolic and anabolic gene changes in chondrocytes resulting in increased extracellular matrix accumulation. Matrix Biol 25:323–331. https://doi.org/10.1016/J.MATBIO.2006.03.005
65. YY L, N T, S O, et al (2010) Applying an excessive mechanical stress alters the effect of subchondral osteoblasts on chondrocytes in a co-culture system. Eur J Oral Sci 118:151–158. https://doi.org/10.1111/J.1600-0722.2010.00710.X
66. Huang CP, Lu J, Seon H, et al (2009) Engineering microscale cellular niches for three-dimensional multicellular co-cultures. Lab Chip 9:1740–1748. https://doi.org/10.1039/b818401a
67. Wu H-W, Lin C-C, Hwang S-M, et al (2011) A microfluidic device for chemical and mechanical stimulation of mesenchymal stem cells. Microfluid Nanofluidics 2011 115 11:545–556. https://doi.org/10.1007/S10404-011-0820-7
68. Lee D, Erickson A, You T, et al (2018) Pneumatic microfluidic cell compression device for high-throughput study of chondrocyte mechanobiology. Lab Chip 18:2077–2086. https://doi.org/10.1039/C8LC00320C
69. Rosser J, Bachmann B, Jordan C, et al (2019) Microfluidic nutrient gradient–based three-dimensional chondrocyte culture-on-a-chip as an in vitro equine arthritis model. Mater Today Bio 4:. https://doi.org/10.1016/J.MTBIO.2019.100023
70. Nasello G, Alamán-Díez P, Schiavi J, et al (2020) Primary Human Osteoblasts Cultured in a 3D Microenvironment Create a Unique

Representative Model of Their Differentiation Into Osteocytes. Front Bioeng Biotechnol 0:336. https://doi.org/10.3389/FBIOE.2020.00336
71. H L, TP L, PG A, et al (2014) Stem cell-based microphysiological osteochondral system to model tissue response to interleukin-1β. Mol Pharm 11:2203–2212. https://doi.org/10.1021/MP500136B
72. Lin Z, Li Z, Li EN, et al (2019) Osteochondral Tissue Chip Derived From iPSCs: Modeling OA Pathologies and Testing Drugs. Front Bioeng Biotechnol 0:411. https://doi.org/10.3389/FBIOE.2019.00411
73. Moraes C, Wang G, Sun Y, Simmons CA (2010) A microfabricated platform for high-throughput unconfined compression of micropatterned biomaterial arrays. Biomaterials 31:577–584. https://doi.org/10.1016/J.BIOMATERIALS.2009.09.068
74. Mansoorifar A, Gordon R, Bergan RC, Bertassoni LE (2021) Bone-on-a-Chip: Microfluidic Technologies and Microphysiologic Models of Bone Tissue. Adv Funct Mater 31:. https://doi.org/10.1002/ADFM.202006796
75. Sheyn D, Cohn-Yakubovich D, Shiran Ben-David ·, et al (2019) Bone-chip system to monitor osteogenic differentiation using optical imaging Graphic abstract Keywords Organ-on-a-chip · Mesenchymal stem cells · Osteogenesis · Optical Imaging. 1:3. https://doi.org/10.1007/s10404-019-2261-7
76. Chou DB, Frismantas V, Milton Y, et al (2020) On-chip recapitulation of clinical bone marrow toxicities and patient-specific pathophysiology. Nat Biomed Eng 2020 44 4:394–406. https://doi.org/10.1038/s41551-019-0495-z
77. Visone R, Ugolini GS, Vinarsky V, et al (2019) A Simple Vacuum-Based Microfluidic Technique to Establish High-Throughput Organs-On-Chip and 3D Cell Cultures at the Microscale. Adv Mater Technol 4:1800319. https://doi.org/10.1002/admt.201800319

2 *Hyperphysiological compression of articular cartilage induces an osteoarthritic phenotype in a cartilage-on-a-chip model*

The work described in this chapter was carried out in the framework of a collaboration between the Microfluidic and Biomimetic Microsystems Laboratory of Politecnico di Milano, (Milan, Italy) and the Tissue Engineering Laboratory of the University Hospital of Basel (Basel, Switzerland).

This chapter partially refers to:

Hyperphysiological compression of articular cartilage induces an osteoarthritic phenotype in a cartilage-on-a-chip model. Paola Occhetta$, Andrea Mainardi$, Emiliano Votta, Queralt Vallmajo-Martin, Martin Ehrbar, Ivan Martin, Andrea Barbero & Marco Rasponi

Nat Biomed Eng 3, 545–557 (2019). https://doi.org/10.1038/s41551-019-0406-3

$ Equally contributing authors

and to:

Mechanical induction of osteoarthritis traits in a cartilage on chip model. Andrea Mainardi, Paola Occhetta & Marco Rasponi.

Methods in Molecular Biology 2022, 2373, pp. 231–251 https://doi.org/10.1007/978-1-0716-1693-2_14

2.1 Introduction

Osteoarthritis (OA) is the most prevalent human musculoskeletal disease [1]. The incidence of symptomatic OA is expected to increase due to the aging of the population, making OA the worldwide fifth leading cause of disability [2]. Given the high prevalence, the current absence of an effective pathology-reversing treatment makes the research for new therapies extremely urgent.

While promising disease modifying anti-OA drugs able to stop or revert OA's degenerative tendency are under investigation [3, 4], their preclinical to clinical translation is still a major obstacle.

This is strictly linked to the lack of reliable and representative surrogate disease models that would allow both to faithfully test drugs response once *in vivo* and to help unravel OA's origin and mechanisms of progression in order to find effective therapeutic solutions [5].

A whole joint pathological active response to environmental factors, being abnormal mechanical loading and oxidative stresses among the most relevant, characterize the multifactorial disease [6]. Such factors trigger an unbalance of anabolic/catabolic activities, which causes a dysfunction of articular chondrocytes and the onset of inflammation, eventually resulting in cartilage degeneration and alterations of subchondral bone, synovium and ligaments [7]. The multifactorial etiology of the disease increases the difficulty in generating relevant pre-clinical models of OA [5]. *In vivo* models provide a better reflection of the naturally-occurring whole-joint disease, but they are costly and time consuming; furthermore, the application of 3R principles in preclinical studies makes *in vitro* modeling of the disease highly desirable [8]. However, currently available *in vitro* reproductions are too simplistic and often fail in predicting drug candidates effects, thus calling for more complex and physiologically relevant systems [5].

The lack of a clear knowledge of OA mechanisms of origin, and the observation that cartilage alterations are the prevalent pathological modifications make the case for the introduction of an OA cartilage model.

Articular cartilage's extracellular matrix (ECM) is a complex environment whose biochemical composition and hierarchical structure allow a lifelong withstanding of cyclic loading with up to 300% of the body weight [9, 10]. Specifically, cartilage ECM is composed by a fluid phase consisting of water and electrolytes, and a solid phase, primarily constituted by fibrillar and non-fibrillar collagens (mainly collagen type-II and type-I, but also type-VI, IX and XI), negatively charged proteoglycans (PGs) (mostly aggrecan and lubricin) and hyaluronic acid [6, 10]. Physiological compression of articular cartilage induces a complex mechanical environment that is characterized by stresses, strains, osmotic and hydrostatic pressures, interstitial fluid flow and electrokinetic effects varying in time and space [10–12].

In OA the degenerative processes lead to an alteration of the anabolism-catabolism balance which brings to degradation of cartilage extracellular matrix (ECM) (e.g. through an alteration of collagen type II to collagen type I ratio and a decrease in the glycosaminoglycan content of the tissue), augmented production of degradative enzymes (e.g. metalloproteinases such as MMP13), and onset of tissue inflammation (e.g.

increase in production of inflammatory cytokines such as IL6 and IL8) [13–15]. Moreover, chondrocytes, cartilage resident cells, upregulate the production of hypertrophic markers such as collagen type X, eventually resulting in another OA hallmark: cartilage calcification [16].

Lately, three-dimensional (3D) macroscale systems integrating cells, soluble factors and ECM-like matrices have been used to model articular cartilage, aiming at recapitulating both cellular specific architecture and mechanical environment [11, 17, 18]. Whilst holding huge promises as grafts to promote repair of joint injuries [19, 20], the generation of such engineered cartilage constructs requires bioreactor systems which may be bulky and hard-to-use, thus prevent their wide-spreading as *in vitro* models and drug screening tools [21].

Difficulties in reproducing *in vitro* a cartilaginous tissue increase when trying to recapitulate a pathological, OA cartilage status. Of commonly adopted OA representation, cytokine-based and load-based models, cytokine-based models are built on over-dosages of inflammatory cocktails, which induce a downstream effect rather than recapitulating the actual OA environment found *in vivo*[5]. On the other hand, load-based models hold the potentiality of triggering an OA-like response without the need for supraphysiological doses of biochemical stimuli. Indeed, increasing evidence correlates mechanical abnormalities such as obesity, trauma, or joint misalignment to OA onset [6], classifying the biomechanical environment as a key player involved in disease evolution. Load-based models introduced so far are largely based on macroscale bioreactors and were instrumental in defining a background of the mechanisms involved in the pathological load response [22, 23]. However, they often fail in finely tuning the stimuli provided to the tissue and thus in capturing the native joint physiological/pathological environment [24]. Existing load control systems, on one side, do not account for pathophysiological levels of compression, while strain-controlled devices are affected by reaction forces largely dependent on scaffolds' mechanical responses [5].

Organs-on-chip (OoCs) are able to recapitulate organ functions into microscale platforms, with unprecedented adherence to pathophysiological conditions [8, 25]. Recent advances in microfabrication techniques allowed to precisely control the 3D architecture of cellular compartments [26] while integrating medium perfusion, delivery of soluble factors, and accurate biophysical stimulation (i.e. 3D mechanical stimuli) [27–29]. These characteristics render the organs-on-chip technology an extremely promising candidate for pre-clinical disease modelling. Furthermore, the micrometric scale confers OoCs the advantages of reduced reagents requirement and ease of manipulation, which makes them particularly appropriate for high-throughput discovery campaigns [30]

In this chapter, a microscale platform able to reproducibly generate *in vitro* models of human Cartilage-on-Chip (CoC) was developed. Through the proposed mechanically active system OA traits could be induced in the CoC model. Both shifting in matrix deposition/resorption balance towards catabolism and triggering of a gene profile correlated with clinical OA evidences were obtained, recapitulating the main components

of cartilage deformation involved in OA pathogenesis, specifically compression. Clinically approved and under-development anti-inflammatory/anti-degrading drugs were administered to the established osteoarthritic CoC model proving its potentiality to serve as an effective pre-clinical tool for testing new disease modifying drug candidates in a predictive fashion.

2.2 Microfluidic platform design and fabrication

2.2.1 Device concept: A microscale platform for 3D mechanical confined compression

A microscale platform to apply a uniform and confined mechanical compression to a 3D cartilage microconstruct was ideated. The assembled device comprises two chambers divided by a flexible membrane (Fig. 1a): i) an upper culture chamber hosting the 3D microconstruct, and ii) a lower chamber exploited as actuation compartment. Specifically, the culture chamber consists in a central channel hosting the 3D microconstruct (Fig. 1b, c blue channel), surrounded by two side channels for culture medium supplementation (Fig. 1b, c red channels). Based on a concept previously developed by our group [29], the central channel is limited by two parallel arrays of hanging posts, conceived with the double function of i) confining a cell-laden pre-polymer solution throughout the seeding and polymerization phases and subsequently ii) defining a stroke length controlling the mechanical actuation mechanism. In rest position (Fig. 1d), a gap divides the hanging posts from the flexible membrane, maintaining the 3D microconstruct in a relaxed state. Upon pressurization of the actuation compartment, the flexible membrane bends upwards till it abuts against the posts' bottom ends (Fig. 1e), causing a confined compression of the 3D microconstruct. When the pressure is released, elastic recoil causes the membrane and the 3D microconstruct to relax to their original rest configurations.

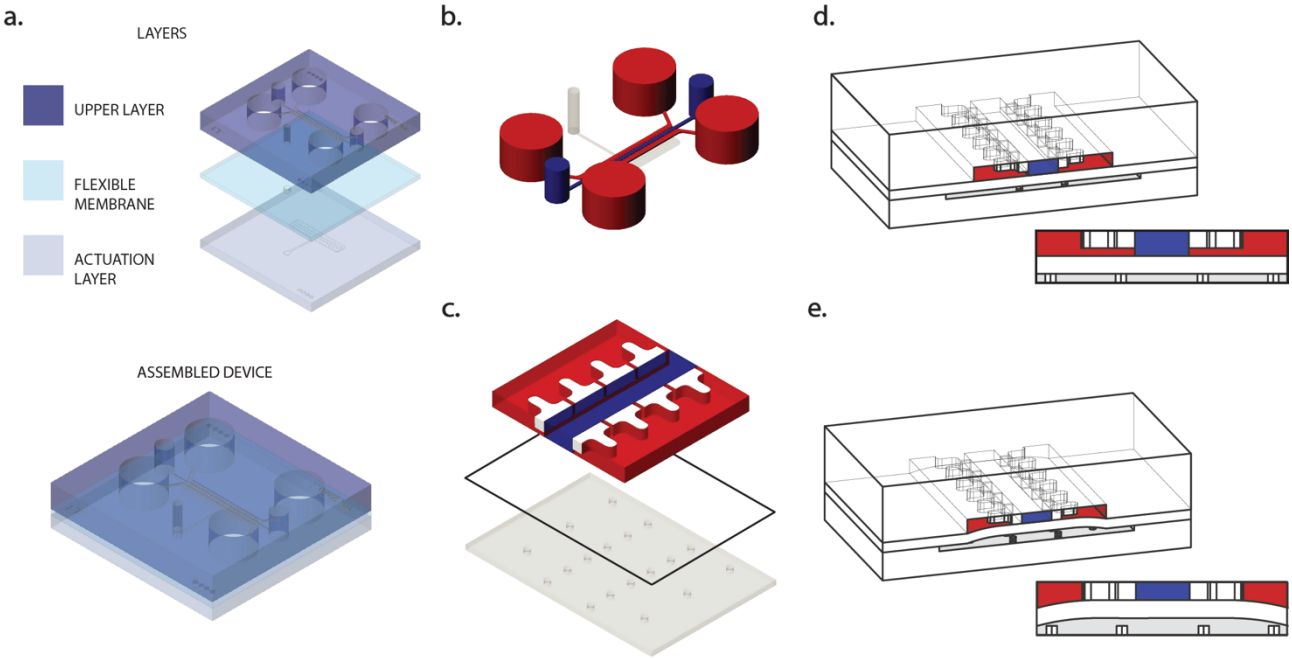

Figure 1: ***Microscale platform for mechanical confined compression of 3D cell microconstructs:*** ***a****, Schematization of the layers adopted for the fabrication of the device. The final assembled device is also depicted.* ***b, c,*** *The microscale platform consists in two compartmentalized microchambers featuring configurable geometries and separated by a flexible membrane. The top compartment is subdivided, by means of two rows of T-shaped hanging posts (white), into a central channel hosting the 3D microconstruct (blue) and two side channels for medium supplementation (red). The bottom chamber (grey) represents the actuation compartment.* ***d, e*** *schematization of a cross section of the device under rest(d) and compression (e) conditions by pressurizing the bottom*

compartment, the PDMS membrane deforms, compressing the 3D microconstruct and eventually abutting against the posts' ends, causing a confined compression of the microconstruct.

Notably, the proposed microscale platform allows to precisely tailor the level of mechanical compression by tuning the gap underneath the hanging posts. In this study, in particular, two gap sizes were designed to achieve a 10% and a 30% compression level, respectively. Furthermore, the shape of the posts was specifically conceived to minimize the lateral expansion of the 3D microconstruct during compression, while permitting mass exchanges at the interface between cells and culture medium. A T-shaped resistant section was selected to minimize posts' outward bending arising from the increased pressure generated upon 3D microconstructs compression (Fig. 1b, white features). The actuation compartment included four rows of scaffolding posts to prevent the flexible membrane from buckling.

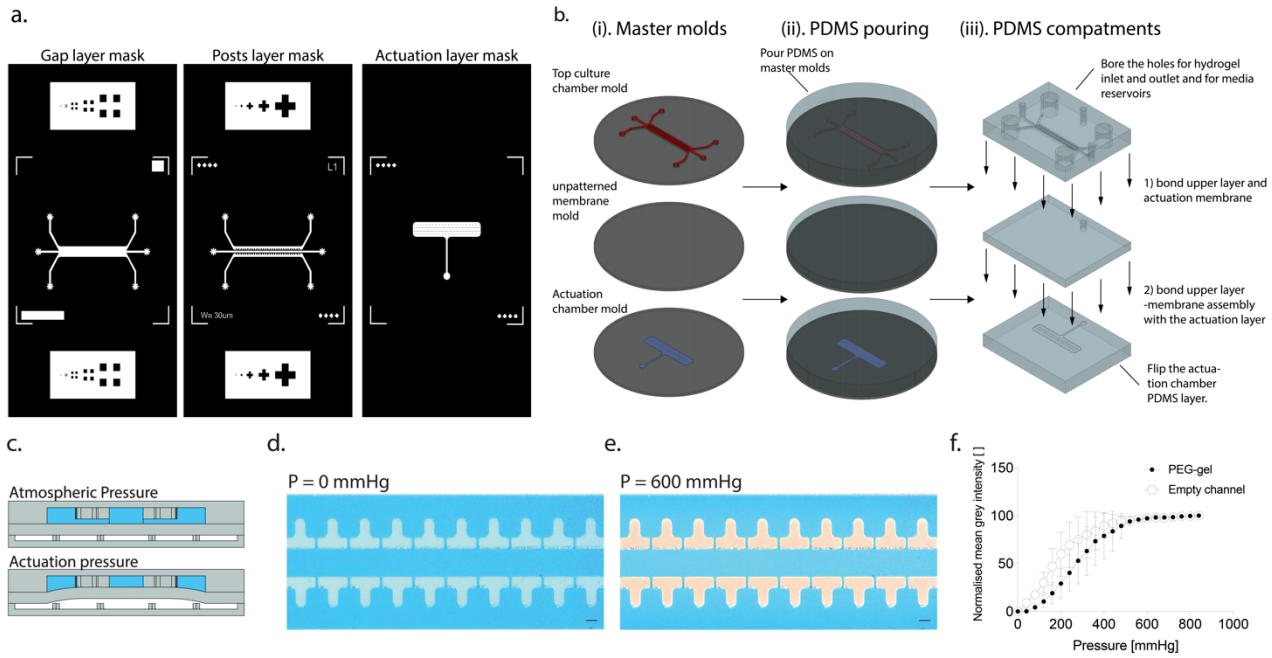

Figure 2: ***Device fabrication and actuation pressure characterization: a****, Layout of the masks for the three layers. Gap layer and Posts layer masks are used for realization of the upper culture chamber through multi-layer soft lithography. The actuation mask is used for realization of the actuation chamber through classic single layer photolithography.* ***b****, Passages for the realization of the master-moulds and of the PDMS device. (i) realization of Master moulds, (ii) PDMS pouring on moulds, ad (iii) PDMS compartments refinement and access holes boring. The final thickness of the flexible membrane was optimized so that the pressure required for the flexible membrane to touch the bottom surface of the posts, i.e. the actuation pressure, was independent from the properties of the construct hosted in the upper culture chamber. The procedure is illustrated in* ***c-f.*** *Both central channel and medium channels were filled with blue dye and the actuation chamber subjected to increasing pressure levels.* ***c****, Schematization of a device cross section in rest state, at atmospheric pressure and at the actuation pressure.* ***d****, Brightfield image of the top chamber. Rest state (relative pressure, p=0 mmHg). Posts appear blue given the dye filled gap between posts end and actuation membrane. Reference background was subtracted to enhance picture luminosity. Scale bar 100 µm.* ***e****, Brightfield image of the top chamber. Compressed state (relative pressure p = 600 mmHg). Under pressure the membrane is in contact with posts bottom surface. Posts appear therefore white. Reference background was subtracted to enhance picture luminosity. Scale bar 100 µm.* ***f,*** *Normalized mean grey intensity versus pressure in the actuation chamber measured in areas within the posts cross section. Experiments were performed leaving the central channel empty or filling it with a PEG based gel formulation. Chips with a 750 µm membrane were adopted; n = 6 devices were considered for each condition. Measurements were performed in n = 3 different areas for each device and averaged. Results are expressed as mean ± SD. Background mean grey intensity obtained at atmospheric pressure was subtracted from subsequent measurements. Results are expressed as percentage of the mean grey intensity obtained at the highest pressure applied (840 mmHg) to normalize for lighting conditions. Results refer to 30% compression devices, the most critical in terms of actuation pressure. Complete adherence of the actuation membrane to the bottom surface of the posts is*

evidenced by mean grey intensity plateau onset. Plateau onset pressure (p ~= 500 mmHg) does not vary with or without the gel presence given a sufficient actuation membrane thickness.

2.2.2 Device fabrication procedure

The microscale platform was realized in polydimethylsiloxane (PDMS, Sylgard 184, Dow Corning) polymerized in defined casts at 10:1 weight ratio of base to curing agent at 65 ºC for at least 3 hours. Appropriate Computer Assisted Design (CAD) software (AutoCAD, Autodesk) was adopted to design the geometrical features (Fig 2a). Corresponding photomasks were printed at full size, high resolution (64000 dpi) on Mylar polyester film. Master moulds were fabricated in a clean room environment using standard photolithography techniques with SU-8 2050 photoresist (MicroChem) on 102 mm silicon wafers substrates. The cross-sectional size of the features was 1.4 mm (width) x 143 μm (height) for the top layer, and 1.6 mm (width) x 50 μm (height) for the bottom layer. In addition, top and bottom layers included two rows of posts delimiting the culture channel. Devices' realization procedure is depicted in Fig 2b.

Posts in the top layer were fabricated with a T-shaped cross-section; each branch of the T-shape was 300 μm long and 100 μm thick. The end of the branch pointing outwards from the culture channel was rounded to avoid air entrapment during device operation. Within each row, posts were separated by a 30 μm gap, and the distance the two rows was 300 μm. Separate moulds were fabricated for the physiological and hyper-physiological top layers of the microscale device, i.e., to induce a -10% and -30% vertical compression on the construct. This criterion led to defining gaps of 14 μm and 43 μm, respectively, underneath the posts

The membrane separating top and bottom layers was fabricated with a thickness of 750 μm by accurately dosing the PDMS poured on a flat substrate. This value ensured that the membrane's bending stiffness was the sole determinant of the actuation pressure (defined as the pressure required for the membrane to abut against posts bottom ends), independently from the CoC mechanical properties (Fig. 2c-f). This prevented from undesired changes in the compression stroke throughout the culture period.

PDMS stamps were peeled off the moulds and assembled layer-by-layer as depicted in Figure 2b. Before assembly, the top layer was finalized by punching circular access ports with biopsy punchers: cell in/out ports had a 750 μm diameter, ports for cell culture medium reservoirs had a 5 mm diameter. Subsequently, the surface containing features of the top layer and the membrane were treated with air plasma (Harrick Plasma Inc) and brought in conformal contact to achieve irreversible bonding upon additional 30 minutes of incubation at 80 °C. The inlet for the actuation compartment was thus punched on the top layer/membrane unit (defining the cell culture compartment), with a 500 μm biopsy puncher, upon manual alignment with the bottom layer. Finally, through a further air plasma treatment, the bottom layer was permanently bonded on the membrane side of the cell culture compartment after careful manual alignment with the top layer and allowed to cure overnight at 80 °C.

A picture of the assembled device is shown in Fig. 3a, while Fig. 3b highlight a detail depicting the T-shaped hanging posts and, in conformity to the necessity of obtaining devices providing two compression levels, Fig. 3c depicts the cross section of devices designed to provide 10% and 30% compressive strains, the difference in the height of the gaps regulating the compressive stroke is appreciable.

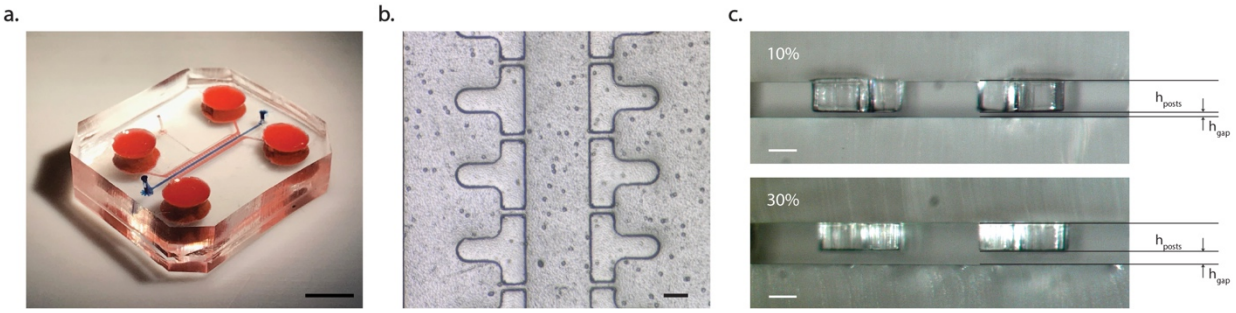

Figure 3: ***Produced device a,*** *Picture of an actual assembled device. Scale bar 4 mm.* ***b,*** *Inset of the T-shaped posts viewed from above. (Scale bar, 100 μm).* ***c,*** *Gap and posts dimensions of the device on stereomicroscope sections. 10% and 30% versions are both presented. h_{posts} and h_{gap} indicates the heights of the hanging posts and of the gap respectively. Heights vary according to compression levels. 10%: h_{posts} = 129 μm, h_{gap} = 14 μm; 30% h_{posts}= 100 μm, h_{gap} = 43 μm. (Scale bar 100 μm).*

2.3 Compression level validation and strain field determination.

The proposed microdevice was designed to provide 3D cellular constructs with confined compression. A global assessment of the strain field was obtained through a Finite element model (FEM) and experimentally validated. An enzymatically cross-linked and matrix metalloproteinase (MMP)-degradable poly (ethylene glycol) (PEG) based hydrogel[31] was considered as the material filling the central culture chamber to provide cells with a tissue-mimicking 3D environment.

2.3.1 Finite element model analysis.

FEM analyses aimed at determining i) whether undesired lateral or longitudinal stretching of the gel could be generated and ii) if strains in the hydrogel control volume were homogeneous and consistent with the desired compression level.

Cartilage and hydrogels exhibit a largely non-linear and strain rate-dependent behaviour resulting from the interaction between the two material constituents, namely a solid matrix and an incompressible permeating fluid, as well as from the inherently viscoelastic property of the former and the viscosity of the latter [32, 33].

A biphasic poroelastic (BPE) finite element (FE) model of the cell-laden hydrogel PEG based hydrogel[31] was implemented [10, 32, 34, 35]. The BPE model describes the hydrogel through the equivalent mechanical behaviour of a continuum resulting from the multiphase interaction of an elastic solid phase and an incompressible inviscid fluid phase. This description of the hydrogel neglects the intrinsic viscoelasticity of the solid matrix and captures exclusively the viscous effects related to the interaction

between the two phases. As such, when simulating confined compression it leads to underestimation of the short-term reaction forces, but accurately captures the short-term deformation field [35].

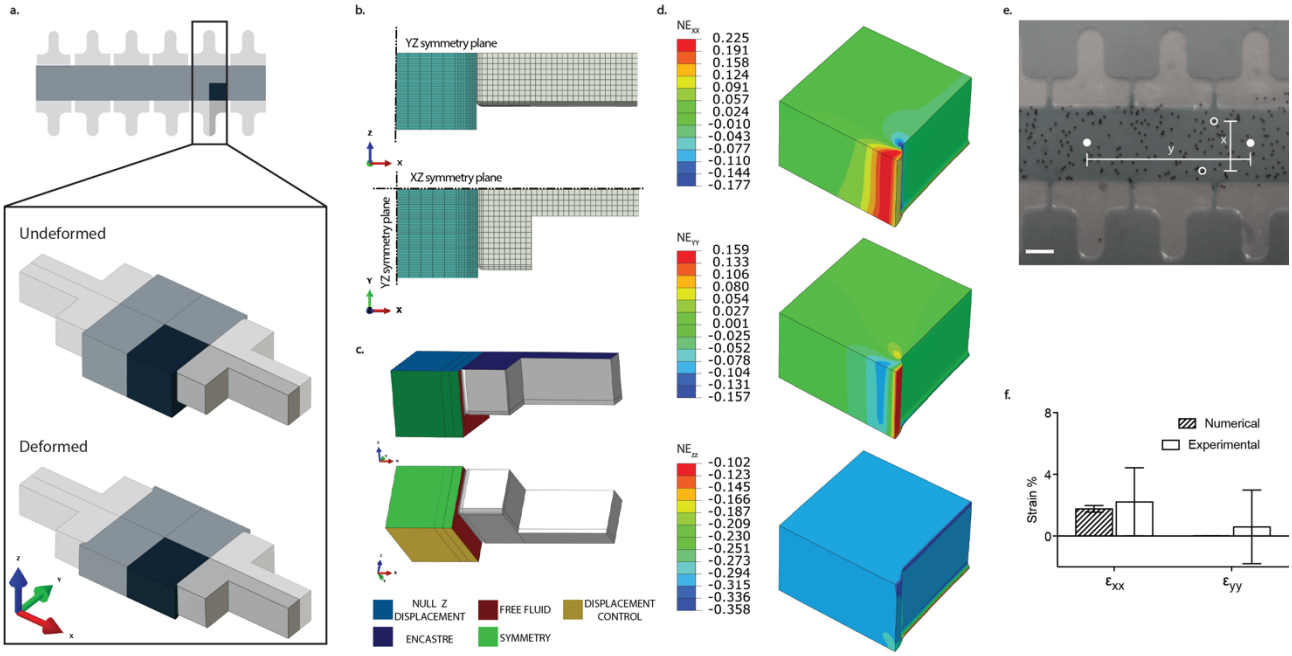

Figure 4: ***Constructs deformation field: computations and experimental validation. a,*** *Top view and 3D schematization of the region considered in computations. The minimal region of interest is shaded. Symmetry planes were considered as boundary conditions. Both the rest position (Undeformed) and the compressed gel state (Deformed) are displayed.* ***b,*** *XZ and XY plane views of the geometry adopted in computations. Considered planes of symmetry are indicated and the adopted mesh is reported.* ***c,*** *Colour coded schematization of FEM boundary conditions.* ***d,*** *Strain deformation field normal directions. The strain field is reported through Nominal strains (NE) values in the normal directions XX, YY and ZZ. Lateral and longitudinal expansions are limited in the central gel constructs and the strain distribution is homogeneous. Peaks appear in correspondence of the windows between posts.* ***e,*** *Experimental evaluation of the deformation field. Polystyrene beads were embedded in PEG gel. The beads displacement was assessed upon compression of the gel and strains measured along X and Y, resulting respectively equal to 2.21% ± 2.20% and 0.59% ± 2.38%. White dots and clear circles are representative of two couple of beads used for strain measurement along X and Y respectively. (Scale bar, 100 µm; picture showing the deformed state). A total of n=9 independent experiments was considered. 7 couples of beads per experiment were used in assessing the strain along each direction.* ***f,*** *Resulting NE_{xx} and NE_{yy} predicted numerically and estimated experimentally were compared. Experimental results show good adherence to computational estimates for strains along both the X (ε_{xx}) and Y(ε_{yy}) directions. Data are plotted as mean ± SD. A total of 63 couples of beads (for experimental results) and nodes (for computational results) was considered for each direction.*

Model parameters were inferred from literature data on PEG-based hydrogels. In details, Young modulus, Poisson's ratio and permeability of 0.1 MPa [31, 32, 36], 0.33 [37] and 1.72×10^{-15} m^4/Ns[38], respectively, were considered.

Computations were performed using Abaqus Standard 6.10. (Abaqus FEA, Dassault Systemes). The software adequacy in the biomechanical description of biphasic tissues had previously been demonstrated[38, 39]. As described, two variants of the device were produced to obtain two compression levels, corresponding to -10% or -30% nominal strains, in the construct. The FE analysis focused only on the latter condition, which was potentially more critical in terms of unwanted lateral and longitudinal expansions. Consistently, the height of the hanging posts was set to 100 µm and the gel's uncompressed height was set to 143 µm.

Owing to the periodic structure of the device, a repetitive unit, which consisted of two posts facing each other with the PEG hydrogel volume comprised in between, was determined (Fig. 4a). Due to the symmetry of the repetitive unit, the region of interest for the FE analysis was reduced to half a post and a quarter of the hydrogel volume and kinematic boundary conditions were imposed to account for geometrical symmetries (Fig. 4a, shaded area, Fig. 4b, c). Considered planes of symmetry are reported in Fig. 4b.

The modelled portion of the post was therefore 300 μm in width (X direction) and 150 μm in length (Y direction), with a thickness of 100 μm. The hexahedron representing the gel was 150 μm wide and 165 μm long, thus including the gel region corresponding to the gap between two adjacent posts. Post's edges in contact with the gel were chamfered to reduce geometrical discontinuities, rounding corners with a 5 μm curvature radius. The post's outer end, despite being rounded in the physical device (Fig. 1c), was squared off to reduce the total number of elements after assessing negligible differences in deformation values through preliminary simulations.

Both pillar and gel were meshed using 8-node linear hexahedral elements with hybrid formulation (Abaqus C3D8PH elements) as depicted in Fig. 4b. A total of 5427 elements, with an average size of 10 μm, was used for the post. The mesh was refined around the corners of the surface in contact with the gels. These, having been chamfered to reduce geometrical discontinuities, needed smaller element size (1.6 μm) to be accurately rendered as geometrical features. A total of 63954 hexahedral elements were adopted for the hydrogel. The characteristic dimension of the elements varied over the hydrogel volume: it was equal to 20 μm at the side of the gel corresponding to the culture channel's mid-line and it progressively decreased down to 1.5 μm as regions closer to the hydrogel face in contact with the post were considered, so to cope with local geometrical complexity (Fig. 4b).

Perfect lubrication was considered in the contact between the gel and the lateral posts; interactions between the PDMS post and the gel were modelled using a surface-to-surface contact. The top surface of the post was encastred to account for its continuity with the overhanging thick PDMS layer. The top surface of the gel was impeded to move along the Z direction simulating the presence of the top layer. A zero-pore pressure was imposed on the portions of the outer face of the hydrogel which was not in contact with the post so to allow for fluid outflow. Adopted boundary conditions are reported in Fig. 4c. The mechanical properties of PDMS were described as non-linear elastic and incompressible through the Mooney-Rivlin strain energy function (equation 1):

$$W = C_1(I_1 - 3) + C_2(I_2 - 3) + \frac{1}{D}(J - 1)^2 \qquad (1)$$

where I_1, and I_2 are the first and second invariant of the right Cauchy-Green strain tensor **C**, J is the determinant of the deformation gradient tensor **F** and represents the ratio between the deformed and initial

volume of the material, while C_1, C_2, and D are the constitutive parameters of the model. C_1 and C_2 were set equal to 254 KPa and 146 KPa respectively, as reported in the literature concerning PDMS with a base to curing agent ratio equal to 10:1[40], D was set equal to zero as for a perfectly incompressible material.

The PEG based hydrogel's Young Modulus was assumed equal to 0.1 MPa. This value is higher as compared to data reported in the literature for similar hydrogels, but it allowed to account for the increased resistance to compression exhibited by the hydrogel due to the negatively charged glycosaminoglycans accumulating during the CoC maturation in the construct. Poisson ratio was fixed at 0.33[41], and the specific weight of the permeating fluid to 9.965×10^{-6} N/mm3[32].

In order to model the poroelastic behaviour of the hydrogel, Abaqus requires the specific material permeability defined as $K_s = \gamma_w k$ where γ_w is the permeating fluid specific weight and k is the absolute permeability. K_s was set to 0.3×10^{-3} mm/s. The initial void ratio $e = dV_w/dV_g$ (where dV_w is the volume of the fluid phase and dV_g is the volume of the solid phase) was estimated by the swelling ratio of the hydrogel formulation used in this study and set to 45 [40]. Complete fluid saturation was assumed for the hydrogel.

To capture the time dependent non-linear behaviour of the hydrogel a transient analysis was conducted using the Soil Consolidation option in Abaqus. An automatic Δt incrementation was adopted, with a minimum value of 1×10^{-6} s. The 30% compression in the Z direction (Fig. 4a) was applied by imposing a displacement of 43 μm to the hydrogel bottom with constant velocity over a 1 s timeframe.

The strain distribution was evaluated through nominal strain components acting in the X, Y and Z directions, and calculated according to Abaqus' definition at integration points of each finite element. In particular, nominal strains are defined as defined in equation 2:

$$\varepsilon^N = \bar{\bar{V}} - \bar{\bar{I}} = \sum_{i=1}^{3} (\lambda_i - 1)\, \bar{n}_i\, \bar{n}_i^T \qquad (2)$$

where $\bar{\bar{V}} = \sqrt{\bar{\bar{F}}\bar{\bar{F}}^T}$ is the left stretch tensor (where $\bar{\bar{F}}$ is the deviatoric deformation gradient), λ_i are the principal stretches and $\bar{n}_i$ are the principal stretch directions in the current configuration.

Lateral and longitudinal expansion values associated to the hydrogel compression along the z-direction were valued through the estimation of the nominal strains (NE_{xx}, NE_{yy}, NE_{zz}), Nominal strains contour plots are reported in Fig. 4d.

FEM predictions attested low and overall uniform axial and lateral strain values in the control volume, with peak values in lateral and longitudinal expansion appearing near the windows between posts.

To achieve a global evaluation of the strain field upon compression accounting for the non-homogeneity of the mesh, nominal strains were extracted from the numerical model replicating the procedure adopted in evaluating the strain experimentally (Section 2.3.2).
A random 9 point-cloud was generated within the control volume. The displacement and the coordinates of the nodes nearest to the resulting point were used in computations. Owing to the system's symmetry, strains were calculated as defined in equation 3:

$$\varepsilon_{rr} = \frac{\left((r_i - r_{sim}) + U_r\right) - \left((r_i - r_{sim})\right)}{(r_i - r_{sim})} = \frac{U_r}{(r_i - r_{sim})} \qquad (3)$$

Where the index r indicates the r-th direction considered, r_i is the r coordinate of the node i, r_{sim} is the r coordinate of the symmetry plane and U is the node i displacement in the r direction. Mean and standard deviation where computed. The process was repeated 7 times and results averaged. Computed strains resulted (Mean ± SD) of 1.76% ± 0.22% and 0.02% ± 0.006% for NE_{xx} and NE_{yy}, respectively.

2.3.2 Confined compression experimental validation.

Numerical results of the strain field upon compression were validated experimentally assessing expansion levels in the lateral end longitudinal directions. A 2% PEG hydrogel was prepared as indicated in section 2.4.1: polystyrene beads (diameter 10 μm) were laden in the gel to visualize the strain field. Lateral and longitudinal expansions were assessed measuring beads' displacements upon subjecting the gel to the desired compression (Fig. 4e). A coloured dye was added in the chambers to better highlight the posts profile. Images of the beads were acquired during the rest phase and upon gel compression. ImageJ software was used to post-process acquired images. Seven devices were adopted in the evaluation. For each device, nine couples of beads were considered and for each couple the mutual distance was measured along the X and Y directions, i.e., along the width and the axial direction of the culture channel, prior and after compression. Strains in lateral and longitudinal directions were calculated as defined in equation 4:

$$\varepsilon_{ii} = \frac{L_i' - L_i}{L_i} \qquad (4)$$

Where the index i indicates the i-th direction considered, L' and L are the measured distances after and prior to compression. Mean value and standard deviation over the nine couples of beads were assessed and used to verify computational predictions. Strains experimental values along X and Y resulted respectively 2.21±2.20% and 0.59 ± 2.38%, in good accordance with numerical estimations (Fig. 4f) and confirmed the achievement of a uniform confined compression state.

2.4 Cartilage on Chip (CoC) model establishment

The microscale device was used firstly to establish a model of healthy human Cartilage-on-Chip (CoC), secondly to evaluate the effect of different compression values, and finally as a tool to determine the response to known and innovative anti-inflammatory and anti-degradative compounds. Cartilaginous constructs were obtained from human articular chondrocytes (hACs) isolated from healthy donors, embedded in PEG gel, and injected into the microscale device. A schematization of the experimental timeline is reported in Fig. 5.

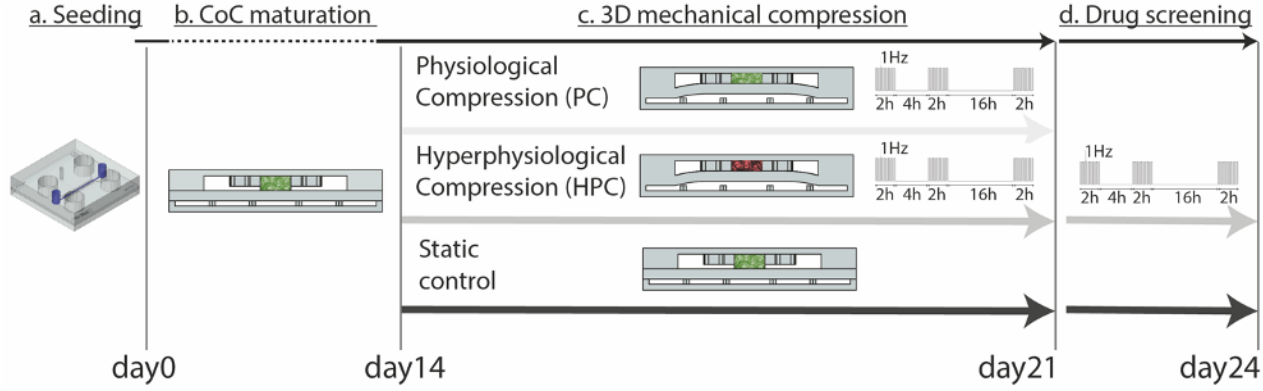

Figure 5: ***Experimental plan. a,*** *Human articular chondrocytes (hACs) isolated from healthy donors were embedded in PEG gel and injected into the microscale platform.* ***b,*** *14 days of chondrogenic culture under static condition led to the generation of a CoC.* ***c,*** *Two different levels of mechanical compression were then applied for seven additional days, physiological (i.e. PC, 10%) and hyper-physiological (i.e. HPC, 30%). A static condition was included as control.* ***d,*** *While maintaining a HPC, anti-inflammatory/anti-degrading compounds were supplemented to the model and their effect analysed after three additional days.*

2.4.1 PEG precursors production and PEG hydrogel preparation.

PEG hydrogels were produced and characterized as earlier described [42]. Briefly, 1 ml FXIII (200 U/mL, Fibrogammin, CSL Behring, Switzerland) was activated with 100 µl of thrombin (20 U/mL, Sigma-Aldrich, Switzerland) for 30 min at 37 °C and resulting activated FXIII (FXIIIa) was stored in small aliquots at −80°C. Eight-arm PEG vinylsulfone (mol wt 40kDa; NOF Europe, Germany) was functionalized with peptides that contained either a FXIII glutamine acceptor substrate (Gln-peptides; NQEQVSPL-ERCG-NH2; Bachem AG, Switzerland) or matrix metalloproteinase (MMP)-degradable FXIII lysine donor substrate (Lys-MMPsensitive-peptides; Ac-FKGGGPQGIWGQ-ERCG-NH2; Bachem AG, Switzerland) resulting in 8-PEG-Gln or 8-PEG-MMPsensitive-Lys precursors, respectively. A stoichiometrically balanced solution 8-PEG-Gln and 8-PEG-MMPsensitive-Lys was mixed for an indicated final dry mass content of hydrogel precursors in Tris buffer (50mM Tris, pH7.6; 50mM calcium chloride) leaving a spare volume of 12.5% v/v for the addition of cell culture medium and cells. The hydrogel cross-linking was initiated by adding 10 U/ml FXIIIa and vigorous mixing. Hydrogels were formed containing a final concentration of 2% PEG precursors and $50x10^6$ cells/ml.

2.4.2 Healthy human cartilage samples collection, cell isolation and expansion.

Macroscopically normal human articular cartilage was obtained from the knee joints of a total of 5 patients with unknown clinical history of joint disorders (mean donor age: 66 years; range: 54-84 years, 5 male), after informed consent by relatives and in accordance with the local ethics committee (University Hospital Basel, Switzerland). Cartilage biopsies were minced and digested enzymatically to isolate and use cells. Briefly, human articular chondrocytes (hACs) were isolated using 0.15% type II collagenase (10 ml solution/g tissue, 300 U/mg, Worthington Biochemical Corporation, Lakewood, NJ) for 22 h and resuspended in Dulbecco's modified Eagle's medium (DMEM) containing 10% foetal bovine serum, 4.5 mg/ml D-Glucose, 0.1 mM nonessential amino acids, 1 mM sodium pyruvate, 100 mM HEPES buffer, 100 U/ml penicillin, 100 µg/ml streptomycin, and 0.29 mg/ml L-glutamine (complete medium). The isolated chondrocytes were counted using trypan blue, plated in tissue culture flasks at a density of 10^4cells/cm^2 and cultured in complete medium with the supplementation of 1 ng/ml of transforming growth factor-β1 (TGF-β1) and 5 ng/ml of fibroblast growth factor-2 (FGF-2) in a humidified 37°C/5% CO2 incubator. The growth factor combination was selected based on the previously reported ability to increase human chondrocyte proliferation and capability to redifferentiate, even upon an initial dedifferentiating culture [43][44]. After approximately 10 days, when cells were about 80% confluent, first passage cells (P1) were rinsed with phosphate buffered saline (PBS), detached using 0.05% trypsin/0.53 mM EDTA and replated at 5×103cells/cm^2. After one more week, when cells were again about 80% confluent, second passage cells (P2) were detached and exploited to generate either 2D monolayer controls or the CoC model as described below.

In order to characterize the gene expression profile of native healthy cartilage, macroscopically normal human articular cartilage was obtained from the knee joints of additional 5 patients with unknown clinical history of joint disorders (mean donor age: 55.8 years; range: 51-60 years old, 1 female and 4 male), after informed consent by relatives and in accordance with the local ethics committee (University Hospital Basel, Switzerland). Again, cartilage biopsy was minced and digested enzymatically as aforementioned. Freshly isolated, healthy hACs from the different donors were pooled and frozen to further perform RT-PCR analysis.

2.4.3 Healthy human CoC model generation.

The healthy human CoC model was generated by embedding hACs into an enzymatically cross-linkable and PEG based hydrogel matrix into the microscale device. Hydrogels with a final dry mass content of 2% were prepared, as described in section 2.4.1, by stoichiometrically balanced ([Lys]/[Gln] = 1) precursor solutions of 8-PEG-Gln and 8-PEG-MMPsensitive-Lys in Tris-Buffer (TBS, 50 mM, pH 7.6) containing 50 mM calcium chloride, leaving open a spare volume of 12.5% v/v for addition of cell culture medium

with hACs. The precursor solution was thus mixed to a hACs cell suspension at a final concentration of 5×10^4 cells/µl and allowed to polymerize by adding 10 U/mL thrombin-activated factor XIIIa and vigorous mixing. The cell-laden PEG pre-polymer solution was manually injected into the culture channel of the microscale device (~0.45 µl/device) and incubated for 15 minutes (5% CO2 and 37 °C) before filling the lateral channels with chondrogenic medium (DMEM (Sigma Aldrich), containing 2% foetal bovine serum, 4.5 mg/ml D-Glucose, 0.1 mM nonessential amino acids, 1 mM sodium pyruvate, 100 mM HEPES buffer, 100 U/ml penicillin, 100 µg/ml streptomycin, and 0.29 mg/ml L-glutamine and supplemented with 0.1 mM ascorbic acid 2-phosphate, 10 µg/mL insulin, and 10 ng/mL TGF-β3). 3D hACs-laden microconstructs were cultured under static regimen for two weeks in chondrogenic medium (Fig.5). Culture medium was changed every second day and collected for further analysis. Upon two weeks, samples were collected for RT-qPCR, immunofluorescence, GAG and DNA quantification analyses as described below.

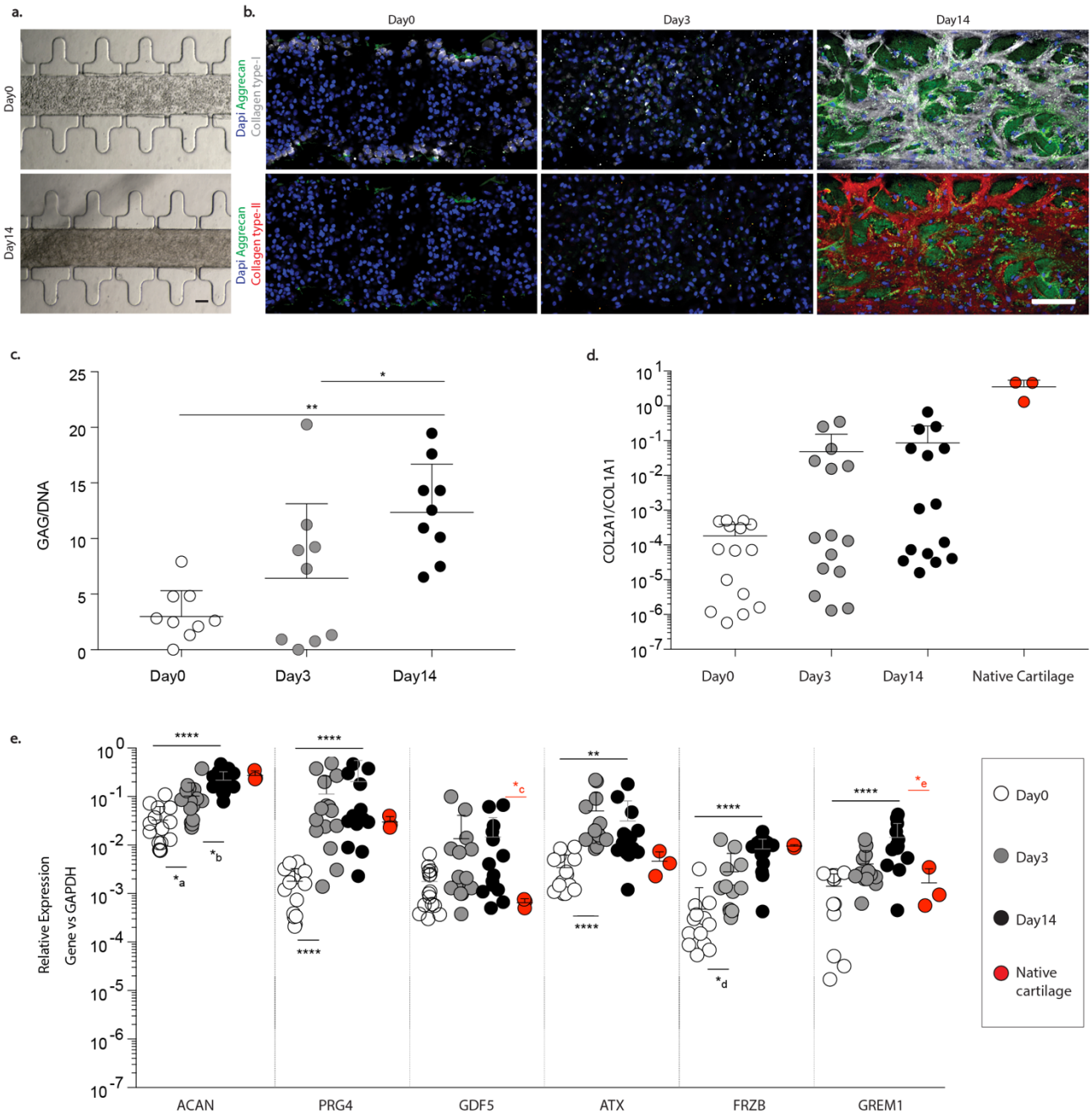

Figure 6: ***Establishment of a human model of healthy CoC. a,*** *Brightfield images of the constructs at day 0 and after 14 days of culture. At the end of the maturation period constructs were still confined to the central channel. Scale bar 100 µm* ***b,*** *Aggrecan, collagen type-I and collagen type-II expression was assessed by immunofluorescence revealing a dense cartilage-like extracellular matrix deposition upon 14 days of differentiation. Representative pictures for one donor are shown (a). Scale bar, 100 µm.* ***c,*** *CoC maturation was also confirmed by the statistically significant increase in GAG production during the 14 days of differentiation. Statistics by One-way ANOVA with Bonferroni's, single pooled variance, multiple comparison test. *P = 0.0446, **P= 0.0011. n=9 biologically independent samples from 3 different donors were considered.* ***d,*** *the COL2A1/COL1A1 expression ratio (n=15 biologically independent samples from 5 different donors) and* ***d,*** *the time course expression of a panel of genes characterizing articular cartilage (n=15 biologically independent samples from 5 different donors) were quantified by RT-qPCR and compared with expression level in native freshly isolated healthy chondrocytes (in red, n=3 biologically independent samples from a pool of 5 different donors). All gene expression values are normalized relative to GAPDH expression and values are log scale. Results are expressed as mean (centre values) + SD (measure of dispersion), *aP = 0.0268, *bP = 0.0237, *cP = 0.0353, *dP = 0.019, *dP = 0.0393, **P = 0.0021, ***P < 0.001 ****P<0.0001). Statistics by one way ANOVA and Bonferroni's multiple comparison tests (normal distributions), or Kruskal-Wallis test with Dunn's multiple comparison test (non-normal distributions) in all graphs where*

statistical analysis is reported. A two tailed Mann-Whitney test was used to compare gene expression of cells cultured in the device for 14 days and of a pool of 5 healthy donors. Statistical significance is indicated in red.

After 14 days of chondrogenic conditioning under static regimen (Fig. 5), a cartilage microconstruct was obtained. Notably, the 3D microconstruct was still confined within the two arrays of hanging posts (Fig. 6a), thus ensuring the geometrical control over the subsequently imposed mechanical stimulation.

Immunofluorescence analysis revealed a high deposition of cartilaginous proteins upon two weeks of differentiation. In details, a dense extracellular matrix rich in collagen type-I, collagen type-II and aggrecan was detected at day 14 (Fig. 6b). Collagen type-I and aggrecan were already slightly expressed by hACs at day 0 but remained mostly intracellular up to day 3. Quantification of glycosaminoglycans (GAGs) synthesized during the culture period confirmed a statistically significant increase of GAGs at day 14, as compared to both day 0 and day 3 (Fig. 6c). Gene expression analysis through real-time quantitative polymerase chain reaction (RT-qPCR) also indicated an upward trend in COL2A1/COL1A1 ratio during the two weeks of differentiation, approaching the level found in native cartilage (Fig. 6d). The time course of articular cartilage signature genes expression was also assessed by RT-qPCR (Fig. 6e). Expression of the articular cartilage-specific genes aggrecan (ACAN) and lubricin (PRG4), significantly increased during the culture and matched, at day 14, the level of the genes detected in native chondrocytes. Specifically, ACAN expression showed a constant increasing trend along the two differentiation weeks, while PRG4 expression was already highly upregulated after three days. The expression of GDF5 and autotaxin (ATX), low in native adult chondrocytes and associated with joint interzone embryonic development [45] and regulation of cartilage formation [46], increased over time, with the expression of ATX reaching a plateau already after three days. Finally, expressions of wingless-type MMTV integration site (Wnt) antagonist Frizzled-related protein (FRZB) and Bone Morphogenetic Protein (BMP) antagonist Gremlin-1 (GREM1), genes expressed in adult hACs [47], were characterized by a statistically significant upward trend during the two weeks of culture, again approaching, after 14 days, the level found in native chondrocytes.

2.5 Compression mediated OA traits induction in the healthy COC model

Upon two weeks of maturation, CoC constructs were subjected to two different levels of confined mechanical compression for the following 7 days (Fig. 5c). Specifically, a physiological compression (PC) of 10% or a hyper-physiological 30% compression (HPC) were applied. Notably high strain levels were reported to induce directly cellular damage chondrocytes apoptosis [6]. A cyclic loading regimen with negligible impact on cellular viability was optimized before assessing compression levels biological implications. A Live/Dead evaluation of constructs after 7 days of cyclic mechanical loading (at the 30% compression level) is reported in Fig 7a. The Applied loading regimen, resembling a daily walk routine, is

reported in Fig 7b. In details, a frequency of 1Hz was chosen and the following temporal windows of stimulation applied: 2h stimulation, 4h rest, 2h stimulation, 16h rest per day.

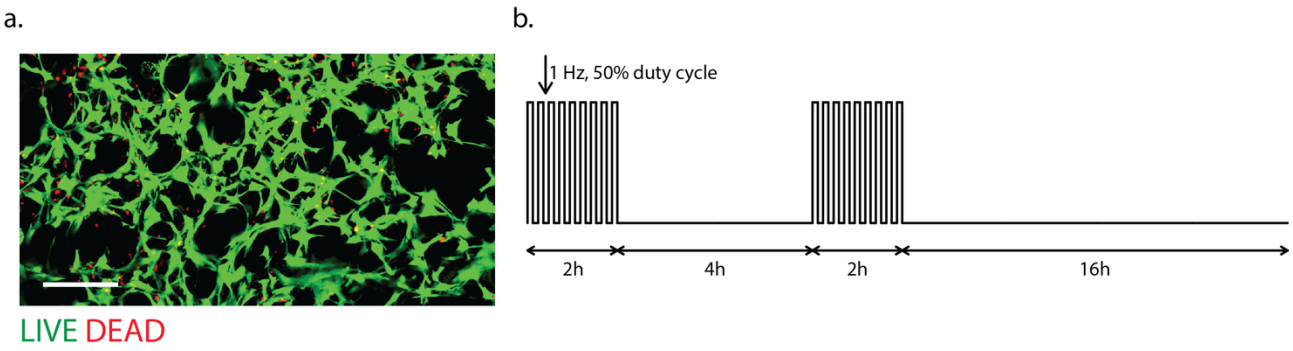

Figure 7: ***Live/Dead. a,*** *LIVE/DEAD assay of CoC. A 30% compression was applied, for 7 consecutive days with the pattern presented in* ***b,*** *following 14 days of static culture in chondrogenic differentiation medium. Scale bar 100 μm. (n=3 biologically independent samples were considered from a single donor).* ***b,*** *Applied stimulation pattern. Each day two 2 hours cycles were divided by 4 hours pause. Cyclical compression was provided with a frequency of 1Hz and applying the actuation pressure with a 50% duty cycle.*

2.5.1 Effect of mechanical compression on CoC anabolism, catabolism and inflammation.

The microscale device was used to mechanically control the environment of the achieved CoC. Mechanical stimulation was applied through a custom made electro-pneumatical actuation system (section 2.8). Upon 14 days of maturation, the established CoC model underwent seven days of mechanical stimulation at different levels of compression. Control devices were cultured under static conditions during the stimulation period.

In all conditions, chondrogenic medium was changed every second day and collected for further analysis. Upon seven days of stimulation, samples were collected for RT-qPCR, immunofluorescence, GAG and DNA quantification analyses as described below.

As regard the modulation of anabolic processes, GAG production was not affected by any compression regimen (Fig. 8a) but maintained an increasing trend when compared to the beginning of mechanical stimulation. HPC, however led to a decreasing trend in *COL2A1/COL1A1* mRNA and a significant reduction in *ACAN* mRNA expression, as compared to both control and PC (Fig. 8b, c). This result indicates that the hyperphysiological load condition simulated in the CoC triggers a loss of expression of anabolic genes.

Concerning the effect of seven days of mechanical compression on the CoC catabolic and inflammatory profile the expression and release of degradative enzymes and inflammatory cytokines was assessed. MMP-13 is the main enzyme responsible for collagen type-II and aggrecan degradation in OA, playing a role in cartilage degeneration [48]. Immunofluorescence analysis revealed that both mechanical compression

levels promoted the intracellular expression of MMP-13 (Fig. 8d). However, HPC led to a higher co-localization of DIPEN, an aggrecan MMP-generated C-terminal aggrecan neoepitope [49], within MMP-13 positive cells, suggesting a higher matrix-degrading activity (Fig. 8d). Coherently, HPC induced a statistically significantly higher secretion of pro-MMP13 (Fig. 8e) and enhanced *MMP13* gene expression (Fig. 8f), as compared to both control and PC. The degrading effect of mechanical HPC was specific for MMP-13, being ADAMTS5 expression not modulated among the different conditions (data not shown). The effect of HPC on inflammatory genes expression was also assessed. Interestingly, HPC induced a significant upregulation of a key pro-inflammatory cytokine, namely IL8, as compared to both control and PC (Fig. 8f), thus suggesting the onset of inflammation in the model. Moreover, IL6 expression exhibited a slight increase upon HPC.

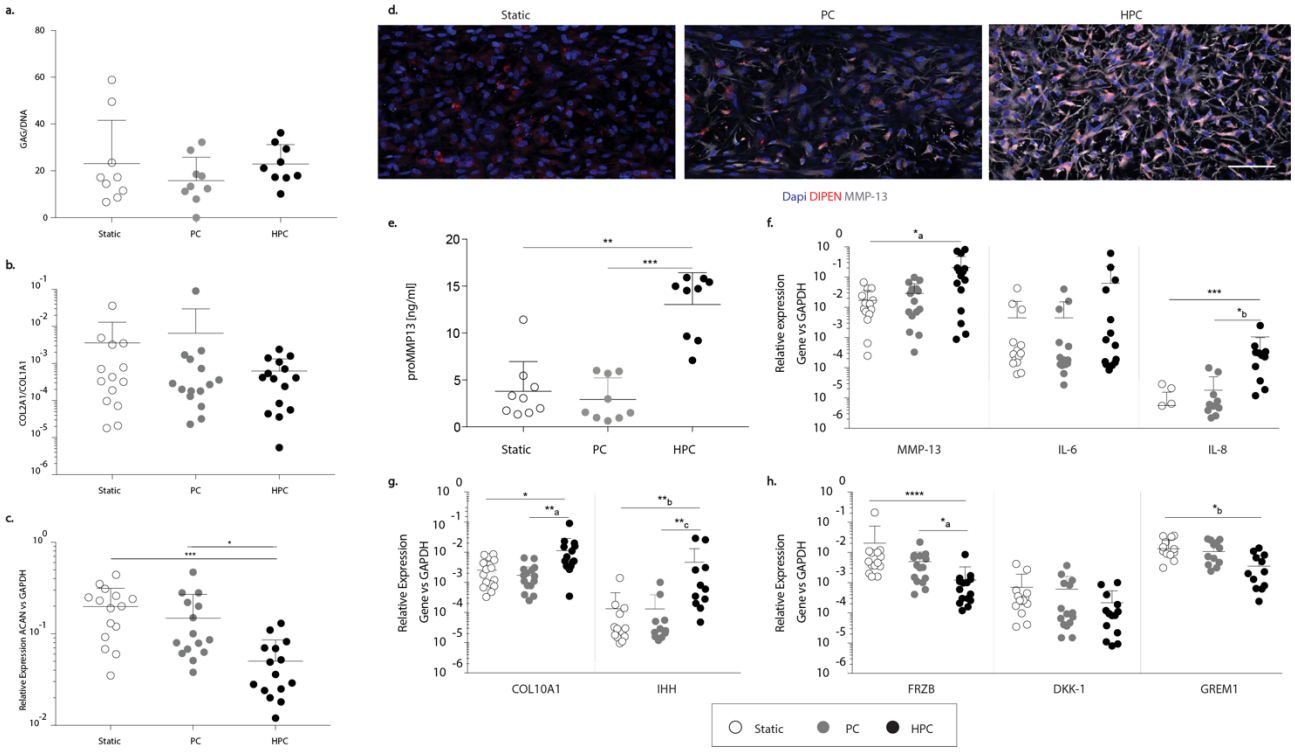

Figure 8: ***Effect of mechanical compression on CoC anabolic traits, catabolic enzymes, inflammation, hACs phenotypic switch and OA-correlating gene profile. a,*** *At the protein level, GAG production was not modulated upon mechanical compression. (n=9 biologically independent samples from 3 different donors; results are mean + SD).* ***b, c,*** *RT-qPCR analysis revealed a decreasing trend for COL2A1/COL1A1 mRNA expression upon HPC and a statistically significant down-regulation of ACAN mRNA expression in the same condition, as compared to static control and PC. (n=15 biologically independent samples from 5 different, results are mean + SD, *P = 0.0108 ***P < 0.001). All gene expression values are normalized relative to GAPDH expression and values are log scale. Statistics by Kruskal-Wallis test with Dunn's multiple comparison test (non-normal distributions) in all graphs where statistical analysis is reported.* ***d,*** *MMP-13 (grey) and DIPEN (red) expression were analysed by immunofluorescence staining, revealing a higher intracellular expression of MMP-13 in both mechanical compression conditions. DAPI was used as nuclear counterstaining. Representative pictures for one donor are shown (for each condition 27 images were acquired from 9 biologically independent samples from 3 different donors). Scale bar, 100 µm.* ***e,*** *Pro-MMP13 secreted in the culture medium was quantified and indicated a statistically significant higher production upon HPC, as compared to control and PC. (n=9 biologically independent samples from 3 different donors, statistics by Kruskal-Wallis test with Dunn's multiple comparison test (non-normal distributions) **P = 0.0045, ***P < 0.001).* ***f,*** *Expression of genes responsible for matrix degradation and inflammation (MMP13,*

*IL6, IL8) was measured by RT-qPCR, indicating unbalance towards a catabolic-preferential and inflamed microenvironment upon HPC. (Statistics by Kruskal-Wallis test with Dunn's multiple comparison test (non-normal distributions), n=15 biologically independent samples from 5 different donors; *aP = 0.0307, *b = 0.0337, ***P < 0.001). All gene expression values are normalized relative to GAPDH expression and values are log scale.* ***g,*** *Gene responsible for cartilage hypertrophic differentiation (COL10A1, IHH) significantly increased their expression upon HPC. (Statistics by Kruskal-Wallis test with Dunn's multiple comparison test (non-normal distributions), n=15 biologically independent samples from 5 different donors; *P = 0.0233, **aP = 0.0017, **bP = 0.0018, **cP = 0.0048). All gene expression values are normalized relative to GAPDH expression and values are log scale.* ***h,*** *Expression of genes inversely correlated to OA in clinics was downregulated in the proposed CoC model upon HPC. (Statistics by Kruskal-Wallis test with Dunn's multiple comparison test (for non-normal distributions, FRZB and DKK-1),or by one way ANOVA with Bonferroni's multiple comparison tests (normal distributions, GREM1) in all graphs where statistical analysis is reported; n=15 biologically independent samples from 5 different donors; *aP = 0.0109, *bP = 0.0261 ****P<0.0001). Results are mean + SD.*

2.5.2 HPC induces a gene profile correlating with OA.

The effect of mechanical compression on the induction of hypertrophic traits in the CoC as assessed. *COL10A1*, naturally not expressed by healthy hACs, was poorly expressed at a gene level by CoC cultured under static condition. While *COL10A1* expression was not altered upon seven days of PC, HPC induced a significant upregulation of *COL10A1* expression, suggesting the triggering of a hypertrophic differentiation of hACs towards transient chondrocytes (Fig. 8g). Similarly, the expression of Indian Hedgehog (*IHH*), a master regulator of hypertrophic chondrocytes differentiation[50], was significantly increased upon HPC (Fig. 8g).

BMP and Wnt signalling antagonists *GREM1, FRZB* and dickkopf 1 homolog (*DKK1*) were defined as articular cartilage's natural brakes of hypertrophic differentiation [47] and their expression was inversely correlated with OA onset[51]. Interestingly, the pure application of HPC was sufficient to trigger a significant down-regulation of those genes in our CoC model, with levels matching those detected in native OA hACs (Table 1, section 2.5.3), thus suggesting the onset of a gene expression profile correlating with OA (Fig. 8h).

		Static	PC	HPC	Native OA hACs
FRZB	Average	2,04E-02	5,04E-03	1,23E-03	6,03E-03
	Max	*2,10E-01*	*2,20E-02*	*8,60E-03*	*9,60E-03*
	Min	*1,60E-03*	*4,10E-04*	*1,20E-04*	*3,90E-03*
DKK1	Average	7,07E-04	6,15E-04	2,17E-04	2,70E-04
	Max	*4,20E-03*	*3,70E-03*	*1,00E-03*	*4,90E-04*
	Min	*3,50E-05*	*1,50E-05*	*8,10E-06*	*1,50E-04*
GREM1	Average	1,34E-02	1,08E-02	3,53E-03	7,00E-03
	Max	*3,60E-02*	*2,80E-02*	*1,40E-02*	*1,20E-02*
	Min	*1,40E-10*	*5,10E-10*	*1,10E-09*	*3,40E-03*

Table 1: Selected genes expression (normalized to GAPDH) in static, PC and HPC CoC models (Donors = 5) and in native freshly isolated OA chondrocytes (Donors = 10).

2.5.3 OA human cartilage samples collection and analysis.

Macroscopically fibrillated human articular cartilage was obtained from the knee joints of a total of 10 patients with clinical history of OA (mean donor age: 74 years; range: 55-82 years, 6 female and 4 male) undergoing a total knee replacement, after informed consent and in accordance with the local ethics committee (University Hospital Basel, Switzerland). Cartilage biopsy was minced and digested enzymatically as aforementioned. Freshly isolated, hACs from the different donors were pooled and frozen to further perform RT-PCR analysis.

2.6 Comparison of OA traits induction through HPC confined compression, unconfined compression, and cytokine administration

A comparison of the OA traits induced by confined HPC with those that could be induced by unconfined compression, applied through a similar microscale model, or that induced by cytokine administration, both in 2D and 3D, was performed.

2.6.1 Comparison of confined and unconfined compression

Confined compression and the subsequent cartilage permeating fluid outflow were correlated to mechanotransduction signalling activation due to transient osmolarity changes in chondrocytes microenvironment [52, 53]. A specific experiment was performed to demonstrate the necessity of confinement in the applied compression introducing unconfined compression controls. In detail, a hyper-physiological 30% unconfined compression (UC) was applied through a device characterized by similar micro-scale dimensions but allowing construct lateral expansion upon compression [29]. This was possible through a different post shape and architecture which was designed to channel the cell-laden hydrogel upon injection but minimizing the hindrance to lateral expansion upon compression. Results of gene expression quantification are reported in Fig. 9. Unconfined compression did not induce OA traits in COC constructs.

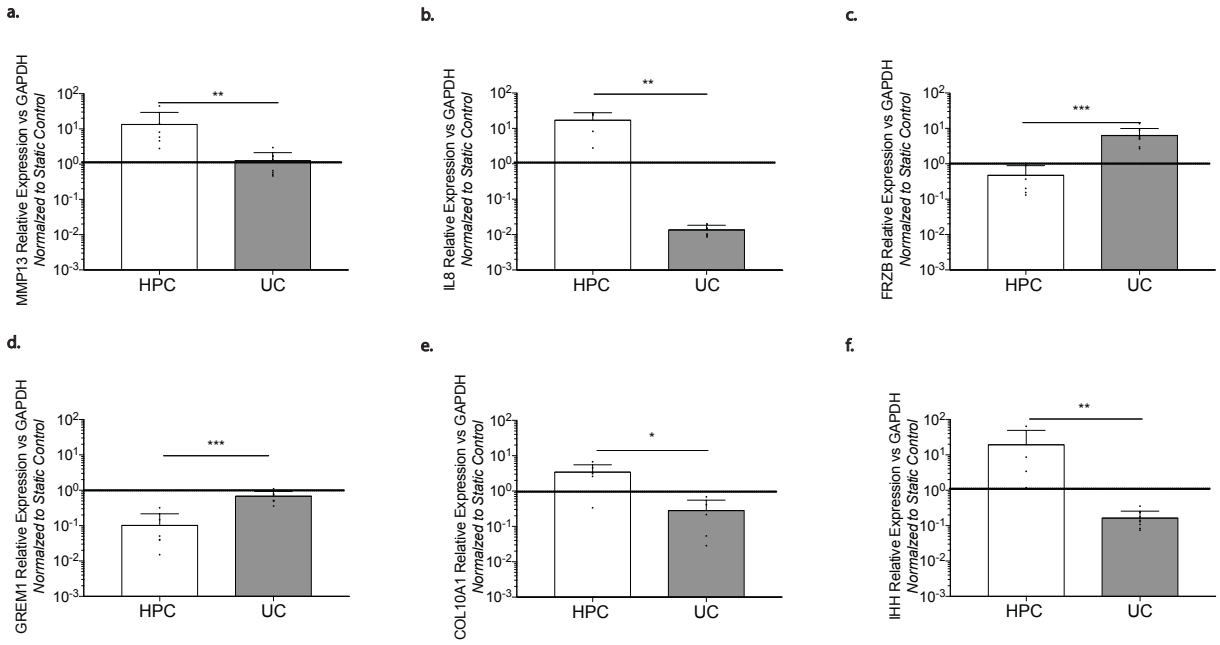

Figure 9: ***Comparison between Hyper Physiological confined compression (HPC) and Hyperphysiological Unconfined Compression (UC).*** *Expression of genes responsible for* ***a,*** *cartilage degradation (MMP13),* ***b,*** *inflammation (IL8)* ***c, d,*** *cartilage hypertrophy brakes (FRZB, and GREM1), and* ***e, f,*** *hypertrophy, was measured by RT-PCR (n=9 biologically independent samples from 3 different donors were considered). The HPC stimulus was compared to an Unconfined compression (UC) stimulus of the same magnitude (i.e. 30%) using a previously reported microfluidic device, with similar dimensions and construction but where the microconstructs are able to expand laterally upon compression*[29]*. All gene expression values are normalized relative to GAPDH expression and refer to basal expression in the corresponding static control; values are log scale. Statistical significance was calculated comparing HPC and UC. Static controls expression level is indicated by the horizontal dotted line. Results are mean + SD, Statistics by Two tailed Mann-Whitney test (non-normal distributions).* ***a,*** ***P = 0.0013;* ***b,*** ***P = 0.0016;* ***c,d*** ****P < 0.001;* ***e,*** **P = 0.0173;* ***f,*** ***P = 0.0040. Individual experimental data era represented by the black dots overlaid to histograms.*

2.6.2 Comparison of OA traits induction through HPC and cytokine administration

Cytokine-based controls were established. Specifically, upon two weeks of maturation, CoC were subjected to two different concentrations of IL1β for the following 7 days: a low dose of IL1β (10pg/ml, IL1β low), reported to be found in the synovial fluid of OA patients [54], and a supraphysiological dose (1ng/ml, IL1β high), previously reported to be used in 2D models [5]. A 2D cytokine-based control was finally established following traditional protocols [55]. In details, human articular chondrocytes were plated at a density of 20,000 cells/cm^2 and cultured for 10 days in complete medium. High dose of IL1β (1ng/ml) was then supplemented to the medium for seven days.

Treatment of the CoC with a supraphysiological dose of Interleukin 1 beta (IL1β) (Fig. 10a, IL1β high) resulted in a similar increase of MMP13 to that observed for HPC as compared to static control, while low doses of IL1β did not affect MMP13 expression (Fig. 10a, IL1β low). Treatment of the CoC with a supraphysiological dose of IL1β (Fig. 10b, c, IL1β high) resulted in a significant increase of IL6 and IL8 as compared to static control, while low doses of IL1β didn't affect their expressions (Fig. 10b, c, IL1β low).

Moreover, treatment with a supraphysiological dose of IL1β resulted in a significant decrease of FRZB (Fig. 10d, IL1β high), while it didn't affect GREM1 or DKK1 expression levels (Fig. 10e, f, IL1β high). None of these genes were instead modulated by treating the CoC with a low dose of IL1β (Fig 10d-f, IL1β low).

Concerning the induction of hypertrophic traits through cytokine administration, the application of IL1β (either at low [54] or high doses [55]) to articular chondrocytes cultured either in monolayer or in 3D, within the established CoC model, didn't lead to an increase of COL10A1 and IHH expression, thus not mirroring hypertrophic traits characterizing OA progression (Fig. 10h, i).

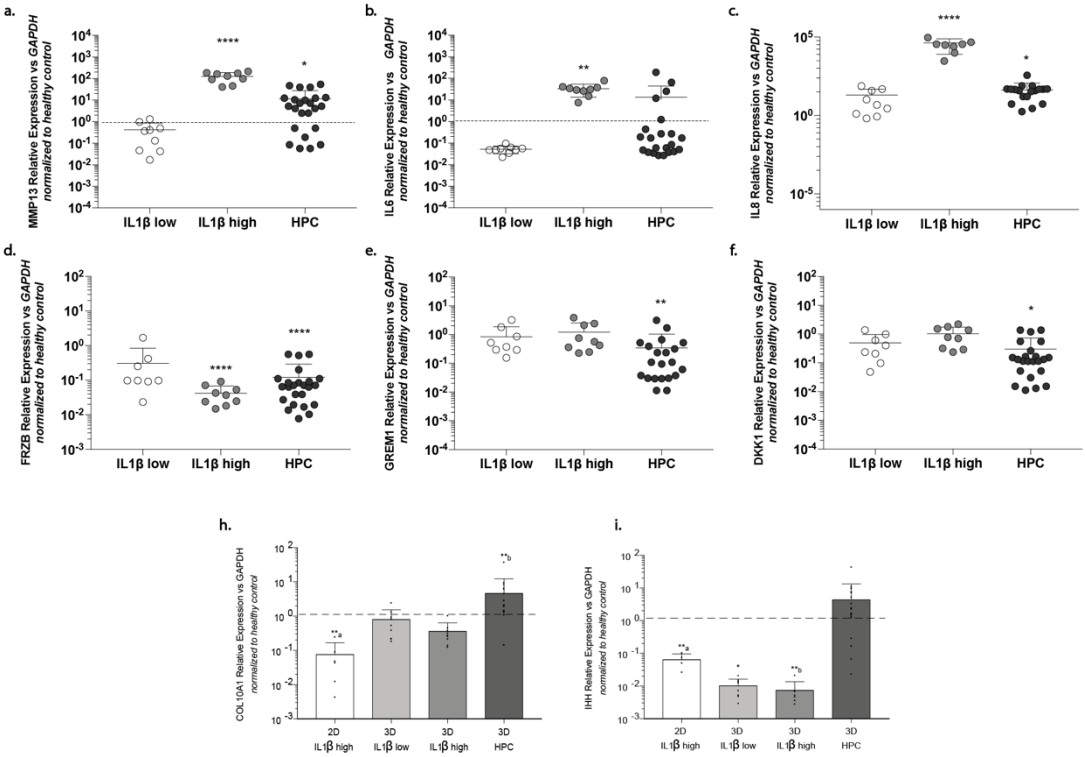

Figure 10: ***Comparison between traditional "cytokine-based" models and HPC-based CoC in modulating degradation, inflammation hypertrophy brakes expression, and hypertrophy.*** *Expression of genes responsible for* ***a,*** *cartilage degradation (MMP13),* ***b, c,*** *inflammation (IL6 and IL8) and* ***d, e, f,*** *cartilage hypertrophy brakes (FRZB, DKK1, and GREM1) was measured by RT-PCR (n=21 biologically independent samples from 5 different donors were considered for 3D HPC and healthy control; n=9 biologically independent samples from 3 different donors were considered for 2D IL1β high, 3D IL1β low and 3D IL1β high). Results are mean + SD. Statistics by statistics by Kruskal-Wallis test with Dunn's multiple comparison test for non-normal distributions in all graphs where statistical analysis is reported.* ***a,*** **P = 0.0304;* ***b,*** ***P = 0.0025;* ***c,*** **P = 0.0113;* ***e,*** ***P = 0.0082;* ***f,*** **P = 0.0129. ****P < 0.0001 in all graphs. The HPC stimulus was compared to "cytokine-based" treatments with high (1ng/ml) and low (10pg/ml) doses of IL1β. All gene expression values are normalized relative to GAPDH expression and refer to basal expression in the corresponding healthy control; values are log scale. Statistical significance was calculated against the respective healthy control.* ***i, h****, Comparison between traditional "cytokine-based" models (both in 2D or inside the 3D CoC model), and HPC-based CoC in modulating chondrocytes hypertrophy.* *Expression of genes responsible for cartilage hypertrophic differentiation (COL10A1, IHH) was measured by RT-PCR (n=24 biologically independent samples from 5 different donors were considered for 3D HPC and controls; n=6 biologically independent samples from 3 different donors were considered for 3D IL1β low and 3D IL1β high, n=6 biologically independent samples from 2 different donors were considered for 2D IL1β high and 2D control). Treating a chondrocytes monolayer with a high dose of IL1β resulted in a significant reduction of COL10A1 and IHH expression as compared to the 2D healthy control. Both the same treatment or a lower dose applied to the 3D CoC model didn't lead to any change in COL10A1 and IHH expression as compared to the 3D healthy control. The application of a HPC to the 3D CoC model upregulated COL10A1 and IHH gene expression, as compared to the 3D healthy control, coherently with the induction*

*of an OA-like phenotype. All gene expression values are normalized relative to GAPDH expression and refer to basal expression in the corresponding healthy control; values are log scale. Statistical significance was calculated against the respective healthy control. Results are mean + SD. Statistics by two tailed Mann-Whitney for 2D culture and by Kruskal-Wallis test with Dunn's multiple comparison test for non-normal distributions for 3D culture in all graphs where statistical analysis is reported. a, **aP = 0.0022 **bP = 0.0014; b, *P = 0.0201, **aP = 0.0095, **bP = 0.0073. Individual experimental data era represented by the black dots overlaid to histograms.*

2.7 Pharmacological validation of the OA CoC model.

A validation of the CoC Oa model as drug screening tool was performed. Upon two weeks of maturation and one week of HPC, the effect of different drugs was tested. Specifically, for three additional days while maintaining the hyperphysiological compression regimen, the culture medium was supplemented with different concentrations of compounds previously shown to have anti-inflammatory and anti-degrading effects in preclinical and clinical studies.

Notably, serum and transforming trowth factor beta (TGFβ) were removed from the culture medium prior to drug administration, as possible masking/confounding factors.

In details, Dexamethasone (DEX,10μM), a corticosteroid drug that prevents collagen degradation through the inhibition of inflammatory cytokines [56], Interleukin-1 receptor antagonist (IL1Ra, 10ng/ml and 500ng/ml), Rapamycin (10nM, 1μM), a mammalian target for rapamycin (mTORC1) activity inhibitor [57] as mTOR is macrolide compound demonstrated to be acritical mediator of mechanotransduction involved in the process of cartilage degeneration associated with post-traumatic OA [58], and the non-steroidal anti-inflammatory drug Celecoxib (0.1μM) [59] were tested (Fig 11a, b). In addition, the depolymerized hyaluronic acid alkylamide HYADD®4 and a low molecular weight hyaluronic acid (≈ 50kDa), provided by Fidia Farmaceutici Spa (Italy), were tested in the system at a concentration of 1mg/ml (Fig 11c, d). All drugs were diluted in DMSO, also used as vehicle (dilution 1:5000). A static device was used as "healthy control".

DEX (10μM), was considered as the reference compound [60] and as expected strongly inhibited MMP13 expression, while not affecting the expression of IL8. Both tested doses of IL1Ra [43] induced a statistically significant reduction in the expression of MMP13 and IL8 in the CoC model. Rapamycin reduced the expression of MMP13 at both tested doses but had a significant effect on IL8 only at the highest dose (previously shown to increase autophagy [61]). Celecoxib significantly reduced both MMP13 and IL8 expression in the CoC model.

Once the model was validated on well-established anti-inflammatory/anti-catabolic compounds, a candidate anti OA compound currently under development by Fidia Farmaceutici SpA with proven MMP inhibition activity was tested [62]. The hyaluronic acid alkylamide HYADD®4, contained in the already approved viscosupplement Hymovis® (Fidia Farmaceutici SpA, Italy) and known to exert a competitive inhibition on matrix metalloproteases (MMPs) [3], was supplemented to the system after thermal

depolymerization, in order to reduce its viscosity, and compared to unmodified HA of similar low molecular weight (~50 kDa, LMW-HA). The anti-inflammatory effect of the two compounds was comparable in terms of reduction of inflammation, as demonstrated by the decrease in IL8 expression, a pro-inflammatory cytokine that has a key role in the pathophysiology of OA[63] (Fig. 6c). HYADD®4 instead exhibited a statistically significant and selective effect on reducing the expression of MMP13 (Fig. 6d), one of its main hypothesized targets [62], consistent with previous preclinical and clinical reports [64].

A cytokine-based control based on inflammation with a traditionally used high dose of IL1β [55] was finally established as previously described. In details, upon two weeks of maturation and one week of high dose of IL1β (1ng/ml), the effect of IL1Ra (500ng/ml) and Rapamycin (1μM) was tested, while maintaining IL1β stimulation (Fig 11 e, f). Upon three days of drug treatment, samples were collected for RT-qPCR analysis as described below. Neither MMP13 nor IL8 expression was modulated by Rapamycin (1 μM) in the IL1β treated system (Fig.11 e, f). Instead, treatment with the high IL1Ra dose exhibited a tendency to diminish IL8 expression in a similar manner to the HPC model, while the compound had a limited effect on MMP13 modulation (Fig 11 e, f).

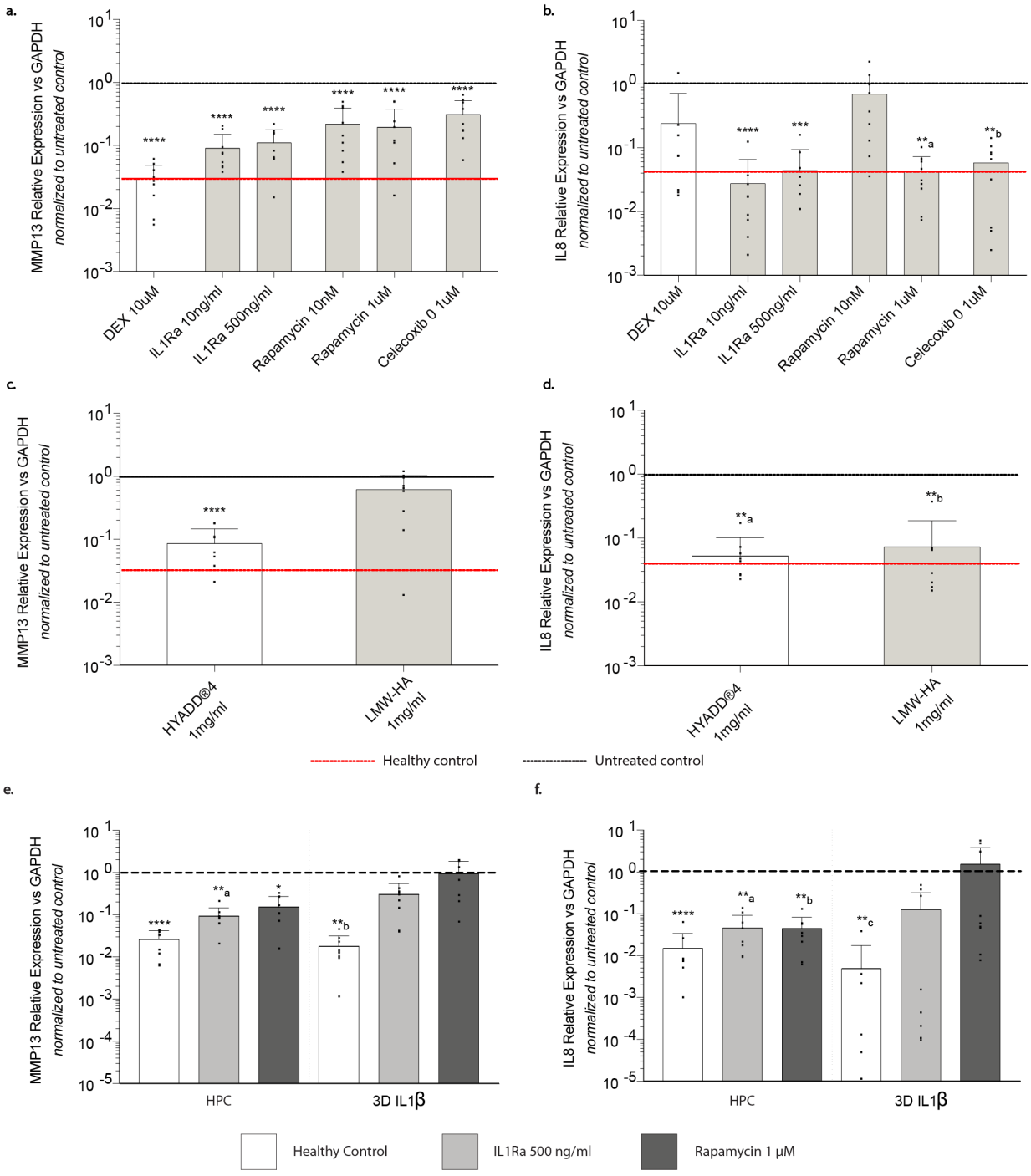

Figure 11: ***Drug screening on OA CoC model. a, b,*** *The expression of MMP13 and IL8 in response to administration of known anti-inflammatory/anti-catabolic compounds was evaluated by RT-qPCR. Upon generation of the OA CoC model, drugs were supplemented to the culture medium for three days, while maintaining HPC. DMSO was used as vehicle. The mean expression value of the healthy control (i.e. Static CoC) is represented by the red horizontal line, while the mean expression of the untreated control (i.e. HPC CoC supplemented with DMSO only) is represented by the black horizontal line. All gene expression values are normalized relative to GAPDH expression and refer to the basal expression in the untreated control; values are log scale. Individual experimental data era represented by the black dots overlaid to histograms (n=9 biologically independent samples from 3 different donors). Statistical significance was calculated against the respective untreated control. Statistics by one way ANOVA with Dunnett's multiple comparison tests (normal distributions, MMP13) or Kruskal-Wallis test with Dunn's multiple comparison*

*test (non-normal distributions, IL8). **aP = 0.0012, **bP = 0.0030, ***P < 0.001 ****P < 0.0001. Results are mean + SD.* ***c, d,*** *The expression of MMP13 and IL8 in response to the administration of thermally depolymerized HYADD®4 and low molecular weight HA (~50 kDa, LMW-HA) was evaluated by RT-qPCR. Upon generation of the OA CoC model, drugs were supplemented to the culture medium for three days, while maintaining HPC. DMSO was used as vehicle. The mean expression value of the healthy control (i.e. Static CoC) is represented by the red horizontal line, while the mean expression of the untreated control (i.e. HPC CoC supplemented with DMSO only) is represented by the black horizontal line. All gene expression values are normalized relative to GAPDH expression and refer to the basal expression in the untreated control; values are log scale. Individual experimental data era represented by the black dots overlaid to histograms (n=9 biologically independent samples from 3 different donors). Statistical significance was calculated against the respective untreated control. Statistics by Kruskal-Wallis test with Dunn's multiple comparison test (non-normal distributions) in all graphs where statistical analysis is reported. **aP = 0.0023, **bP = 0.0016, ****P<0.0001. Results are mean + SD.* ***e,f,*** *Drug screening: comparison between the proposed HPC model and a 3D "Cytokine-based" model, both established within the CoC. The expression of MMP13 and IL8 in response to administration of two known anti-inflammatory/anti-degrading compounds (i.e. Il1Ra and Rapamycin) was evaluated by RT-qPCR both on HPC and "cytokine-based" (i.e. 1ng/ml IL1β) models. DMSO was used as vehicle. All gene expression values are normalized relative to GAPDH expression and refer to the basal expression in the untreated (i.e. HPC CoC supplemented with DMSO only) control; values are log scale. The mean expression value of the untreated control (i.e. HPC CoC supplemented with DMSO only) is represented by the black horizontal line. PCR (n=9 biologically independent samples from 3 different donors were considered). Statistical significance was calculated against the respective untreated control. Results are mean + SD, *. Statistics by one-way ANOVA and Bonferroni's multiple comparison test or Dunnett's multiple comparison tests (normal distributions), or Kruskal-Wallis test with Dunn's multiple comparison test (non-normal distributions) in all graphs where statistical analysis is reported. a, *P = 0.0322, **aP = 0.0076, **bP = 0.0042; b, **aP = 0.0043, **bP = 0.0050, **cP = 0.0070; ****P < 0.0001. Individual experimental data era represented by the black dots overlaid to histograms.*

2.8 Analysis procedures and methodologies

2.8.1 Device actuation and mechanical characterization.

The electro-pneumatical system illustrated in Fig. 12 was assembled to apply to the CoC model the selected mechanical stimulation pattern. It comprises two Arduino microcontroller boards (Arduino Uno R3 and Arduino Nano, ATmega328P), an air pump (TM40-A12-P23012, Topsflow), two pressure sensors (MPX5500 Series, case 867C-05, Freescale semiconductor and 26PC Series, Honeywell), a miniaturized pressure regulator (ARJ1020F Series, SMC), an integrated relay (Songle), a solenoid valve (Festo Miniature Valve MH1), a custom made stripboard, a manifold, a cylindrical Poly(methyl methacrylate) (PMMA) pressure reservoir, a resistive touchscreen (PIXNOR UNO R3 2.8 TFT Touch Screen) and a cooling fan. All components were fixed to a PMMA supporting base. In detail, the air pump was connected to the pressure reservoir so to limit its duty cycle. The activation of the pump was regulated through the Arduino Nano. The microcontroller, receiving the value provided by the MPX5500 pressure sensor, turns on or off the pump according to the pressure level in the reservoir (1600 mmHg was set as the pump stop value, 840 mmHg as the pump start value). The pump outlet is connected to a manifold linked to the pressure reservoir, to the pressure sensor and to the pressure regulator. The Honeywell pressure sensor, after signal amplification, provides the Arduino Uno with the pressure value downstream of the pressure regulator. A parallel air-line runs from the pressure regulator to the solenoid valve. The valve aperture is regulated by the Arduino Uno. The touch screen was programmed with a user interface for the regulation of the stimulation regimen. A dedicated section provided the user with the working pressure, which can be manually adjusted. Stimulation frequencies of 0.5 Hz, 1 Hz and 2 Hz could be selected by the user.

Stimulation frequency and pattern could be regulated according to each experimental design. A ramp of stopcocks was connected to the miniature valve outlet to multiply the number of addressable microfluidic devices. Up to 24 devices have been stimulated simultaneously.

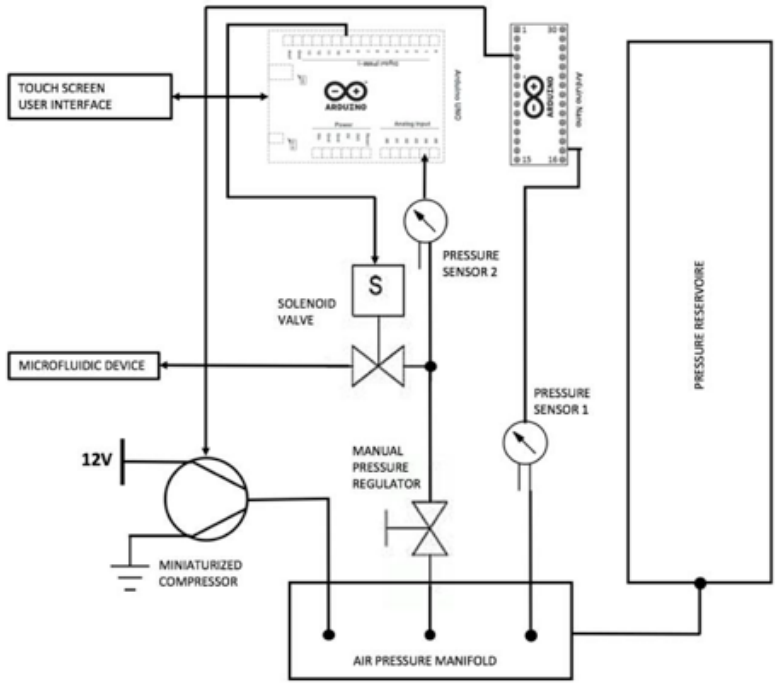

Figure 12: ***Electro-pneumatical actuation system.*** *Single components and connections are schematized.*

2.8.2 Immunofluorescence analyses

Immunofluorescence analyses were performed on CoC models directly within the microscale device at day 0, day 3, day 14 and day 21. Samples were fixed in 4% paraformaldehyde (PFA) overnight at 4°C. Subsequently, the microscale device was disassembled by removing the actuation compartment and carefully pealing-off the PDMS membrane from the culture compartment, eventually exposing the CoC model. Cells were permeabilized with 0.3% Tween (Sigma) PBS solution for 10 minutes. A blocking solution (3% bovine serum albumin (BSA), 0.5% Triton (Sigma) in PBS) was applied for 1 hour at room temperature to block nonspecific bindings. Samples were incubated overnight at 4°C with primary antibodies. Rabbit anti-human aggrecan (dilution 1:200, Abcam), mouse anti-human collagen type-I (dilution 1:200, Abcam) and mouse anti-human collagen type-II (dilution 1:200, Abcam) were used to evaluate the maturation of CoC at day 0, day 3 and day 14. Rabbit anti-human MMP-13 (dilution 1:200, Abcam) and mouse anti-human DIPEN (dilution 1:200, MDBioscience) were used to assess the effect of mechanical compression on CoC model. DAPI staining was used to identify the cell nuclei. As appropriate,

secondary antibodies labelled with Alexa Fluor 488, Alexa Fluor 546, Alexa Fluor 647 (Invitrogen) were used at 1:200 for 45 minutes at room temperature.
Representative images of three different regions of each CoC model were acquired with a 20x objective with fluorescence Nikon A1R Nala Confocal microscope (Nikon, Tokyo, Japan), and analysed by using ImageJ software. For the IF of aggrecan, collagen type-I and collagen type-II, fifteen biologically independent samples from five different donors were considered for each time point. For the IF of MMP13 and DIPEN, nine biologically independent samples from three different donors were considered for each condition.

2.8.3 Biochemical analyses.

Samples were extracted from the microscale device and digested in 300 µl of proteinase-K (1 mg/mL proteinase-K in 50 mM Tris with 1 mM EDTA, 1 mM iodoacetamide, and 10 µg/mL pepstatin-A) overnight at 56°C. GAG amounts were measured spectrophotometrically after reaction with dimethylmethylene blue using chondroitin sulphate as a standard [65]. The amount of DNA was measured spectrophotometrically using the CyQuant cell proliferation assay Kit (Molecular Probes, Eugene, OR), according to manufacturer's instructions. GAG contents were reported as GAG/DNA. Nine biologically independent samples from three different donors were considered for each condition.

2.8.4 Quantitative real-time reverse transcriptase polymerase chain reaction (RT-PCR).

Total RNA extraction by Trizol, cDNA synthesis and real-time reverse transcriptase-polymerase chain reaction (RT-PCR; 7300 AB Applied Biosystem) were performed according to standard protocols to quantitate expression levels of the following genes of interest (Applied Biosystems): COL2A1 (Hs00264051_m1), COL1A1 (Hs00164004_m1), ACAN (Hs00153936_m1), PRG4 (Hs00981633_m1), GDF5 (Hs00167060_m1), ATX (Hs00905117_m1), FRZB (Hs00173503_m1), GREM1 (Hs01879841_s1), MMP13 (Hs00233992_m1), IL6 (Hs00985639_m1), IL8 (Hs00174103_m1), COL10A1 (Hs00166657_m1), IHH (Hs01081800_m1), DKK-1 (Hs00183740_m1). The house-keeping gene Glyceraldehyde 3-phosphate dehydrogenase (GAPDH) was used as reference (Hs02758991_g1). Fifteen biologically independent samples from five different donors were considered for each condition and time point.

2.8.5 MMP-13 release quantification.

MMP-13 production was selectively assayed using enzyme specific fluorescence substrate kits SensoLyte 520 MMP13 Assay Kit (AnaSpec Fremont, CA 94555), according to manufacturer's instructions. Briefly,

cell supernatants were collected at days 16, 18, 20 and 21 during the mechanical compression phase and the time points samples pooled to measure the accumulation of MMP-13 during the whole stimulation period. The kit uses 96-well plates coated with a monoclonal anti-human MMP-13 antibody that recognizes both the latent and active forms of the enzyme. The specificity of the monoclonal antibodies prevents cross-reactivity with other MMPs. Pro-MMP-13 is activated by incubation with 4-aminophenylmercuric acetate (APMA) at 37 °C. Proteolytic activity of the enzymes is measured using a fluorescence resonance energy transfer (FRET) peptide containing a quenched fluorophore. Upon cleaving MMP-13, fluorescence of the fluorophore was recovered and was measured on configurable multi-mode microplate reader (Synergy H1, Biotek Instruments GmbH) following a five hours incubation period at room temperature, with an excitation and emission wavelength of 485±20 nm and 530±25 nm, respectively. Nine biologically independent samples from three different donors were considered for each condition.

2.8.6 Statistical analysis.

Results of computational simulations and strain field validation are presented as mean ± SD. Results of quantitative RT-qPCR, biochemical analyses and proMMP-13 quantification are presented as mean + SD. Statistical analysis was performed using GraphPad Prism 7.00. Data Populations normal distribution was assessed through D'Agostino-Pearson Test. Two tailed Student's T-test (normal distributions) and Mann-Whitney test (non-normal distributions) where used when comparing two populations. Multiple comparisons were realized using ordinary one-way ANOVA. When comparing normally distributed variables, Bonferroni's or Dunnett's multiple comparison tests with single pooled variance were used for small or large numbers of populations and statistical significance was indicated by $P<0.05$ (*) and $P<0.01$(**), respectively. When comparing non-normally distributed variables, the Kruskal-Wallis test with Dunn's multiple comparison test was used and statistical significance was indicated by $P<0.001$(***) and $P<0.0001$(****), respectively.

2.9 Discussion

In the present study, a microscale platform integrating i) a PEG hydrogel-based 3D microenvironment and ii) a mechanical actuation system able to provide defined levels of confined compression, was proposed as a tool to generate an *in vitro* model of Cartilage-on-Chip (CoC). The platform was successfully used to elicit the acquisition of osteoarthritic traits by the newly formed cartilaginous tissue, through the sole imposition of a hyper-physiological mechanical stimulation. A proof of principle of the advantageous applicability of the generated OA CoC model as drug screening tool was finally provided.

In the native cartilage, chondrocytes are subjected to a variety of mechanical stimuli, which are yet difficult to recapitulate *in vitro*[12]. Dissecting the complexity of such joint mechanical microenvironment, this study focused on the compressive component, which is representative of the deformation field experienced by chondrocytes [6]. Recent advances in microfluidic and microfabrication technologies have enabled the integration of key mechanical cues (i.e. cyclic uniaxial strain) within 3D *in vitro* models, featuring a cellular relevant scale and an unprecedented level of control [29]. Building upon these cutting-edge technologies, we designed a platform able to apply, at the microscale, a controlled and confined axial compressive strain to a 3D cell-laden microconstruct, while limiting lateral and longitudinal expansion. Finite element modelling was used to optimize the geometrical features of the device and to evaluate the strain field within the 3D microconstruct volume. Remarkably, an overall homogeneity could be achieved in the Nominal Strains. Homogeneity in the applied mechanical cues indeed avoids exacerbating the response heterogeneity that is inherent to cell populations, thus limiting the presence of uncontrolled and confounding factors. Furthermore, the experimental validation proved a strong correspondence to the *in-silico* computations in terms of confined compression applied over the entire volume of the 3D microconstruct. Existing macroscale bioreactors-based compressive models are either force-controlled or strain controlled. Force-controlled systems often induce not physiologically relevant strains [5], since the associated forces are largely dependent on the mechanical properties of the artificial scaffold [22, 23]. Strain-controlled systems, on the other hand, exhibit poor control over the actual provided mechanical stimuli. Compression of biphasic materials such as hydrogels, in fact, induces deformation of the solid component resulting into transient increases in the pressure of the permeating fluid. Pressure equilibrates as the fluid is forced out of the gel, generating unwanted pressure waves. Thanks to the increased surface to volume ratio characterizing microfluidic systems, a rapid attenuation of the generated waves is instead possible at the microscale, thus avoiding this undesired effect of matrix-fluid coupling [66]. The proposed device allows to provide a strain-controlled and locally well-defined mechanical stimuli to confined constructs characterised by a cartilage-like ECM, achieving compressive levels tailored to be consistent with those measured *in vivo* [67, 68].

The designed microscale device was first exploited to generate an *in vitro* model of human articular CoC, and subsequently to shift its mechanical microenvironment towards a hyper-physiological level. To this

aim, we took advantage of a previously introduced 3D enzymatically cross-linked and MMP-degradable PEG hydrogel matrix [31]. The constitutive PEG hydrogel network is synthetic thus benefitting from a higher standardization with respect to naturally derived biomaterials [69]. Furthermore, it was chemically modified to enable metalloproteinase-mediated degradation, thus permitting tissue remodelling through physiologically relevant processes. By encapsulating adult hACs within PEG hydrogels and culturing them for 14 days, microtissues rich in collagen type-II and aggrecan, constitutive elements of the articular cartilage ECM, were obtained. A panel of genes highly expressed in human articular cartilage (i.e. *ACAN, PRG4, COL2A1/COL1A1* ratio) were upregulated in the CoC and showed, after 14 days of maturation, an expression level comparable to that found in native healthy chondrocytes, confirming the physiological relevance of the system as a cartilage model. Canonical Wnt inhibitor Frizzled-Related Protein (*FRZB*) and BMP antagonist Gremlin (*GREM1*) were recently identified as cartilage brakes of hypertrophic differentiation in adult human cartilage [51]. Their upregulation up to levels comparable with native chondrocytes further demonstrates the maturation of the obtained CoC towards a stable articular cartilaginous tissue. Finally, the reported increased expression of *ATX* and *GDF5* over time could indicate an evolution of the presented model towards stable cartilage through the recapitulation of a developmental pathway[45]. It is worth noting that in the CoC cells mostly presented an elongated morphology after two weeks of maturation, while an ideal cartilaginous model would comprise chondrocytes with a rounder morphology. Nevertheless, the fact that a dense matrix rich in cartilage ECM components could be achieved together with a gene expression panel not dissimilar to that of native chondrocytes make the adopted model adequate in representing the functional response of cartilage on chip. Notably, the presented platform allowed achieving CoC models in a highly reproducible fashion starting from five different human donors, without any exclusion. This demonstrates the capability of the model in generating articular cartilage constructs, regardless of the reported high donor-to-donor variability proper of primary hACs [70].

A series of clinical evaluations indicates mechanical abnormalities (e.g., due to obesity, trauma, joint misalignment) as one of the key risk factors in developing OA [6]. We thus hypothesized that a hyper-physiological mechanical stimulation could trigger the onset of early OA traits also *in vitro*. The intensity of the strain field in the cartilage upon mechanical compression is currently under debate and its reported values vary depending on the considered region within the joint, on the physical activity undertaken by the subjects, and on the eventual disease progression state[6]. Based on existing reports, two compression levels were chosen as representative of physiological (10%, PC) and hyper-physiological (30%, HPC) mechanical stimulations. While load-based *in vitro* models currently used to induce OA often rely on mechanical stimuli that disregard the *in vivo* joint condition and induce direct cell damage [5, 6], the compressive values applied here were demonstrated to modulate inflammation [71], while still falling within the range of cartilage deformations occurring *in vivo* [67, 68]. Moreover, cellular viability assays permitted to exclude

that the anabolic-catabolic imbalance observed in our model was caused by overload-mediated cellular death [6].

The pathological changes observed in OA joints include a substantial alteration of stable articular cartilage homeostasis, mainly resulting in i) loss of cartilage matrix components, ii) increased inflammation and production of degrading mediators, and iii) acquisition of hypertrophic traits. Accordingly, the HPC applied in this study was sufficient alone to induce a catabolic imbalance in the CoC model, characterized by reduction of cartilage ECM constituents (i.e. *COL2A1*, *ACAN*), in line with previous findings [72], and by the onset of an inflammatory microenvironment through *IL6* and *IL8* upregulation. Moreover, the production of degrading enzymes (i.e. MMP13) was significantly enhanced in response to HPC, suggesting the triggering of a tissue degradation process. ProMMP13 levels released in the supernatant were incremented only by the HPC, thus suggesting the presence of a triggering threshold for the mechanical overload. The onset of a hypertrophic cartilage phenotype [16] was also observed in our model, with increased gene expression level of *COL10A1* and *IHH* upon HPC. Notably, this trend was not visible when a "cytokine-based" model was used, regardless of the concentration of IL1β or the dimensional scale of the model (2D vs. 3D), suggesting the better adequacy of our HPC-based system in modelling hypertrophic traits characterizing OA progression.

FRZB, DKK1, inhibitors of Wnt pathway, and *GREM1,* antagonists of BMP pathway, have been reported to play a key role in cartilage homeostasis[73]. A downregulation of these genes was demonstrated in human OA as compared to healthy cartilage, with a further drop in load bearing degraded zones within the same joint [47]. HPC led to a significant reduction of these genes' expression, demonstrating the capability of the presented model to capture the Wnt and BMP antagonists' dysregulation reported in osteoarthritis patients. Notably, previous *in vitro* studies [47, 73] achieved the downregulation of these genes following cytokine administration (i.e. IL1β), and their upregulation upon mechanical stimulation within a physiological range. Here, an *in vitro* a downregulation in the expression of these genes was induced upon application of an OA-like hyper-physiological compression.

Presented data demonstrate the capability of the proposed platform to effectively induce cellular responses of our CoC model that have been correlated with the onset of OA in human joints, by the sole imposition of a mechanical hyper-physiological compression. Notably, these responses showed to be strictly dependent on both the compression level and the compression nature (confined) achieved by the specific design, highly suggesting that they are mediated by mechanobiology rather than mere mass transfer phenomena. It is however worth mentioning that the identification of univocal and commonly accepted biomarkers for determining the switch between healthy and pathological cartilage is still a critical issue in the field. On one hand, the translation of clinically used prognostic and diagnostic biomarkers to *in vitro* systems is still poorly defined; on the other hand, a clear definition of pathways deregulation involved in OA aetiology is

still lacking even in the clinical scenario [74]. This huge gap makes the *in vitro* representation of the disease particularly cumbersome and recommends caution in claiming effective mirroring by proposed models of the joint pathology. Overall, a deeper understanding of the pathology basic mechanisms will be pivotal in bridging this gap and eventually defining the ideal *in vitro* model of OA. It is also worth mentioning that OA is a whole joint disease involving cartilage but also osteochondral bone and synovial tissue. While dissecting factors affecting single tissues, as proposed in this study, is instrumental in reducing complexity, the inclusion of multi-tissue interfaces and inter cellular cross-talks [75, 76] will be the next essential step towards a "joint-on-chip" perspective.

Even if far from recapitulating a "whole OA joint", the proposed HPC-based CoC model presents key cellular responses correlated with the onset of OA in the cartilage compartment (i.e. inflammation, catabolism/anabolism unbalance, onset of an hypertrophic phenotype) and it is thus a promising tool for testing the anti-OA effects of drug candidates. We here demonstrated that anti-inflammatory and anti-catabolic responses of both known drugs [43, 57, 59] and compounds currently under investigation [62] could be predicted by our model. Our results were consistent with data from previously reported animal studies [43, 59, 77, 78], and in some cases were able to predict effects not detectable by a traditional "cytokine-based" model (i.e. effects of Rapamycin).

2.10 Conclusive remarks

An in vitro microscale platform enabling the application of a finely strain-controlled compression to a 3D microconstruct was presented. The possibility to obtain stable and highly reproducible CoC and to elicit a biological response to mechanical overload, which correlates with key traits triggered during OA onset was demonstrated. Moreover, the proposed model could predict the effects of anti-inflammatory/anti-catabolic drugs and results were consistent with existing preclinical and clinical reports. The prediction of drug responses was instead poor in commonly used cytokine-based models. The proposed technological tool gives, therefore, a first proof of concept of the possibility of creating miniaturized *in vitro* models closely representing a joint degenerative pathology such as OA. The here presented CoC model will serve both in performing basic research towards a better understanding of OA pathophysiology and, possibly through the implementation of a higher-throughput version [30], as a powerful tool to screen anti-OA candidates, speeding up the discovery process and potentially decreasing the need for animal models.

In a broader perspective, this technology could also be beneficial to studying the response to mechanical stimulation of different tissues naturally subjected to deformation under physiological or pathological conditions (e.g., bone), while combining the efficacy of scale reduction with the capability of reproducing key structural and functional cues with unprecedented precision.

2.11 References

1. JW B, F B, FP L (2011) Osteoarthritis: an update with relevance for clinical practice. Lancet (London, England) 377:2115–2126. https://doi.org/10.1016/S0140-6736(11)60243-2
2. Wittenauer R, Smith L, Aden K (2013) Background Paper 6.12 Osteoarthritis
3. Pavan M, Galesso D, Menon G, et al (2013) Hyaluronan derivatives: Alkyl chain length boosts viscoelastic behavior to depolymerization. Carbohydr Polym 97:321–326
4. Li C, Zheng Z, Ha P, et al (2020) Neural EGFL like 1 as a potential pro-chondrogenic, anti-inflammatory dual-functional disease-modifying osteoarthritis drug. Biomaterials 226:119541. https://doi.org/10.1016/j.biomaterials.2019.119541
5. Johnson CI, Argyle DJ, Clements DN (2016) In vitro models for the study of osteoarthritis. Vet J 209:40–49. https://doi.org/10.1016/j.tvjl.2015.07.011
6. Sanchez-Adams J, Leddy HA, McNulty AL, et al (2014) The Mechanobiology of Articular Cartilage: Bearing the Burden of Osteoarthritis. Curr Rheumatol Rep 16:451. https://doi.org/10.1007/S11926-014-0451-6
7. Arden N, Nevitt MC (2006) Osteoarthritis: Epidemiology. Best Pract Res Clin Rheumatol 20:3–25. https://doi.org/10.1016/J.BERH.2005.09.007
8. Esch EW, Bahinski A, Huh D (2015) Organs-on-chips at the frontiers of drug discovery. Nat Rev Drug Discov 14:248–260. https://doi.org/10.1038/nrd4539
9. Kutzner I, Heinlein B, Graichen F, et al (2010) Loading of the knee joint during activities of daily living measured in vivo in five subjects. J Biomech 43:2164–2173. https://doi.org/10.1016/j.jbiomech.2010.03.046
10. Mow VC, Ratcliffe A, Robin Poole A (1992) Cartilage and diarthrodial joints as paradigms for hierarchical materials and structures. Biomaterials 13:67–97. https://doi.org/10.1016/0142-9612(92)90001-5
11. Grodzinsky AJ, Levenston ME, Jin M, Frank EH (2000) Cartilage tissue remodelling in response to mechanical forces. Annu. Rev.:691–713
12. Choi JB, Youn I, Cao L, et al (2007) Zonal changes in the three-dimensional morphology of the chondron under compression: The relationship among cellular, pericellular, and extracellular deformation in articular cartilage. J Biomech 40:2596–2603. https://doi.org/10.1016/J.JBIOMECH.2007.01.009
13. Occhetta P, Mainardi A, Votta E, et al (2019) Hyperphysiological compression of articular cartilage induces an osteoarthritic phenotype in a cartilage-on-a-chip model. Nat Biomed Eng. https://doi.org/10.1038/s41551-019-0406-3
14. Arden N, Nevitt MC (2006) Osteoarthritis: Epidemiology. Best Pract Res Clin Rheumatol 20:3–25. https://doi.org/10.1016/J.BERH.2005.09.007
15. Bijlsma JW, Berenbaum F, Lafeber FP (2011) Osteoarthritis: an update with relevance for clinical practice. Lancet 377:2115–2126. https://doi.org/10.1016/S0140-6736(11)60243-2
16. Dreier R (2010) Hypertrophic differentiation of chondrocytes in osteoarthritis: the developmental aspect of degenerative joint disorders. Arthritis Res Ther 12:216. https://doi.org/10.1186/ar3117
17. Lin H, Lozito TP, Alexander PG, et al (2014) Stem cell-based microphysiological osteochondral system to model tissue response to interleukin-1?? Mol Pharm 11:2203–2212. https://doi.org/10.1021/mp500136b
18. Goldman SM, Barabino GA (2016) Spatial Engineering of Osteochondral Tissue Constructs Through Microfluidically Directed Differentiation of Mesenchymal Stem Cells. Biores Open Access 5:109–117. https://doi.org/10.1089/biores.2016.0005
19. Mumme M, Barbero A, Miot S, et al (2016) Nasal chondrocyte-based engineered autologous cartilage tissue for repair of articular cartilage defects: an observational first-in-human trial. Lancet 388:1985–1994. https://doi.org/10.1016/S0140-6736(16)31658-0
20. Kafienah W, Jakob M, Démarteau O, et al (2002) Three-Dimensional Tissue Engineering of Hyaline Cartilage: Comparison of Adult Nasal and Articular Chondrocytes. Tissue Eng 8:817–826. https://doi.org/10.1089/10763270260424178
21. Tsimbouri PM, Childs PG, Pemberton GD, et al (2017) Stimulation of 3D osteogenesis by mesenchymal stem cells using a nanovibrational bioreactor. Nat Biomed Eng 1:758–770. https://doi.org/10.1038/s41551-017-0127-4
22. Lee DA, Bader DL (1997) Compressive strains at physiological frequencies influence the metabolism of chondrocytes seeded in agarose. J Orthop Res 15:181–188. https://doi.org/10.1002/jor.1100150205
23. De Croos JNA, Dhaliwal SS, Grynpas MD, et al (2006) Cyclic compressive mechanical stimulation induces sequential catabolic and anabolic gene changes in chondrocytes resulting in increased extracellular matrix accumulation. Matrix Biol 25:323–331. https://doi.org/10.1016/J.MATBIO.2006.03.005
24. Khozoee B, Mafi P, Mafi R, Khan W (2017) Mechanical Stimulation Protocols of Human Derived Cells in Articular Cartilage Tissue Engineering – A Systematic Review. Curr Stem Cell Res Ther 12:260–270. https://doi.org/10.2174/1574888X11666160614103840
25. Huh D, Matthews BD, Mammoto A, et al (2010) Reconstituting organ-level lung functions on a chip. Science (80-) 328:1662–1668. https://doi.org/10.1126/science.1188302
26. Ugolini GS, Visone R, Redaelli A, et al (2017) Generating Multicompartmental 3D Biological Constructs Interfaced through Sequential Injections in Microfluidic Devices. Adv Healthc Mater 6:1601170. https://doi.org/10.1002/adhm.201601170
27. Occhetta P, Visone R, Rasponi M (2017) High-throughput microfluidic platform for 3D cultures of mesenchymal stem cells. Methods Mol Biol 1612:303–323. https://doi.org/10.1007/978-1-4939-7021-6_23
28. Ng JMK, Gitlin I, Stroock AD, Whitesides GM (2002) Components for integrated poly(dimethylsiloxane) microfluidic systems. Electrophoresis 23:3461–3473. https://doi.org/10.1002/1522-2683(200210)23:20<3461::AID-ELPS3461>3.0.CO;2-8
29. Marsano A, Conficconi C, Lemme M, et al (2016) Beating heart on a chip: a novel microfluidic platform to generate functional 3D cardiac microtissues. Lab Chip 16:599–610
30. Visone R, Ugolini GS, Vinarsky V, et al (2018) A Simple Vacuum-Based Microfluidic Technique to Establish High-Throughput Organs-On-Chip and 3D Cell Cultures at the Microscale. Adv Mater Technol 1800319. https://doi.org/10.1002/admt.201800319
31. Ehrbar M, Rizzi SC, Schoenmakers RG, et al (2007) Biomolecular hydrogels formed and degraded via site-specific enzymatic reactions. Biomacromolecules 8:3000–3007. https://doi.org/10.1021/bm070228f
32. Blum MM, Ovaert TC (2012) Experimental and numerical tribological studies of a boundary lubricant functionalized poro-viscoelastic PVA hydrogel in normal contact and sliding. J Mech Behav Biomed Mater 14:248–258. https://doi.org/10.1016/j.jmbbm.2012.06.009
33. Kalyanam S (2009) Poro-Viscoelastic Behavior of Gelatin Hydrogels Under Compression-Implications for Bioelasticity Imaging. J Biomech Eng 131:081005. https://doi.org/10.1115/1.3127250

34. DiSilvestro MR, Suh JKF (2001) A cross-validation of the biphasic poroviscoelastic model of articular cartilage in unconfined compression, indentation, and confined compression. J Biomech 34:519–525. https://doi.org/10.1016/S0021-9290(00)00224-4
35. DiSilvestro MR, Zhu Q, Wong M, et al (2001) Biphasic Poroviscoelastic Simulation of the Unconfined Compression of Articular Cartilage: I—Simultaneous Prediction of Reaction Force and Lateral Displacement. J Biomech Eng 123:191. https://doi.org/10.1115/1.1351890
36. Villanueva I, Hauschulz DS, Mejic D, Bryant SJ (2008) Static and dynamic compressive strains influence nitric oxide production and chondrocyte bioactivity when encapsulated in PEG hydrogels of different crosslinking densities. Osteoarthr Cartil 16:909–918. https://doi.org/10.1016/J.JOCA.2007.12.003
37. Phelps EA, Enemchukwu NO, Fiore VF, et al (2012) Maleimide cross-linked bioactive PEG hydrogel exhibits improved reaction kinetics and cross-linking for cell encapsulation and in situ delivery. Adv Mater 24:64–70. https://doi.org/10.1002/adma.201103574
38. Wu JZ, Herzog W, Epstein M (1997) Evaluation of the finite element software ABAQUS for biomechanical modelling of biphasic tissues. J Biomech 31:165–169. https://doi.org/10.1016/S0021-9290(97)00117-6
39. Meng Q, Jin Z, Fisher J, Wilcox R (2013) Comparison between FEBio and Abaqus for biphasic contact problems. Proc Inst Mech Eng Part H J Eng Med 227:1009–1019. https://doi.org/10.1177/0954411913483537
40. Ehrbar M, Sala A, Lienemann P, et al (2011) Elucidating the Role of Matrix Stiffness in 3D Cell Migration and Remodeling. Biophys J 100:284–293. https://doi.org/10.1016/J.BPJ.2010.11.082
41. Phelps EA, Enemchukwu NO, Fiore VF, et al Maleimide cross-linked bioactive PEG hydrogel exhibits improved reaction kinetics and cross-linking for cell encapsulation and in-situ delivery. https://doi.org/10.1002/adma.201103574
42. Lienemann PS, Lutolf MP, Ehrbar M (2012) Biomimetic hydrogels for controlled biomolecule delivery to augment bone regeneration. Adv Drug Deliv Rev 64:1078–1089. https://doi.org/10.1016/J.ADDR.2012.03.010
43. Braddock M, Quinn A (2004) Targeting IL-1 in inflammatory disease: new opportunities for therapeutic intervention. Nat Rev Drug Discov 3:330
44. Caron MMJ, Emans PJ, Coolsen MME, et al (2012) Redifferentiation of dedifferentiated human articular chondrocytes: comparison of 2D and 3D cultures. Osteoarthr Cartil 20:1170–1178. https://doi.org/10.1016/J.JOCA.2012.06.016
45. Ray A, Singh PNP, Sohaskey ML, et al (2015) Precise spatial restriction of BMP signaling is essential for articular cartilage differentiation. Development 142:1169–1179
46. Nishioka T, Arima N, Kano K, et al (2016) ATX-LPA1 axis contributes to proliferation of chondrocytes by regulating fibronectin assembly leading to proper cartilage formation. Sci Rep 6:23433
47. Leijten JCH, Emons J, Sticht C, et al (2012) Gremlin 1, Frizzled-related protein, and Dkk-1 are key regulators of human articular cartilage homeostasis. Arthritis Rheumatol 64:3302–3312
48. Takaishi H, Kimura T, Dalal S, et al (2008) Joint diseases and matrix metalloproteinases: a role for MMP-13. Curr Pharm Biotechnol 9:47–54
49. Embry Flory JJ, Fosang AJ, Knudson W (2006) The accumulation of intracellular ITEGE and DIPEN neoepitopes in bovine articular chondrocytes is mediated by CD44 internalization of hyaluronan. Arthritis Rheum 54:443–454. https://doi.org/10.1002/art.21623
50. Kronenberg HM (2003) Developmental regulation of the growth plate. Nature 423:332–336
51. Leijten JCH, Bos SD, Landman EBM, et al (2013) GREM1, FRZB and DKK1 mRNA levels correlate with osteoarthritis and are regulated by osteoarthritis-associated factors. Arthritis Res Ther 15:R126
52. O'conor CJ, Leddy HA, Benefield HC, et al TRPV4-mediated mechanotransduction regulates the metabolic response of chondrocytes to dynamic loading. https://doi.org/10.1073/pnas.1319569111
53. Lee W, Leddy HA, Chen Y, et al (2014) Synergy between Piezo1 and Piezo2 channels confers high-strain mechanosensitivity to articular cartilage. Proc Natl Acad Sci U S A 111:E5114–E5122. https://doi.org/10.1073/pnas.1414298111
54. Tsuchida AI, Beekhuizen M, `t Hart MC, et al (2014) Cytokine profiles in the joint depend on pathology, but are different between synovial fluid, cartilage tissue and cultured chondrocytes. Arthritis Res Ther 16:441. https://doi.org/10.1186/s13075-014-0441-0
55. Bau B, Gebhard PM, Haag J, et al (2002) Relative messenger RNA expression profiling of collagenases and aggrecanases in human articular chondrocytes in vivo and in vitro. Arthritis Rheumatol 46:2648–2657
56. Grodzinsky AJ, Wang Y, Kakar S, et al (2017) Intra-articular dexamethasone to inhibit the development of post-traumatic osteoarthritis. J Orthop Res 35:406–411
57. Yan B, Zhang Z, Jin D, et al (2016) mTORC1 regulates PTHrP to coordinate chondrocyte growth, proliferation and differentiation. Nat Commun 7:11151
58. Pal B, Endisha H, Zhang Y, Kapoor M (2015) mTOR: a potential therapeutic target in osteoarthritis? Drugs R D 15:27–36
59. Zweers MC, de Boer TN, van Roon J, et al (2011) Celecoxib: considerations regarding its potential disease-modifying properties in osteoarthritis. Arthritis Res Ther 13:239
60. Lim H, Min DS, Kang Y, et al (2015) Inhibition of matrix metalloproteinase-13 expression in IL-1β-treated articular chondrocytes by a steroidal saponin, spicatoside A, and its cellular mechanisms of action. Arch Pharm Res 38:1108–1116
61. Sasaki H, Takayama K, Matsushita T, et al (2012) Autophagy modulates osteoarthritis-related gene expression in human chondrocytes. Arthritis Rheumatol 64:1920–1928
62. Pavan M, Galesso D, Secchieri C, Guarise C (2016) Hyaluronic acid alkyl derivative: a novel inhibitor of metalloproteases and hyaluronidases. Int J Biol Macromol 84:221–226
63. Kapoor M, Martel-Pelletier J, Lajeunesse D, et al (2011) Role of proinflammatory cytokines in the pathophysiology of osteoarthritis. Nat Rev Rheumatol 7:33
64. Guarise C, Pavan M, Galesso D, et al (2018) Matrix metalloprotease 3 (MMP3) inhibition effect of a viscosupplement based on a hyaluronic acid amide derivative (HYADD4). Osteoarthr Cartil 26:S286–S287
65. Farndale RW, Buttle DJ, Barrett AJ (1986) Improved quantitation and discrimination of sulphated glycosaminoglycans by use of dimethylmethylene blue. Biochim Biophys Acta (BBA)-General Subj 883:173–177
66. Moraes C, Sun Y, Simmons CA (2011) (Micro) managing the mechanical microenvironment. Integr Biol 3:959–971
67. Greaves LL, Gilbart MK, Yung AC, et al (2010) Effect of acetabular labral tears, repair and resection on hip cartilage strain: A 7 T MR study. J Biomech 43:858–863. https://doi.org/10.1016/J.JBIOMECH.2009.11.016
68. Wong BL, Sah RL (2010) Effect of a focal articular defect on cartilage deformation during patello-femoral articulation. J Orthop Res 28:1554–1561. https://doi.org/10.1002/jor.21187
69. Lutolf MP, Hubbell JA (2005) Synthetic biomaterials as instructive extracellular microenvironments for morphogenesis in tissue

engineering. Nat Biotechnol 23:47–55. https://doi.org/10.1038/nbt1055
70. Barbero A, Grogan S, Schäfer D, et al (2004) Age related changes in human articular chondrocyte yield, proliferation and post-expansion chondrogenic capacity. Osteoarthr Cartil 12:476–484. https://doi.org/10.1016/J.JOCA.2004.02.010
71. Nam J, Aguda BD, Rath B, Agarwal S (2009) Biomechanical Thresholds Regulate Inflammation through the NF-κB Pathway: Experiments and Modeling. PLoS One 4:e5262. https://doi.org/10.1371/journal.pone.0005262
72. Hunter CJ, Imler SM, Malaviya P, et al (2002) Mechanical compression alters gene expression and extracellular matrix synthesis by chondrocytes cultured in collagen I gels. Biomaterials 23:1249–1259. https://doi.org/https://doi.org/10.1016/S0142-9612(01)00245-9
73. Zhong L, Schivo S, Huang X, et al (2017) Nitric oxide mediates crosstalk between interleukin 1β and WNT signaling in primary human chondrocytes by reducing DKK1 and FRZB expression. Int J Mol Sci 18:1–18. https://doi.org/10.3390/ijms18112491
74. Mobasheri A, Bay-Jensen A-C, van Spil WE, et al (2017) Osteoarthritis Year in Review 2016: biomarkers (biochemical markers). Osteoarthr Cartil 25:199–208. https://doi.org/10.1016/J.JOCA.2016.12.016
75. Goldring SR, Goldring MB (2016) Changes in the osteochondral unit during osteoarthritis: structure, function and cartilage–bone crosstalk. Nat Rev Rheumatol 12:632–644. https://doi.org/10.1038/nrrheum.2016.148
76. Yuan XL, Meng HY, Wang YC, et al (2014) Bone-cartilage interface crosstalk in osteoarthritis: potential pathways and future therapeutic strategies. Osteoarthr Cartil 22:1077–89. https://doi.org/10.1016/j.joca.2014.05.023
77. Takayama K, Kawakami Y, Kobayashi M, et al (2014) Local intra-articular injection of rapamycin delays articular cartilage degeneration in a murine model of osteoarthritis. Arthritis Res Ther 16:482
78. Matsuzaki T, Matsushita T, Tabata Y, et al (2014) Intra-articular administration of gelatin hydrogels incorporating rapamycin–micelles reduces the development of experimental osteoarthritis in a murine model. Biomaterials 35:9904–9911. https://doi.org/https://doi.org/10.1016/j.biomaterials.2014.08.041

3 Uniting in vitro models' relevance with higher throughput: a multi chamber mid-throughput mechanically active device for the study of degenerative processes in mechanically active districts

The work described in this chapter was carried out in the framework of a collaboration between the Microfluidic and Biomimetic Microsystems Laboratory of Politecnico di Milano, (Milan, Italy) and the Cardiac Surgery and Engineering laboratory of the University Hospital of Basel (Basel, Switzerland).

This chapter partially refers to:

A dynamic microscale mid-throughput fibrosis model to investigate the effects of different ratios of cardiomyocytes and fibroblasts Andrea Mainardi, Francesca Carminati, Giovanni Stefano Ugolini, Paola Occhetta, Giuseppe Isu, Diana Robles Diaz, Gregory Reid, Roberta Visone, Marco Rasponi, Anna Marsano Lab Chip. 2021 (In press) DOI: 10.1039/D1LC00092F

3.1 Introduction

For each possible identified drug target about 10^6 chemical entities are run through high-throughput screens (HTS). The selection is refined through serial assays yielding roughly 200 qualified leads that enter the cost intensive preclinical and (potentially) clinical phases. A single New Molecular Entity (NME) is identified in the end. Especially critical and costly in this progression are compounds that fail during the later stages of Research and Development (R&D) processes [1]. This high inefficiency has led to the search for new models and paradigms in drug development allowing "resolution of technical uncertainty early in development" with a direct assessment of pharmacological activity in human samples [2].

Organs-on-chip (OoCs) models better recapitulate *in vivo* occurring pathophysiological processes providing the basis for preclinical assays with greater predictive power [3]. However, a further promise of the OoC technology, that is, the capability for parallelization and, at least, medium-throughput experimentation, has not been realized yet.[4] Although most of the developed OoC systems feature micron-sized footprints, they still consist of single culture chambers. Even devices with a higher throughput are often based on the repetition, in an array fashion, of a single platform unit without a net increase of the operational ease [5]. Therefore OoCs have, so far, been applied primarily in mechanistic studies, functional validation assessments, and toxicity screening characterized by labour intensive and low-throughput workflows not suited for the early phases of R&D processes [1].

The lack of relevant models featuring also a satisfactory throughput is particularly evident for body districts (e.g. the musculoskeletal apparatus or the cardiac muscle) in which mechanical cues (whose incorporation complicates models realization and usage procedures) are necessary to attain a physiologically relevant environment.

In this chapter, cardiac fibrosis was considered as a case study to demonstrate how a mechanically active environment and a higher experimental throughput could be coupled in an OoC model.

Cardiac fibrosis is a maladaptive pathological remodelling that follows myocardial infarction (MI), leading to cardiac dysfunction and enhanced risk of arrythmias [6]. Quiescent cardiac fibroblasts (FBs), activated by the wound healing cascade, switch their phenotype into myofibroblasts increasing the expression levels of contractile proteins such as α-smooth muscle actin (SMA) and the deposition of extracellular matrix (ECM) proteins (e.g. collagen type-I and fibronectin) endorsing a profibrotic environment [7, 8]. This adaptive course prevents rupturing of the ventricular wall but results, ultimately, in tissue stiffening and altered current conductivity that impair altogether the normal heart function [9].

Therapeutic solutions under study generally aimed at increasing the self-healing properties of cardiomyocytes and/or fostering angiogenesis [10, 11]. Only a few research studies directly focused on the fibrotic processes, inhibiting key upregulated signalling pathway such as Transforming Growth Factor beta

(TGF-) or connective tissue growth factor [12, 13]. Consequently, there are no established anti-fibrotic treatments in the current clinical setting.

Innovative fibrosis models could help in deciphering the pathological mechanisms highlighting therapeutic targets.

Animal models of myocardial infarction have often been employed for examining the fundamental mechanisms underlying the pathology [14, 15] but their complexity does not allow to investigate the role and the interplays of individual pathological cues (e.g. altered mechanics, dysregulated cellular populations, inflammation etc.). Conversely, *in vitro* models of scar formation are easily operable and allow a higher control of the environmental parameters [16] but the achievement of a comprehensive preclinical model remains a challenge.

Indeed, key aspects such as the type [17], age [18], origin [19], and stage of differentiation of adopted cells as well as the substrate composition and stiffness [17] were all proved to be highly relevant in mimicking fibrosis.

Classic plasticware-based two-dimensional (2D) rigid substrates were demonstrated inadequate as they cause spontaneous fibroblasts differentiation into myofibroblasts due to their non-physiological stiffness [16]. More advanced fibrosis *in vitro* models ranging from hydrogels micropatterns with mechanical properties close to the stiffness of the post-infarction myocardium [9], to three dimensional (3D) models [6, 20, 21] were proposed, but most studies were often limited to a single cell type (i.e. FBs), making it impossible to address the complex intercellular interactions that distinguish the fibrotic process [6].

Cardiomyocytes (CMs) and FBs interactions, in fact, were shown to be key for the comprehension of heart homeostasis and pathological conditions as arrythmia, fibrosis, and hypertrophy [15], but also in the determination of ECM alterations effects [22]. CMs were indicated to have protective properties, hindering the scar formation process led by activated FBs and thus making their incorporation instrumental in studying a possible cross-talk with activated FBs [19, 23]. Moreover including increasing percentages (from 5 to 15%) of FBs, either preactivated or not by TGF-β1 supplementation, in 3D cardiac constructs, negatively affected constructs electromechanics performances and CMs functionality [24]. Notably, FBs percentages greater than 50% caused a significant drop in the beating frequency and contraction force of cardiac microtissues *in vitro*, while the same effect was not obtained by simply mimicking the augmented stiffness of fibrotic myocardium increasing microtissues collagen content [22]. Similar results were obtained adopting different ratios of FBs and CMs (i.e. 1:1 [16] or 10:3 [18]) emphasizing how incorporation of both cellular population is necessary in relevant *in vitro* models.

Different OoC based fibrosis [20, 25], and more in general cardiac [26], models have been proposed in recent years. OoCs in particular allowed to introduced a mechanically active environment. It was this demonstrated that mimicking of myocardial beating advances the maturation and the contractile properties

of cardiac microconstructs, leading to a more representative heart model [26] and, moreover, that cyclic uniaxial stimulation of 3D cardiac FBs-laden fibrin gels can, alone, induce some of the key steps of a scar formation usually obtained through to the supplementation of TGF-1 [20].

Proposed mechanically active platforms were however based on single chamber units [4]. An OoC device in which multiple biologically independent 3D cardiac microtissues could be cultured independently was reported but constructs were limited to static culture conditions[27].

For cardiac disease applications, therefore, it is still an open challenge to generate a microfluidic based 3D system capable of providing adequate mechanical stimuli and the necessary microenvironmental conditions, while maintaining a sufficient throughput level.

Addressing this deficit, the object of this chapter was the development of a microfluidic device consisting of multiple chambers equipped with a mechanically active and finely tuneable 3D microenvironment to recapitulate some of the representative steps of cardiac fibrosis *in vitro*. The device was exploited to verify the hypothesis that the presence of functional CMs could reduce the percentage of activated FBs and, therefore, hinder the triggering of fibrotic processes. Specifically, the role of CMs in dampening the onset of fibrosis traits was investigated through their coculture with different percentages of FBs when exposed to mechanical stretching or to the supplementation of the pro-fibrotic factor TGF-β1.

Finally, a modified version of the device designed to apply confined compression (instead of uniaxial stretching), was introduced generalising the applicability of the proposed model.

3.2 Microfluidic platform design and fabrication

3.2.1 Device concept: increasing the throughput of mechanically active devices

A device to provide a controlled mechanical stimulation (i.e. uniaxial stretching) to multiple 3D micro-constructs cultured in independent culture chambers, was conceived uniting features previously belonging to different models [26, 28, 29]. To increase the number of independent replicates, doormat-like valves were introduced between adjacent individual culture chambers. This technology allowed a simultaneous seeding of the micro-engineered tissues and a tight-sealed environment during their culture [30] leading to a higher experimental throughput compared to previously established systems [20, 26].

The device is composed of four layers (Fig. 1a): (i) top chamber, (ii) thin membrane, (iii) doormat valves layer, and (iv) pneumatic chamber layer.

The top chamber is constituted by six different culture chambers in series, separated from each other by 200 μm wide walls. Each of the culture chambers is composed of a central channel (300 μm wide) separated by two rows of hexagonal overhanging posts (28 μm side, 50 μm apart from each other) from lateral medium channels. A gap is present between the posts and the layer underneath. Posts and gap heights (100 μm and 50 μm respectively) were designed so that a defined lateral expansion of the constructs could be achieved (i.e. 10%) [26].

The valves, conceived in the fashion of normally closed doormat-like valves [30], are constituted by interconnected rectangular shaped cavities (1200 μm x 700 μm x 150 μm) closed by the thin membrane (100 μm in thickness) and positioned underneath the walls separating the culture chambers. A squared post (300 μm x 300 μm) is present in the middle of the valves to prevent the thin layer from collapsing under normal pressure conditions. Each actuation chamber is equipped with two rows of round posts (diameter 50 μm and set 200 μm apart) to prevent sagging.

The valve mechanism is coupled with a mechanical actuation system through the pneumatic chambers layer. This layer is made of actuation chambers positioned directly underneath and in correspondence to the culture chambers. Upon application of a positive pressure to this layer, the assembly constituted by the thin membrane and valve layer together (i.e. the actuation membrane), bends upwards until it touches the bottom surface of the posts.

The device layout was realized so that three of the six chambers of the device were exposed to cyclic stretching while the other three lacked a corresponding actuation chamber underneath (thus serving as static controls). In this way, both a static and a dynamic triplicate can be achieved in the same device. A single inlet was present in both cases.

A schematic representation of the device version with the separated chambers can be observed in Fig. 1b. while Fig. 1c depicts sections of the device in the middle of a culture chamber (AA) and in between two

adjacent chambers (BB) emphasizing how adjacent culture chambers are normally physically separated. A schematic of the seeding procedure is depicted in Fig. 1d. All chambers can be filled with a single injection but rendered independent during the culture period. Specifically, if a negative pressure is applied to the valves the thin membrane bends downwards, creating a passage underneath the walls separating the chambers that are thus connected and can be filled together. Upon release of the pressure the thin membrane returns in contact with the walls assuring constructs independence. Both valve and actuation layers have a single inlet. Details, of the device structure from a top view can be observed in Fig. 1e.

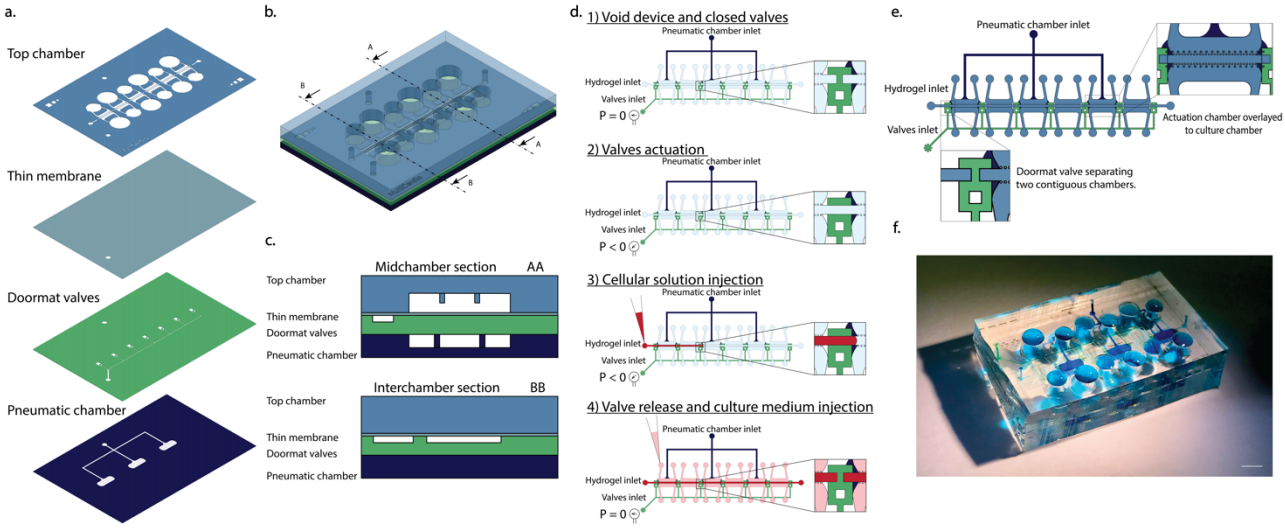

Figure 1: ***Device layout and functioning principle. a,*** *Device layers. Supporting structures are coloured while inner channels and apertures are left transparent.* ***b,*** *Device schematization. A mid-chamber section and intra-chamber sections are indicated with AA and BB respectively.* ***c,*** *Schematization of two sections of the device.* ***d****, Device seeding operations schematics. 1) The device is initially empty, and the closed valves separate the chambers from each other. 2) Applying a negative pressure from the valves' inlet causes the valves to open putting the chambers in connection with each other. 3) While the negative pressure is still being applied to the device the cellular solution (depicted in red) is injected in the chambers through a normal micropipette. From the zoom in it is visible how the advancing front of the cellular solution crosses from one chamber to the other. The two rows of posts flanking the central channel confine the cellular solution within the proper space. 4) The valve pressure is released bringing it back to the atmospheric value. This causes the valves to close separating the different compartments as highlighted from the zoom in where it is visible how the cellular solution represented in red is divided by the valve (in green). Once the pressure has been released and the hydrogel containing cells has finished crosslinking it is possible to inject culture media in the lateral channels and start the cyclic mechanical stimulation.* ***e,*** *Device view from top. The Zoom ins (insets) emphasize the intersection of separating walls and valves and the actuation chambers.* ***f,*** *Example of realized device. The different compartments were filled with coloured dyes to make them more visible. Culture chambers are highlighted in light blue, doormat valves in green, and pneumatic chambers in blue. The same colour code of the schemes in a, b, and c was maintained. Scale bar 4mm.*

3.2.2 Device fabrication procedure

Layers constituting the device, namely top culture chamber, thin un-patterned membrane, doormat valves layer, and pneumatic chambers layer (Fig. 1a), were fabricated in polydimethylsiloxane (PDMS, Sylgard 184 Dow Corning) trough master moulds replica moulding.

Device's layouts were designed through AutoCAD (Autodesk) and corresponding photomasks printed at high-resolution (64'000 DPI) on polyester transparent films (JD Photodata). Layers' master moulds were

obtained through photolithography. Multilayer photolithography was employed for the fabrication of the culture layer. Briefly, a gap layer (height 50 μm) and a posts layer (height 100 μm) were subsequently realized with SU-8 photoresist (Microchem) onto a 102 mm silicon wafer substrate carefully aligning the appropriate features through a mask aligner (Karl-Süss MA6/MA8 mask aligner).

Classic photolithography was employed for the generation of doormat valves (height 150 μm) and pneumatic chambers layers (height 150 μm). Master-moulds were realized in a clean room facility.

PDMS layers were obtained by mixing base and curing agent at a 10 : 1 w/w ratio, and making it polymerize on master-moulds at 65°C for at least 2 hours.

Thin membranes, which are un-patterned PDMS layers, were realized pouring PDMS on a smooth, 102 mm, silicon wafer. A 100-μm thickness was obtained through spin coating (800 rpm, 60s).

The valves layer overall thickness (900 μm) was controlled pouring defined quantities of PDMS onto the valves layer master moulds.

PDMS stamps were peeled off the moulds and appropriate holes bored for the various inlets/outlets (1mm diameter for the culture chambers, 0.5 mm diameter for the valve layer, 0.5 mm for the pneumatic chambers layer, and 3 or 4 mm for the media reservoirs in the culture chambers). Surfaces to be bonded together were treated with air plasma (Harrick Plasma Inc.) and brought in contact after careful manual alignment. Bonded layers were left at 65 ° C for at least 30 minutes after bonding. The doormat valves layer was bonded directly onto the thin membrane coated 102 mm wafer. Bonding of the valve layer before peeling off the membrane eased the detachment without tearing of the membrane. During bonding between the culture chamber and the valves-thin membrane layer assembly, a negative pressure was applied to the valves layer. This procedure prevented permanent bonding of the thin membrane to the bottom surface of the PDMS walls which separate the different culture chambers, thus prejudicing the device working principle. A photograph of an assembled device is visible in Fig. 1f.

3.3 Device validation

3.3.1 Device Functional Validation

The proper functioning of the device was evaluated according to the design specifications. Both the negative pressure necessary for valve opening during injection and the positive pressure necessary for device actuation were characterized.

The negative pressure required to obtain full opening of the valve depends on the thickness of the thin membrane. A fixed thickness of 100 μm was adopted, as previously optimized [27], to ensure valve movement with a negative pressure of -0.5 Bar. Confirmation of full aperture of the valves at the chosen pressure was carried on as previously described [27].

The valve layer thickness was optimized so that the cumulative thickness of the thin membrane (100 μm) and the valve layer (900 μm), constituting together the actuation membrane, reached 1 mm. A calibration procedure was performed, with a previously introduced methodology [26, 29], to assess the minimal pressure sufficient to obtain contact between the bottom surface of the posts and the thin membrane.

Concisely, the entire top culture chamber was filled with a blue dye. Given the transparency of PDMS and the presence of the dye filled gap underneath the posts, the posts themselves appear as blue in the rest condition (Fig. 2a). Upon contact between posts and actuation membrane, no more dye is left in between the PDMS structures and posts appears as white. The grey mean intensity of images taken at different pressures of the actuation chambers was measured as an indication of the distance between posts and actuation membrane. The actuation pressure was defined as the pressure at the beginning of the plateau present in the grey mean intensity versus pressure graph (Fig. 2b). Three regions of interest corresponding to three different posts were considered per each image. Three chambers per device, belonging to 6 different devices were used in the measurement. Grey mean intensity levels where normalized for the value measured at atmospheric pressure. The procedure was also adopted to evaluate how incorporation of multiple chambers in the same device can increase the homogeneity of the provided stimulation. The standard deviation of the normalized mean grey intensity at the different pressure levels of three chambers belonging to the same device or to three separated devices was used as an indicator of devices uniformity.

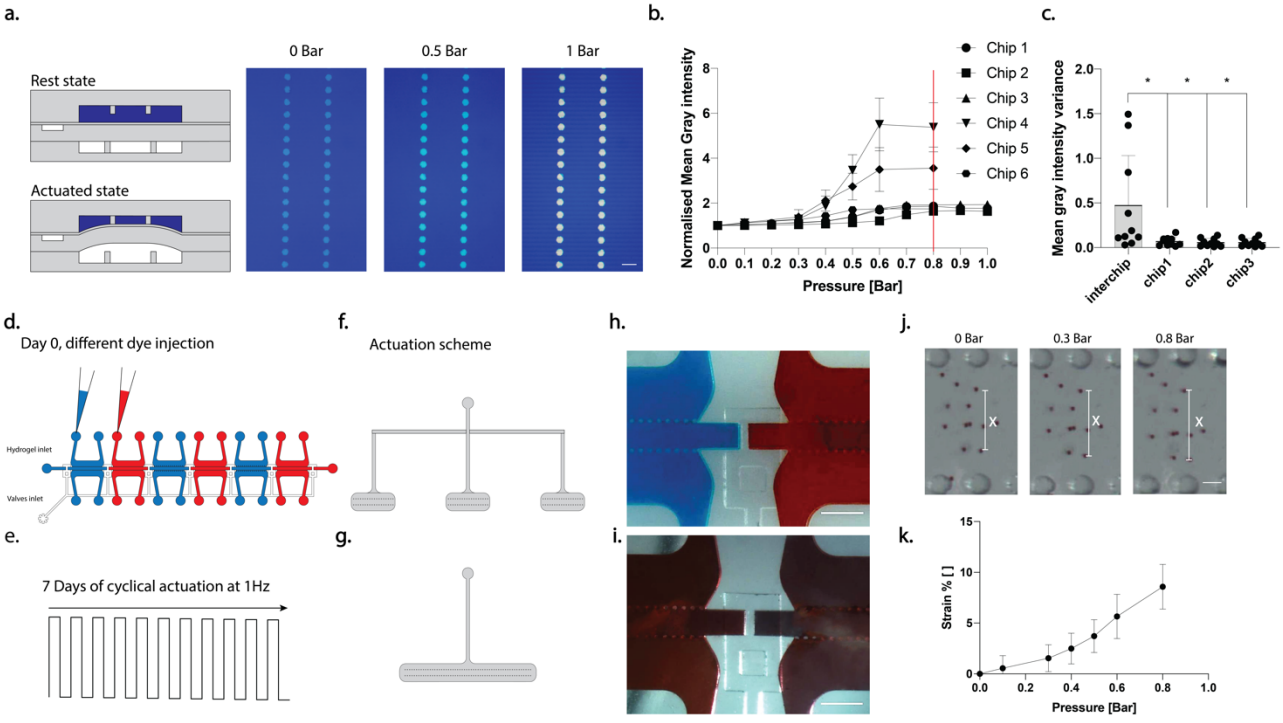

Figure 2: ***Device functional validation****.* ***a,*** *Schematization of the device in rest and actuated state upon filling of the culture chambers with blue dye and top views of the chamber when different pressures where applied. Scale bar 100 μm.* ***b****, Mean grey intensity of regions of interest within posts areas against pressure applied in the actuation chamber. Results are presented as the mean in the three chambers for every device. Six different devices were considered.* ***c,*** *Variance of the mean grey intensity calculated*

*among different devices or among different chambers of the same device. Each dot represents the variance of the mean grey intensity at a given pressure * p< 0.05, ** p<0.01. Statistics by one-way ANOVA with Dunnett's post hoc test. Populations' normality was assessed with Shapiro-Wilk and Kolmogorov-Smirnov tests. Three different devices were considered to have an immediate comparison with the three chambers of a single device.* ***d****, Schematization of the coloration of the chambers used to assess chamber independency.* ***e,*** *Scheme of the stimulation applied for 7days.* ***f****, Layout of the actuation layer, three separate actuation chambers correspond to three alternate culture chambers* ***g,*** *Scheme of the actuation layer: Three consequent culture chambers are stimulated by a single actuation chamber.* ***h,*** *Device picture after 7days of stimulation with the separated actuation chamber layout. Colour diversity testifies the chamber separation. Scale bar 500 μm.* ***i,*** *Device picture after 7days of stimulation with the single chamber layout. Colour uniformity testifies a connection between the chambers. Scale bar 500 μm.* ***j,*** *Evaluation of the strain field within constructs. Polystyrene beads (diameter 10)were incorporated in fibrin gel and injected into the central channel of the device. Different pressure levels are depicted, from 0 to 0.8 Bar. 5 different couples of beads were considered per chamber; 6 different chambers belonging to 2 devices were measured. The distance along the X direction of the chosen couples of beads at different pressures was measured. The result was used as an indication of the stretch level experienced by cells in the same conditions. Scale bar 50 μm* ***k,*** *Correlation between applied pressure and strain entity.*

0.8 Bar was found to be the optimal actuation pressure (as highlighted by the red line in Fig. 2b) and adopted in the following experiments. While variability among different devices was noticed, multiple chambers in the same device resulted more homogeneous in terms of actuation pressure. Fig. 2c depicts the variance of the mean grey intensity calculated among different devices (inter-chip variability) or among the three actuated chambers of a single device. It can be noticed how the chamber-to-chamber variability resulted to be significantly lower than the inter-chip variability. By incorporating more chambers into a single device, therefore, it was feasible to further improve the control over the homogeneity of the applied mechanical stimulation.

In the proposed mechanical actuation system, constructs stretching is achieved by increasing the pressure in the pneumatic chambers, leading to the membrane constituted by the PDMS layers in between the pneumatic chamber and culture chamber to bend upwards until it reaches the bottom surface of the overhanging posts. The final stroke depends, therefore solely on the gap present underneath the posts during the resting state [29].

To ensure the proper functioning of the device in generating independent constructs, it is crucial that the doormat-like valves between chambers remained closed despite the deflection caused by the cyclic mechanical activation. To verify this requirement, the sealing of the valves during 7 days of cyclical stimulation was tested.

Two configurations of the actuation layer were taken into consideration: three separate actuation chambers positioned in correspondence to every other culture chamber (each 3900 μm x 1600 μm in dimensions) (Fig. 2f), and a single common actuation (12300 μm x 1600 μm in dimension) covering three subsequent culture chambers (Fig. 2g). While maintaining the valves closed, the top culture chambers were filled with coloured food dyes in alternating different colours (blue and red in Fig. 2d) and a cyclic stimulation (0.8 Bar, 1 Hz) was applied for 7 days (Fig. 2e). Pictures of adjacent chambers were taken during the stimulation time.

The separate actuation configuration allowed to maintain chambers independent even in the presence of mechanical stimulation, as evidenced by the maintenance of colour segregation in adjacent compartments (Fig. 2h). Conversely, the single actuation configuration was not effective and, after 7 days, led to diffusion of the coloured dyes between adjacent chambers indicating their fluidic connection (Fig. 2i). The separate actuation configuration was thus adopted in following experiments.

The effective strain field applied to constructs was measured as previously described [26]. Briefly, polystyrene beads were embedded in the same fibrin gel later on used for cell culture and images taken under different pressure condition. (Fig. 2j) The relative position of different couples of beads was used to determine the monoaxial stretching applied following the formula:

$$\varepsilon_{xx} = \frac{((\Delta x)_p - (\Delta \mathrm{x})_0}{(\Delta \mathrm{x})_0} = \frac{\left[(x_1)_p - (x_2)_p\right] - [(x_1)_0 - (x_2)_0]}{[(x_1)_0 - (x_2)_0]}$$

Where $(\Delta x)_p$ is the distance projected along the X axis between two beads at a definite pressure level p, and $(\Delta x)_0$ is the distance projected along the X axis between two beads at atmospheric pressure. Four couples of beads were considered for each chamber. Six different chambers belonging to two different devices were used in the quantification. A mean stretching strain value of 8.5% was detected (Fig. 2k) coherently with the desired nominal value and with reported results for a previously introduced single chamber device [26].

3.3.2 Device Biological Validation

A proof-of-concept biological validation of the newly proposed multi-chamber design functioning was performed replicating experiment previously made in a single chamber platform [26]. Cardiac engineered tissues were generated from neonatal rat cells embedding a mixed population of 80% CMs and 20% FBs in fibrin hydrogels [20] (isolation and hydrogel formation procedures are described in sections 3.4.1 and 3.4.2). Cells were injected into devices and cultured either under cyclic loading (8.5% strain, 1 Hz) or under static conditions for 5 days. Comparisons were made among statically and mechanically stimulated constructs cultured in the same device. A custom made setup (described in section 3.6.4) was adopted to deliver an external electrical pace to constructs at the end of the culture period. At the end of the culture time constructs were employed for immunofluorescence analyses as described in sections 3.6.1.

Brightfield images of the constructs after 5 days of culture are visible in Fig. 3a. No tissue compaction was observed over time. Both constructs in static condition and under cyclic loading completely filled the central culture chamber at the end of the 5 days of culture (Fig. 3a). Only mechanically stimulated constructs exhibited synchronous beating, no homogeneous beating activity was detected for static controls. Moreover,

only mechanically stimulated constructs responded homogeneously to the external electrical pace (Fig. 3b) [16], showing a higher functionality and contraction ability (excitation threshold 3.35V/cm±1.62 V/cm, maximum capture rate 3.8Hz ±1.48Hz). No differences were however visible in the overall cell morphology as evident by stainings for the cardiomyocytes marker cardiac troponin (cTROP) (Fig. 3c). These data confirmed achievement of an increased cardiac constructs maturation and functionality following cyclical stretching.

A further biological validation was performed replicating, in the multi chamber device, results previously obtained in a single chamber *in vitro* scar model [20]. Fibrotic constructs were obtained lading a population of 100% rat FBs in fibrin hydrogels. Constructs were exposed for 5 days to either a biochemical cue (TGF-β1 supplementation, 5 ng mL^{-1}) or to mechanical stimulation (8.5 % strain ,1 Hz). Congruently with previously reported results [20], both stimuli resulted in FBs increased expression of αSMA ,a marker of the phenotypic switch of FBs into myofibroblasts (Fig. 3d), further demonstrating that it was feasible to replicate previously obtained results using the newly proposed multi-chamber device.

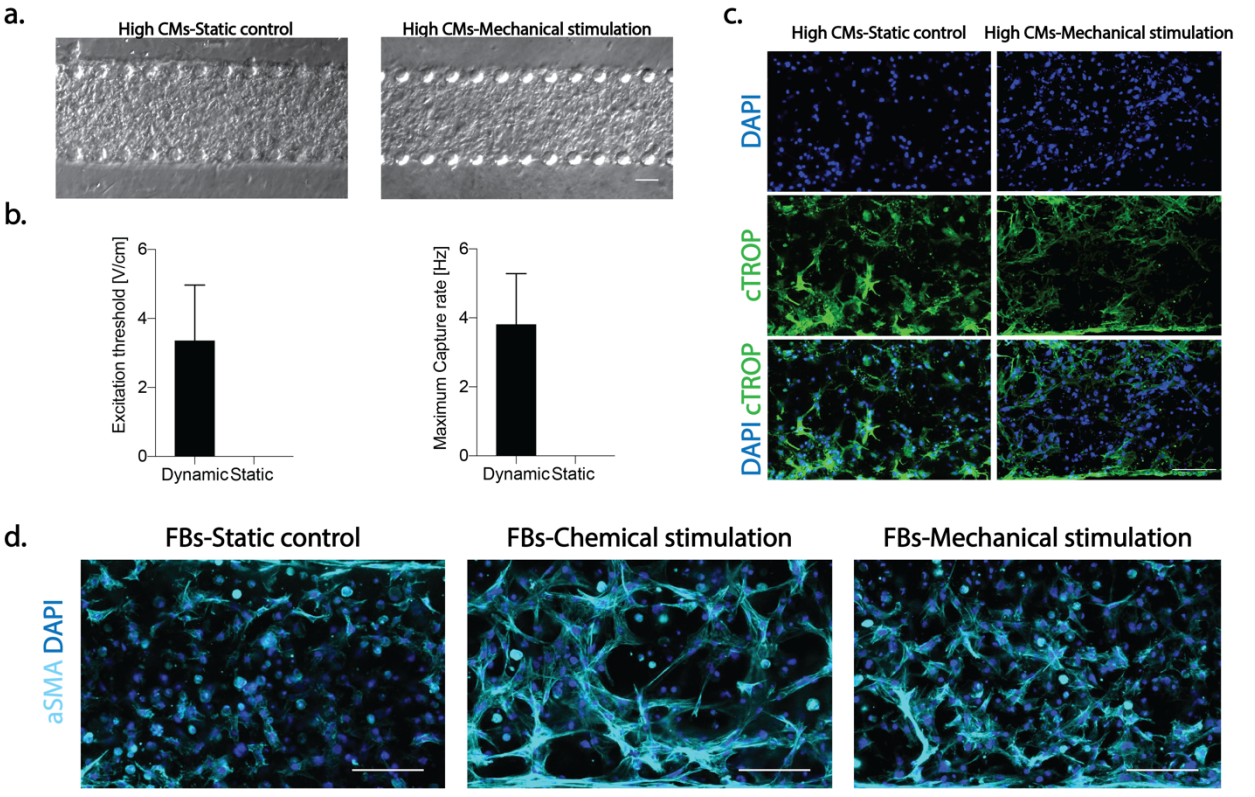

Figure 3: ***Device biological validation****. Device usability for biological experiments was assessed replicating previously obtained results.* ***a,*** *Brightfield images of a population constituted by 80% CMs and 20% FBs (High-CMs) seeded in the device and cultured for 5 days under static conditions or cyclic mechanical stimulation. At the end of the culture periods construct still completely filled the central culture channel. Scale bar 100 .* ***b,*** *Confirmation of the effect of mechanical stretching on maturation was obtained. After 5 days of culture within the same device, only mechanically stimulated micro-constructs exhibited synchronous beating, while no homogeneous beating activity was detected for the static condition. Upon electrical pacing, mechanically stimulated construct exhibited an excitation threshold of 3.35V/cm±1.62V/cm and a maximum capture rate of 3.8Hz ±1.48Hz, while no values could be detected for static constructs. At least N=4 biologically independent samples were considered in measurements.* ***c,*** *Immunofluorescence images of High-CMs population cultured under static conditions or mechanical stimulation for 5 days. DAPI*

is represented in blue, cTROP in green. Scale bar 100 . Images were analysed exclusively in a qualitative fashion in this phase. No major differences in cell morphology were detectable in the two conditions. ***d,*** *A 100%FBs population was used to assess the possibility of obtaining a hypertrophic phenotype induction, either through administration of TGF-β1 (5 ng mL^{-1}) or through the application of cyclical stretching (8.5%) for 5 days. Both the pro-fibrotic factor TGF-β1 and mechanical stimulation were sufficient in increasing the number of fibroblasts expressing αSMA, thus assuming a hypertrophic phenotype, as compared to the static condition. Images were analysed exclusively in a qualitative fashion in this phase. DAPI is represented in blue, αSMA in cyan. Scale bar 100 . Static culture without TGF-β1 was used for controls.*

3.4 Device exploitation in determining the effects of cardiomyocytes and fibroblasts co-culture in the assumption of fibrotic traits

An assessment of the assumption of fibrotic traits by different co-cultures of CMs and FBs was performed using the presented multi chamber device.

3.4.1 Cell harvesting and isolation

Neonatal rat CMs and FBs were isolated from 2-3 days old Sprague Dawley rat hearts as previously described [31]. Isolation was performed according to the Swiss Federal guidelines for animal welfare with procedures approved by the Veterinary Office of the Canton Basel (Basel, Switzerland). Rat ventricles were quartered, digested overnight in a 0.06% (w/v) solution of trypsin in Hank's balanced salt solution (HBSS, Gibco), and further subjected to five digestion steps, of 4 min each, in a 0.1% (w/v) type II collagenase (Worthington, Biochemical Corporation) solution at 37 °C and 150 rpm. Isolated cells were pre-plated in growth medium (high glucose DMEM supplemented with 10% v/v foetal bovine serum (FBS, Hyclone), 1% v/v penicillin streptomycin, 1% glutamine, and 1% v/v HEPES) for 45 min to allow FBs adhesion (all reagents were purchased from Sigma Aldrich unless differently specified). Following the pre-plating, a 100% FBs population was adherent to the flask and was kept in culture, while a mixed cardiac cell population enriched for CMs (roughly 80% CMs and 20% FBs) was collected and cultured separately overnight (37 °C, 95% humidity and 5% CO_2) before starting the experiment [26]. FBs were either used following overnight incubation or frozen in liquid nitrogen and used later (up to passage 3).

3.4.2 3D cell culture in microfluidics device

Four different co-culture ratios of CMs and FBs were considered: 20% FBs and 80% CMs (High-CMs), 50% CMs and 50% FBs (Medium-CMs), 20% CMs and 80% FBs (Low-CMs), and a population composed exclusively of FBs used as control [20]. Medium and low CMs experimental groups were obtained diluting with FBs the initially isolated cardiac population enriched for CMs (80% CMs and 20% FBs).

CMs and FBs were detached using 0.25% trypsin/ 1 mM EDTA (Gibco), mixed at the appropriate ratios, embedded in fibrin hydrogels (20 mg ml^{-1} of fibrinogen, 2.5 U ml^{-1} of thrombin, 2.24 TIU mL^{-1} of aprotinin, 20 mM of calcium chloride), and immediately injected into micro devices. All co-culture populations were

seeded at a density of 100 x 10^6 cells/ml. The 100% FBs control group was prepared with a cell density of 14.5 x10^6 cells/ml as previously optimized. [20]

Cell-based fibrin gels were simultaneously injected in the six chambers of the microfluidic device by applying a negative pressure to the valve layer allowing the valves, normally closed, to open. Immediately after the injection of the cell laden fibrin solution the pressure was released and microdevices were incubated (at 37 °C, 95% humidity and 5% CO_2) for 10 minutes to complete the hydrogel polymerization before filling the side channels of the culture layer with growth medium. Constructs were cultured for additional 5 days in growth medium. Culture medium was changed every day simply removing the exhaust medium from the reservoirs and adding fresh one.

To reduce the fibrin gel degradation, aprotinin (Sigma-Aldrich) was supplemented during the first days of culture at the concentration of 1.15 TIU mL^{-1} on day 0 and at a decreasing amount in the following three days (80%, 60% and 40% of day 0 on day 1, 2 and 3, respectively). Cyclic stimulation (1Hz, 0.8 Bar) was started immediately after hydrogel polymerization and applied for the 5 culture days. A custom-made controller [29] connected to a pressure regulator (Comhas) was used to provide devices with mechanical stimulation.

3D micro-tissues generated by 80% CMs and 20% FBs cultured in growth medium with the daily supplementation of 5 ng mL^{-1} of human recombinant Transforming Growth Factor-β1 (TGF-β1, Sigma-Aldrich) in addition to the mechanical stimulation were also considered.

To verify the ratio of CMs and FBs in the freshly isolated enriched CMs cell population, both 3D micro-tissues and cell monolayers (125 x 10^3 cells/cm^2) on glass slides (Ted-Pella Inc., 10 mm diameter, 0.13mm-0.17mm thickness) were prepared and stopped for immunofluorescent analysis at day 0. At the end of the culture period, constructs were harvested for immunofluorescence analyses and real time quantitative polymerase chain reactions (RT-qPCR) as described in section 3.6.

3.4.3 Assessment of co-culture population percentages

The effective distribution of CMs and FBs populations among the different experimental conditions was assessed by immunofluorescence stainings both at day 0 (i.e. on the starting populations) and at day 5 (i.e. at the end of the culture period).

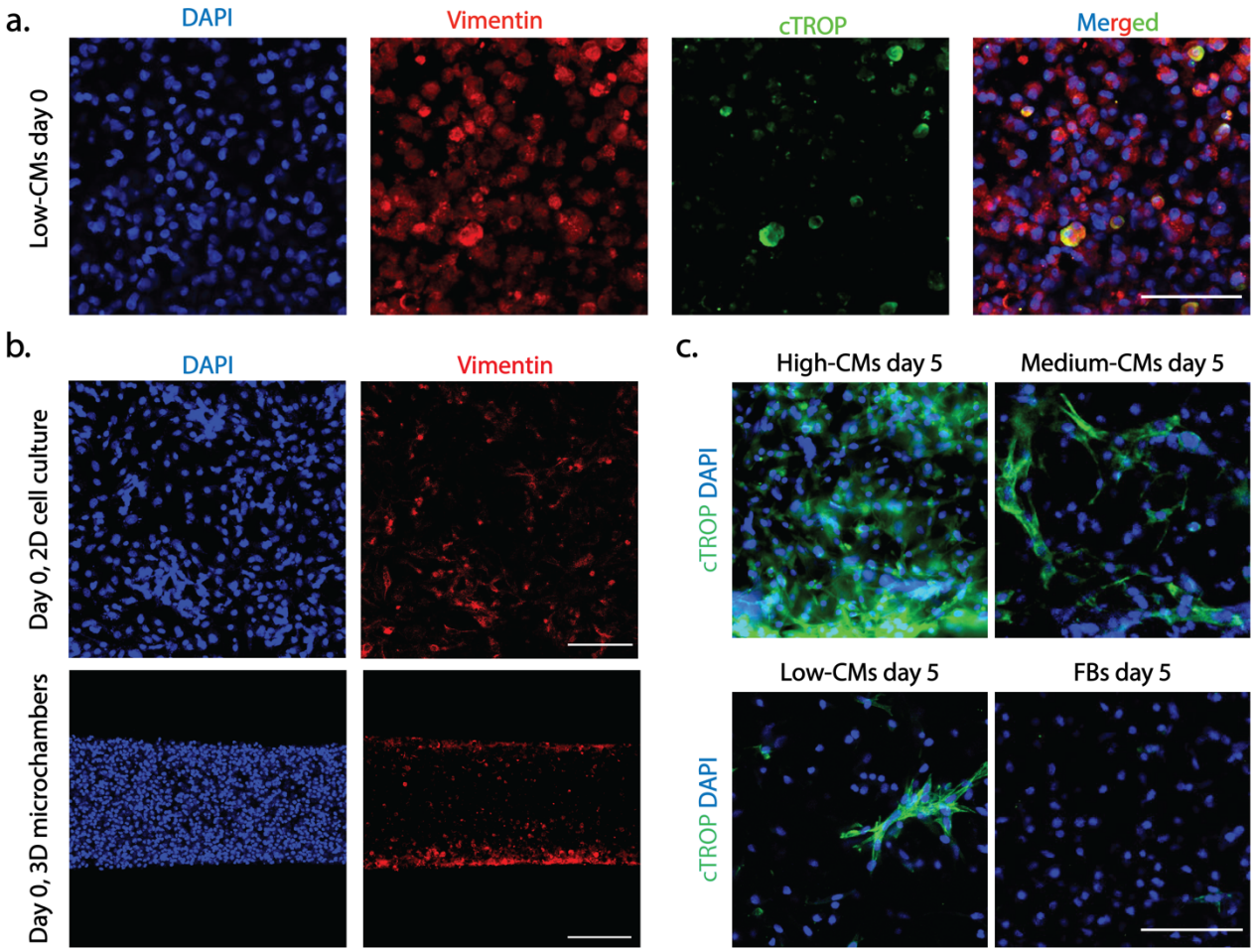

Figure 4: ***Populations' quantifications.*** *Populations were quantified both at day 0 (4 hours after seeding), and at day 5 at the end of the culture period.* ***a,*** *Representative images of the low-CMs population at day 0. DAPI is represented in blue, Vimentin in red, cTROP in green. Close to no cells were negative for both markers. Scale bar 100* ***b,*** *Populations' quantifications at day 0, high-CMs population only. Staining for Vimentin was performed both in 2D culture and in 3D within microfluidic devices. No differences in the assessment of the population in between the two quantification methods was visible. DAPI is represented in blue, Vimentin in red. Scale bar 100 .* ***c,*** *Populations' quantifications at day 5. Representative images of the four co-culture ratios are represented. At the end of the culture, CMs were defines as cTROP positive cells and FBs as cTROP negative. DAPI is represented in blue, cTROP in green. Scale bar 100 .*

cTROP and vimentin co-stainings were performed to determine the presence of other cellular types. After a preliminary evaluation showing that cells were either CMs (i.e. cTROP positive) or FBs (i.e. Vimentin positive) (Fig. 4a), quantifications were performed according to either cTROP or Vimentin positivity alone. Cells nuclei, stained with DAPI, were counted to quantify the total number of cells.

At day 0, the effective populations percentages obtained after cell isolation, nominally 80%CMs-20%FBs, were determined through immunofluorescence both in monolayer and 3D micro-constructs cultures. Vimentin positive cells were considered to be FBs, vimentin negative (DAPI positive) cells to be CMs.

At day 5, cTROP expressing cells were considered as CMs, cells negative for cTROP (but positive for DAPI) were considered as FBs. Representative images of populations both at day 0 and at day 5 are reported in Fig. 4. Percentages were calculated as the number of CMs and FBs over the total number of cells,

respectively. At least five images belonging to three biologically independent samples per each condition were considered in quantifications.

Population ratios in 2D cell culture at day 0 resulted to be 80.3% ± 2.99% of CMs and 19.7% ± 2.99% FBs, while the percentages resulted to be 82.1% ± 17,8% CMs and 17,9 ± 155,92% FBs in 3D microchambers (Fig. 5a). Quantifications of CMs and FBs showed similar values in 2D and 3D systems and no statistical differences with respect to populations nominal values were detected. After 5 days of culture under cyclic stimulation and considering different nominal population ratios in co-culture, no statistical differences were detected in the overall constructs cell density ($p>0.05$, Fig. 5b). The four experimental groups investigated consisted nominally of 80% CMs and 20% FBs (i.e., High-CMs), 50% CMs and 50% FBs (i.e., Medium-CMs), 20% CMs and 80% FBs (i.e., Low-CMs), and 100% FBs (i.e., FBs). The assessed CMs and FBs percentages did not exhibit any statistically significant difference with respect to such nominal population values (Fig. 5c).

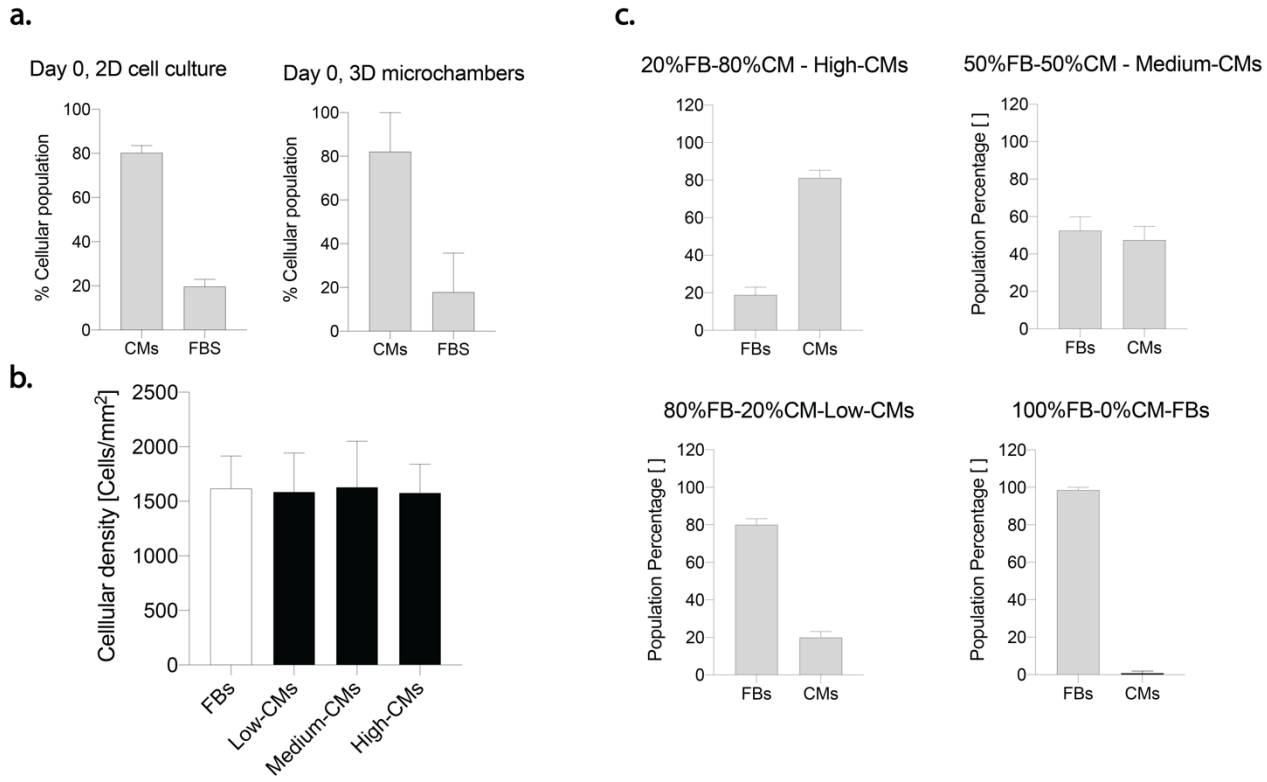

Figure 5: ***Assessment of effective populations percentages. a,*** *Percentage of FBs and CMs in 2D and 3D culture systems. No statistically significant differences were found with respect to the nominal values of 80%CM and 20%FBs respectively. n=5 images belonging to N=3 biological independent samples were used for 3D quantifications and n=6 images belonging to N=3 biologically independent samples were used for 2D quantifications. At day 0 Vimentin positivity was used to distinguish between cellular populations. Vimentin positive cells were considered to be FBs, Vimentin negative cells to be CMs.* ***b****, Assessment of the cellular density after 5 days of culture. In light of the results of a previous FBs-based fibrotic model [21] all co-culture populations were seeded with an initial cellular density of 100 x 10^6 cells/ml while the control group (i.e. the 100% FBs population) was prepared with a cell density of 14.5 x10^6 cells/ml as previously established. The different seeding densities were chosen to account for the different proliferation rates. After 5 days of culture in 3D microchambers, no statistical difference could be detected in cellular density (i.e. the number of cells per mm^2). At least n=5 images belonging to N=3 biologically independent samples for each condition were used for quantifications. Statistics by one-way ANOVA with Tukey's post hoc test for gaussian populations.*

Populations' normality was assessed through Shapiro-Wilk and Kolmogorov-Smirnov tests. ***c,*** *Quantification of population percentages at day 5. Percentages of CMs and FBs in culture were quantified after 5 days of culture and compared to expected nominal values of the cocultures, indicated in the graphs' titles. At least n=5 images belonging to N=3 biologically independent samples were considered in quantifications. At day 5 cTROP expressing cells were considered as CMs, cells negative for cTROP were considered as FBs. One sample t-test or Wilcoxon signed rank test was adopted to assess differences between a sample population, Gaussian or not respectively, and a theorical value. Populations' normality was assessed with Shapiro-Wilk and Kolmogorov-Smirnov tests. Statistical significance was indicated by * P< 0.05, **P< 0.01, ***P<0.001 and ****p<0.0001.*

3.4.4 Effects of mechanical stimulation and different cardiomyocyte concentrations on cell proliferation and phenotype switch

The device was exploited to verify the mitigating effects played by different ratios of CMs on the early key steps of the wound healing cascade that follows myocardial infarction, namely FBs proliferation [7] and FBs phenotype switch into myofibroblasts [32]. To this aim, constructs of the four experimental groups were cultured under cyclical loading (1 Hz) for 5 days. At the end of the culture period, constructs were stopped and analysed through immunofluorescence stainings performed as described in section 3.6.1.

Proliferating cells, defined as Ki67-positive cells, were uniformly distributed throughout the constructs in all conditions (Fig 6a.)

A distinction between proliferative CMs (defined as cells positive for both cTROP and Ki67) and FBs (defined as cells positive for Ki67 but negative for cTROP) was performed. Representative images are reported in Fig.6a. A slightly diminished percentage in Ki67 positive FBs over the total of FBs was registered in the High-CMs condition (Fig. 6b) but the presence of an increasing number of CMs did not modulate the proliferative tendency of FBs. Extremely low numbers of Ki67 positive CMs were, instead, registered in all conditions (Fig. 6b). An assessment of the overall percentages of Ki67 positive cells was also performed (Fig 7a). The percentage of proliferating cells was assessed by quantifying the Ki67 positive cells over the total number of cells. At least five areas belonging to five biologically independent samples were considered in quantifications.

Proliferating cells percentage slightly decreased with the increase of CMs number (percentages resulted to be 12.7 ± 11.2% in FBs, and 11.6 ± 4.7%, 9.8 ± 2.8%, and 7.8 ± 2.0% in low-, medium- and high- CMs populations, respectively) ($p>0.05$, Fig. 7b).

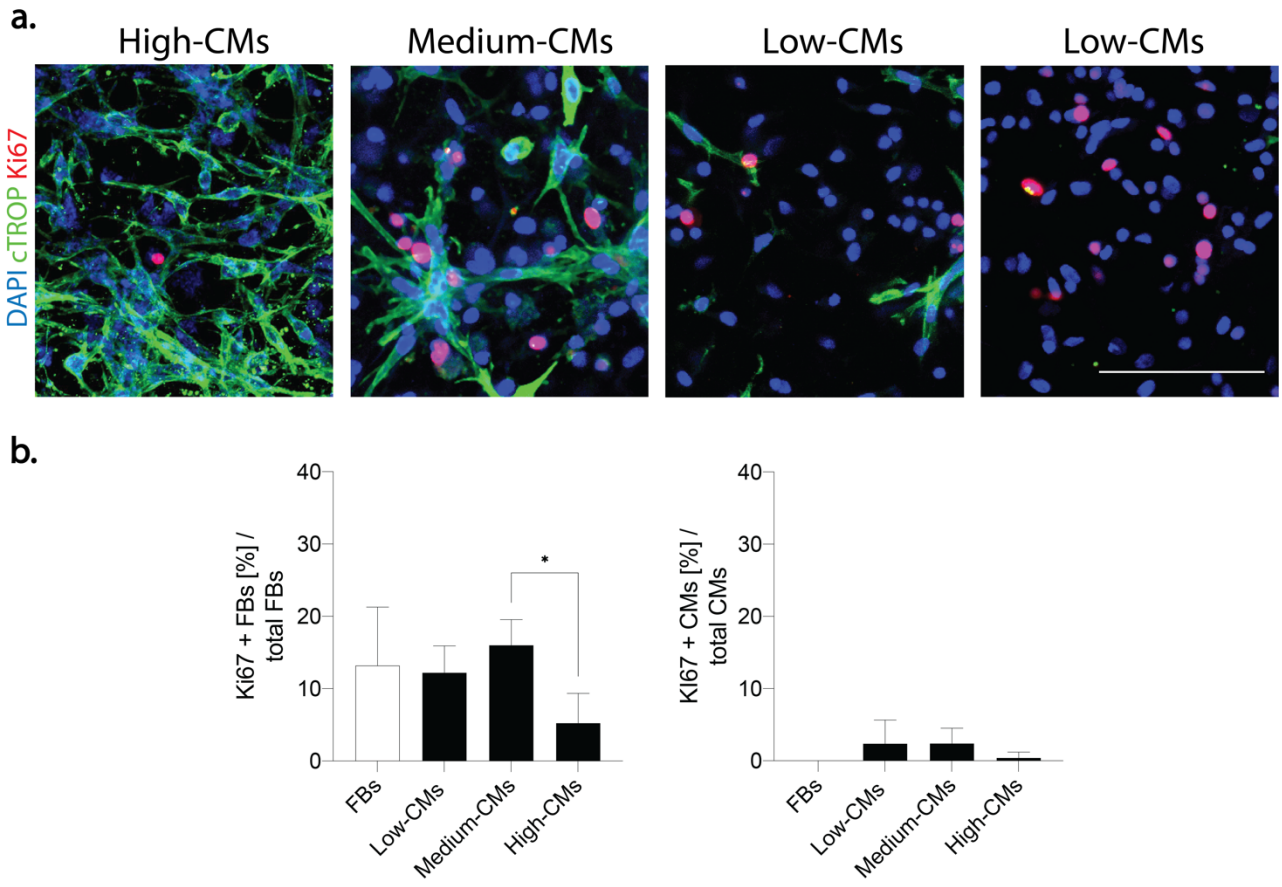

Figure 6: ***Determination of the Ki67 positive populations. a,*** *Representative images of the different populations. DAPI is represented in blue, cTROP in green, and Ki67 in red. Scale bar 100 .* ***b,*** *Left: percentage of Ki67 positive FBs (cTROP negative cells) over the total amount of FBs; Right: percentage of Ki67 positive CMs (cTROP positive cells) over the total amount of CMs. At least N=4 biological independent images were considered in quantifications. Statistics by one-way ANOVA with Tukey's post hoc test for Gaussian populations and Kruskal-Wallis test with Dunn's post hoc test for non-Gaussian populations. Populations' normality was assessed with Shapiro-Wilk and Kolmogorov-Smirnov tests. *p< 0.05.*

αSMA was considered as a marker of FBs differentiation into myofibroblast and of CMs assumption of a hypertrophic phenotype as reported for in diseased conditions [33]. Notably, αSMA is also a marker of less mature CMs during *in vitro* culture. Indeed, neonatal rat CMs were reported to be prone to a temporary re-arrangement and dedifferentiation of the contractile apparatus leading to a superior expression of αSMA instead of typical cardiac actin isoforms in *in vitro* culture [34].

Immunofluorescence stainings of αSMA showed a generally increased number of αSMA positive cells with the decrease of CMs (cTROP-positive cells) in culture (Fig. 7c).

The typical "spread myofibroblast" morphology, as well as an increased number of αSMA positive stress fibres were more evident in the 100% FBs and in the Low-CMs conditions. Quantification of the total percentage of αSMA positive cells confirmed that the highest number of αSMA positive cells was present in the 100% FBs condition (49.8% ± 6.4%) and was statistically different when compared to all other conditions (9.4% ± 1.1%, 13.2% ± 4.5%, and 29.3% ± 14.2% in the High-, Medium- and Low- CMs

condition, respectively) (Fig. 7b). A statistical difference in the total percentage of αSMA positive cells was moreover detected in the Low-CMs with respect to both the High-CMs and Medium-CMs conditions. A distinction between αSMA positive CMs and FBs was then introduced. The percentage of αSMA expressing CMs over the total amount of CMs was calculated as the number of cells positive for both αSMA and cTROP, over the number of cells positive for cTROP. The percentage of myofibroblasts over the total amount of FBs was calculated as the number of cells negative for cTROP and positive for αSMA over the number of cells negative for cTROP. At least five different images belonging to three biologically independent samples were used for quantifications.

The myofibroblast percentage (i.e. αSMA-positive/cTROP-negative cells normalized for the total number of FBs negative for cTROP) was 50.3%±6.5% in the FBs condition, while it was statistically significantly lower in the High-CMs condition (13.6±3.2%), in the Medium-CMs condition (16.3%±4%), and in the Low-CMs condition (30.9%±15.7%) (Fig. 7b). A statistically significant difference was also evident between the Low-CMs and the High-CMs populations.

The percentage of αSMA expressing CMs (i.e. the number of αSMA-positive/cTROP-positive cells normalised for the total number of CMs positive for cTROP) did not show statistically significant differences. However, a clear downward trend corresponded to decreasing quantities of FBs in the co-culture (7.6 ± 1.6 %, 10.1 ± 4.2 %, and 24.4 ± 16.8 % in the High-, Medium- and Low- CMs condition, respectively) (Fig. 7b).

Compared to the other conditions, in the High-CM condition αSMA-positive CMs were present exclusively at the edges in correspondence with the pillars (data not shown).

Overall, these data indicate that it was feasible to model two of the key cardiac fibrosis markers, namely increased cellular proliferation and assumption of a hypertrophic phenotype, modulating the percentages of CMs and FBs in culture.

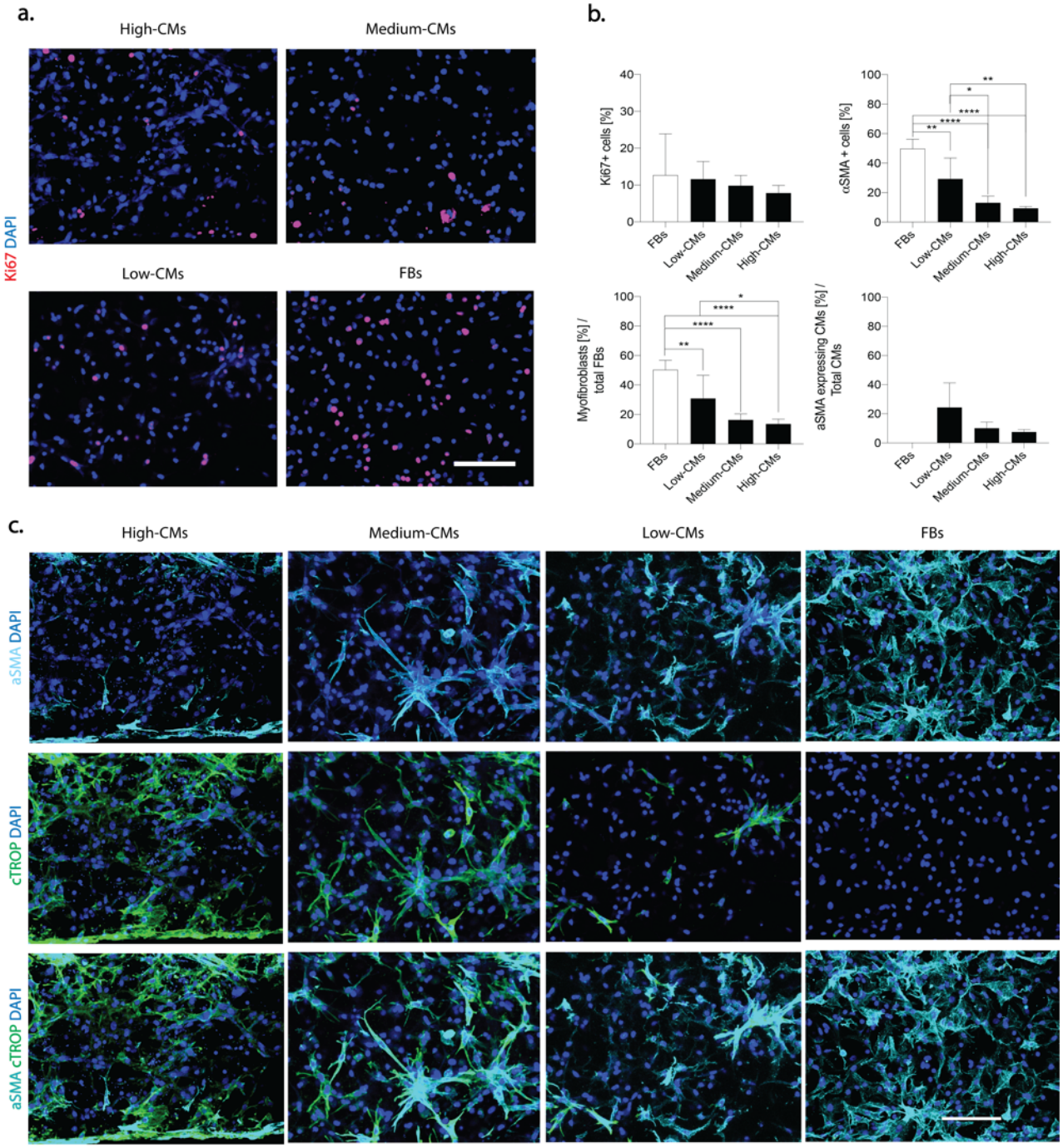

Figure 7: ***Onset of a fibrotic phenotype investigation****.* ***a,*** *Representative immunofluorescence pictures for ki67 (red). Nuclei were stained with DAPI (blue) Scale bar 100 μm.* ***b,*** *Quantification of total proliferating cells; quantification of αSMA positive cells over the total cellular population; quantification of myofibroblasts over the total fibroblast population; quantification of hypertrophic cardiomyocytes over the total number of cardiomyocytes. At least n=5 images belonging to N=3 biologically independent samples for each condition were used for quantifications. The percentage of αSMA positive cells was determined as the number of cells expressing αSMA over the total number of cells. CMs were defined as cTROP+ cells; αSMA expressing CMs as cTROP+αSMA+ cells; Myofibroblasts were defined as cTROP-αSMA+ cells; FBs were defined as cTROP- αSMA- cells. Statistics by one-way ANOVA with Tukey's post hoc test for Gaussian populations and Kruskal-Wallis test with Dunn's post hoc test for non-Gaussian populations. Populations' normality was assessed with Shapiro-Wilk and Kolmogorov-Smirnov tests. *p< 0.05, **p< 0.01, ***p<0.001 and ****p<0.0001.* ***c,*** *Representative images of αSMA (cyan) and cardiac Troponin I (green) of the*

four considered conditions after 5 days of culture under dynamic stretching. Nuclei were stained with DAPI (blue). Scale bar 100 μm.

3.4.5 Effect of coculture on matrix deposition and remodelling processes

An excessive matrix deposition leading to the formation of a fibrotic tissue is one of the hallmarks of cardiac fibrosis[7]. Deposition of type I collagen and fibronectin, two of the main constituents of the interstitial ECM, was investigated in the engineered micro-constructs (Fig. 8a, b). An enhanced accumulation of both fibronectin and type I collagen was detectable in micro-constructs with higher FBs percentages. While fibronectin was present in all conditions and its deposition seemed to increase with the increase of FBs ratio in the culture, type I collagen was mainly deposited in the low CMs conditions and in the FBs control.

Constructs' assumption of an anabolic fibrotic phenotype was also assessed quantifying the expression of fibronectin (*Fn*) collagen type I (*Col1a1)* and Collagen type III (*Col3a1*) associated genes through RT-qPCR.

mRNA levels were normalized to the expression of 100% FBs constructs.

A decreasing trend in the gene expression of *Fn, Col1a1,* and *Col3a1* was observed with the increase of CMs percentage in culture. Specifically, the fold change in expression of *Fn*, *Col1a1* as well as *Col3a1* was significantly higher in Low-CMs compared to High-CMs culture condition (0.71±0.14 vs 0.22±0.04, 0.99±0.15 vs 0.27±0.07, and 0.66±0.06 vs 0.21±0.06 for *Fn*, *Col1a1,* and *Col3a1,* respectively) (Fig. 8b).

RT-qPCR analyses were also adopted to better characterize the gene expression of different fibrosis correlated markers in the CMs and FBs co-cultures (Fig. 8c, d)

Cardiac fibrosis was also associated with an altered balance between deposition and degradation of extracellular matrix. To assess this hallmark in the developed model, samples were analysed for the expression of the matrix metalloproteinases *Mmp2* and *Mmp9*. *Mmp2* gene expression fold change (with respect to the 100% FBs condition) showed a statistically significant decrease in the High-CMs condition with respect to the Low-CMs one. No difference in *Mmp9* expression were instead detected among the different experimental groups (Fig. 8c).

Notably, a statistically significant decreasing trend from Low-CMs to High-CMs was also visible in the fold change of *TGF-1,* a pro-fibrotic factor, and tenascin-C (*TnC*) (Fig. 8d), an extracellular matrix protein expressed in various diseases associated with inflammation and correlated with the onset of fibrosis in *in vivo* pathological settings [35]. In particular, while *TnC* expression is highly increased during embryonic development, it is suppressed in adult tissues but it is enhanced again upon injury or during remodelling, as well as in response to myofibroblasts under mechanical stretching [36]. Finally, the expression of *Nppa,* a factor known to contrast fibrosis and usually upregulated under mechanical stretching [37], was increased in the High-CMs condition compared to the other culture ratios (Fig. 8d).

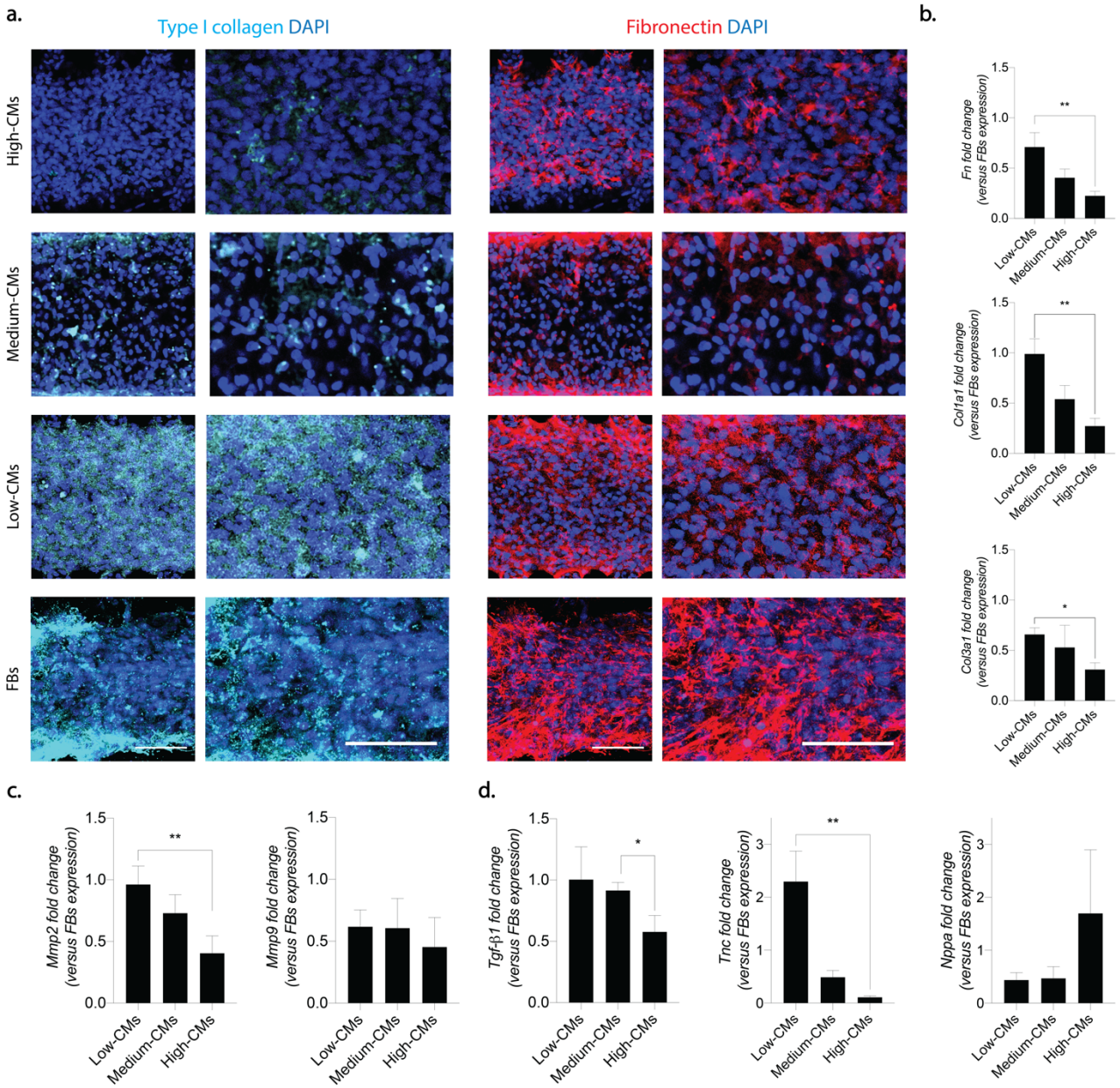

Figure 8: ***Matrix deposition and fibrosis associated genes expression evaluation in the different conditions. a,*** *Immunofluorescence of matrix components collagen type I (in cyan) and fibronectin (in red). DAPI staining for nuclei is represented in blue. Images with a higher magnification are represented on the right of both columns. Scale bar 100 μm. At least four areas belonging to two biologically independent samples were considered.* ***b,*** *Relative gene expression of Col1a1, Col3a1 and Fibronectin quantified by RT-qPCR. ed.* ***c, d,*** *Expression of factors involved in Fibrosis modulation quantified by RT-qPCR.* ***(c)*** *Expression of the degradative enzymes Mmp2 and Mmp9.* ***(d)*** *Expression of TGF-β1, TnC, and Nppa. bActin was adopted as housekeeping gene. Results were normalised to the FBs population expression. Statistics by one-way ANOVA with Tukey's post hoc test for Gaussian population and Kruskal-Wallis test with Dunn's post hoc test for non-Gaussian populations. Populations' normality was assessed with Shapiro-Wilk and Kolmogorov-Smirnov tests. At least N=4 biologically independent samples were considered per condition. *p< 0.05, **p< 0.01.*

The expression of the same genes was also evaluated in the starting populations, before seeding into microfluidic devices (Fig. 9) to detect possible changes during the culture period. While *TnC* and *Nppa* at day 0 showed diminished but similar trends to those achieved after 5 days of cyclical stimulation (i.e. *TnC*

diminished, and *Nppa* increased with the percentage of CMs in culture), the decreased fold change which was visible for *TGF-1* in the High-CMs condition after stimulation was not observed at day 0. Moreover, *Mmp*2 and *Mmp9* revealed opposite trends before and after the culture under mechanical stimulation, with *Mmps* fold change increasing (and not diminishing) with the percentage of CMs in co-culture.

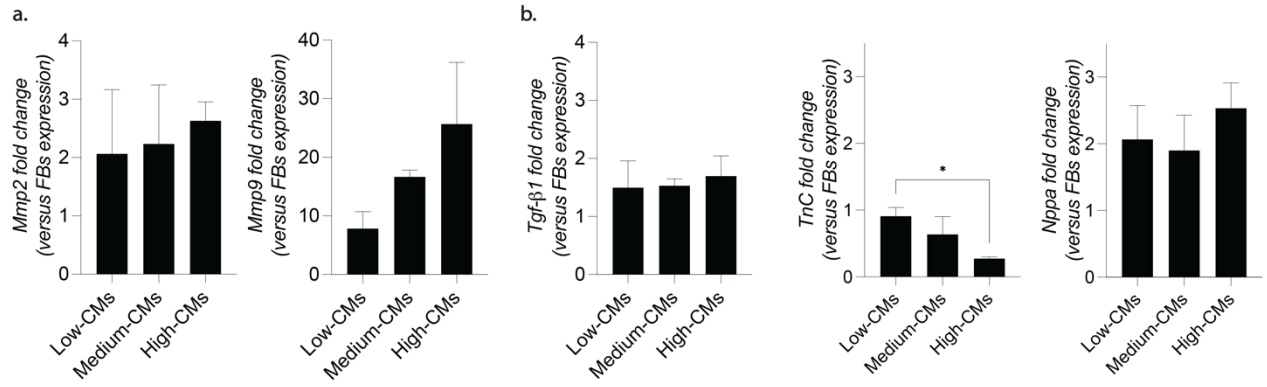

Figure 9: ***Gene expression quantification of factors involved in Fibrosis modulation in starting populations.*** *Fibrosis-related markers, namely, the degradative enzymes Mmp2 and Mmp9(**a**), and, TGF-β1, TnC, and Nppa (**b**) in the different CMs and FBs co-cultures (i.e. Low-, Medium- and High- CMs) were quantified by quantified by RT-qPCR at day 0 (i.e. of the populations before injection in microfluidic devices. bActin was used as housekeeping gene. Results were normalised to the expression of the FBs population expression. Kruskal-Wallis test with Dunn's post hoc test for non-Gaussian populations. Populations' normality was assessed with Shapiro-Wilk and Kolmogorov-Smirnov tests. N=3 samples per kind of cellular ratio were analysed. *p< 0.05.*

3.4.6 Functional analysis

The functional beating capability of the 3D micro-tissues obtained through the different co-cultures of CMs and FBs was assessed, after 5 days of culture, imposing an electrical pacing as described in section 3.6.4. Specifically, two parameters were evaluated: the excitation threshold (ET), defined as the minimum voltage (per *cm*) required to achieve synchronous beating of the whole constructs at a pacing frequency of 1 Hz; and the maximum capture rate (MCR), defined as the maximum imposed beating frequency a construct was capable of following with a stimulation voltage of 1.5 times the ET.

Only 3D engineered micro-constructs generated with either High-CMs or Medium-CMs were functional and followed the imposed external pacing. The ET was similar in the two conditions (3.5 ± 1.7 V / cm and 3.6 ± 0.7 V / cm, respectively for High- and Medium-CMs constructs). Congruently, no statistical difference was found in the MCR of High- and Medium-CMs experimental groups (3.8 ± 1.5 Hz and 2.7 ± 1.0 Hz, respectively) (Fig. 10a).

Upon application of the external pacing the motion of cells within the constructs was recorded to (i) estimate the beating synchronicity of different cells within constructs and (ii) evaluate the cellular contraction direction.

Cells motion was recorded only when constructs' synchronous beating was detected after electrical pacing was applied (i.e., for High-CMs and Medium-CMs conditions). For each recorded movie (N = 2 at least for each experimental condition), at least three region-of-interest (ROI) were chosen and a minimum number of five different single cells were identified to track their motion with respect to adequate reference points during three entire contraction cycles. The entire contraction trajectory of each single cell was calculated manually collecting the image coordinates of the cells and extracting the position vector magnitude with respect to the frame of origin for each cell (Fig. 10b) at each photogram using Image J. The variation of the position vector magnitude was plotted against time to quantify the contraction frequency and compare it with the pacing frequency. For each trajectory of contraction, the contraction direction was calculated as the angle created between the contraction direction and the horizontal axis of the frame. Ultimately, for each analysed ROI the probability density function (PDF) of the contraction direction was estimated non-parametrically by a kernel smoothing estimation function (MATLAB 2018b, Mathworks), in order to quantify and identify the most probable contraction direction within each ROI. For each video two parameters were evaluated: (i) synchronicity of contractions peaks in each cell and (ii) the most probable cell contraction direction within the recorded ROI.

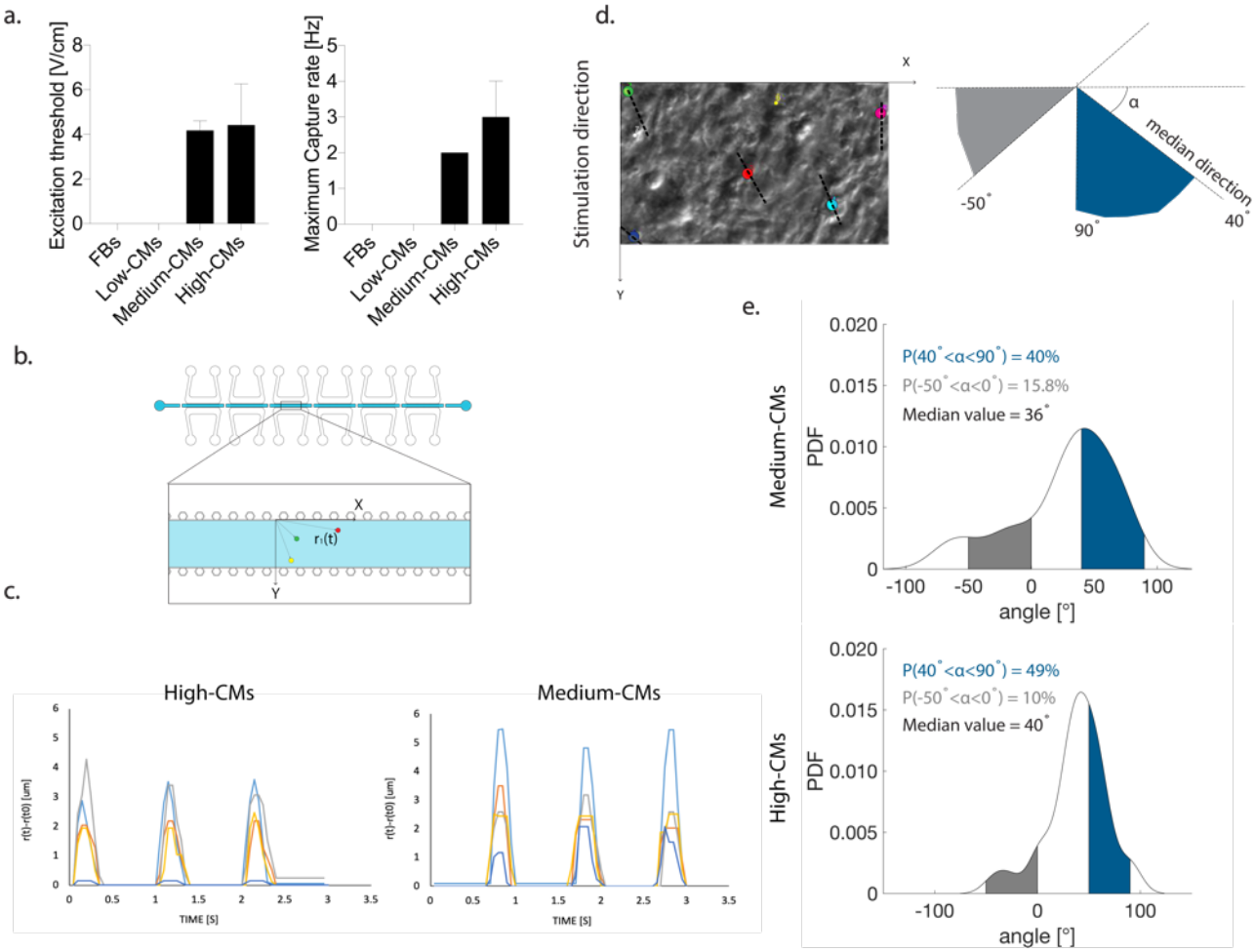

Figure 10: ***Evaluation of contraction functionality of constructs. a****, ET and MCR measured in the High and Medium-CMs conditions. Statistics by Mann-Whitney test for non-Gaussian populations. (p>0.05).* ***b,*** *Schematization of the coordinate reference system used in the assessment of beating synchronicity and contraction direction. Example position-vectors connecting the origin with three cells highlighted by coloured dots are displayed.* ***c,*** *Synchronicity of beating. Coloured lines represent the variation in the position vectors modulus in time. Peaks corresponding to contraction demonstrate that cells beat synchronously in both conditions.* ***d,*** *example of highlighted cells (coloured dots) used for the determination of the orientation angle. The direction along which each cell beats is highlighted by the dotted line. A schematization of the orientation along which cells contract is depicted on the right.* ***e,*** *The Probability Density Functions (PDF) of the contraction direction was calculated. Areas of alignment to the stimulation direction and opposite to it are highlighted in blue and grey respectively.*

Both High-CMs and Medium-CMs constructs exhibited synchronicity of cellular beating upon the application of an external electrical field. The variation of the position vector magnitude of the tracked cells during the contraction cycles displayed synchronicity in contraction, with well synchronized contraction peaks and a contraction frequency coherent with the pacing (Fig. 10c). In the High-CMs group the contraction direction was more aligned with the stimulation direction (namely 90°) compared to the Medium-CMs condition (Fig. 10e). The Medium-CMs group showed a higher probability (15.8 vs 10%, in Medium- and High-CMs conditions, respectively) to find cells contracting perpendicularly to the stimulation direction (Fig 10e). Overall these data suggest that, while High-CMs constructs exhibited the

highest functional capabilities, Medium-CMs constructs had comparable functionality while lower CMs percentages impaired constructs response to electrical pacing.

3.4.7 Combination of mechanical stimulation and profibrotic factor TGF-β1

Mechanical stimulation alone induced neither an upregulation of pro-fibrotic markers, nor an increased myofibroblast phenotype switch in the High-CMs condition (coherently with previously shown data [26]). To further confirm the resistance conferred by CMs with respect to the onset of a fibrotic phenotype, the effect of the supplementation of a fibrosis trigger, namely TGF-β1, on top of mechanical loading was assessed. Evaluations were made exclusively in the High-CMs condition, thus investigating the effect of the pro-fibrotic factor on physiological-like cellular ratios. Constructs obtained from High-CMs were exposed either to mechanical stimulation alone, namely TGFβ(-), or to mechanical stimulation and TGF-β1 (5 ng mL^{-1}), namely TGFβ(+), for 5 days (Fig. 11). CMs showed a similar morphology and density in both conditions and only few cells were positive for SMA (Fig. 11a). Few cells were positive for the proliferation marker (Ki67, Fig. 11a) and the number of proliferating cells slightly increased following TGFβ-1 supplementation. Based on image analysis, a trend of increase was found when TGFβ-1 was supplemented, however no statistically significant differences were found between the two conditions for the percentage of proliferating (7.7% ± 1.8% and 12.5% ± 7.9% in TGFβ(-) and TGFβ(+), respectively) or of SMA-positive (21.34 ± 7.25% and 29.9 ± 4.4% in TGFβ(-) and for TGFβ(+) conditions, respectively) cells (Fig. 11b). Notably, both the number of hypertrophic CMs over the total number of CMs and of myofibroblasts over the total amount of FBs did not vary following TGFβ-1 supplementation. Levels of genes associated to fibrosis (*Col1a1, Col3a1* and *Fn*) and ECM degradation (*Mmp2* and *Mmp9*) yielded comparable results in the two conditions (Fig. 11c). A slight increase in the expression of *Col1a1* and *Col3a1* was detected in the TGFβ(+) condition. No statistical difference was anyway generally present between the two experimental conditions. The expression of *TGF-β1*, *Tnc* and *Nppa* also did not change between the two experimental conditions confirming an overall High-CMs constructs resistance to fibrosis induction.

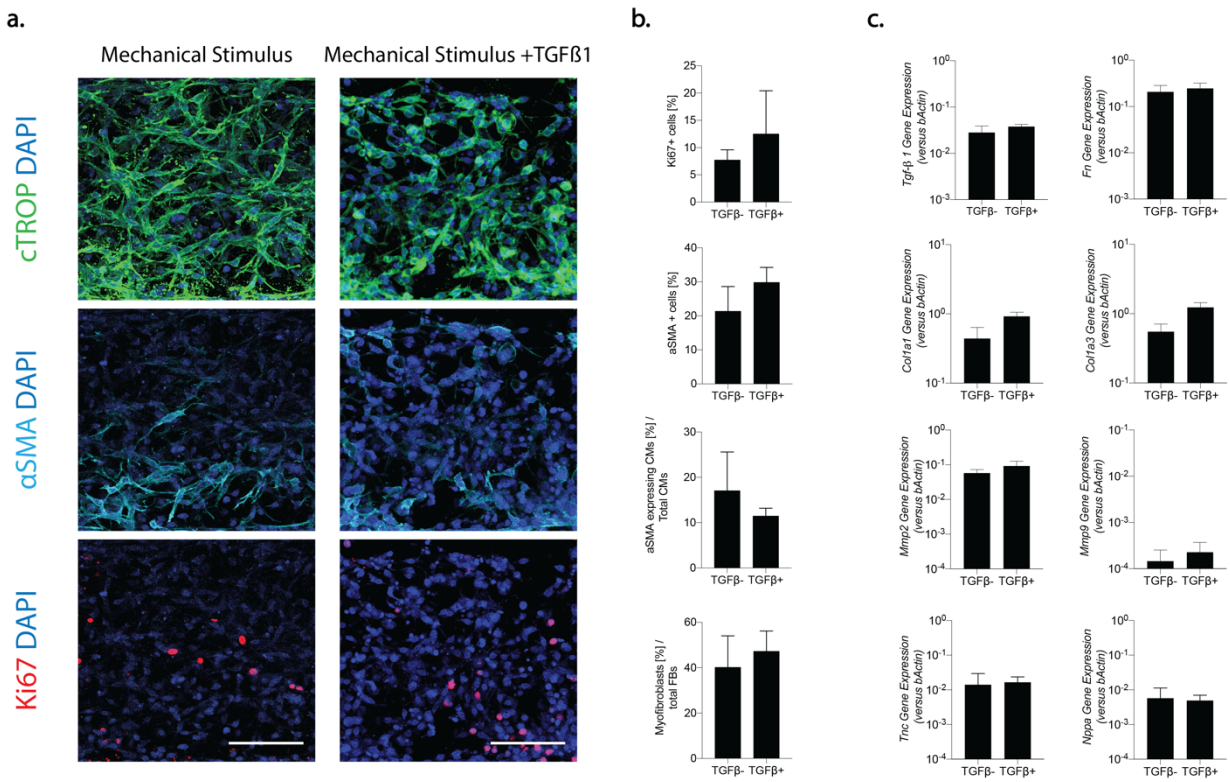

Figure 11: ***The effect of the pro-fibrotic factor TGF-B1 on the High-CM microtissue control (80%CM-20%FB) was determined.*** ***a,*** *Immunofluorescence staining of the two conditions for αSMA (cyan), cTROP (green), and Ki67 (red). DAPI marking nuclei is represented in blue. Scale bar 100 μm.* ***b,*** *Image quantifications. n=6 representative areas belonging to N=4 biologically independent samples were adopted in analyses.* ***c,*** *Quantification of representative genes made by RT-qPCR. At least N=3 biologically independent samples were adopted in analyses. Comparisons were performed using two tailed t-test for Gaussian populations and Mann-Whitney test for non-Gaussian ones. Populations' normality was assessed with Shapiro-Wilk and Kolmogorov-Smirnov tests (p>0.05).*

3.5 Device design generalization for compressive stimulation

After the demonstration that a multi-chamber, mechanically active device could be developed and its exploitation for the study of fibrosis traits onset in CMs and FBs co-culture populations, a generalized version of the device was introduced to be applied in different contexts of use.

Firstly, augmentation of the distance in between adjacent culture chambers (specifically up to 2.1 mm) allowed the implementation of an actuation compartment under each chamber, without impairment of chambers independence since doormat valves did not overlap with any part of the actuation chamber. It was thus possible to further increasing the device throughput in terms of mechanically active constructs.

Secondly, an alternative mechanical stimulation modality was introduced. The device presented in this Chapter 3 was designed to provide three-dimensional construct with defined levels of stretching. A modification of the confining posts allowed the realization of a device meant for confined compression. T shaped pillars (300 μm wide, 30 μm apart from each other) were in fact demonstrated to be adequate for the achievement of homogeneous confined compression of cartilaginous constructs [29] (as also

demonstrated in Chapter 2). Notably, it was feasible to change the provided stimulus (e.g. from stretching to confined compression) simply changing the geometry of the pillars in the culture chamber (e.g. from hexagonal to T shaped). The adopted multi-layer construction of the device consists therefore in a modular approach that could easily be adapted to provide 3D constructs with different mechanical stimuli adequate to the mimicry of different tissue targets.

A schematization of the modified version of the device including six mechanically active chambers and pillars designed to achieve confined compression is depicted in Fig. 12.

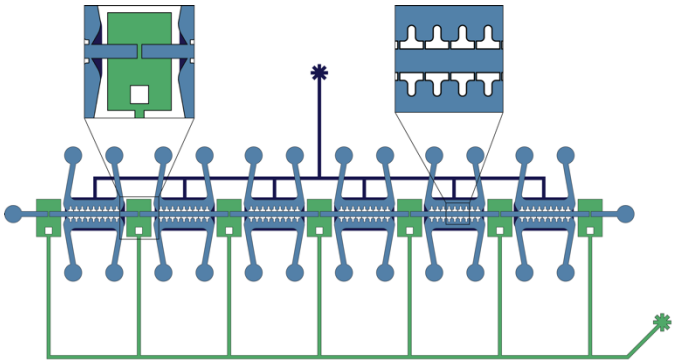

Figure 12: ***Multi chamber device to provide confined compression****. A schematization of an alternative design is presented. Culture chambers are represented in light blue, actuation chambers in dark blue and doormat valves in green. Increasing the distance between the different chambers allows coupling of each culture chamber with an actuation compartment without impairing the chambers' hydraulic separation. The inset on the left depicts a zoom in of the area between two adjacent chambers, alighting the lack of overlapping between the valve and the two adjacent culture chambers. T shaped pillars previously demonstrated to be adequate for the provision of 3D constructs with confined compression*[29] *were introduced. A zoom in on the pillars is depicted in the inset on the right.*

3.6 Analysis procedures and methodologies

3.6.1 Immunofluorescence staining

Immunofluorescence was performed on both cells seeded on glass slides at day 0, and on 3D whole micro-tissues, directly within the culture chamber (either at day 0 or after 5 days of culture). Samples were fixed in 4% paraformaldehyde (PFA) for 180 minutes at room temperature and further incubated for 45 minutes at room temperature in a solution of 0.3% Triton X-100 (Sigma), 2% BSA, and 5% serum (donkey serum was used for 3D micro-tissues and cell monolayer stained at day 0, goat serum in all other samples) in Phosphate-Buffered Saline (PBS, Gibco) in order to permeabilize cells and block nonspecific binding. Samples were then incubated overnight at 4 °C with the following primary antibodies: polyclonal rabbit anti-rat Ki67 (Ab15580, dilution 1:200), monoclonal IgG2a mouse anti-rat alpha-smooth muscle actin (a-SMA, A2547, dilution 1:400), monoclonal mouse IgG2b anti-rat cardiac troponin I (ab200080, dilution 1:100), polyclonal goat anti-rat vimentin (SC-7557, dilution 1:200), polyclonal mouse anti-rat collagen type

I (NB60450, dilution 1:200), and polyclonal rabbit anti-rat fibronectin (Ab2413). Appropriate fluorescent labelled secondary antibodies (Alexa Fluor) were used at a 1:200 dilution and incubated for 6 hours at 4 °C. 4′,6-diamidino-2-phenylindole (DAPI) was used to stain nuclei.

3.6.2 Image analyses

All images were taken with a 20X objective on a fluorescence confocal laser scanning microscopy (Zeiss LSM 710 confocal microscope for quantification and Nikon AR 1 ALA for matrix staining and cell monolayer culture) and analysed by using Image J (NIH) software. Images of the 3D micro-tissues were acquired longitudinally and included the two rows of posts at the top and bottom so that the cell strain direction coincides with the top-bottom axis of the image. Image analyses were conducted on regions of interests excluding areas near the posts, focusing on the effect of the cyclic strain and avoiding any confounding effect due to the passive tension of posts adhering CMs.

3.6.3 Quantitative RT-PCR

Micro-tissues were retrieved opening the microdevices, and digested in TRI-Reagent (Sigma). Total mRNA was isolated adapting a previously described protocol [38]. The Ominiscript reversion Transcription kit (Qiagen) was used for retro-transcription of mRNA into cDNA. Real-time reverse transcriptase-polymerase chain reaction (RT-PCR; 7300 AB Applied Biosystem) was performed according to standard protocols to quantitate expression levels of the following genes of interest (Applied Biosystems): *Col1a1* (Rn01463848_m1), *Col3a1* (Rn01437681_m1), *Fn* (Rn00569575_m1), *Tnc* (Rn01454947_m1) *Mmp2* (Rn01538170_m1), *Mmp9* (Rn00579162_m1), *Tgf1* (Rn00572010_m1), and *Nppa* (Rn00561661_m1). *Actb* (Rn00588290_m1) was used as housekeeping gene. At least three biologically independent samples were considered for each condition.

Analyses were repeated on cellular populations before the culture period. CMs and FBs were mixed according to the different specified ratio and digested in TRI-Reagent (Sigma). Three samples for each condition were considered.

3.6.4 Contractile functionality assessment

Electrical pacing was imposed using two carbon rod electrodes aligned with the longitudinal direction of the chambers, symmetrical with respect to the central axis of symmetry of the chamber themselves (Fig. 13). The electrodes, put 1 cm apart, were connected to a custom electrical stimulator [39] allowing different voltages (0-23 V) and frequencies (1-10 Hz) to be imposed on the constructs with a square wave (2 ms duration).

Contractile functionality of at least N=3 biologically independent constructs per condition was assessed by acquiring videos of their response to external electrical stimulation in brightfield. Videos were acquired with an inverted microscope (Olympus IX81, 10X objective) equipped with a thermo-controlled chamber (5%CO_2/ 37°C) and captured with a sampling frequency of 20 frames per second (CCD camera/DP30BW). Three areas of interest for each condition were further analysed.

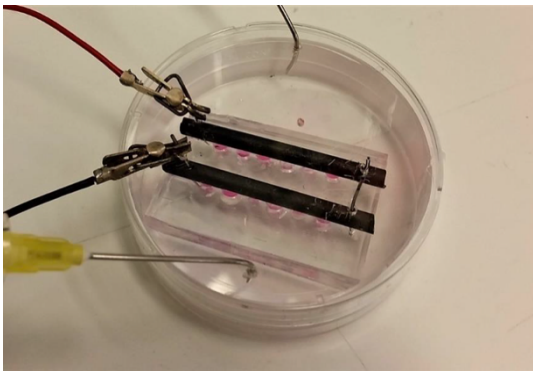

*Figure 13: **Electrical stimulation setup**. Picture of the metallic electrodes used for constructs electrical stimulation. Rods, visible in black, are in direct contact with the culture medium filling the appropriate reservoirs but not directly immerged in the reservoirs.*

3.6.5 Statistical analysis

All data were presented as mean ± standard deviation. Statistical analyses were performed using Prism 8.0 (GraphPad). Population normality was assumed when both Shapiro-Wilk and Kolmogorov-Smirnov tests gave a positive result. Double comparisons were performed using two tailed t-test for Gaussian populations and Mann-Whitney test for non-Gaussian ones. Multiple comparisons were realized using one-way ANOVA with Dunnett's or Tukey's post hoc test for Gaussian population and Kruskal-Wallis test with Dunn's post hoc test for non-Gaussian populations. One sample t-test or Wilcoxon signed rank test was adopted to assess differences between a sample population, Gaussian or nor respectively, and a theorical value. Statistical significance was indicated by *p< 0.05, **p< 0.01, ***p<0.001 and ****p<0.0001.

3.7 Discussion

In this study, a new mid-throughput OoC including multiple independent samples within the same device and providing cyclic isotonic loading to 3D cardiac micro-constructs was generated. The device was then exploited to recapitulate some of the hallmarks of cardiac fibrotic processes.

A doormat-like valving system was implemented building upon previous experience [27]. Serially distributed, normally separated culture chambers could be thus connected during the injection of a 3D cell laden hydrogel and divided immediately afterwards. Moreover, properly tailoring the valve layer thickness made it possible to exploit it as an actuation membrane mobilised by pneumatic actuation chambers.

While the cyclical mechanical stimulation led to leakage, impairing samples' biological independence, when the actuation and the valve were overlapped, this could be avoided by simply alternating static and dynamic chambers and/or by properly dimensioning the distance among them.

Additionally, by evaluating the variance in actuation pressure using three separate devices or three chambers of the same device it was here demonstrated that including multiple chambers in a single device reduces the experimental variability occurring among different devices.

Previous works had addressed the incorporation of various types of mechanical stimulation in OoCs, mimicking biological features of constantly active organs and tissues (e.g., lungs [40], liver [41], kidney [42] cartilage [29], and heart [26]). However, OoCs capable of delivering mechanical loading were so far limited to single-chamber devices. Schneider et al., introducing a centrifuge based system to generate parallel cardiac microconstructs [4], were among the first to address the parallelization issue in a systematic way. While this methodology was adeguate for CMs rich populations, their model did not comprise a mechanical actuation system but beating was the result of cardiac constructs spontaneous contraction. The proposed platform, therefore, would not be able to directly apply a heart beat mimicking stretching to FBs rich, fibrotic models where synchronous beating does not happen spontaneously but needs to be externally provided.

A systematic review of the present OoCs panorama in terms of throughput ad experimental yield was recently proposed by Probst, Schneider, and Loskill [1]. Exclusively a few attempts have been made at delivering multiple independent chambers, with devices incorporating from 12 to 96 well-like structures and defined as high-throughput.

Introducing 6 independent chambers the proposed device is collocated in the mid-throughput range in terms of currently available OoCs. Of note, the initial design was conceived to have, in a single device, both static and a dynamically stimulated triplets of samples, thus allowing the inclusion of static controls. Still, as previously demonstrated [27], multiple chambers lines could easily be incorporated within the area of a 96 well plate with the same principle here reported (i.e. incorporation of doormat valves), further increasing the overall throughput.

The proposed device was key in analysing the effects of different ratios of CMs and FBs in the assumption of cardiac fibrosis reminiscent traits within a 3D mechanically active environment and without the supplementation of pro-fibrotic factors.

FBs proliferation, together with FBs migration, is one of the first cellular processes starting upon injury and it was demonstrated to increase, upon either chemical or mechanical stimulation, in microconstructs composed of either only FBs [20] or of 80% CMs and 20%FBs [26]. At day 5, the expression of Ki67 was not statistically different among conditions, but a slight decreasing trend was visible in the experimental groups with a lower number of FBs and the percentages measured in this work were in line with previously reported values (around 10% of the total cell population) [20]. Moreover, no differences were detectable in the cellular density at the end of culture despite the lower density used to seed FBs alone.

Another salient tract of fibrosis is the expression of contractile stress fibres. Previous models based on OoCs highlighted the expression of αSMA in fibrotic constructs [25]. When cells were allowed to self-assemble, however, they resulted in constructs with high expression of stress fibres also without the supplementation of fibrotic stimuli. Moreover αSMA expression was linked to CMs dedifferentiation in *in vitro* cultures [34]. In this work, the usage of a soft fibrin hydrogel and of a tailored confining chamber design allowed to achieve a physiological condition (i.e., high-CMs constructs) with minimal αSMA expression.

Conversely when a low or medium % of CMs was present cyclic mechanical stimulation alone induced a profibrotic phenotype in FBs and CMs with both cell types expressing the contractile protein αSMA. This suggests that a physiological stretching level (i.e., 8.5%) is sufficient to trigger a pathological remodelling in the presence of altered non-physiological population ratios. Remarkably, the total percentage of αSMA expressing cells decreased with respect to the FBs condition used as positive control [20], even with just the 20% of CMs present in co-culture suggesting a dampening effect of CMs on the profibrotic environment and modulation of FBs behaviour through a probable cross talk.

The presented model allowed also to recapitulate the altered anabolic and catabolic processes characterising fibrosis. An increase in the deposition of ECM components (i.e. type I collagen and fibronectin) and associated gene expression (i.e. *Col1a1, Col3a1* and *Fn*) which is typical of scar formation could be observed in FBs rich co-cultures. Moreover, matrix turnover was also increased as indicated by the expression of the degrading metalloproteinases *Mmp2* (but not of *Mmp9*). Numerous *in vivo* and *in vitro* studies revealed the involvement of the gelatinases Mmp2 and Mmp9 in the altered ECM homeostasis typical of fibrosis.

Evidences showed that MMP9, together with MMP8 and MMP12 [44], is however, linked to the presence of infiltrating neutrophils and macrophages, not present in this study.

Additionally, the fact that *Mmp2* expression positively correlated with the percentage of CMs before the culture and negatively after, together with the observation that a *TGF-β1* expression decrease in High-CMs

constructs was visible exclusively after 3D co-culture and stimulation, further supports the validity of the presented model in inducing fibrosis hallmarks.

An analysis of two possible indicators of cross-talks between FBs and CMs was also performed. TnC is an extracellular protein [36] expressed during heart development and suppressed in adult tissues. Its expression is nonetheless activated again upon injury or remodelling, and in response to mechanical strain in FBs [35, 45]. Coherently, in the presented model *TnC* expression decreased with a decreasing constructs FBs percentage. The *NppA* gene correlates with inflammation/degradation and ECM promotion. A slight increase in the expression of *NppA* was detected in the high-CMs population as expected given the enhanced expression by CMs .[19] These trends were visible also in the initial populations, although with lower modulations. Further enquiries should therefore be conducted in order to be able to ascribe the observed modulations to a particular phenomenon or cellular population.

A model where different FBs concentrations are considered would allow to represent different stages of deterioration and could possibly give insights on the effect of pharmacological treatments as well as on the functional properties of cardiac tissues at different pathological levels .

On this last matter, constructs contractive functionality was assessed revealing that constructs engineered with a low number of CMs could not synchronously follow the external electrical stimulation. This lack might be indicative of the representativeness of the proposed model of an advanced fibrotic state, in which the combined effects of a low number of CMs, increased ECM deposition, and presence of myofibroblasts, impair the electrical signal propagation. Medium-CMs constructs could beat synchronously confirming previous findings, demonstrating the presence of a 50% FBs threshold, above which the contractility properties of the engineered cardiac constructs are severely compromised [22].

Notably, the custom-made electrical setup adopted in the present work for the functional assessment had a limited contact between the conductive culture media and the electrodes, thus probably resulting in a low local field within constructs. To overcome this issue, electrodes guides bringing them in direct proximity of the cultured constructs might be introduced in the device as recently published [46].

Finally, the resistance of the High-CMs population to fibrosis induction when both cyclical stretching was provided and the profibrotic factor TGF-β1 was administered was tested. Both Immunofluorescence and RT-qPCR revealed that the High-CMs conditions seemed to resist the onset of a fibrotic phenotype even in the presence of TGF-β1, with only a slight increase in fibrosis associated genes expression.

Mastikhina et al. [25] managed to recapitulate the different key features of fibrosis by co-culturing human iPSC-CMs and cardiac FBs (at the ratio of 3:1) in a novel OoC using passive tension and TGF-β1as a fibrotic trigger. In the presented co-culture model of neonatal rat CMs and FBs at High-CMs condition (80%CM-20%FB corresponding to a ratio of 4:1) none of the investigated traits of fibrosis was upregulated, even under an active cyclic stimulation and with the additional supplementation of TGF-β1.

The different outcome obtained in [25] with respect to the present study might, be explained by the use of a different cell origin (human instead of rat), the different adopted culture times (14 days instead of 5), the higher concentration of human recombinant TGF-β1 used in [25] together with its use to pre-activated FBs in monolayer culture, as well as the different mechanical stimulation and 3D environment.

A superior fibrosis stimulus, such as higher TGF-β1concentration or FBs pre-activation in monolayer culture, might hence be needed to induce fibrosis traits with a high CM density in the present setup. Further enquiries should therefore be conducted on this regard, possibly combining TGF-β1 and mechanical stimulation and providing not physiological (i.e. 8.5 % like in our case) but pathological (e.g. with a strain level superior to 15% [21]) deformation.

Overall, an innovative mid-throughput and mechanically active device was presented highlighting the relevance of suitable ratios of FBs and CMs and the possible effects of mechanical loading when aiming at mimicking cardiac fibrosis hallmarks *in vitro*. Nevertheless, there are some limitations of the presented study and of the presented OoC platform that are worth further discussion.

In vivo intracellular communications within the myocardium are mediated by a complex interplay of electrical and mechanical messages together with biochemical factors (e.g. paracrine factors and microRNAs) [43]. Further mechanistic oriented studies should, therefore, be conducted to uncover the mechanisms behind the observed effects. An in-depth investigation of the interplays between CMs and FBs would nevertheless require separated analyses of the two populations after culture. Performing cell sorting and gene expression analysis on different cell subpopulation is however highly technically demanding in such microfluidic devices. *In vitro* models with a higher cellular yield or more sophisticated analysis methods (e.g. single cell RNA) might, therefore, be needed to address mechanistic questions.

Lastly, while the proposed device was designed to provide constructs with cyclic stretch, slight chamber modifications made it possible to widen the applicability of the proposed technology to a different mechanical stimulation and thus to a wider field of study. In fact, while cardiac fibrosis was adopted as an exemplary field of application, tailoring the device for the application of a purely compressive strain (Fig 13), the increased throughput could be introduced in studies addressing musculoskeletal pathologies such as osteoarthritis.

3.8 Conclusive remarks

A new OoC coupling a mechanically active environment with a higher throughput was introduces and successfully exploited to study how differing percentages of CMs and FBs affect the possible onset of a fibrotic phenotype. The different ratios of CMs and FBs could be used to mimic various steps of the pathology and/or distinctive regions of the affected myocardium (e.g. the scar tissue, the border zone with

still few living CMs). Such a model could help in better understanding the development of the pathology and in possibly envisioning new anti-fibrotic therapeutic solutions. Moreover, the proposed design could be generalised and adapted to provide, for instance, compression rather than stretching making it useful in modelling musculoskeletal pathologies. The concept for a possible valuable instrument for both disease research and drug development and screening campaigns was therefore presented.

3.9 References

1. Probst C, Schneider S, Loskill P (2018) High-throughput organ-on-a-chip systems: Current status and remaining challenges. Curr. Opin. Biomed. Eng. 6:33–41
2. Paul SM, Mytelka DS, Dunwiddie CT, et al (2010) How to improve R&D productivity: the pharmaceutical industry's grand challenge. Nat Rev Drug Discov 2010 93 9:203–214. https://doi.org/10.1038/nrd3078
3. Esch EW, Bahinski A, Huh D (2015) Organs-on-chips at the frontiers of drug discovery. Nat Rev Drug Discov 2015 144 14:248–260. https://doi.org/10.1038/nrd4539
4. Schneider O, Zeifang L, Fuchs S, et al (2019) User-Friendly and Parallelized Generation of Human Induced Pluripotent Stem Cell-Derived Microtissues in a Centrifugal Heart-on-a-Chip. Tissue Eng Part A 25:786–798. https://doi.org/10.1089/ten.tea.2019.0002
5. Trietsch SJ, Israëls GD, Joore J, et al (2013) Microfluidic titer plate for stratified 3D cell culture. Lab Chip 13:3548. https://doi.org/10.1039/c3lc50210d
6. Deddens JC, Sadeghi AH, Hjortnaes J, et al (2017) Modeling the Human Scarred Heart In Vitro: Toward New Tissue Engineered Models. Adv Healthc Mater 6:1600571. https://doi.org/10.1002/adhm.201600571
7. Travers JG, Kamal FA, Robbins J, et al (2016) Cardiac Fibrosis: The Fibroblast Awakens. Circ Res 118:1021–40. https://doi.org/10.1161/CIRCRESAHA.115.306565
8. Tomasek JJ, Gabbiani G, Hinz B, et al (2002) Myofibroblasts and mechano: Regulation of connective tissue remodelling. Nat. Rev. Mol. Cell Biol. 3:349–363
9. Zhao H, Li X, Zhao S, et al (2014) Microengineered in vitro model of cardiac fibrosis through modulating myofibroblast mechanotransduction. Biofabrication 6:045009. https://doi.org/10.1088/1758-5082/6/4/045009
10. Nagaya N, Fujii T, Iwase T, et al (2004) Intravenous administration of mesenchymal stem cells improves cardiac function in rats with acute myocardial infarction through angiogenesis and myogenesis. Am J Physiol - Hear Circ Physiol 287:. https://doi.org/10.1152/ajpheart.01071.2003
11. Edelberg JM, Lee SH, Kaur M, et al (2002) Platelet-derived growth factor-AB limits the extent of myocardial infarction in a rat model: Feasibility of restoring impaired angiogenic capacity in the aging heart. Circulation 105:608–613. https://doi.org/10.1161/hc0502.103672
12. Park S, Nguyen NB, Pezhouman A, Ardehali R (2019) Cardiac fibrosis: potential therapeutic targets. Transl. Res. 209:121–137
13. Leask A (2010) Potential therapeutic targets for cardiac fibrosis: TGFβ, angiotensin, endothelin, CCN2, and PDGF, partners in fibroblast activation. Circ. Res. 106:1675–1680
14. Rai V, Sharma P, Agrawal S, Agrawal DK (2017) Relevance of mouse models of cardiac fibrosis and hypertrophy in cardiac research. Mol. Cell. Biochem. 424:123–145
15. Pellman J, Zhang J, Sheikh F Myocyte-Fibroblast Communication in Cardiac Fibrosis and Arrhythmias: Mechanisms and Model Systems. https://doi.org/10.1016/j.yjmcc.2016.03.005
16. Sadeghi AH, Shin SR, Deddens JC, et al (2017) Engineered 3D Cardiac Fibrotic Tissue to Study Fibrotic Remodeling. Adv Healthc Mater 6:1601434. https://doi.org/10.1002/adhm.201601434
17. Kofron CM, Mende U (2017) *In vitro* models of the cardiac microenvironment to study myocyte and non-myocyte crosstalk: bioinspired approaches beyond the polystyrene dish. J Physiol 595:3891–3905. https://doi.org/10.1113/JP273100
18. Li Y, Asfour H, Bursac N (2017) Age-dependent functional crosstalk between cardiac fibroblasts and cardiomyocytes in a 3D engineered cardiac tissue. Acta Biomater 55:120–130. https://doi.org/10.1016/j.actbio.2017.04.027
19. Zhang H, Tian L, Shen M, et al (2019) Generation of quiescent cardiac fibroblasts from human induced pluripotent stem cells for in vitro modeling of cardiac fibrosis. Circ Res 125:552–566. https://doi.org/10.1161/CIRCRESAHA.119.315491
20. Occhetta P, Isu G, Lemme M, et al (2018) A three-dimensional: In vitro dynamic micro-tissue model of cardiac scar formation. Integr Biol (United Kingdom) 10:174–183. https://doi.org/10.1039/c7ib00199a
21. Kong M, Lee J, Yazdi IK, et al (2019) Cardiac Fibrotic Remodeling on a Chip with Dynamic Mechanical Stimulation. Adv Healthc Mater 8:. https://doi.org/10.1002/adhm.201801146
22. van Spreeuwel ACC, Bax NAM, van Nierop BJ, et al (2017) Mimicking Cardiac Fibrosis in a Dish: Fibroblast Density Rather than Collagen Density Weakens Cardiomyocyte Function. J Cardiovasc Transl Res 10:116–127. https://doi.org/10.1007/s12265-017-9737-1
23. Kumar S, Wang G, Zheng N, et al (2019) HIMF (Hypoxia-Induced Mitogenic Factor)-IL (Interleukin)-6 Signaling Mediates Cardiomyocyte-Fibroblast Crosstalk to Promote Cardiac Hypertrophy and Fibrosis. Hypertens (Dallas, Tex 1979) 73:1058–1070. https://doi.org/10.1161/HYPERTENSIONAHA.118.12267
24. Rupert CE, Kim TY, Choi BR, Coulombe KLK (2020) Human Cardiac Fibroblast Number and Activation State Modulate Electromechanical Function of hiPSC-Cardiomyocytes in Engineered Myocardium. Stem Cells Int 2020:. https://doi.org/10.1155/2020/9363809
25. Mastikhina O, Moon BU, Williams K, et al (2020) Human cardiac fibrosis-on-a-chip model recapitulates disease hallmarks and can serve as a platform for drug testing. Biomaterials 233:119741. https://doi.org/10.1016/j.biomaterials.2019.119741
26. Marsano A, Conficconi C, Lemme M, et al (2016) Beating heart on a chip: a novel microfluidic platform to generate functional 3D cardiac microtissues. Lab Chip 16:599–610
27. Visone R, Ugolini GS, Vinarsky V, et al (2018) A Simple Vacuum-Based Microfluidic Technique to Establish High-Throughput Organs-On-Chip and 3D Cell Cultures at the Microscale. Adv Mater Technol 1800319. https://doi.org/10.1002/admt.201800319
28. WO2016174607A1 - Microfluidic device and relative method for the generation and/or culture and/or maturation of three- dimensional cell and/or tissue constructs - Google Patents. https://patents.google.com/patent/WO2016174607A1/en. Accessed 8 Feb 2020
29. Occhetta P, Mainardi A, Votta E, et al (2019) Hyperphysiological compression of articular cartilage induces an osteoarthritic phenotype in a cartilage-on-a-chip model. Nat Biomed Eng. https://doi.org/10.1038/s41551-019-0406-3
30. Mohan R, Schudel BR, Desai A V., et al (2011) Design considerations for elastomeric normally closed microfluidic valves. Sensors Actuators, B Chem 160:1216–1223. https://doi.org/10.1016/j.snb.2011.09.051
31. Radisic M, Marsano A, Maidhof R, et al (2008) Cardiac tissue engineering using perfusion bioreactor systems. Nat Protoc 3:719–738. https://doi.org/10.1038/nprot.2008.40
32. Frangogiannis NG (2012) Regulation of the inflammatory response in cardiac repair. Circ. Res. 110:159–173
33. Bildyug N, Bozhokina E, Khaitlina S (2016) Contribution of α-smooth muscle actin and extracellular matrix to the in vitro

reorganization of cardiomyocyte contractile system. Cell Biol Int 40:472–477. https://doi.org/10.1002/cbin.10577
34. Jourdan-LeSaux C, Zhang J, Lindsey ML (2010) Extracellular matrix roles during cardiac repair. Life Sci. 87:391–400
35. Shimojo N, Hashizume R, Kanayama K, et al (2015) Tenascin-C may accelerate cardiac fibrosis by activating macrophages via the integrin αVβ3/Nuclear Factor-κB/Interleukin-6 Axis. Hypertension 66:757–766. https://doi.org/10.1161/HYPERTENSIONAHA.115.06004
36. Podesser BK, Kreibich M, Dzilic E, et al (2018) Tenascin-C promotes chronic pressure overloadinduced cardiac dysfunction, hypertrophy and myocardial fibrosis. J Hypertens 36:847–856. https://doi.org/10.1097/HJH.0000000000001628
37. Kerkelä R, Ulvila J, Magga J (2015) Natriuretic peptides in the regulation of cardiovascular physiology and metabolic events. J. Am. Heart Assoc. 4:2423
38. Chomczynski P, Sacchi N (1987) Single-step method of RNA isolation by acid guanidinium thiocyanate-phenol-chloroform extraction. Anal Biochem 162:156–159. https://doi.org/10.1016/0003-2697(87)90021-2
39. Tandon N, Cannizzaro C, Chao PHG, et al (2009) Electrical stimulation systems for cardiac tissue engineering. Nat Protoc 4:155–173. https://doi.org/10.1038/nprot.2008.183
40. Huh D, Matthews BD, Mammoto A, et al (2010) Reconstituting organ-level lung functions on a chip. Science (80-) 328:1662–1668. https://doi.org/10.1126/science.1188302
41. Bein A, Shin W, Jalili-Firoozinezhad S, et al (2018) Microfluidic Organ-on-a-Chip Models of Human Intestine. CMGH 5:659–668
42. Herland A, Maoz BM, Das D, et al (2020) Quantitative prediction of human pharmacokinetic responses to drugs via fluidically coupled vascularized organ chips. Nat Biomed Eng 1–16. https://doi.org/10.1038/s41551-019-0498-9
43. Kofron CM, Mende U (2017) In vitro models of the cardiac microenvironment to study myocyte and non-myocyte crosstalk: bioinspired approaches beyond the polystyrene dish. J. Physiol. 595:3891–3905
44. Fan D, Takawale A, Lee J, Kassiri Z (2012) Cardiac fibroblasts, fibrosis and extracellular matrix remodeling in heart disease
45. Chiquet-Ehrismann R, Tannheimer M, Koch M, et al (1994) Tenascin-C expression by fibroblasts is elevated in stressed collagen gels. J Cell Biol 127:2093–2101. https://doi.org/10.1083/jcb.127.6.2093
46. Visone R, Ugolini GS, Cruz-Moreira D, et al (2021) Micro-electrode channel guide (μECG) technology: an online method for continuous electrical recording in a human beating heart-on-chip. Biofabrication. https://doi.org/10.1088/1758-5090/abe4c4

4 Investigation of morphological, compositional, and mechanical modifications in the osteochondral unit of osteoarthritis patients undergoing knee prosthetization: establishment of a methodology for the evaluation of mechanical properties in the osteochondral unit tissues

The work described in this chapter was carried out in the framework of a collaboration between the Microfluidic and Biomimetic Microsystems Laboratory of Politecnico di Milano, (Milan, Italy) the Tissue Engineering laboratory of the University Hospital of Basel (Basel, Switzerland) and the Research and Development Unit of ARTIDIS (ARTIDIS AG, Basel)

4.1 Introduction

Diarthrodial joints are complex structures connecting adjacent bone segments to form functional entities allowing constrained articular motion and load distribution [1]. The biocomposite constituted by cartilage, calcified cartilage (i.e. the mineralized cartilaginous tissues at the interface between cartilage and bone persisting after growth plate closure) and subchondral bone, namely the osteochondral unit (OCU), has the unique capability of providing a wear minimising lubricated surface while allowing the transmission of loads during weight bearing and joint motion [1–3]. Alterations in the composition or in the structure of OCU tissues, the most common form being osteoarthritis (OA) [4], result in disruption of the joint integrity and function.

Musculoskeletal tissues performances in motility and load bearing are made possible by their organization in hierarchical structures allowing the transmission of mechanical cues ranging from gait kinematics to single cells activation of mechanotransduction signalling [5]. Diarthrodial joints tissues, in particular, have been defined as paradigmatic of hierarchical materials whose macroscale properties (10^{-2} – 10^{-3} m) depend on both their elementary constituents and their molecular and ultrastructural organization (ultra-scale 10^{-6}-10^{-8} m)[6].

Cartilage poroviscoelastic behaviour allows to store and dissipate energy upon mechanical deformation withstanding compressive and shear stresses. The tissue load response is mediated by the interaction among cartilage permeating fluid, a crosslinked collagen (mainly collagen type II) network, and aggrecan (the most abundant proteoglycan in cartilage). Aggrecan in particular controls cartilage response to loading due to the electrostatic repulsion of its glycosaminoglycan (GAG) side chains, carrying highly negatively charged carboxyl and sulphate groups [7].

The zone of calcified cartilage provides the attachment of cartilage to bone, the transition of force transmission across the joint, and limits solutes diffusion from subchondral bone [8]. At the microscale the tissues is characterized by a mineralized cartilage-like matrix with intermediate mechanical properties between those of cartilage and bone [9].

Bone resistance to load and limited weight, in turn, are mediated by a collagen type I matrix and its hydroxyapatite content. The mineral phase is the main determinant of the tissue stiffness, whereas the collagen content governs its post-yield ductility. Overall mechanical properties are ultimately determined by the mineral content and its distribution pattern within the collagenous matrix, as well as the tissue's structural, microstructural and nanostructural organization [10].

A wide range of tissues mechanical alterations contradistinguish the onset and the development of OA [11]. Contrasting results have however been reported depending on the scale of observation, and on the study focus being posed either on structural or material properties [12].

At the macroscale, cartilage stiffness was demonstrated to decrease with the onset of osteoarthritis, given the enzymatic degradative processes at play, with an estimated Young's modulus (E) for cartilage of 0.50 ± 0.14 MPa, 0.37 ± 0.13 MPa, and 0.28 ± 0.12 MPa, corresponding to OA grades of 1, 2, and 3 according to the International Cartilage Repair Society (ICRS) classification [13]. Conversely, atomic force microscopy (AFM) based indentation of collagen fibrils revealed an embrittlement of the protein passing from grade 0 (E ~ 320 MPa) to grade 2 (E ~340 MPa) [14]. These evidences demonstrate the high dependency of both E absolute values and modulation direction on the observational scale.

As regards subchondral bone, OA progression is characterised by an increased matrix turnover leading to an abnormal low mineralization pattern reducing the material stiffness [15]. Subchondral bone is however also characterized by changes in the trabecular structure and by an increase in bone volumetric fraction leading to an overall augmentation of its macroscale mechanical properties [16]. Notably subchondral bone Young's modulus determined by quasistatic nanoindentation increases with the OA grade passing from ~12.5 GPa for grade 0, to ~15.2 GPa for grade 4 (ICRS) [11].

Different phenomena are therefore observed focusing on tissues material properties or on their structure, and depending on the measurement technique and observational scale. This realization makes the case for adoption of contest relevant techniques in the determination of native tissues mechanical properties [17].

With the aims of (i) investigating the clinical mechanical and compositional alterations induced by OA, but also to (ii) assess if such alternations can be recapitulated within *in vitro* OA disease models, the properties of interest should be assessed at the same dimensional scale in clinical samples and *in vitro* models. To be able to translate OA related alterations in mechanical properties to an Organ on Chip model, it is therefore necessary to determine how these are modulated at a comparable (i.e. micrometric) length scale.

Indentation type atomic force microscopy (IT-AFM) allows the determination of mechanical properties at a cellular relevant scale (nano-meters to micro-meters) and with a high control over the indented area [7]. The technique was demonstrated capable of assessing the mechanical signature associated with different diseases [18] and was previously adopted in assessing the mechanical properties of cartilage samples [7] and in osteoarthritis investigation [14]. Previous studies focused however on cartilage surface, while knowledge gaps are still presents concerning disease related changes in mechanical properties of other OCU components.

In this context, the present work was dedicated to IT-AFM mediated investigation of OA-derived alterations of OCU mechanical properties, with particular focus on cartilage middle and deep zones, and on tissues across the tidemark (i.e. calcified cartilage and the upper strata of subchondral bone). A workflow for the combination of IT-AFM analyses with classic immunohistochemistry techniques was established to provide a proof-of-concept correlation between microscale mechanical properties and compositional and morphological variations in OCU tissues. The technique was then adopted to determine the elastic modulus

of a chondrocyte based micro-construct obtained through the cartilage on chip model [19] that had previously been established as described in Chapter 2.

4.2 Samples procurement and biopsies procedure

Full osteochondral biopsies were collected from tissues explants of patients undergoing total (TKA, n= 18) or uni-condyle (UKA, n=4) knee arthroplasty. A total of 22 patients (9 females, 13 males; average age 63 ± 10 years old) were considered. Samples procurement and processing were performed according to Swiss federal guidelines, following approval of the local ethical committees (Basel, Switzerland). TKN and UKA were performed at University Hospital Basel (Basel, Switzerland) or at Bethesda Spital Basel (Basel Switzerland). Full knee explants obtained during surgery were placed in sterile plastic containers and submerged in phosphate buffered saline (PBS). After transportation (performed within 2 hours after surgery) samples were kept at 4 °C. Within a maximum of 5 hours from surgery completion, full osteochondral biopsies were obtained from the distal femur condyles through an 8G bone marrow needle (Argon medical devices, diameter 8G (3,2 mm), length 6 inches). Pictures of the condyles were acquired and an overall assessment of the joint status performed depending on the extent of cartilage degradation, the presence of cartilage on one or both condyles, and the overall quality of the sample.

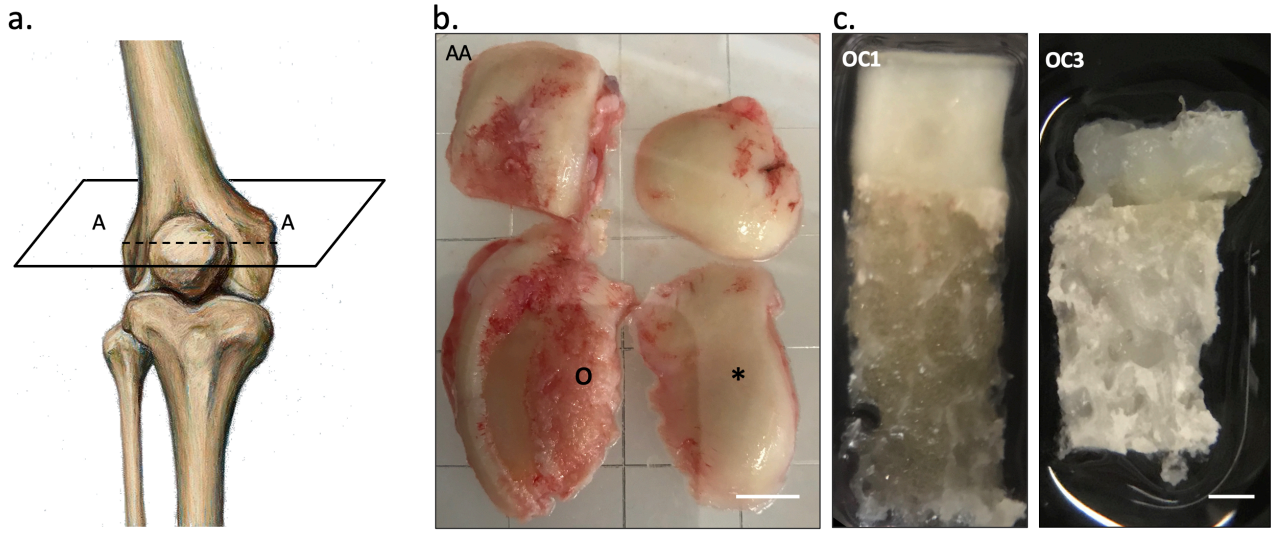

Figure 1: ***Knee explant assessment and osteochondral biopsy procedure****.* ***a,*** *Knee joint Schematization. Both distal femoral condyles and tibial plateau are removed during joint prosthetization surgeries. Exclusively the condyles were considered in this study. An exemplary cutting section AA is indicated.* ***b,*** *Representative image of distal femoral condyles explant. The OC1 area is indicated by the asterisk (*), the OC3 area by the circle (o). Bone exposure was present on one of the two condyles (lower left corner in the picture). Scale bar 1 cm.* ***c,*** *Examples of OC1 and OC3 biopsies. The lower cartilage thickness in OC3 is representative of the typical appearance of biopsies showing fibrillation and absence of cartilage superficial zone. Subchondral bone thickness depended on the indentation site and had no correlation with the specific OA grade. Scale bar 1 mm.*

For each patient, two biopsy areas were identified and labelled as osteochondral grade 1 (OC1) or grade (OC3). The preliminary OA grade of biopsies was determined depending on cartilage surface appearance upon visual inspection. OC1 areas, considered as healthy controls, presented no or minimal fibrillation and a smooth overall appearance. OC3 areas had a medium to high degree of cartilage fibrillation, and/or vascularization, and/or lower mechanical properties as for tactile perception assessment with sterile tweezers. Condyles' areas that presented no cartilage cover were excluded from analyses. Using a surgical scalpel, biopsies were cut in half along their thickness to obtain a flat surface. A representative picture of the considered areas, and respective resulting OCU biopsies is depicted in Fig 1. Collected biopsies were kept in PBS at 4°C prior to measurements.

4.3 Indentation type atomic force microscopy based mechanical properties assessment.

Samples mechanical properties at the nanoscale were measured through IT-AFM. Osteochondral biopsies were fixed to plastic culture dishes (Sigma-Aldrich, 30mm diameter) through two components epoxy resin (Araldite Rapid, Huntsman corporation). As visible in Fig. 2a, in particular, samples were positioned horizontally and carefully oriented so that the cut flat surface faced upward. Indentations were therefore performed on the lateral side of OCU biopsies. Measurements were performed at room temperature in degassed PBS.

IT-AFM was carried out with a noise-isolated TRIX device (ARTIDIS, Basel, Switzerland). To compensate for large surface corrugations on native biological samples, previously introduced customized hardware and software algorithms for automated levelling, which enabled uninterrupted AFM operation during data acquisition, were adopted [18]. Four-sided pyramidal tips (205-mm-long DNP-S10 triangular silicon nitride cantilevers, resonance frequency (air) f = 18 kHz, nominal cantilever spring constant k = 0.06 Nm^{-1}, tip radius = 20 nm) were employed. The exact spring constant of each adopted cantilever was determined through the thermal tune method [20]. Deflection sensitivity was determined directly on the dish as previously reported [7].

IT-AFM measurements were done at room temperature recording up to 22 different 20 × 20 μm force–volume maps over 20 × 20 points grids (400 force–displacement curves per map). Individual force curves were collected at velocity of 16 μm/s. The maximum applied loading force was set to 1.8 nN.

Force displacement curves were corrected for tilt and tip-sample displacement as previously documented [7, 18]. Both Forward and Backward force-displacement (F-D) curves were recorded. Backward curves were adopted to extract average samples Young's modulus making use of the Oliver-Pharr model [21].

Coupling of IT-AFM with brightfield microscopy allowed to precisely correlate the indentation maps with a definite location on the samples. Either samples 3D reconstructions (Fig 2b) or simple 2D images were adopted to choose the indentation points with reference to cartilage layers. Osteochondral biopsies were considered as composed by i) three cartilage zones (i.e. superficial, middle-transitional, and deep zones), ii) calcified cartilage and iii) subchondral bone (Fig 2c) defined as previously reported [22]. The indentation spots on the samples were selected through a proprietary software (ARTIDISNET, ARTIDIS AG, Basel) (Fig 2d). On average, for each sample 4-5 indentation maps were acquired for each of the considered layers (i.e. middle, and deep cartilage zones, and calcified cartilage-subchondral bone). Spots selection did not include points in cartilage superficial zone as this was often absent in OC3 samples thus preventing a direct comparison between experimental groups.

An elastic modulus (E) histogram was derived for each sample; a preliminary evaluation of the overall OC1 and OC3 samples mechanical properties was performed. Results are reported in Fig 2e. OC1 samples had a narrower properties distribution with moduli falling in the 0-4 kPa range with a distribution centred around 1kPa. Conversely, OC3 samples exhibited a wider range of properties with moduli ranging between 0 and 20 kPa and with a broader distribution.

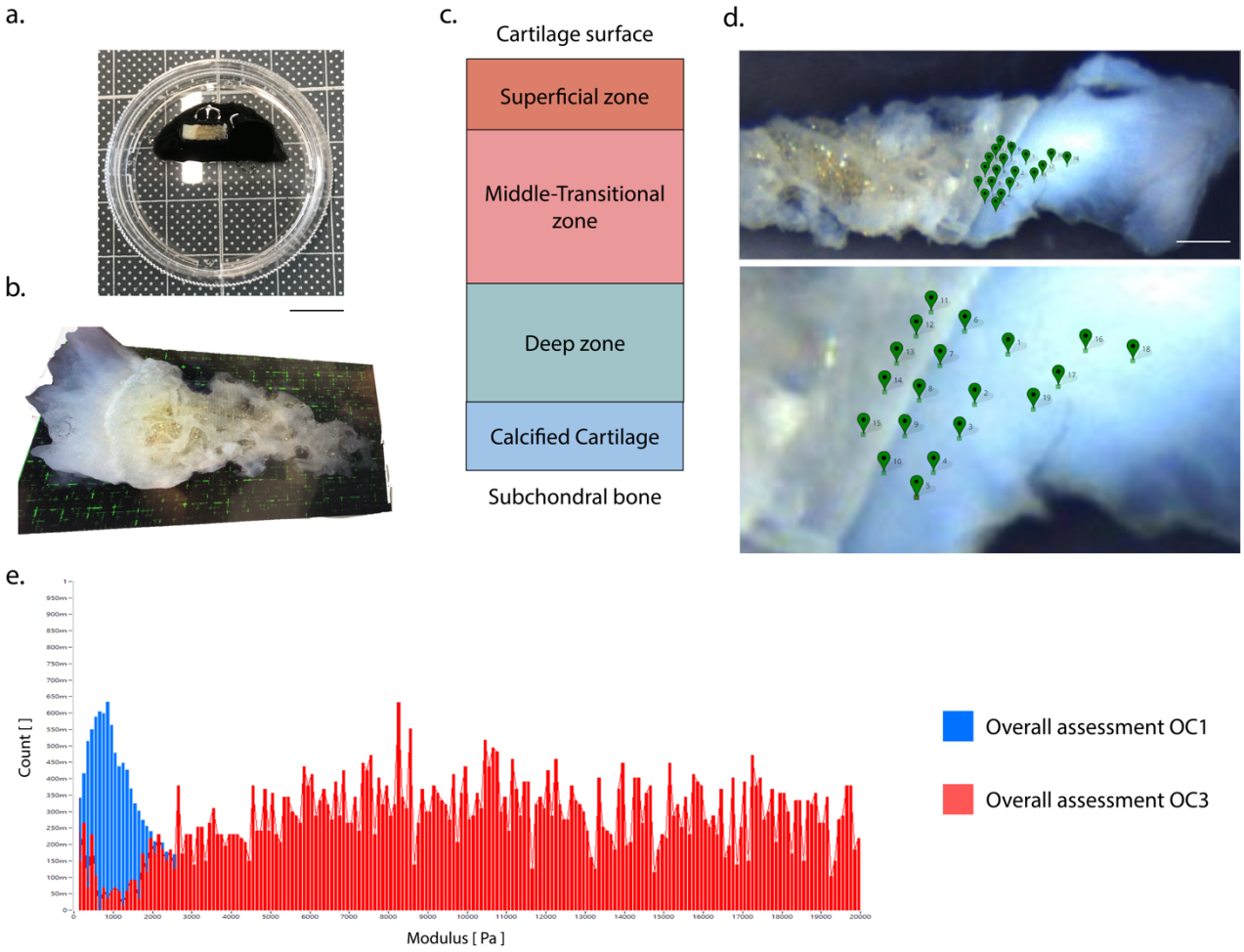

Figure 2: ***AFM measurement procedure and global evaluation of samples Young's modulus. a,*** *Picture of an osteochondral biopsy mounted for measurements. Adoption of black coloured epoxy resins allowed an increased contrast and better samples visualization. Scale bar 1 cm* ***b****. Example of biopsy 3D reconstruction adopted in spots selection (ARTIDIS proprietary software).* ***c.*** *Schematization of considered osteochondral layers.* ***d.*** *Example of spots selection. The zoom in highlights the spots line (nr 6-10) at the interface between cartilage and subchondral bone, on the calcified cartilage line. Scale bar 1mm.* ***e.*** *Elastic modulus histogram global assessment. Images are referred to indentation maps from n=15 donors. A total of 82666 and 81597 indentation points were considered for OC1 and OC3 samples respectively.*

4.4 Morphological and Compositional modification assessments

4.4.1 Samples histological preparation

Immediately after completion of AFM measurements osteochondral biopsies were detached from supports, fixed with 4% paraformaldehyde for 48 hours, and decalcified with a 15% (w/v) ethylenediaminetetraacetic acid (EDTA) solution (Sigma). Samples were subsequently dehydrated and embedded in paraffin so that the first obtained sections corresponded to the sample face probed with IT-AFM. Sections (5 µm thick) were cut through a microtome (Microm HM 340E). Haematoxylin and Eosin (H&E, Baker) staining was performed according to standard protocols to visualise osteochondral structures architecture. Safranin-O (Saf-O)/fast green staining (Fluka) was performed according to standard protocols to visualise the glycosaminoglycan content. Osteochondral biopsies from areas immediately adjacent to those measured by IT-AFM were taken and fixed immediately. An assessment of the effect of the AFM procedure on histological stainings was performed demonstrating that the increased time intercurrent between surgery and fixation required by the indentation procedure (i.e. 1 day) did not alter the result of histological stainings (data not shown).

4.4.2 Samples OA grading

OC1 and OC3 samples effective OA grade was assessed based on Saf-O histological stainings (Fig 3a, b). Two grading or scoring systems were adopted as previously performed by other authors [23, 24]. Briefly, a blind histopathological grade assessment from 0 (heathy sample) to VI (joint deformation) was performed as indicated by [23]. Grading criteria are reported in Table 1.

A second blind scoring system was adapted from [24]. For this latter case, two criteria were considered for the scoring (i.e. the intensity of the staining and the tissue morphology, both derived from Saf-O sections) each with equal weight and with a possible minimum collective score of 0 and a maximum of 6. Criterion 1, intensity of staining, was scored as: 0, no stain; 1, weak stain; 2, moderate, even stain; and 3, even, dark stain. Criterion 2, tissue morphology, was scored as: 0, bone erosion; 1, surface abrasion with matrix loss; 2, surface intact, fibrillation; 3, surface intact. Average grades of samples attributed to the OC1 and OC3 groups were evaluated. Following the first grading system OC1 and OC3 samples had, respectively, average grades of 1.75 ± 0.6 and 3.1 ± 0.7 (mean ± standard deviation); following the second scoring system averages values resulted respectively of 4.4 ± 1.3 and 2 ± 1.7 (mean ± standard deviation) for OC1 and OC3 samples. Both methods revealed a statistically significant difference between experimental groups (Fig. 3c) demonstrating that the criteria adopted to differentiate OC1 and OC3 areas (i.e. cartilage surface visual appearance and haptic feeling) were adequate for the selection of samples with distinctive OA grades and representative, respectively, of early and late degradation states.

OA cartilage histopathology grade assessment—advanced grading methodology

Grade (key feature)	Subgrade (optional)	Associated criteria (tissue reaction)
Grade 0: surface intact, cartilage intact	No subgrade	Intact, uninvolved cartilage
Grade 1: surface intact	1.0 Cells intact 1.5 Cell death	Matrix: superficial zone intact, edema and/or fibrillation Cells: proliferation (clusters), hypertrophy Reaction must be more than superficial fibrillation only
Grade 2: surface discontinuity	2.0 Fibrillation through superficial zone 2.5 Surface abrasion with matrix loss within superficial zone	As above +Discontinuity at superficial zone ±Cationic stain matrix depletion (Safranin O or Toluidine Blue) upper 1/3 of cartilage (mid zone) ±Disorientation of chondron columns
Grade 3: vertical fissures	3.0 Simple fissures 3.5 Branched/complex fissures	As above ±Cationic stain depletion (Safranin O or Toluidine Blue) into lower 2/3 of cartilage (deep zone) ±New collagen formation (polarized light microscopy, Picro Sirius Red stain)
Grade 4: erosion	4.0 Superficial zone delamination 4.5 Mid zone excavation	Cartilage matrix loss, cyst formation within cartilage matrix
Grade 5: denudation	5.0 Bone surface intact 5.5 Reparative tissue surface present	Surface is sclerotic bone or reparative tissue including fibrocartilage
Grade 6: deformation	6.0 Joint margin osteophytes 6.5 Joint margin and central osteophytes	Bone remodelling. Deformation of articular surface contour (more than osteophyte formation only) Includes: microfracture and repair

I. Grade = depth progression into cartilage.

Table 1: ***Cartilage grade assessment as reported in*** [23]

4.4.3 Morphological parameters extraction

A quantification of the morphological alterations caused by the advancement of OA was carried out based on parameters extracted from H&E stainings. Representative H&E histological sections for both OC1 and OC3 samples are represented in Fig. 3d. To assess the development of OA features at the cartilage surface level but also at the interface between cartilage and bone, samples roughness was assessed in correspondence of the cartilage surface and of the tidemark (i.e. the dark line appearing in H&E colorations at the interface between cartilage and calcified cartilage as a result of the diverse permeability of the two tissues [25]). Briefly, the profile of cartilage surface and tidemark was manually extracted from H&E images. Profiles were then interpolated with a line through appropriate software (MATLAB, MathWorks). A mock example of tidemark end interpolating line profiles is depicted in the inset of Fig. 3d. For each curve's pixel i, the distance r_i between the curve and the line was determined. Curve roughness was then assessed calculating (i) the average roughness R_a, (ii) the root mean squared roughness R_q, and (iii) the maximum peak to valley roughness R_t, which were defined respectively as

$$R_a = \frac{1}{N}\sum_{i=1}^{N}|r_i|$$

$$R_q = \sqrt{\frac{1}{N}\sum_{i=1}^{N}|r_1^2|}$$

$$R_t = \left|\min_{1\le i\le N} r_i\right| + \left|\max_{1\le i\le N} r_i\right|$$

Where N is the total number of pixels of the curve.

For all considered parameters, the cartilage surface roughness of OC3 samples resulted statistically higher than that of OC1 samples testifying the soundness of the sample selection procedure. Conversely, no significant differences in the roughness of the tidemark were detected between the two groups. Results are reported in Fig. 3e. Finally, an assessment of the overall thickness of cartilage, calcified cartilage and subchondral bone plate was performed. In details cartilage was defined as the tissue comprised between the articular surface and the tidemark, calcified cartilage as the tissue comprised between the tidemark and the cement line (i.e. the line of interface between calcified cartilage and subchondral bone), and the subchondral bone plate was defined as the bone tissue overlaying the trabeculated spongiosa. n=8 donors were considered. For each tissue layer at least n=5 measurements were performed and results averaged. The overall cartilage thickness resulted statistically diminished in OC3 samples. A similar trend was observed for the calcified cartilage, despite doubling of the tidemark was often observed in higher OA grades. The subchondral bone thickness displayed instead an upward tendency in OC3 samples. Notably, a high inter and intra sample variability was observed overall. Results are displayed in Fig. 3f.

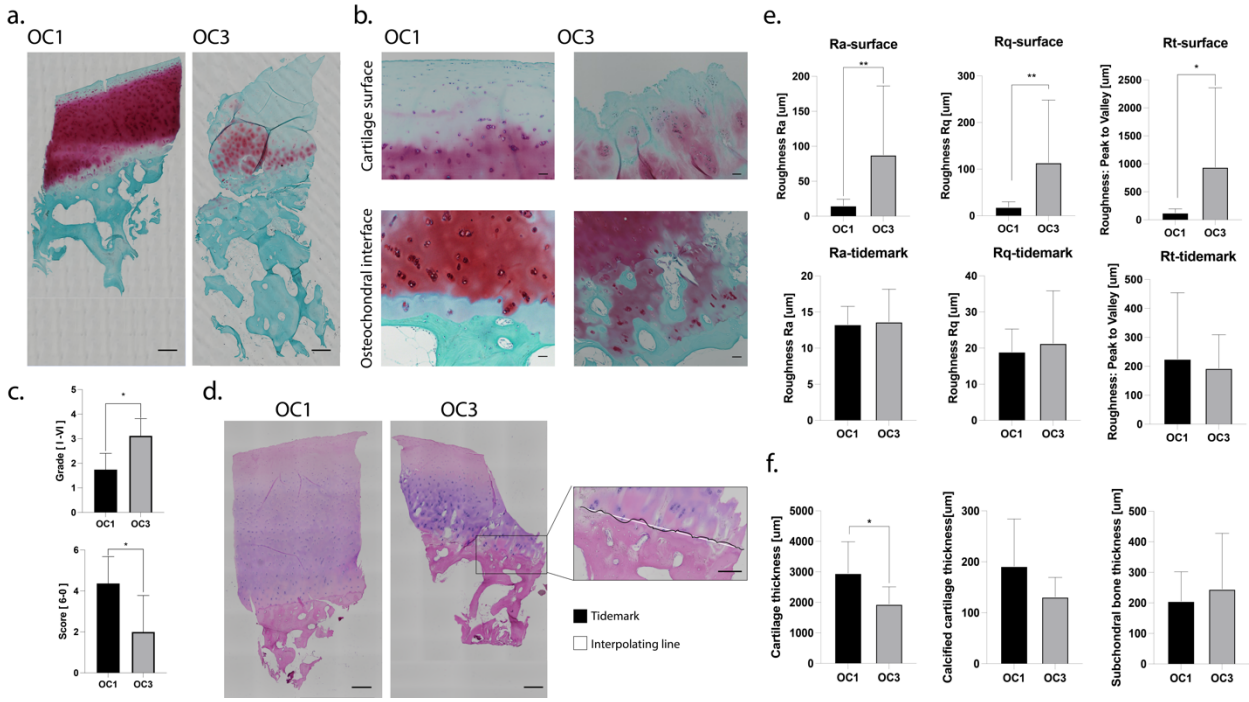

Figure 3: ***Samples OA grade assessment and morphological characteristics determination****. **a,** Representative Saf-O/ Fast green stainings of OC1 and OC3 samples. Scale bar 500 µm. Images from n=15 donors were considered **b,** Details of OC1 and OC3*

samples. Cartilage surface: Higher degraded samples exhibited a lack of cartilage top layer, deep fissures, and partial erosion of the middle one. Proliferating chondrocytes clusters were also visible. Osteochondral interface: OC3 samples exhibited duplication of the tidemark, expansion of calcified cartilage into the deep cartilage zone and vascular invasion of the chondral tissue. Cartilage compenetrating bone areas were also visible. Scale bar 50 µm. ***c,*** *Top: Samples OA scoring based on* [23]*. Bottom: samples scoring as adapted from* [24]*. n= 8 donors were considered in analyses. For each donor both an OC1 and an OC3 samples were analysed. Statistics by paired t test. Population normality was assessed trough D'Agostino-Pearson and Kolmogorov-Smirnov tests. * P<0.05.* ***d,*** *Representative H&E stainings of OC1 and OC3 samples. Scale bar 500 µm. n=15 donors were considered. The inset on the right represents a mock depiction of the tidemark and the interpolating line used for roughness calculations.* ***e,*** *Evaluation of samples surface and tidemark average roughness (Ra), root mean square roughness (Rq), and maximum Peak to valley height (Rt). n=8 donors were considered for each experimental condition. Statistics by paired t test for normal populations and by Wilcoxon test for non-normal populations. Population normality was assessed trough Kolmogorov-Smirnov test. * P<0.05, ** P<0.01.* ***f****, Assessment of cartilage, calcified cartilage and subchondral bone thicknesses. Cartilage was defined as the area between sample's surface and tidemark, calcified cartilage as the area between tidemark and cement line and subchondral bone as the area between cement line and the first trabecula. Samples from n=8 donors were considered for each condition. Statistics by paired t test. Population normality was assessed trough D'Agostino-Pearson and Kolmogorov-Smirnov tests. * P<0.05.*

4.4.4 Matrix composition characterization though immunofluorescence

Immunofluorescence stainings were performed to assess the presence, in OC1 and OC3 samples, of the matrix constituents collagen type I (COL1A1), collagen type II (COL2A1), and lubricin, together with the hypertrophy marker collagen type X (COL10A1), and the MMP-generated aggrecan carboxyterminal neoepitope DIPEN. Stainings were performed on paired OC1 and OC3 samples from n=15 donors. Samples sections (5 µm thick) were deparaffinized and rehydrated following standard protocols. Antigen retrieval enzymatic digestion was performed with subsequent incubations in a 2mg/ml solution of Hyaluronidase (Sigma, H3884) in tris buffered saline (TBS) for 60 mins at 37 °C, and in a 1 mg/ml solution of Pronase (Roche, 065921001) in TBS for 30 mins at 37 °C. Cells were permeabilized with a 0.5% v/v solution of Triton-X (Sigma Aldrich) in PBS for 10 mins. A 3% v/v goat serum, 0.3 % v/v Tween 20, (Sigma Aldrich) in PBS blocking solution was applied for 1h at room temperature to avoid non-specific binding. Samples were incubated with primary antibodies overnight at 4 °C. Mouse monoclonal IgG1 anti human collagen type I (Novusbio, NB600-450), mouse monoclonal IgG2a anti human collagen type II (Abcam ab185430), and rabbit polyclonal anti human Lubricin (Abcam, ab28484) antibodies were used to detect ECM matrix components. Mouse monoclonal IgM anti human Collagen type X (Abcam, ab138492) antibody was adopted to detect the presence of the hypertrophy marker COL10A1, and mouse monoclonal IgG1 anti human DIPEN (MD Biosciences, 1042002) antibody was used to detect the aggrecan degradation product. Staining with 4',6-diamidino-2-phenylindone (DAPI) was used to identify cell nuclei.

Appropriate secondary antibodies labelled with Alexa Fluor 488, Alexa Fluor 546, and Alexa Fluor 647 (Invitrogen) were adopted at a 1:200 dilution incubating the samples for 45 mins at room temperature. Fluorescent images were acquired with a widefield microscope (Nikon, Eclipse Ti2).

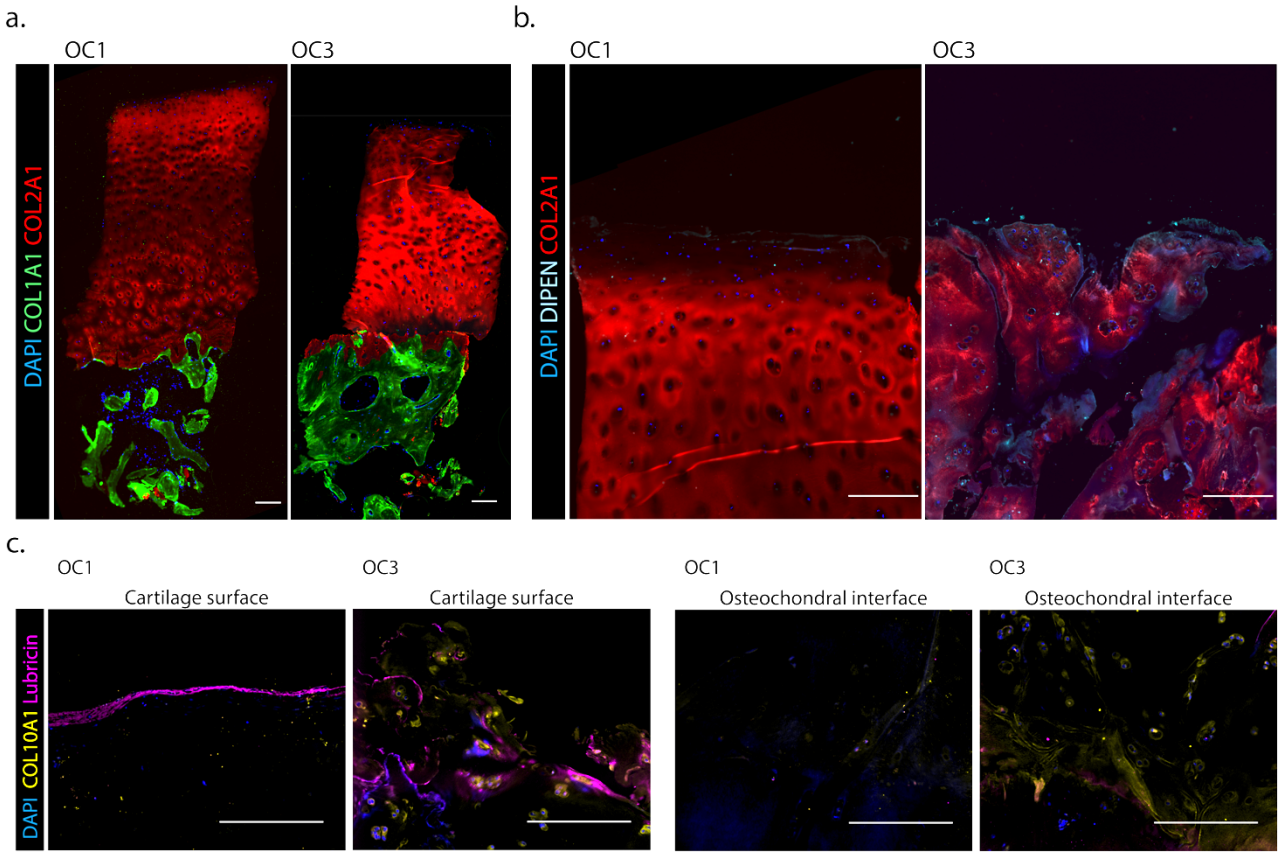

Figure 4: ***Samples compositional analysis assessed by immunofluorescence.*** ***a,*** *Representative images of full osteochondral biopsies, principal matrix components. COL2A1 is represented in red, COL1A1 in green. DAPI, used to localize the cells nuclei, is depicted in blue. Scale bar 500 µm. samples from n=15 donors were evaluated.* ***b,*** *Evaluation of aggrecan degradation bi-products. COl2A1 is represented in red, DIPEN in cyan, and DAPI in blue. Scale bar 500 µm. samples from n=15 donors were evaluated.* ***c,*** *Staining for lubricin (in magenta) and the hypertrophy marker COL10A1 (in yellow). DAPI is represented in blue. Both cartilage surface and osteochondral interface are represented. N=15 donors were considered. Scale bar 500 µm.*

Overall, higher OA grades did not imply a reduction in COL2A1 positivity in cartilage, with episodical increases in the fluorescent intensity of the middle zone (Fig. 4a). A strong positivity for COL2A1 was detected in calcified cartilage in all samples. From the COL1A1 staining marking subchondral bone plate and trabeculae, it was visible how OC3 samples were associated with a higher bone volumetric fraction (i.e. the percentage of area occupied by trabeculae with respect to the empty one), a known sign of bone sclerosis (Fig. 4a).

Positivity for DIPEN was highly variable between donors. A very dim DIPEN positive layer was detected on the cartilage surface of OC1 samples. DIPEN expression was more evident in OC3 samples with an histopathological OA grade of IV or higher[23] which were characterized by upper layer erosion and delamination (Fig. 4b).

Lubricin, marking cartilage surface in healthy joints, was expressed in the very upper layer of OC1 (i.e. cartilage superficial zone) samples characterized by chondrocytes alignment to the surface direction. Conversely, Lubricin was either not expressed in OC3 samples or positive in the cartilage middle zone

following erosion of the superficial one (Fig. 4c). COL10A1 was not present in OC1 samples, the only exception being a very light positivity at the interface with bone. COL10A1 expression in OC3 samples was highly variable among donors. Higher OA grade samples showed COL10A1 positive cells both on the cartilage surface (i.e. the surface resulting from upper layers erosion) and in the deep cartilage layer-in calcified cartilage (Fig. 4c).

4.5 IT-AFM based determination of elastic modulus in OCU layers

A refined analysis of the osteochondral constructs mechanical properties was performed to correlate the IT-AFM derived Young's modulus of each indentation spot with its location within the sample, highlighting possible specific differences at the interface between cartilage and bone. Brightfield images adopted during the spot selection procedure (Fig. 2d) were manually superimposed with Saf-O stainings (Fig. 3a) modulating images transparency to optimize both visualization modalities (Fig. 5a). Overlapped images were adopted to determine (i) where in the different tissue layers a precise indentation spot fell (i.e. if in cartilage middle or deep zones, or in calcified cartilage) and (ii) whether the spot layer was positive or negative for GAG. Notably, images resolution allowed to identify to which layer a particular indentation spot belonged but impeded to determine precisely if the indentation spot location was GAG positive or negative. GAG positivity was therefore referred globally to the whole layer.

Indentation spots were then grouped according to the positivity, or not, of the Saf-O staining as GAG (-) and GAG(+). Notably, in this phase spots were classified exclusively according to Saf-O positivity, not by samples OA grade (i.e. OC1 or OC3). Results varied according to the considered layer. The Young's modulus of Saf-O negative spots exhibited higher values and wider distributions that the ones of Saf-O positive ones. Notably, no statistical differences between the two groups were detected considering cartilage deep zone while evident differences were visible both in the middle zone and in calcified cartilage. Results are reported in Fig. 5b. Both in cartilage middle zone and in calcified cartilage, GAG depletion led to tissues stiffening and an increased elastic modulus range.

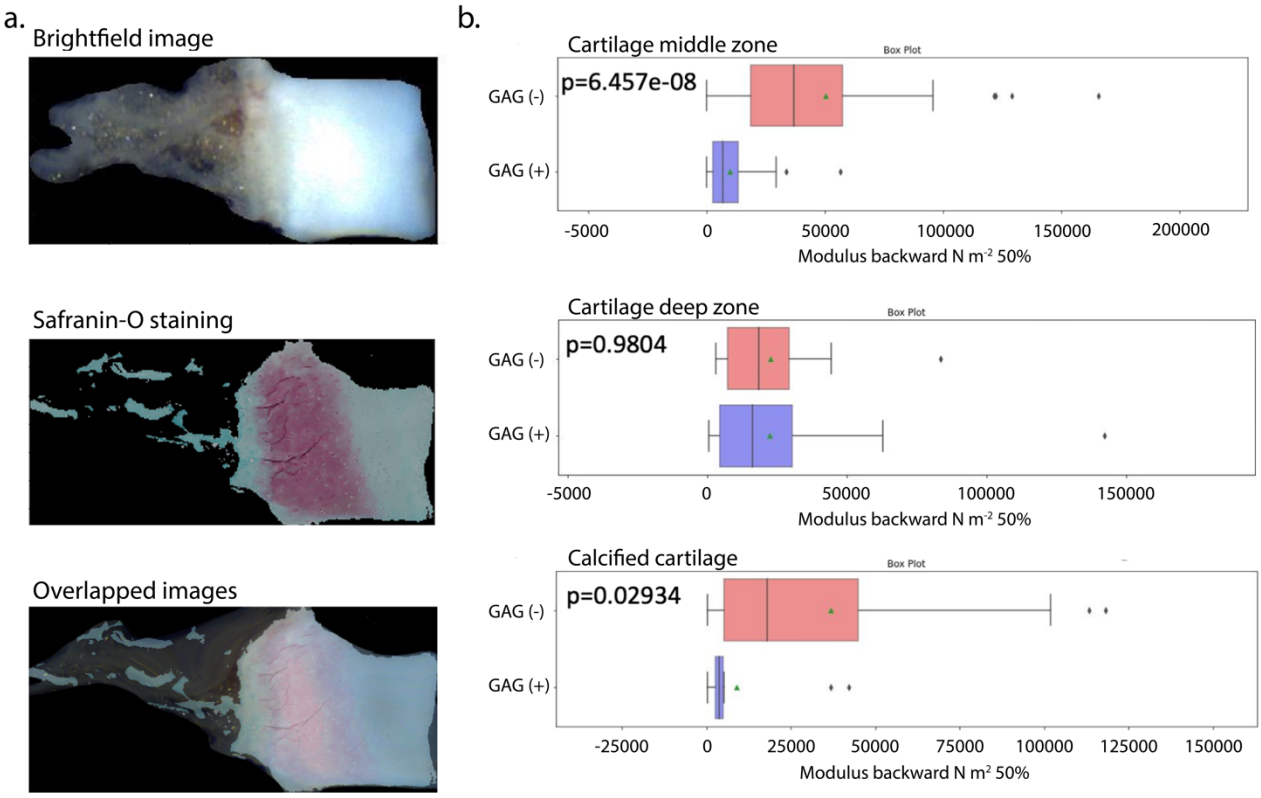

Figure 5: ***Determination of the mechanical properties by layer and correlation with GAG content. a.*** *Example of Brightfield-Saf-O overlapped image. The super imposition of the two visualization modalities allowed to precisely identify the specific layer and the eventual GAG positivity of each indentation spot (not indicated in the images).* ***b,*** *Box plot of Young's modulus of GAG negative and GAG positive indentation spots divided by layer. Statistics by paired t test for normal populations and by Wilcoxon test for non-normal populations. Population normality was assessed trough Kolmogorov-Smirnov test. p= computed p-value. Indentation spots from both OC1 and OC3 samples of n= 15 donors were considered in analyses.*

4.6 IT-AFM translation to a microfluidic based Cartilage on chip model

The developed IT-AFM measurement procedure was adapted to evaluate the microscale mechanical properties of cartilaginous microconstructs obtained as described in Chapter 2. A previously described microfluidic platform [19], capable of hosting 3 dimensional cell laden hydrogels was adopted to achieve cartilaginous tissues. Briefly, human articular chondrocytes (hACs) from a donor with no clinical history of OA (male, 47 years old) were isolated and expanded *in vitro* as previously described ([19], Chapter 2). Cartilage microconstructs generation was achieved embedding hACs into an enzymatically cross-linkable and degradable polyethilenglycole (PEG) based hydrogel [41] with a final dry mass content of 2%. The polymer precursor solution was mixed with hACs so that a final density of $5x10^4$ cells μl^{-1} could be obtained. hACS were cultured statically in microfluidic devices for 14 days. A chondrogenic medium constituted by DMEM (Sigma–Aldrich) containing, 4.5 mg ml^{-1} d-glucose, 0.1 mM non-essential amino acids, 1 mM sodium pyruvate, 100 mM HEPES buffer,100 U ml^{-1} penicillin, 100 µg ml^{-1} streptomycin, 0.29 mg ml^{-1} l-glutamine, 1.0 mg/ml bovine insulin, 0.55 mg/ml human transferrin, 0.5 µg/ml sodium

selenite, 50 mg/ml bovine serum albumin, 470 µg/ml linoleic acid, and 1.25 % of Human serum albumin and supplemented with 0.1 mM ascorbic acid 2-phosphate, 10^{-4} mM Dexamethasone and 10 ng ml^{-1} TGF-β3 was adopted during differentiation [26].

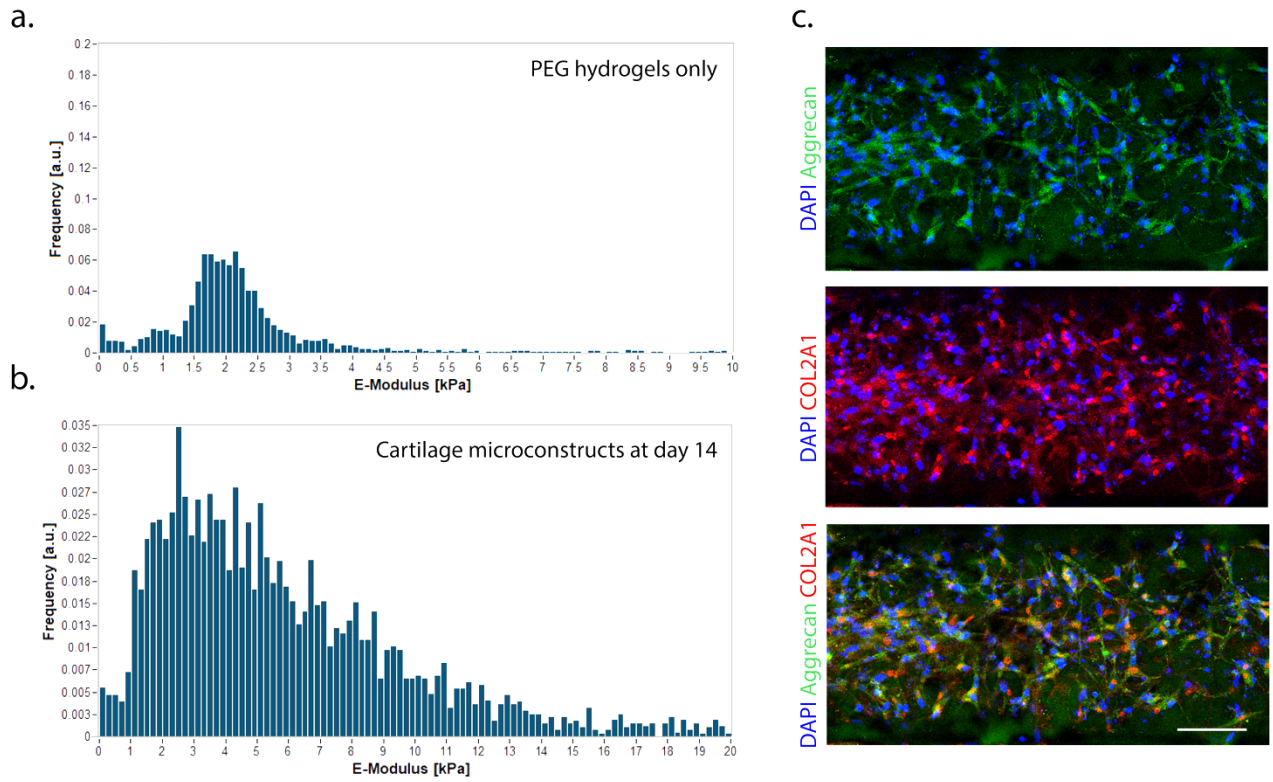

Figure 6: ***Determination of the mechanical properties of cartilage on chip constructs and correlation with immunofluorescence analyses****. **a**, IT-AFM evaluation of the elastic modulus of the 2% PEG hydrogel formulation in microfluidic devices. n= 3 samples were considered; 5 indentation maps were evaluated for each sample* ***b,*** *IT-AFM evaluation of the elastic modulus of hACS based constructs after 14 days of chondrogenic differentiation. n= 3 biologically independent samples were considered; 5 indentation maps were evaluated for each sample* ***c,*** *Immunofluorescence images of the constructs after 14 days of chondrogenic differentiation. n=3 biologically independent samples were considered. Aggrecan is represented in green, COL2A1 in red, and DAPI is depicted in Blue. Scale bar 100 µm.*

At the end of the culture period devices were opened to expose the cartilaginous constructs. IT-AFM and correlated analyses to determine samples Young's modulus were performed with the modalities described in section 4.3. Constructs constituted exclusively by the 2% PEG formulation adopted to encapsulate hACs were adopted as a reference for measurements. Separate devices were fixed with a solution of 4% paraformaldehyde at 4°C for 12 h. Immunofluorescent staining for COL2A1 and Aggrecan was performed as described in section 4.4.4. The staining procedure was carried out directly on chip and no enzymatic antigen retrieval was necessary. Mouse monoclonal IgG2a anti human collagen type II (Abcam ab185430) antibody was adopted to detect COL2A1, rabbit polyclonal anti-human aggrecan (Abcam, ab36861) antibody was adopted to detect Aggrecan. DAPI was used to stain nuclei. Appropriate secondary antibodies

were adopted as described in section 4.4.4. Images were acquired through a confocal microscope (Nikon A1R, Ala).

IT-AFM performed on 2% PEG hydrogels was used as a reference of the initial matrix properties. The hydrogel displayed a narrow elastic modulus distribution centred around 1.9 kPa (Fig. 6a). Conversely, after 14 days of chondrogenic differentiation constructs exhibited an elastic modulus distribution centred on 3.5 kPa but with localized E values reaching 20 kPa (Fig. 6b), not dissimilarly from native samples previously analysed. Immunofluorescent analyses revealed, furthermore, that constructs were positive for Aggrecan and COL2A1. The increase in elastic modulus of the constructs could therefore be correlated to the deposition of a cartilage like matrix.

4.7 Discussion

A workflow to determine cartilage and subchondral tissues microscale mechanical properties was established. Obtained measurements were correlated with classic histological stainings and macroscale morphological parameters. Specifically, IT-AFM was coupled with macroscale images and histological stainings of full osteochondral biopsies to determine the local mechanical properties of the tissues at the interface between cartilage and subchondral bone. A preliminary assessment of how the Young's modulus of these tissues is affected during OA progression was provided comparing non affected (OC1) and affected (OC3) osteochondral areas of OA patients undergoing knee arthroplasty.

OC1 samples adopted as healthier controls presented minimal or no cartilage surface fibrillation and an overall positivity for Saf-O staining demonstrating retention of GAGs in the ECM. Healthy looking areas from osteoarthritic joints display however a different chondrocytes behaviour if compared to healthy controls. Chondrocytes isolated from less affected OA areas were reported to express higher level of hypertrophy markers (e.g. *COL10A1*) and to result in engineered tissues with a lowered capacity for GAGs deposition also after cellular dedifferentiation and redifferentiation [27]. Additionally, chondrocytes from non-affected areas of OA joints exhibit altered activation of Wingless/Int1 (Wnt) and bone morphogenic protein (BMP) pathways [28]. A complete assessment of how OA affects the mechanical properties of OCU tissues would therefore require a comparison with material from healthy donors.

Through the proposed methodology it was however still feasible to detect differences between experimental groups (the overall OCU E distribution of OC1 samples was centred around 1 kPa, while OC3 samples had a uniformly distributed E ranging up to 20 kPa) and the presented work constitutes a demonstration of how IT-AFM and correlated analyses could be used to determine the microscale mechanical properties not only of cartilage surface but also of other OCU tissues.

Previous IT-AFM based studies reported, respectively, a cartilage E value of 1.3 MPa at the microscale (using an indenter with a 10 μm diameter) and a bimodal E distribution centred either around 22kPa (for GAG) or 384 kPa (for collagen) at the nanoscale (with a resolution of 187.5 nm) [7]. Lower E values were detected in the present work (where adopted force-displacement curves had an 833 nm resolution). These dissimilarities could be due to differences in experimental setups, adopted instrumentation, or approaches in E estimation as previously observed when diverse values of the same material properties were obtained through IT-AFM [17]. Notably, previously cited studies focused on cartilage surface while IT-AFM was here performed on the side of OCU biopsies. Further investigations are therefore necessary to clarify the reasons for the differences in properties observed between OC1 and OC3 samples and between values reported in the present study and previous works.

OC1 and OC3 areas were determined upon visual inspection of the cartilage surface. To confirm that the two experimental groups reflected effectively different pathological states a characterization of the samples

was done through histopathological scorings. These confirmed that OC1 and OC3 areas had well differentiated OA grades, but also that the selected non affected joint areas do not represent perfectly healthy samples (displaying initial signals of degradation).

Scorings based on histology are affected by a high variability and an intrinsic qualitative nature [29]. In an attempt to extract quantitative morphological parameters, samples' surface and tidemark roughness were calculated and cartilage, calcified cartilage, and subchondral bone plate thickness measured.

OC3 samples had significantly higher surface roughness and an overall lower cartilage thickness (due to superficial zone fibrillation or complete erosion). These observations reinforced the validity of the criteria adopted to select OC3 and OC1 areas.

Morphological changes in calcified cartilage were demonstrated to affect cross-talks, biomechanical forces distribution, and solutes transportation between hyaline non-calcified cartilage and subchondral bone [29]. Despite a clear separation of OC1 and OC3 samples in terms of surface degradation, limited differences were detected in the groups tidemark roughness in contrast with what previously reported [30]. Dissimilarities with respect to previous studies could be attributed to i) the high variability of probed section, thus simply requiring a larger donors cohort, to ii) the different anatomy considered (tibial plateau versus femoral condyles), or to iii) the OA grade adopted in previous studies where calcified cartilage exposure was associated with more evident morphological alterations. The absence of a difference between OC1 and OC3 tidemark roughness while alterations in mechanical properties of calcified cartilage were detected, could also indicate that microscale and compositional changes precede macroscale morphological alterations; additional analyses are required to prove this hypothesis, but the present study makes a case for the necessity of micro-nano scale investigations of macroscopic tissues properties.

Measuring the tissues thickness corroborated the hypothesis of OA being associated to an abnormal remodelling of subchondral bone. With respect to OC1 samples, OC3 samples had a thicker subchondral plate (as also reported in [1]), but a diminished (although in a non-statistically significant manner) thickness of calcified cartilage. Markedly OC3 samples often presented a doubling of the tidemark which is indicative of the calcified cartilage invading the upper cartilage layers. Given this observation a thinner calcified cartilage could indicate that the bone advancement into upper layer happens at a higher rate than calcified cartilage expansion [12].

Lastly, a dissection of the mechanical properties by layer was performed. Different studies adopted IT-AFM or nanoindentation for the determination of micro-nanoscale mechanical properties of cartilage and OCU tissues [7, 10, 14, 31]. OCU tissues connection and interdigitation makes however particularly cumbersome the analysis of calcified cartilage and subchondral bone [31] and investigation of OA related alterations was largely limited to the cartilage surface. Previous assessments of the mechanical properties of calcified cartilage for instance, required tissues freezing or embedding in polymetric matrices possibly

affecting their (micro) structural architecture [31]. Coupling of IT-AFM with a macroscale tissue visualization and precise indentation spots positioning allowed to operate with fresh and non-fixed samples, thus possibly avoiding processing-linked confounding factors.

IT-AFM measurements were correlated with samples GAG positivity. GAG depletion was associated to an increase in E values in cartilage middle zone and calcified cartilage, but not in cartilage deep zone. Although further investigations need to be performed, different adaptative mechanisms could be at the basis of detected modifications in the two tissues. A decreased GAG content has been correlated to cartilage stiffening due to a shift towards a collagen mediated mechanical response [7, 14]. Observed differences in cartilage middle layer could however also be due to modifications in ECM constituents, as OC3 GAG negative samples resulted positive for lubricin and COL10A1in cartilage middle zone. Moreover, OA samples were associated with a nanoscale cartilage stiffening due to collagen embrittlement [14]. Conversely, the increase of E in calcified cartilage could be correlated to a higher tissue mineralization [31]. Through backscattered electron microscopy, in which sample brightness is correlated to the mineral content, calcified cartilage mineral content was, in fact, estimated to be higher than the one in subchondral bone and reported to increase during OA progression [12].

An evaluation of the mechanical properties of the osteochondral unit was therefore performed distinguishing between the different unit tissues. It should however be highlighted that in order to preserve biopsies integrity, IT-AFM probing was performed from the biopsies side. Given collagen anisotropic distribution in the considered tissues [22], different outcomes could be achieved considering a top down approach.

Conclusively, in the proposed work it was demonstrated that coupling of macroscale morphological and compositional analyses with IT-AFM enabled a tissue specific determination of mechanical properties alterations correlated with the progression of OA.

The proposed methodology was furthermore translated to an *in vitro* Organ-on-Chip based model of cartilage, demonstrating its sensitivity to changes in mechanical properties related to deposition of a COL2A1 and aggrecan rich matrix. Overall, the experimental procedure served as a proof of concept for IT-AFM exploitation to determine the mechanical properties of native human tissues at a scale whose compositional and organizational structure could be recapitulated *in vitro.*

4.8 Final remarks

In this chapter a process flow for the measurements of the micrometre scale mechanical properties of the osteochondral unit was developed and combined with a compositional and morphological assessment of the alterations occurring in the native OCU tissues due to OA. The sample numerosity (n=15) was still limited, given the high variability observed between donors and the intrinsic wide range of degeneration grades found within the same OA joint. Moreover, a complete assessment of OA alterations would require measurements of healthy samples as control. Provided results demonstrated however that IT-AFM is a suitable technique to dissect how cartilage and calcified cartilage mechanical properties are affected by the disease, without inducing artifacts due to sample processing. Furthermore IT-AFM allows determination of properties at an organizational scale which is replicable in miniaturized *in vitro* models lacking, for instance collagen alignment of cartilage layers or bone trabecular structure. A direct assessment of the same alterations detected in native samples could, therefore, be performed in such *in vitro* disease models (e.g. the cartilage on chip described in Chapter 2) and the possible effect of putative therapies evaluated at a compositional level.

4.9 References

1. Goldring SR, Goldring MB (2016) Changes in the osteochondral unit during osteoarthritis: structure, function and cartilage–bone crosstalk. Nat Rev Rheumatol 12:632–644. https://doi.org/10.1038/nrrheum.2016.148
2. Sanchez-Adams J, Leddy HA, McNulty AL, et al (2014) The Mechanobiology of Articular Cartilage: Bearing the Burden of Osteoarthritis. Curr Rheumatol Rep 16:451. https://doi.org/10.1007/S11926-014-0451-6
3. Oláh T, Madry H (2018) The Osteochondral Unit: The Importance of the Underlying Subchondral Bone. Cartil Restor Pract Clin Appl Second Ed 13–22. https://doi.org/10.1007/978-3-319-77152-6_2
4. He Y, Li Z, Alexander PG, et al (2020) Pathogenesis of Osteoarthritis: Risk Factors, Regulatory Pathways in Chondrocytes, and Experimental Models. Biol 2020, Vol 9, Page 194 9:194. https://doi.org/10.3390/BIOLOGY9080194
5. Varady NH, Grodzinsky AJ (2016) Osteoarthritis year in review 2015: mechanics. Osteoarthr Cartil 24:27–35. https://doi.org/10.1016/J.JOCA.2015.08.018
6. Mow VC, Ratcliffe A, Robin Poole A (1992) Cartilage and diarthrodial joints as paradigms for hierarchical materials and structures. Biomaterials 13:67–97. https://doi.org/10.1016/0142-9612(92)90001-5
7. M L, D W, AU D, et al (2010) Micro- and nanomechanical analysis of articular cartilage by indentation-type atomic force microscopy: validation with a gel-microfiber composite. Biophys J 98:2731–2740. https://doi.org/10.1016/J.BPJ.2010.02.013
8. Oegema TR, Carpenter RJ, Hofmeister F, Thompson RC (1997) The interaction of the zone of calcified cartilage and subchondral bone in osteoarthritis. Microsc Res Tech 37:324–332. https://doi.org/10.1002/(SICI)1097-0029(19970515)37:4<324::AID-JEMT7>3.0.CO;2-K
9. Mente PL, Lewis JL (1994) Elastic modulus of calcified cartilage is an order of magnitude less than that of subchondral bone. J Orthop Res 12:637–647. https://doi.org/10.1002/JOR.1100120506
10. PK Z, XE G, CE H, et al (1999) Elastic modulus and hardness of cortical and trabecular bone lamellae measured by nanoindentation in the human femur. J Biomech 32:1005–1012. https://doi.org/10.1016/S0021-9290(99)00111-6
11. Peters AE, Akhtar R, Comerford EJ, Bates KT (2018) The effect of ageing and osteoarthritis on the mechanical properties of cartilage and bone in the human knee joint. Sci Rep 8:. https://doi.org/10.1038/S41598-018-24258-6
12. Burr DB (2004) Anatomy and physiology of the mineralized tissues: Role in the pathogenesis of osteoarthrosis. Osteoarthr Cartil 12:20–30. https://doi.org/10.1016/J.JOCA.2003.09.016
13. RU K, D K, A C, et al (2005) Altered cartilage mechanics and histology in knee osteoarthritis: relation to clinical assessment (ICRS Grade). Osteoarthr Cartil 13:958–963. https://doi.org/10.1016/J.JOCA.2005.06.008
14. Chen Y chun, Brown CP (2020) Embrittlement of collagen in early-stage human osteoarthritis. J Mech Behav Biomed Mater 104:103663. https://doi.org/10.1016/J.JMBBM.2020.103663
15. MD G, B A, I K, et al (1991) Subchondral bone in osteoarthritis. Calcif Tissue Int 49:20–26. https://doi.org/10.1007/BF02555898
16. Chen Y, Hu Y, Yu YE, et al (2018) Subchondral Trabecular Rod Loss and Plate Thickening in the Development of Osteoarthritis. J Bone Miner Res 33:316–327. https://doi.org/10.1002/jbmr.3313
17. Norman MDA, Ferreira SA, Jowett GM, et al (2021) Measuring the elastic modulus of soft culture surfaces and three-dimensional hydrogels using atomic force microscopy. Nat Protoc 2021 165 16:2418–2449. https://doi.org/10.1038/s41596-021-00495-4
18. M P, M L, CA M, et al (2012) The nanomechanical signature of breast cancer. Nat Nanotechnol 7:757–765. https://doi.org/10.1038/NNANO.2012.167
19. Occhetta P, Mainardi A, Votta E, et al (2019) Hyperphysiological compression of articular cartilage induces an osteoarthritic phenotype in a cartilage-on-a-chip model. Nat Biomed Eng. https://doi.org/10.1038/s41551-019-0406-3
20. Sader JE, Chon JWM, Mulvaney P (1999) Calibration of rectangular atomic force microscope cantilevers. Rev Sci Instrum 70:3967. https://doi.org/10.1063/1.1150021
21. Oliver WC, Pharr GM (1992) An improved technique for determining hardness and elastic modulus using load and displacement sensing indentation experiments
22. Baumann CA, Hinckel BB, Bozynski CC, Farr J (2019) Articular Cartilage: Structure and Restoration. Jt Preserv Knee A Clin Caseb 3–24. https://doi.org/10.1007/978-3-030-01491-9_1
23. KP P, S G, SA J, et al (2006) Osteoarthritis cartilage histopathology: grading and staging. Osteoarthr Cartil 14:13–29. https://doi.org/10.1016/J.JOCA.2005.07.014
24. Haeni DL, Lafosse T, Haggerty C, et al (2019) Tissue on the Transferred Coracoid Graft After Latarjet Procedure: Histological and Morphological Findings: https://doi.org/101177/0363546518819825 47:704–712. https://doi.org/10.1177/0363546518819825
25. Simkin PA (2012) Consider the Tidemark. J Rheumatol Rheumatol J March 39:890–892. https://doi.org/10.3899/jrheum.110942
26. Caron MMJ, Emans PJ, Coolsen MME, et al (2012) Redifferentiation of dedifferentiated human articular chondrocytes: comparison of 2D and 3D cultures. Osteoarthr Cartil 20:1170–1178. https://doi.org/10.1016/J.JOCA.2012.06.016
27. Yang KGA, Saris DBF, Geuze RE, et al (2006) Altered in vitro chondrogenic properties of chondrocytes harvested from unaffected cartilage in osteoarthritic joints. Osteoarthr Cartil 14:561–570. https://doi.org/10.1016/J.JOCA.2005.12.002
28. Leijten JCH, Bos SD, Landman EBM, et al (2013) GREM1, FRZB and DKK1 mRNA levels correlate with osteoarthritis and are regulated by osteoarthritis-associated factors. Arthritis Res Ther 15:R126
29. Kauppinen S, Karhula SS, Thevenot J, et al (2019) 3D morphometric analysis of calcified cartilage properties using micro-computed tomography. Osteoarthr Cartil 27:172–180. https://doi.org/10.1016/J.JOCA.2018.09.009
30. Wang F, Ying Z, Duan X, et al (2009) Histomorphometric analysis of adult articular calcified cartilage zone. J Struct Biol 168:359–365. https://doi.org/10.1016/J.JSB.2009.08.010
31. Ferguson VL, Bushby AJ, Boyde A (2003) Nanomechanical properties and mineral concentration in articular calcified cartilage and subchondral bone. J Anat 203:191–202. https://doi.org/10.1046/j.1469-7580.2003.00193.x

5 *Engineering of a microfluidic device for the mechanical stimulation of complex bi-layered 3 dimensional microtissues.*

The work described in this chapter was carried out in the framework of a collaboration between the Microfluidic and Biomimetic Microsystems Laboratory of Politecnico di Milano, (Milan, Italy) and the Tissue Engineering Laboratory of the University Hospital of Basel (Basel, Switzerland).

This chapter partially refers to:

Provision of discrete level of compression to complex bi-layered 3 dimensional cartilaginous constructs via a newly designed Vertical Capillary burst valve enables to recapitulate compression-dependent Osteoarthritic degradative and inflammatory phenotypes. Andrea Mainardi, Paola Occhetta, Martin Ehrbar, Philipp Oertle, Marko Loparik, Ivan Martin, Andrea Barbero & Marco Rasponi
Sci adv. (Under submission)

5.1 Introduction

In Chapter 2, a mechanically active cartilage on chip model was presented, demonstrating that elicitation of osteoarthritis (OA) reminiscent traits (e.g. increased inflammation, unbalanced catabolic and anabolic processes, and chondrocytes hypertrophy) could be obtained through the sole application of precise levels of hyper-physiological cyclic compression [1]. While cartilage breakdown is the most prominent disease feature, the entire osteochondral unit (OCU) is involved during OA pathogenesis. Timing and causal relationship of observed pathological alterations are, however, subjected to controversy [2] being still debated if the pathological process is initiated in cartilage, in hypertrophic cartilage, or in subchondral bone. *In vivo,* cartilage strain levels depend on the performed activity [3], its duration, the location within the body [4], and the specific cartilaginous layer depth. Cartilage strains were indeed demonstrated to vary deeply within tissue layers with an overall compression of -5% resulting in strain levels of -35% in the superficial zone, -5% in the transitional zone, and -1% in the deep zone [5]. Moreover, strain across the OCU varies deeply given its configuration as a series of mechanical springs with increasing stiffnesses. The estimated macroscopic Young's moduli of cartilage and subchondral bone differ of almost four orders of magnitude (0.8-1.3 MPa for cartilage [6, 7], 11-14 GPa for subchondral bone [8]) with calcified cartilage functioning as a transition zone [9]. As a result, during daily activities, cartilage upper layers are subjected to higher deformation levels whereas only minimal strains are experienced by subchondral layers.

Proper OCU modelling requires therefore devices capable of providing complex mechanical cues while simultaneously hosting multiple three-dimensional (3D) tissues in precise spatial configurations.

Organs-on-Chip (OoCs) devices are often made of hyperelastic rubber-like materials such as polydimethylsiloxane (PDMS) and to model 3D tissues rely on cell-laden hydrogels exhibiting elastic moduli in the range of a few kPa [10], orders of magnitude lower than the ones described for the OCU. Differences tissues layers strains cannot therefore be obtained modulating their mechanical properties at physiological levels.

Beside compression, the other key aspect of OCU modelling concerns the achievement of multiple interfaced tissues. By taking advantage of the increased relevance of surface forces at the microscale, microfluidic devices often use capillary burst valves (CBVs), i.e. channels' restrictions that allow the creation of a pinning interface [11], to engineer liquids routes in networks [12], to precisely control devices priming and emptying [13], or to confine polymerizing cell laden hydrogels one next to the other to obtain stratified tissues [14, 15]. Owing to the intrinsic difficulty of using photolithographic techniques to fully achieve 3D structures (the so called 2.5D configuration of photolithography), the use of CBVs has been limited to generate flanked microconstructs. As the OCU function depends on its different constituent being superimposed and aligned to the load direction, a step forward in OoCs design is needed in order to couple

the mechanical stimulation introduced in Chapter 2 with a vertical tissues disposition to achieve compartmentally defined, *in vivo* reminiscent strain levels in complex 3D constructs.

In the present chapter a new OoC platform enabling for the first time to provide well defined and discrete levels of mechanical compression to directly interfaced superimposed 3D microconstructs was presented. To achieve this aim, a new microfluidic concept (namely Vertical Capillary burst valve, VBV) was introduced, to enable the vertical superimposition of two 3D cell-laden hydrogels and the spatially precise modulation of the strain field experienced by the two tissues. Both a physiological tissue organization reminiscent of the OCU, and the application of defined and compartment dependent pathophysiological mechanical stimuli could be obtained. The device was validated demonstrating that different layers of cartilaginous constructs can effectively be subjected to various levels of compression resulting in distinct mechanotransduction signalling activations. The platform was then exploited to demonstrate that local perturbations in the composition of acellular subchondral layers modulate the load responses of cartilage-like micro-constructs.

5.2 Microfluidic Platform design and fabrication

5.2.1 Device concept: Vertical burst Valve (VBV) introduction and coupling with pneumatic actuation compartment

A new microfluidic concept was envisioned to vertically superimpose two directly interfaced micro-tissues. The concept was implemented in a microscale system capable of providing defined compression levels to the different layers of a complex bicompartmental 3D construct.

CBVs are strictions within microfluidic channels providing a pinning interface for a forward proceeding fluid front [11]. Classically, CBVs were designed to stop an advancing front from going further on, left or right. (Fig. 1a, left). Owing to the limited role played by volumetric forces (e.g. gravity) at the microscale, a basic concept was to flip by 90° such CBV configuration to obtain a Vertical capillary Burst Valve (VBV) designed for stopping an advancing fluid from moving upward or downward (Fig 1a, right).

Indeed, the integration of the methodology developed to provide 3D homogeneous constructs with well-defined confined compression levels [1] with this new VBV concept, would serve as a basis to obtain devices capable of providing more complex tissues with well-defined levels of cyclical confined compression. The resulting unified geometry, schematized in Fig. 1b, is constituted by a top cell culture chamber, a compression chamber, an unpatterned membrane, and an actuation chamber. The compression chamber consists in a central channel hosting a hydrogel or a cellular construct, separated by two rows of overhanging pillars from culture medium lateral channels. A gap is present between the pillars bottom surface and the chamber floor. Upon application of a positive pressure in the actuation chamber the unpatterned flexible membrane deflects upward until it reaches the bottom surface of the pillars. Appropriately dimensioning the dimensions of pillars and gaps it is possible for a precise compression level to be applied to the construct. Moreover, tailoring the design and the spacing of the pillars allows to finely control the cell laden hydrogel strain field in all dimensions. T shaped pillars with a width of 300 μm and with 30 μm spacings in between them were adopted to limit constructs lateral expansion upon compression [1]. Through the conceived VBV a methodology to superimpose a second hydrogel chamber, namely the top culture chamber, to this compression compartment was developed. (Fig. 1b) The VBV allows for two different cell-laden hydrogels, respectively in blue and red in Fig. 1b, to be injected in the top and compression chambers while maintaining a direct intra-tissue interface.

Notably, the hourglass shaped striction of the VBV provides also a separation interface between the compressive strain experienced by the hydrogel in the compression chamber (bottom construct, in red) and the one in the top culture chamber (top construct, in blue). As a result, while the bottom construct is subjected to a compression level dictated by the ratio between pillars and gap heights, the top construct

compressive strain is limited by the VBV structure and the geometry of the top culture chamber. The two constructs are therefore exposed to defined and discrete compression levels.

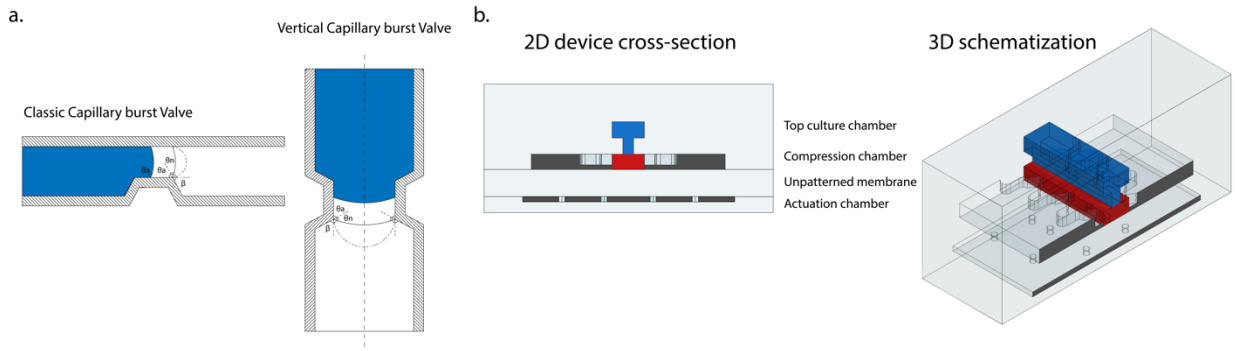

Figure 1: ***Vertical capillary Burst Valve (VBV) introduction and microscale system for the compression of directly interface double layered constructs: a****, Working principle schematization of the classic capillary burst valve and of the newly introduced vertical capillary burst valve. The walls of the channels are indicated by the etching. The advancing liquid is portrayed in blue. The advancing contact angle is indicated with θa, the angle change caused by the valve with β, and the contact angle that the advancing liquid interfaces assumes with the new wall after the striction with θn = θa – β. The interface required for the liquid to have a contact angle θa with the new interface and resuming advancement is indicated by the dashed line.* ***b****, Schematization of a device incorporating the VBV to obtain two-layer cellular constructs (depicted in red and blue respectively). Both a 2D cross section and a 3D schematization are reported highlighting how the VBV could be incorporated in a mechanically active device applying confined compression via an actuation chamber.*

5.2.2 Device fabrication procedure

Chambers were designed through a Computer Aided Design (CAD) Software (AutoCAD 2020, Autodesk). Master moulds were fabricated in a cleanroom environment (Class ISO6) using multilayer direct laser writing (Heidelberg MLA100) of SU-8 2035 or SU-8 2100 (MicroChem) onto 102 mm silicon wafer substrates. Microscale systems were realized in PDMS (Sylgard 184; Dow Corning), polymerized with defined casts at a 10:1 weight ratio of base to curing agent. All PDMS parts were cured for at least 2 hours at 65°C.

Classic photolithographic techniques do not allow the development of suspended structures, as those required for the realization of the VBV master moulds. Master moulds for the replica moulding of PDMS devices are obtained by the selective sequential polymerization of photo curable resists (e.g. SU-8) layers, normally preventing the realization of structures that are narrow at the base and larger at the top. Techniques for the development of simple closed SU-8 channels and suspended structures had however been introduced based on a fine control of the exposure dose during the fabrication process [16] so that polymerization happens exclusively in a portion of the photoresist thickness. An effort at obtaining both pillar-based compression chamber and top culture chamber (together with simpler VBV example structures) from a monolithic SU-8 structure on a silicon master mould was therefore attempted. The envisioned SU-8 structure, realized through multi-layer photolithography, is visible in Fig. 2a. While the simple VBV

structure could be achieved, exposure intensity modulation did not allow the realization of more complex structures, resulting, for instance, in un-shapely pillars due to photoresist overexposure (Fig. 2b). The preliminary version of the device with a united top culture chamber and compression chamber layer was therefore discarded due to poor quality of achieved geometrical features.

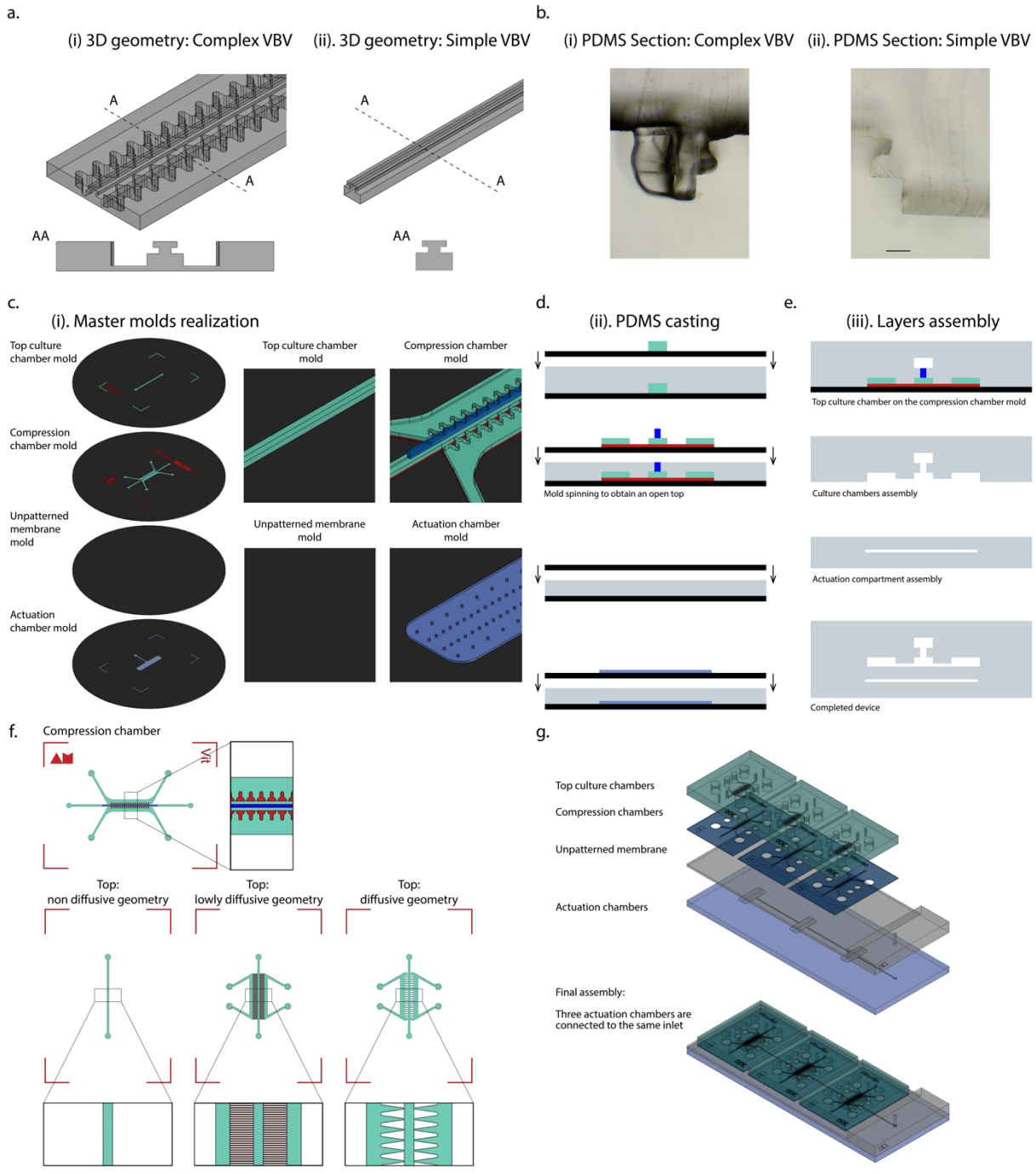

Figure 2; ***Device realization procedure: a, b,*** *Assessment of the feasibility of realizing the desired geometry starting from a monolithic master mould.* ***a,*** *Master mould structures schematization: 3d representations and sections (AA) of the constructions.*

Geometries were realized in SU-8 on Silicon wafers through direct laser writing multi-layer photolithography. The VBV structure was obtained modulating the exposure energy so that only partial polymerization of the last layer could be achieved. ***b****, PDMS sections of the devices obtained by replica moulding of the monolithic master moulds depicted in a. Left, complete structure with VBV geometry and compression chamber pillars; right, simple VBV. Scale bar 100 µm. Obtainment of a monolithic master mould comprehensive of top culture chamber and compression chamber would lead to a diminished number of operations during the fabrication process and reduce the risk of misalignment between the two chambers. While a VBV like structure could be achieved in a simpler setup (a, b right), geometrical aberrations appeared when complex structures comprehensive of the compression chamber pillars beside the VBV geometry were introduced (a, b left).* ***c, d, e*** *Multi-layer VBV mechanically active device production steps schematization. The different required phases, namely master moulds production (c), PDMS casting (d) and layers production and assembly (e) are indicated. In c selected master moulds particulars are depicted.* ***f,*** *Schematization of the compression chamber layout and of the three possible versions of the top chamber that were introduced. From left to right the layouts of a top chamber with a non-diffusive geometry constituted by a simple channel, a lowly diffusive geometry where the central channel is connected with lateral media channels exclusively by narrow channels (10 µm width, 50 µm height, 50 µm separation between the channels), and a diffusive geometry where channels are separated by pillar shaped structures (300 µm large at the channel level) with a distance of 30 µm between them.* ***g,*** *3D schematization of the final device. 3 different actuation chambers were connected to the same actuation inlet. The different layers and the assemble device are depicted.*

A methodology based on the realization of multiple PDMS layers was then introduced. The final realization procedure required four master moulds (Fig. 2c) corresponding nominally to top culture chamber, compression chamber, unpatterned membrane, and actuation chamber.

Features in the compression chamber had a cross section of 1800 µm (width) x 293 µm (height).

The VBV structure was realized producing the compression chamber mould through as a sequence of three SU-8 layers: gap (height:43 µm, represented in red in Fig. 2c), pillars (height 100 µm, green) and narrowing (height 150 µm, blue) layers. The latter representing the restriction of the VBV. Magnifications of selected features in the master moulds are depicted in Fig. 2c. Heights were tailored to obtain a 30% compression value for the cellular construct hosted in the compression chamber. Overall, the compression chamber is constituted by the central hydrogel chamber (300 µm in width) separated by the two rows of overhanging pillars from the lateral culture medium channels. Pillars in the compression chamber layer, positioned 30 µm apart, were designed with a T cross section, each arm of the shape being 300 µm long and 100 µm wide. The T tails facing the culture medium channels were rounded to avoid air entrapment during the media filling phase. Pillars extremities were tapered to obtain a wider contact angle and better confine the hydrogel formulation in the central channel during injection.

The actuation chamber was designed as a rectangular compartment with a cross section of 3397 µm (width) x 50 µm (height), connected to an inlet. Six rows of round pillars (diameter 28 µm) were introduced in the chamber to prevent it from collapsing.

PDMS structures were obtained by replica moulding of the master moulds. Unpatterned membranes were obtained dosing defined quantities of PDMS into a Petry dish (Sigma Aldrich; 100 mm x 15 mm polystyrene Petri dishes) containing a clean silicon wafer so to obtain a final thickness of 800 µm. This thickness was demonstrated to allow for the actuation pressure (i.e. the pressure necessary to obtain contact between the membrane and the compression chambers pillars bottom surface) to depend exclusively on the bending stiffness of the membrane itself, thus preventing the effective compression level achieved during culture to vary as a result of tissues maturation[1].

Top culture chamber and actuation chamber were realized pouring PDMS on master moulds to get heights of roughly 3 mm and 1.5 mm respectively. PDMS stamps were then detached from master moulds, cut, and appropriate holes bored for hydrogel inlets (diameter 1mm), culture medium reservoirs (diameter 4 mm) and actuation tubing inlet (diameter 1.5 mm).

The compression chamber layer was realized pouring a small quantity of PDMS (4 ml Ca.) on the master mould and then spinning the master itself so that a thin PDMS layer would cover everything but the top surface of the narrowing layer (Fig. 2d). An optimization procedure was carried out to find the optimal spinning velocity which consisted in a 5 second ramp to 500 rpm held for 15 seconds followed by 30 seconds at 230 rpm.

The device layers were bonded treating surfaces to be united with air plasma (Harrick plasma) and bringing them in conformal contact for at least 30 min at 80°C to achieve irreversible adhesion.

PDMS replicas of the top culture chamber were bonded directly on the thin compression chamber spinned PDMS layer, and the top chamber-compression chamber assembly detached from the mould together (Fig. 2e). Appropriate holes for hydrogel inlets and outlets and culture medium reservoirs were bored through both layers. The assembly was united with unpatterned membrane and actuation chamber, bonded together in a previous moment (Fig. 2e), and the whole device assembled.

The introduced modular fabrication approach based on the achievement of the final device through assembly of multiple PDMS layers allowed for different top culture chambers to be coupled with the compression chamber. Specifically, culture media channels were also introduced in the top chamber layer, to differently condition the two superimposed constructs with biochemical cues. The adopted layouts are represented in Fig. 2f, namely non diffusive geometry (NDG), lowly diffusive geometry (LDG), and diffusive geometry (DG). Final features had a nominal height of 150 μm, while the width depended on the design version. While the NDG is simply constituted by the hydrogel hosting channel, LDG and DG comprise two lateral culture medium channels, connected to the central cell compartment respectively by narrow channels (10 μm wide, 50 μm tall, 50 μm apart), or by apertures (30 μm wide, 150 μm tall, 300 μm apart) standing between triangular shaped pillars. Both channelled walls and pillars were designed to completely cover the space occupied by culture medium channels in the compression compartment. Schematics of the different features are reported in Fig. 2f. All versions of the top culture chamber were realized with a central gel width of 300 μm, 400 μm, and 500 μm.

After an initial single actuation chamber version device (Fig. 2c) the actuation chamber layer was designed so that three actuation chambers could be connected with the same actuation inlet (Fig. 2g). A sketch of the final version of the device depicting both the different layers and the assembled device is reported in Fig. 2g. A thick PDMS slab was bonded to the unpatterned membrane and a hole (1.5 mm) bored through both layers in correspondence of the actuation inlet of the actuation chamber layer. The increased thickness

provided by the slab was required to assure retention of the tube providing pressure during mechanical actuation.

Details of the geometries adopted for the three versions of the top culture chamber are reported in Fig. 3.

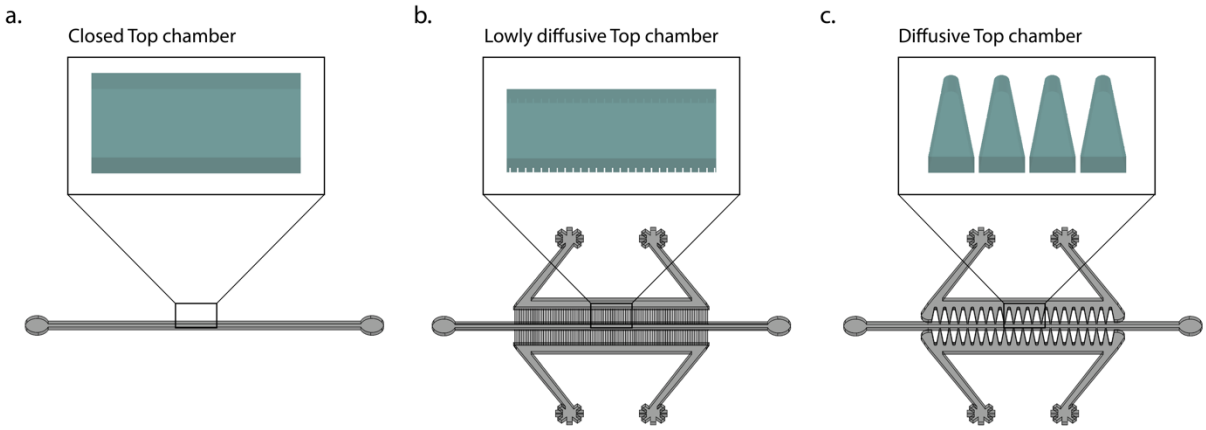

Figure 3: ***Schematization of the different geometries realized for the top culture chamber layer****. From left to right: Closed* ***(a)****, Lowly diffusive* ***(b),*** *and Diffusive top chamber* ***(c)*** *layouts. All chambers were realized with a total height of 150 µm. In the closed chamber the top layer is simply constituted by a straight channel hosting a hydrogel, no culture medium channels are present. In the lowly diffusive layout, a series of narrow channels (width 10 µm, height 50 µm, inter channel space 50 µm) allows diffusion of media and differentiating factors from two lateral channels but the walls are contentive enough so that it is possible to inject a second cell laden hydrogel later on during the culture despite the PDMS lost its hydrophobicity as a result of the exposure to the incubator humidity. In the Diffusive layout triangular pillar structures with a base of 300 µm are set 30 µm apart. The pillars cross section was made longer so that they would cover the whole medium channels of the compression chamber underneath in order to provide better support to the compression chamber layer during bonding and easing the peeling off from the master mould.*

5.3 VBV geometrical and functional validation

A functional validation of the device was performed assessing the accuracy of the fabrication process, the functioning of the VBV-mediated double injection procedure, and the feasibility of controlling compounds diffusion kinetics between top culture chamber and compression chamber by appropriately designing the geometry of the former.

5.3.1 Device geometrical characterization and production feasibility determination

A picture of an assembled device (LDG) is reported in Fig. 4a. Achievement of the desired micro-structured geometrical configuration was first evaluated by sectioning the device in correspondence of the VBV. A device cross section can be appreciated in Fig. 4b, clearly identifying the channel hourglass-like striction characterizing the VBV and demonstrating the efficacy of the production process.

Thin PDMS sections (1-2mm thick) were cut with a razorblade and observed through a brightfield microscope connected to a digital camera (AmScope MU500), geometrical features dimensions of the devices were measured from acquired images.

Assembled top culture chambers and compression chambers layers were moreover imaged through Scanning Electron Microscopy (SEM). PDMS devices were coat-sputtered with a few nanometres of gold. Images were acquired with a SEM (LEO 1525 Field Emission Scanning Electron Microscope) adopting an Electron High Voltage (EHV) of 10.00 kV (Fig. 4c). In SEM images the 43µm gap between the T-shaped compression chamber pillars and the VBV geometry is appreciable (Fig. 4c), together with a general view of designed geometric features of both top culture chamber (DG) and compression chamber.

Given the necessity of aligning the top chamber and the compression chamber for each device, an assessment of the alignment process precision was performed.

To optimize the top culture chamber - compression chamber alignment procedure, devices with a top chamber central channel width of 300 µm, 400 µm, and 500 µm were assembled with compression chambers featuring 300 µm wide central channels. Top view images of the assembled devices were acquired to assess the precision of the alignment procedure. While a wider top chamber central channel allows an easier centring on the compression chamber one, it decreases the relative portion of interfaced surface between the two constructs.

The alignment success was determined calculating the overlapping area defined as the area in between the two innermost pillars rows. Layers central channel areas were calculated from the distance between pillar rows of the same layer. A schematization of perfectly and non-perfectly aligned chambers is depicted in Fog. 4d. The percentage of overlapping area of each layer was calculated as:

$$Overlapping\ area\ ratio\% = \frac{Overlapping\ area}{Total\ layer\ area} * 100$$

The product of the overlapping area ratio percentages of the two layers was adopted to evaluate which configuration maximized the production success. Image analysis was performed using Image J. Examples of aligned devices are reported in Fig. 4e.

Surfaces interface values resulted respectively, 82% ± 8 %, 75% ± 11% and 77 % ± 6% for the 300 µm, 400 µm, or 500 µm top culture chambers, being statistically significantly higher in the narrower device version (Fig. 4f). The smaller top chamber central channel width (i.e. 300 µm) was therefore adopted in the final design, maximizing the portion of interfaced surfaces without affecting the alignment precision.

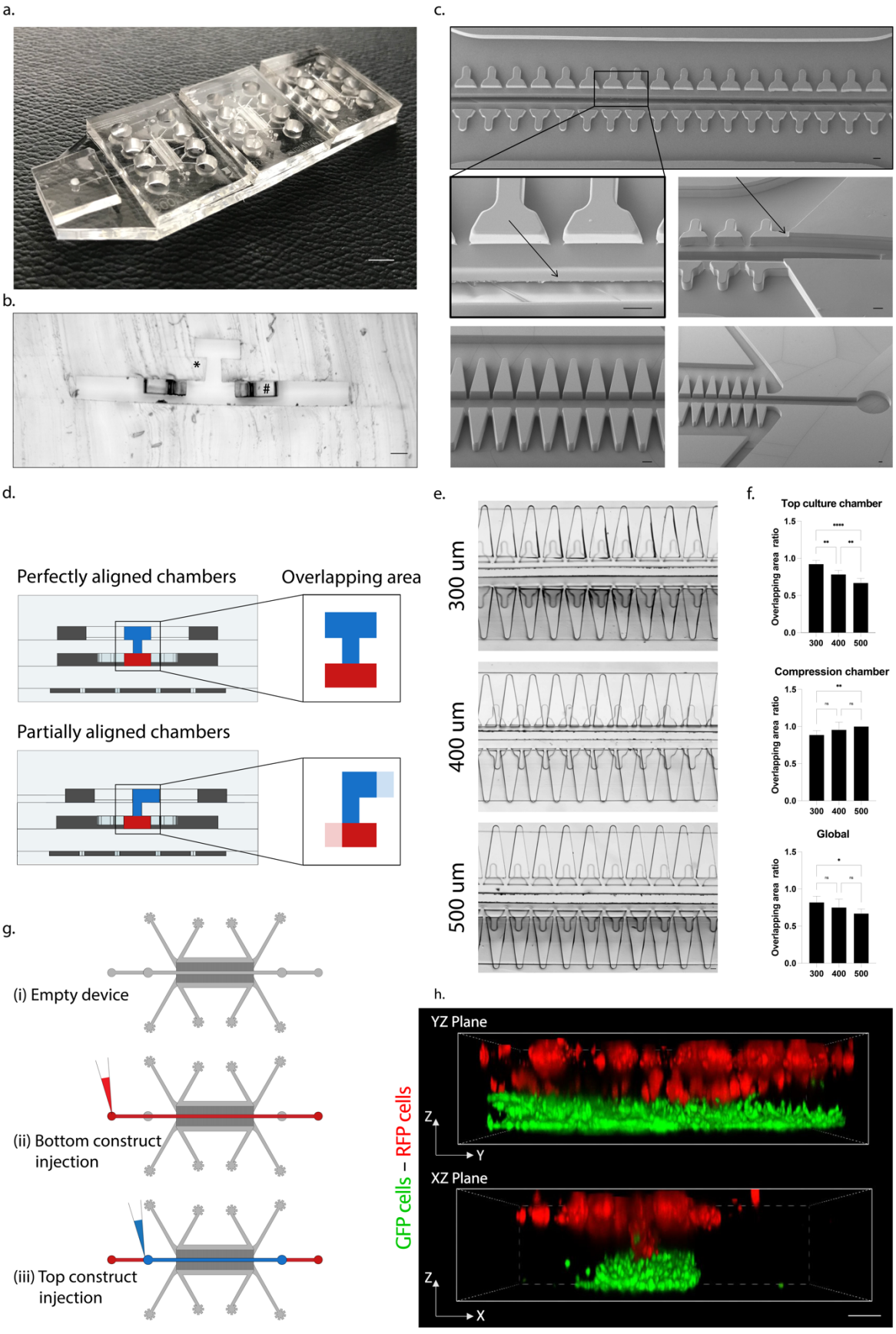
a.
b.
c.
d.
Perfectly aligned chambers
Overlapping area
Partially aligned chambers
e.
300 um
400 um
500 um
f.
Top culture chamber
Compression chamber
Global
Overlapping area ratio
300 400 500
g.
(i) Empty device
(ii) Bottom construct injection
(iii) Top construct injection
h.
YZ Plane
XZ Plane
GFP cells – RFP cells

Figure 4: ***VBV realization feasibility and functional validation****. **a**. Photograph of a completed PDMS device. Scale bar = 4 mm **b**, cross section of a device. The two chambers, the suspended pillars rows and the VBV geometry, respectively indicated by (#) and (*), are clearly visible and highly reminiscent of the ideal geometry. Scale bar = 100 µm. **c**, Scanning Electron Microscopy (SEM) images of the device observed from the compression chamber. The T geometry of the pillars is appreciable. Black arrows point to the restriction of the VBV structure (left) and to the gap present below the pillars (right). In the last row images of the DG are reported as examples of the top culture chamber. Scale bar = 100 mm. **d, e, f,** Determination of the top chamber's alignment precision. **d**, Schematization of a perfect alignment and that of partially aligned chambers. The aligned area in the top chamber (blue) and in the bottom chamber (red) is depicted in both cases. Non overlapping areas are depicted in a fainter color. **e**, Three device versions were realized with the central gel channel in the top culture chamber of 300 µm, 400 µm, and 500 µm respectively (while the compression chamber gel channel remained of 300 µm) to determine if a wider top channel was necessary to achieve overlapping of top and compression chambers. Scale bar 100 µm. **f**, Determination of the ratio of the overlapping area with respect to the chamber area calculated as the percentage of one chamber aligned with the other one divided by the total area of the chamber. The Global ratio was calculated as the product of the ratios of top culture chamber and compression chamber. n=6 devices for each version were considered. Populations' normality was assumed if both Shapiro-Wilk and Kolmogorov-Smirnov tests resulted positive. Ordinary One-Way Anova with Tukey's multiple comparison test was adopted for normal populations; Kruskal-Wallis test with Dunn's multiple comparison test was adopted for non-normal populations. *P<0.05, **P<0.001, ****P<0.0001, ns statistically non-significant. **g**, Device injection principle. Given the VBV geometry, starting from an empty device, the user can simply inject the first hydrogel in the compression chamber (bottom construct), wait the appropriate time for complete polymerization, and inject the second hydrogel in the top culture chamber (top construct). The order of injection can also be inverted. **h,** Demonstration of the functioning of the VBV concept. A confocal microscopy reconstruction of cell laden constructs seeded in the proposed device is represented. Green fluorescent protein (GFP) labelled chondrocytes are depicted in green, Red Fluorescent Protein (RFP) labelled Human Umbilical Vein Endothelial Cells (HUVECs) are represented in red. The direct contact between the two tissues can be observed in the middle of the construct both in the YZ and in the XZ planes. Scale bar = 100 µm.*

5.3.2 VBV functional validation

A complex biphasic construct can be achieved sequentially injecting two different cell-laden hydrogels in the two superimposed compartments of the VBV. Complete polymerization of the first hydrogel needs to be achieved before injection of the second one. A schematization of the injection procedure is depicted in Fig. 4g. An assessment of such VBV functioning was carried out by seeding RFP human umbilical vein endothelial cells (HUVECs) and GFP human articular chondrocytes (hACs) embedded in an enzymatically cross-linkable and degradable polyethyleneglycole (PEG) based hydrogel [17] in the top culture chamber and in the compression chambers, respectively. Both hydrogel formulations could successfully be injected in the device. In Fig. 4h a confocal microscopy reconstruction of the two chambers seeded with RFP HUVECs and GFP hACs shows the cells distribution, highlighting how there is direct contact between the two constructs both in the ZY and in the ZX planes (Fig. 4h). Successful injection of both hydrogels could be achieved in ~90% of cases (injection in n= 60 devices was considered in the assessment).

5.3.3 Actuation pressure determination

The pressure required to achieve the defined compression level of 30% in the compression chamber was determined as previously described [1, 18]. Briefly, the actuation chamber was slowly filled with PBS applying a mild continuous positive pressure (i.e. 0.2 Atm) until all air bubbles were removed.
Subsequently, top and compression chambers were filled with blue dye, both the central channel and lateral medium channels. As a result of the blue dye filling the gap between the pillars in the compression chamber and the unpatterned membrane, these (the pillars) appear blue at atmospheric pressure. Increasing the

pressure in the actuation chamber and causing the membrane to deflect upward reduces the gap space until the membrane abuts against the pillars' bottom surface leading them to appear as white. A correlation between the mean grey intensity measured in correspondence of the pillars and the provided pressure could be established. The actuation pressure, i.e. the pressure necessary for the membrane to touch the pillars, was defined as the pressure at the beginning of the plateau in the Mean Grey intensity vs pressure curve and found to be 0.4 Atm as highlighted in Fig. 5a. At least three chambers were considered for each version of the device. For each chamber the Mean Grey intensity of three different pillars was measured and results averaged. Images were analysed with ImageJ. Devices representative images at different pressure levels are reported in Fig. 5b.

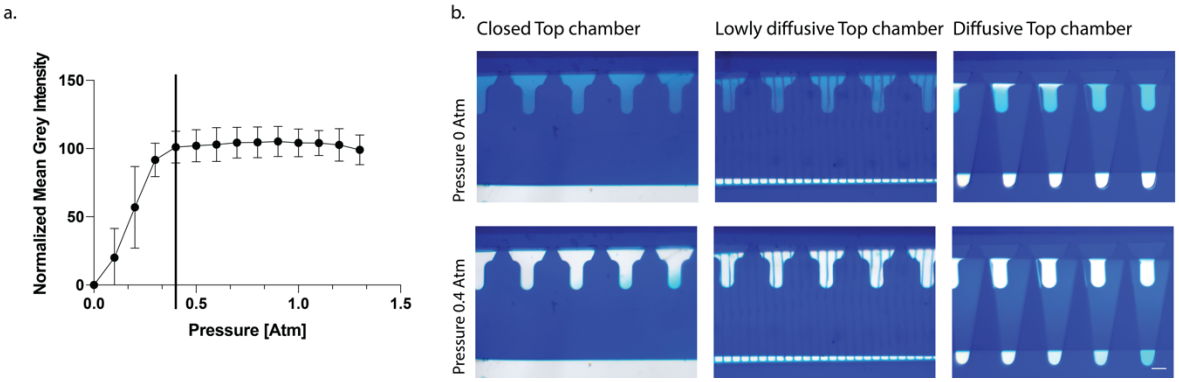

Figure 5: ***Determination of the actuation pressure. a****, Normalized Mean Grey Intensity versus the pressure in the actuation chamber. The actuation pressure, defined as the pressure necessary to achieve contact between the top surface of the actuation membrane and the bottom surface of the pillars in the compression chamber, was determine with a previously described methodology* [1]*. Briefly, the compression chamber, both the hydrogel channel and the culture medium channels, was filled with a blue coloured dye. Pillars in the compression chamber (T shaped) appear blue as a result of the colour filling the gap between pillars and membrane. When the membrane bends upward as a result of the increased pressure in the actuation chamber, the gap narrows and the Mean Grey Intensity increases, that is to say the pillars start appearing whiter. Once contact is reached a further increase in pressure does not correspond anymore to an increase in Mean Grey Intensity and a plateau is reached.* ***b****, Examples of top view images of the three version of the device. Scale bar 100 µm.*

5.3.4 Diffusion kinetics determination

While sustainment of a constant concentration gradient between top and bottom compartments would require the application of fluid flow, this would drastically increase the operational complexity of the device. To validate the feasibility of differently conditioning the two compartments even in the absence of such a fluid flow, the diffusion kinetic of solutes between the compression chamber and the top culture chamber was assessed in static conditions.

Primary human articular chondrocytes (hACs) were incorporated into an enzymatically cross-linkable and degradable PEG-based hydrogel matrix and injected into devices, both in the top and compression compartments, as described in section 5.3. Hydrogels with a final dry mass content of 2% were prepared by stoichiometrically balanced ([Lys]/ [Gln] = 1) precursor solutions of 8-PEG-Gln and 8-PEG-

MMPsensitive-Lys in Tris buffer (50 mM; pH 7.6) containing 50 mM calcium chloride, leaving open a spare volume of 12.5% v/v for the addition of cell culture medium with hACs [17].

The diffusion assay was performed either on the same day of chondrocytes seeding (i.e. Day 0) or after static maturation in chondrogenic medium (37 °C, 5% CO_2) for 14 days (i.e. Day 14), performed as described in section 5.3, demonstrated to be sufficient for the deposition of a cartilage like matrix in microfluidic devices [1].

LDG top chambers and DG top chambers only were considered given the absence of media reservoirs connected to the top chamber in the NDG configuration. A solution of 1 mg/ml of fluorescent dextran with a molecular weight of 20 KDa (FITC-Dextran, Sigma Aldrich) in culture medium was injected in the medium reservoirs of the compression chamber, while pure culture medium was added to the top culture chamber. A qualitative assessment of the diffusion was achieved through direct fluorescent observation of the devices. Fluorescent images were acquired with a widefield microscope (Nikon, Eclipse Ti2) after 1, 3, 5, 10, 30, and 60 minutes while devices remained incubated in a humidified chamber at 37 °C and with 5% CO_2. Two devices for each configuration and for each experimental timepoint (i.e. day 0 and day 14) were considered. Quantitative measurements of the diffused dextran quantity were performed measuring the dextran concentration in the top culture chamber reservoirs at different time points through a quantification of the fluorescent intensity. Each reservoir was filled with 60 µl of either 1mg/ml of dextran solution (compression chamber) or with plain culture medium (top chamber). At each time point, i.e. after 1, 3, 5, 10, 30, 60, 120, and 720 minutes a total of 10 µl was retrieved from the top culture reservoirs. Immediately after each withdrawal 5 µl of dextran solution were added to the compression chamber reservoirs and 5 µl of plain medium to the top culture chamber. Devices were kept in a cell culture incubator in between withdrawals. A calibration curve with known dextran concentration was introduced. Fluorescent intensity (emission wavelength 520 nm, excitation wavelength 480 nm) was measured trough a configurable multimode microplate reader (synergy H1, BioTek instruments). Three devices for each version of the top culture chamber were considered for each experimental timepoint.

Representative images of FITC dextran diffusion after 10 mins and 60 mins are depicted in Fig. 6a, both for DG and LDG configurations, at Day 0 and at Day 14. The limited inter-compartments diffusion after 14 days with adoption of the LDG can be observed in Fig. 6a, where it is visible how the top chamber lateral channels remained almost FITC dextran free after 60 mins of diffusion time.

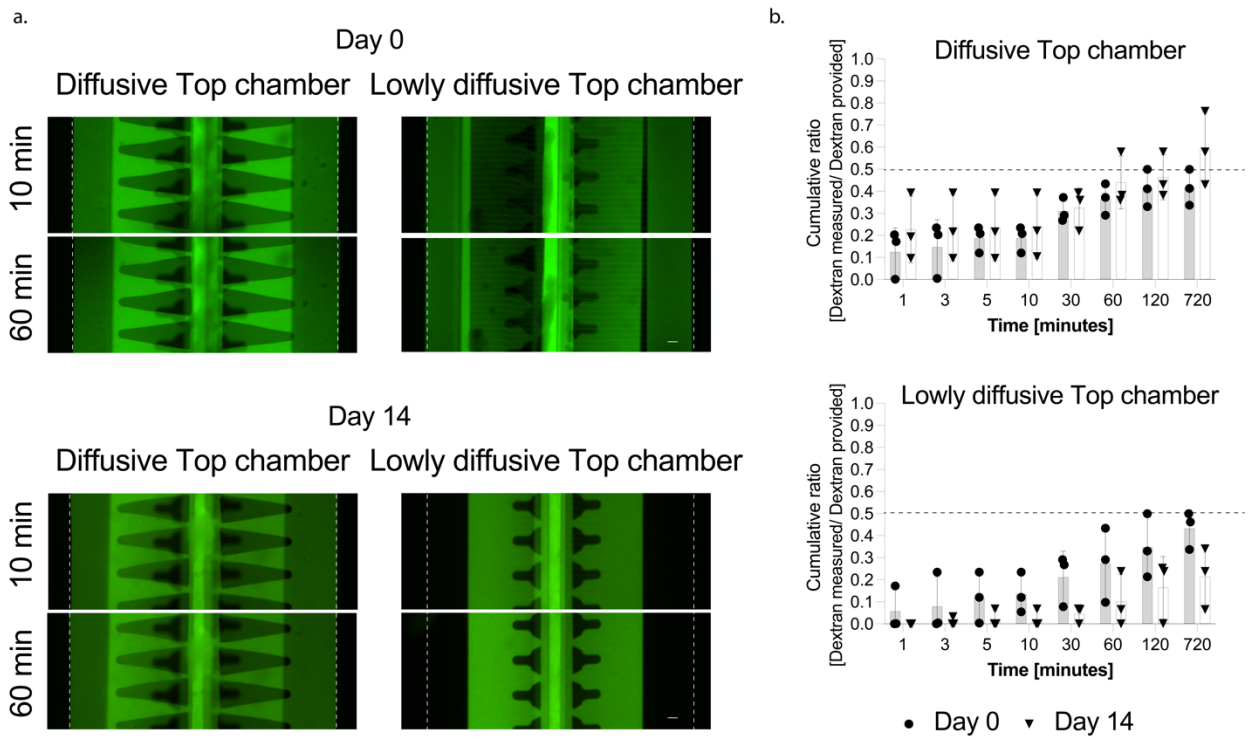

Figure 6: ***Diffusion kinetic determination. a,*** *Top view widefield microscope fluorescent images of the devices at different time points and after either 0 or 14 days of culture. The dashed line indicated the outer limit of the top culture chamber. Very limited dextran diffuses from the bottom to the top compartment was visible at Day 14 in the LDG configuration. Scale bar = 100 µm.* ***b,*** *Quantification of the diffusion rate of 20 KDa FITC dextran between the compression chamber and the top chamber in the case of top chambers with a DG (top) and a LDG (bottom). Both central chambers were seeded with hACs in a PEG based hydrogel. The diffusion kinetic was assessed at Day 0 and Day 14 of static culture in chondrogenic medium.*

As concern the diffusion quantification, dextran concentration in time was expressed as the cumulative ratio between the dextran injected in the compression chamber and the quantity measured in the top chamber at selected time point. Adoption of the DG favoured fast diffusion of the molecule and resulted in cumulative ratios, after 60 mins, of 0.37 ± 0.07 and 0.44 ± 0.121, respectively, at Day 0 and at Day 14, with no difference introduced by construct maturation. Conversely, a slower diffusion was registered in the LDG, when coupled with mature constructs. Cumulative ratios after 60 mins resulted of 0.27 ± 0.17 and 0.1 ±0.12 for Day 0 and Day 14, respectively (Fig. 6b). Remarkably, in this latter case the ratio remained low (i.e. 0.21 ± 0.14) even after 12 hours. Taken together these data demonstrate how the adoption of the LDG configuration for the top culture chamber, combined with a low cartilaginous construct permeability reached after a 14 days maturation period, allow limited inter-compartments diffusion of molecules with a molecular weight in the range of common growth factors [19, 20]. This suggests the possibility of adopting the device to study the direct effect of a given compound on one of the constructs and the indirect possible crosstalk effects on the other provided a transient exposure is sufficient for the stimulation.

5.4 Cartilage on chip model recapitulation

Before assessment of the effect of cyclic compression on the complex bilayer construct the achievement of cartilaginous like microtissues on chip was assessed culturing hACs under chondrogenic differentiative conditions for 14 days. A PEG based hydrogel formulation was adopted to encase hACs upon injection in microfluidic devices.

5.4.1 PEG precursor production and PEG hydrogel preparation.

PEG hydrogels were produced as previously described [21]. 1 ml FXIII (200 U ml−1; Fibrogammin; CSL Behring) was activated with 100 µl thrombin (20 U ml^{-1}; Sigma–Aldrich) for 30 min at 37 °C and the resulting activated FXIII (FXIIIa) was stored in small aliquots at −80 °C. Eight-arm PEG vinylsulfone (molecular weight: 40 kDa; NOF Europe) was functionalized with peptides that contained either an FXIII glutamine acceptor substrate (Gln peptides; NQEQVSPL-ERCG-NH2; Bachem) or an MMP-degradable FXIII lysine donor substrate (Lys-MMPsensitive peptides; Ac-FKGGGPQGIWGQ-ERCG-NH2; Bachem), resulting in 8-PEG-Gln or 8-PEG-MMPsensitive-Lys precursors, respectively. A stoichiometrically balanced solution of 8-PEG-Gln and 8-PEG-MMPsensitive-Lys was mixed for an indicated final dry mass content of hydrogel precursors in Tris buffer (50 mM Tris (pH 7.6) and 50 mM calcium chloride, leaving a spare volume of 12.5% v/v for the addition of cell culture medium and cells. The hydrogel cross-linking was initiated by adding 10 U ml^{-1} FXIIIa and vigorous mixing. Adopted Hydrogels had a final concentration of 2% PEG precursors and contained cells at a 50 x 106 cells ml^{-1} density.

5.4.2 Healthy human chondrocytes samples collection, cell isolation and expansion.

Cartilage material from a total of 6 patients (age: 60 ± 12, 4 males, 2 females) with no clinical history of OA and without evident signs of cartilage fibrillation upon inspection was collected after informed consent from the relatives and in accordance with the local ethical committee (University hospital Basel). Cartilage pieces were minced and digested enzymatically to isolate cells as previously described [22].

Briefly, hACs were isolated using a solution of 0.15% type II collagenase (10 ml solution g^{-1} tissue; 300 U mg^{-1}; Worthington Biochemical Corporation) for 22 h and resuspended in Dulbecco's modified Eagle's medium (DMEM) containing, 4.5 mg ml^{-1} d-glucose, 0.1 mM non-essential amino acids, 1 mM sodium pyruvate, 100 mM HEPES buffer, 100 U ml^{-1} penicillin, 100 µg ml^{-1} streptomycin, 0.29 mg ml^{-1} l-glutamine and 10% foetal bovine serum (complete medium).

Isolated chondrocytes were counted using Trypan blue, plated in culture flasks at a density of 10^4 cells/cm^2 and expanded in complete medium supplemented with 1 ng ml^{-1} of transforming growth factor-β1 (TGF-

β1) and 5 ng ml^{-1} of fibroblast growth factor-2 in a humidified, 37 °C-5% CO_2 incubator. Added factors were previously demonstrated to increase chondrocytes proliferation in plate and foster re-differentiation even in the presence of dedifferentiation during 2D cell culture. After approximately 10 days 80% of confluency was reached. First passaged cells were rinsed with Phosphate Buffered Saline (PBS) and detached using Trypsin–ethylenediaminetetraacetic acid (EDTA; Gibco) and re-plated at 7 x 10^3 cells cm^{-2}. Upon reaching 80% of confluency cells were detached once more. Passage 3 cells were used to generate cartilage microconstructs on chip as described below.

5.4.3 Cartilage microconstructs generation on chip.

A proof of concept biological validation of the device was performed to assess the feasibility of obtaining a model of healthy cartilage on chip (CoC) as previously done in a simpler configuration [1]. The DG was adopted in this phase.

Cartilage microconstructs generation was achieved embedding expanded hACs into an enzymatically cross-linkable and degradable PEG based hydrogel [23] with a final dry mass content of 2% prepared as described above. Subsequent injections of the same cell-laden hydrogel were realized in the compression and top culture chambers.

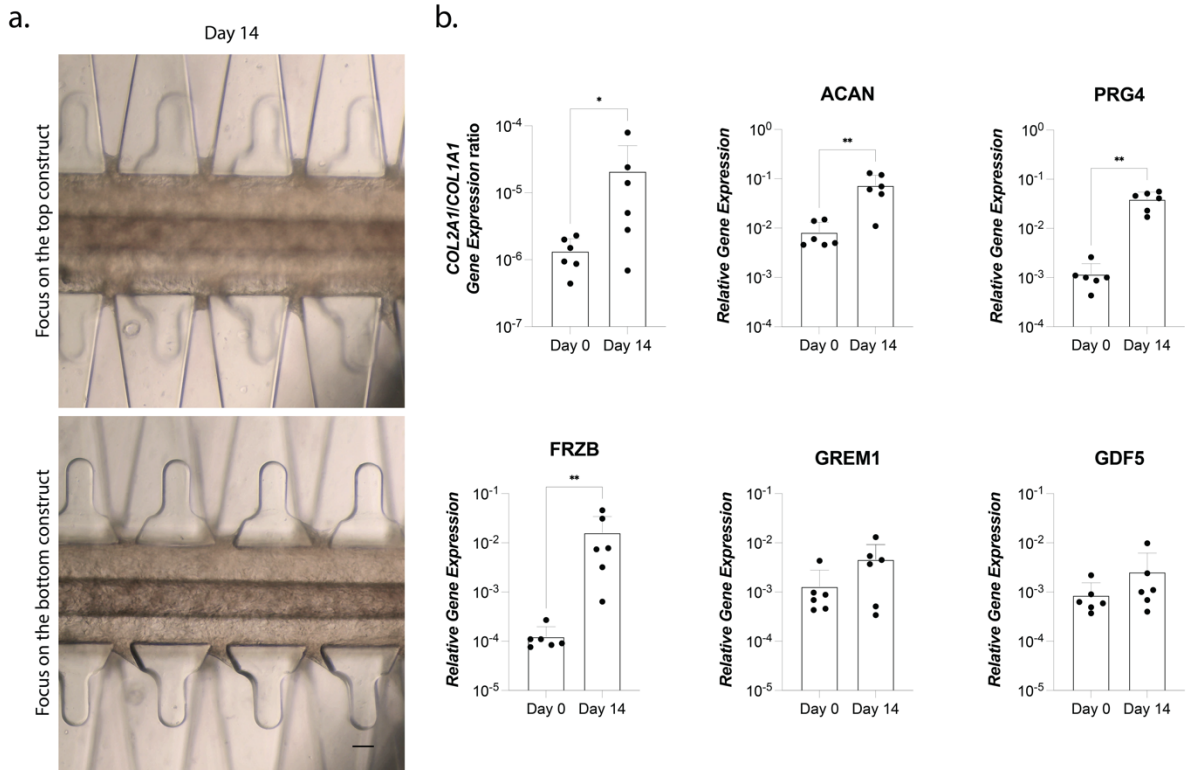

Figure 7: ***Cartilaginous constructs maturation on chip****.* ***a****, Brightfield pictures of hACs statically cultured in devices for 14 days. After 2 weeks of culture cells are still confined in the central channels. Similar results were obtained with more than 60 devices. Scale bar 100 µm.* ***b****, Gene expression quantification through RT-qPCR. N=6 biologically independdent samples from n=2 donors were considered for each time point. Populations' normality was assumed if both Shapiro-Wilk and Kolmogorov-Smirnov tests*

*resulted positive. Statistics by two tailed t-test for normal populations and Mann-Whitney test for non-Gaussian ones. * P<0.05, **P<0.01.*

Specifically, the polymer precursor solution was mixed with hACs so that a final density of $5x10^4$ cells ml^{-2} could be obtained. The cell-polymer precursor solution was then mixed with 10 U ml^{-1} of thrombin activated factor FXIIIa, mixed vigorously, and immediately manually injected into microscale devices and incubated for 10 minutes (37°C, 5% CO_2). The procedure was repeated for the gel in the second compartment. Notably, it was feasible to inject both the top cell culture chamber and the compression chamber channels first, demonstrating the robustness of the VBV functioning. After 10 minutes of incubation of the second cell laden hydrogel, chondrogenic medium was injected into the dedicated channels. A chondrogenic medium constituted by DMEM (Sigma–Aldrich) containing, 4.5 mg ml^{-1} d-glucose, 0.1 mM non-essential amino acids, 1 mM sodium pyruvate, 100 mM HEPES buffer,100 U ml^{-1} penicillin, 100 μg ml^{-1} streptomycin, 0.29 mg ml^{-1} l-glutamine, 1.0 mg/ml bovine insulin, 0.55 mg/ml human transferrin, 0.5 μg/ml sodium selenite, 50 mg/ml bovine serum albumin, 470 μg/ml linoleic acid, and 1.25 % of human serum albumin and supplemented with 0.1 mM ascorbic acid 2-phosphate, 10^{-4} mM Dexamethasone, and 10 ng ml^{-1} TGF-β3 previously demonstrated to induce the re-differentiation of de-differentiated chondrocytes [24] was adopted during the chondrogenic culture. Culture medium was changed every 2 days. Samples were cultured in static regimen for 14 days previously demonstrated to be sufficient for achievement of cartilage on chip constructs [1]. Notably, after 14 days of static culture constructs were still confined in the central gel chamber of both layers (Fig. 7a). At the end of the culture period the cartilaginous features of the resulting microconstructs were assessed by quantitative reverse-transcription PCR (RT-qPCR) as described in section 5.7. Results are depicted in Fig. 7b. A statistically significant increase was registered in the chondrogenic index *COL2A1/COL1A1* mRNA ratio, as well as in the cartilage-specific genes aggrecan (*ACAN*) and lubricin (*PRG4*) at day 14 with respect to day 0. Moreover, as previously observed [1], hACs cultured in the new device exhibited a statistically significant increase in the expression of wingless-type MMTV integration site (Wnt) antagonist frizzled-related protein (*FRZB*), and upwards trends in that of bone morphogenic protein (BMP) antagonist gremlin-1 (*GREM1*), and *GDF5,* thus demonstrating the assumption a molecular signature reminiscent of that found in native chondrocytes.

5.5 Device provided strain field evaluation: VBV combination with a pneumatic compartment allows compartment specific compression levels to be applied to complex bi-layer constructs on chip.

The proposed device was conceived to provide well defined and discrete compression levels to the two superimposed constructs obtained through the VBV. The strain field in the two constructs was estimated through a finite element (FE) model. A preliminary model setup was introduced to evaluate the strain field adopting the three device's geometries introduced (i.e. NDG, LDG, and DG). An estimate of the strain distribution varying the mechanical properties of the gel in the two compartments was performed on a computational level. Finally, the effective elastic modulus of cartilaginous constructs after 14 days of maturation was determined through indentation type atomic force microscopy (IT-AFM) and adopted in the evaluation of the strain distribution in the top cell culture chamber and in the compression chamber upon compression.

5.5.1 Finite Element analysis.

Considering the largely non-linear and strain rate dependent behaviour characterizing hydrogels and cartilage ([25, 26]), a biphasic poroelastic (BPE) constitutive model was introduced to describe both the PEG gel and cellular cartilaginous constructs. Adoption of a BPE constitutive behaviour to describe cartilage-like constructs and hydrogels was previously demonstrated to underestimate reaction forces upon compression, but allows accurate prediction of the deformation [27, 28] and was thus adopted in the description of the strain field in the two constructs. The constitutive description adopted is based on a homogeneous continuous constituted by an elastic solid phase and an incompressible inviscid liquid phase. Consequently, the BPE description accounts for the strain and time dependent behaviour resulting from the phases interaction but neglects the intrinsic viscoelasticity of the solid phase. Notably, moreover, eventual inhomogeneities present in the construct are not captured in the model which assumes uniform properties throughout the control volume.

FE analyses were introduced to (i) confirm the application of two defined average strain levels in the constructs hosted in the top and compression chambers with low dependence on the properties of the constructs themselves, (ii) evaluate the strain field in the different versions of the device, and (iii) determine the effective strain field applied when compressing two chondrocyte-based constructs.

Given the geometric repeatability of the channels, a minimal repetitive unit volume was highlighted and adopted in the simulations to reduce the computational cost. The considered region is highlighted in Fig. 8a. Briefly, the unit of volume was constituted by the PDMS region corresponding to two facing T shaped compression chamber pillars and the corresponding PDMS areas above, together with the portion of constructs hosted in the middle

The hydrogel/construct volume was divided in two regions to simulate the presence of different materials filling the top and compression chambers as highlighted by the blue and red colour depicted in Fig. 8a. The PDMS region was comprehensive of the two pillars in the compression chamber, the PDMS layer dividing the chambers, and two pillars (or the alternative geometric versions) of the top chamber. All three version of the device introduced in this work were simulated. Symmetry boundary conditions were adopted to further reduce this unit to half of a pillar and a quarter of the hydrogel area (as indicated by the shaded area in Fig. 8a) introducing cinematic boundary conditions representing the status of symmetry. The thickness of the gel and the represented portion of the PDMS structure along Y were 165 μm thus accounting for half a pillar and half of the hydrogel regions between posts (nominally 30 μm in total). The total height of the PDMS portion was 400 μm and given by 100 μm of the pillar, 150 μm of the connection region and 150 μm of the top chamber. The hydrogel region was divided as follows: the bottom compartment (height 143 μm) and the medium and top compartment (height 150 μm + 150 μm respectively). The Edges of the PDMS structures were rounded with a 9 μm curvature radius in conformity to measurements performed on physical devices.

Abaqus 6.14 (Abaqus FEA: Dassault systems), formerly established to be adequate in the biomechanical description of biphasic tissues [27], was adopted to perform computations.

The PDMS region was represented using either twenty-node quadratic elements with hybrid formulation (C3D20H elements: Abaqus) or ten-node quadratic modified tetrahedral elements with hybrid formulation (C3D10MH elements: Abaqus). Hydrogels were meshed using eight-node linear hexahedral elements with hybrid formulation and trilinear pore pressure (C3D8PH elements: Abaqus) required for porous materials. Characteristic dimensions of the elements varied across the hydrogel volumes with smaller elements adopted in the lower part of the bottom construct/hydrogel which is subjected to higher strain levels. PDMS region's elements dimension varied accordingly, depending on the dimension of the hydrogel elements at the interface. Different plane views of the adopted geometry and mesh are depicted in Fig. 8b. A mesh sensitivity analysis was conducted to assure consistency of the solutions. (Fig 8c). The ratios between the dimensions of the elements in the different areas were kept constant varying the total number of elements. A final total number of 51282 element was adopted for the hydrogel region. Elements with an average characteristic dimension of 12 μm, 5 μm, and 3 μm were adopted in the different regions of the hydrogel volumes. The total number of elements adopted to describe the PDMS constructs depended on the particular geometry. 29809 elements were adopted in the non-diffusive top chamber configuration, 32930 elements were used in the lowly diffusive top chamber configuration, and 29502 elements were adopted for the diffusive top chamber configuration.

Hard contact between hydrogels and PDMS was modelled assuming tangential perfect lubrication. Interactions were modelled using a surface-to-surface contact. The top surface of the PDMS compartment

was fixed modelling its continuity with the thick PDMS overlaying portion. In the case of the non-diffusive top geometry the outermost lateral part of the PDMS region was also fixed simulating continuity with the lateral walls

Displacements along the Z directions were impeded on the top surface of the hydrogel compartment simulating the presence of the PDMS ceiling. A zero pore pressure was assumed on the hydrogel lateral portions initially not in contact with the PDMS to allow fluid outflow.

PDMS was described as a non-linear elastic material adopting Mooney-Rivlin strain energy function equation:

$$W = C_1(I_1 - 3) + C_2(I_2 - 3) + \frac{1}{D}(J - 1)^2$$

Where I1 and I2 are the first and second invariant of the right Cauchy-Green strain tensor C, J is the determinant of the deformation gradient tensor F representing the ratio between the deformed and initial volumes of the object and C1, C2, and D are the constitutive parameters of the model. C1, and C2, were assumed respectively equal to 254 kPa and 146 kPa, as reported in the literature for PDMS with a 10:1 base to curing agent ratio [29]. D was set equal to zero assuming a perfectly incompressible material.

As introduced, the hydrogel or cell laden constructs were described with a BPE constitutive behaviour. Poisson's ratio was fixed at 0.33 (as previously reported for similar materials [30]) the specific weight of the permeating fluid at 9.956 x 10^{-6} Nmm^{-3} [25] . The description of a BPE model in Abaqus makes use of the specific material permeability defined as $K_s = \gamma_w k$, where γ_w is the permeating fluid specific weight and k is the absolute permeability. Ks was set to 3x10^{-4} mm s^{-1} as previously done for similar hydrogel formulations [25]. The initial void ratio e=dVw / dVg where dVw is the volume of the fluid phase and dVg is the volume of the solid phase was set to different values according to the different simulated materials. An initial value of 45 was adopted modelling the PEG-based hydrogel formulation used in this work with an estimated dry mass of 2%. Subsequently, the void ratio was assumed equal to 7.5 for mature cartilaginous construct accounting for the presence of both hydrogel initial dry mass and cellular volume fraction [31]. Complete fluid saturation was assumed in all occasions.

The Young modulus (E) of both the 2% PEG hydrogel only and of mature cartilaginous constructs were estimated through IT-AFM indentation as briefly described in section 5.4.2 and previously detailed in Chapter 4. 2% PEG based hydrogel Young modulus (E) was set equal to 1.9 kPa, , as measured by IT-AFM, and consistently with estimates based on rheological data [23, 32]. The E of cartilaginous constructs was set to 3.66 kPa.

The Abaqus solid consolidation option was adopted to perform a transient analysis implementing an automatic Δt incrementation with a minimum time increment of 10^{-8} s and a maximum pore pressure incrementation allowed for time increment of 10^{-5} MPa. The volumetric strain compatibility tolerance for hybrid elements was set to 10^{-4}. Compression was applied imposing a 43 μm vertical displacement of the hydrogel bottom surface mimicking the deflection imposed by the membrane in the physical device. Displacement was ramped in a timeframe of 0.5 s accounting for the 1 Hz frequency adopted with a 50% duty cycle in cyclical mechanical stimulation during experiments.

The strain field was evaluated through the nominal strain components actin in the X, Y, and Z direction and calculated according to Abaqus definition as:

$$\varepsilon^N = V - I = \sum_{i=1}^{3} (\lambda_i - 1) n_i n_i^T$$

Where $V = \sqrt{FF^T}$ is the left stretch tensor (F being the deviatoric deformation gradient), λ_i are the principal stretches and n_i are the principal stretch directions in the current configuration.

Mean nominal strains in the different compartments, namely bottom and top, were calculated averaging the elements strains calculated in the centroid. The top compartment was considered comprehensive of the connection region as highlighted in Fig. 8a. To compensate the bias introduced by the usage of higher mesh densities in certain model regions, mean strains were calculated separately for each of the areas with different mesh dimensions and averaged subsequently weighting for the volumetric fraction of the areas.

An initial assessment was performed considering both compartments as filled only with the 2% PEG gel (E=1.9 kPa). Given the introduction of the three different geometries for the top culture chamber, the strain field was evaluated in all cases and results compared. Fig. 8d, e, and f show the adopted model geometries, contour plots of the nominal strains in the principal directions xx, yy, zz (i.e. NE11, NE22, and NE33 respectively), and NE mean values divided per chamber (i.e. top culture and compression chambers), in the three cases. All geometries allowed homogeneous strain levels distribution in the compartments' volumes, exhibiting at the same time very limited longitudinal and lateral expansion in response to the imposed compression. Lateral expansion peaks appeared exclusively in the narrow areas between the T shaped pillars in the compression chamber and between the pillars of the top compartment in the DG configuration. Specifically, in the top constructs NE11 resulted to be 0.2% ± 1.0%, 0.2% ± 1.1%, and 0.8% ± 2.6% for the NDG, LDG and DG respectively while the correspondent NE11 values in the bottom construct resulted to be 1.1% ± 5.7%, 1.1% ± 5.7%, and 1.1% ± 5.8%. Analogously, NE22 in the top constructs was equal to 0.0% ± 0.0, -0.0% ± 0.1%, and-0.0% ± 1.2% in the NDG, LDG and DG, while respective NE22 values in the bottom construct resulted -0.0% ± 1.9%, -0.0% ± 1.9%, and -0.0% ± 1.9%. NE33 in the top constructs

resulted respectively of -2.5% ± 1.6%, -2.5% ± 1.6%, and -2.6% ± 1.6% in the NDG, LDG and DG while NE33 values in the bottom construct were equal to -25.7% ± 6.4%, -25.7% ± 6.4%, and -25.5% ± 6.7%. In all three cases, well distinct NE33 values were therefore registered for bottom and top constructs demonstrating the achievement of defined and different mechanical stimuli.

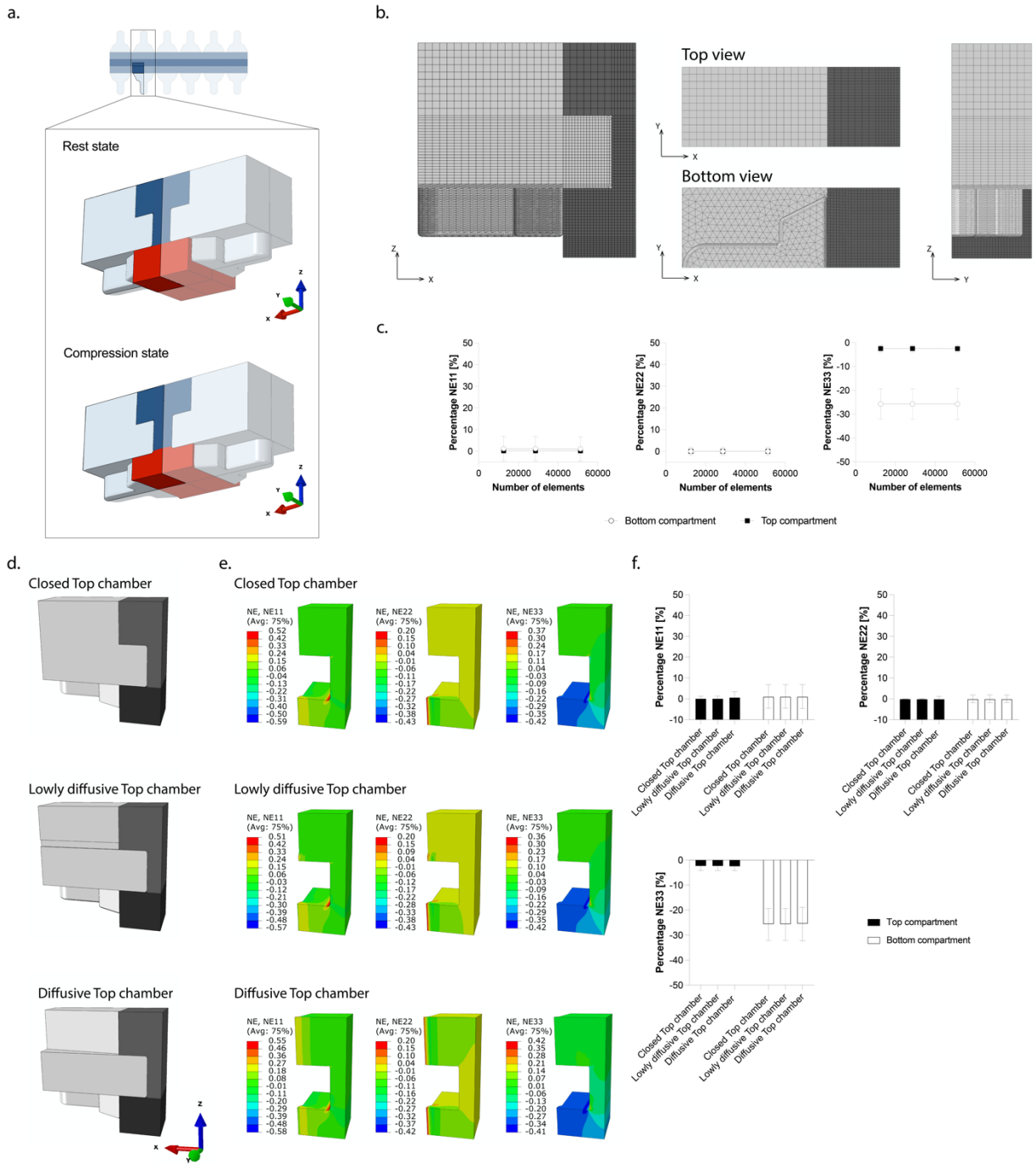

Figure 8: ***Compartments strain field evaluation****. **a**, Schematization of the geometry adopted for FE simulation. A top view of the construct is represented at the top; the black rectangle encircles the minimal repetitive unit element. The shaded area represents the region of interest (ROI) adopted in simulations. Boundary conditions were adopted to reduce the minimal repetitive unit to the*

selected ROI. Both Rest state and compressed state are represented. The gel filling the top compartment is represented in blue, the one in the compression compartment in red. ***b****, Geometry adopted in computations, views from orthogonal planes. The adopted element mesh is represented.* ***c****, Mesh sensitivity analysis. The nominal strain along the principal directions, NE11, NE22 and NE33 was evaluated in the top (comprehensive of middle area) and bottom compartments as a function of the constructs' elements number. FE models of devices with all three top chamber configurations, namely closed top chamber, lowly diffusive top chamber and diffusive top chamber were realized. The complete geometries adopted in computations are visible in* ***d****. Contour plots of the nominal strains in the principal directions in the three cases are reported in* ***e****. No noticeable differences could be detected in the strain field exception for an increased lateral expansion in the top compartment in the diffusive top chamber configuration.* ***f****, Mean NE11, NE22, and NE33 in the different geometrical configurations. Values, extrapolated from the elements' centroids are reported as mean ± s.d.*

5.5.2 Indentation Type Atomic Force Microscopy mediated estimation of hydrogels and cartilaginous constructs elastic moduli

IT-AFM was adopted to determine the local Young Modulus, E, of cartilaginous constructs matured in microfluidic devices and that of the 2% PEG hydrogel adopted to encapsulate chondrocytes. After 14 days of static maturation, or immediately after hydrogel injection in the device and polymerization for PEG only measurements, devices actuation chamber and un-patterned membrane (Fig. 1g) were carefully peeled off to expose the constructs. Devices were cut with a razor blade to minimize the presence of excessive PDMS and glued onto a plastic culture dish (Sigma-Aldrich, 30mm diameter), with the exposed cellular construct facing upward. Two components epoxy resin (Araldite Rapid, Huntsman corporation) mixed with black dye to increase image contrast was adopted for sample fixation. Measurements were performed at room temperature in degassed PBS.

IT-AFM was carried out, as described in Chapter 4, with a noise-isolated TRIX device (ARTIDIS, Basel, Switzerland). Four-sided pyramidal tips (205-mm-long DNP-S10 triangular silicon nitride cantilevers, resonance frequency (air) f = 18 kHz, nominal cantilever spring constant k = 0.06 Nm-1, tip radius = 20 nm) were employed. The exact spring constant of each adopted cantilever was determined through the thermal tune method [33]. Deflection sensitivity was determined directly on the dish as previously reported [7]. IT-AFM measurements were done at room temperature recording up to 22 different 20 × 20 μm force–volume maps over 20 × 20 points grids (400 force–displacement curves per map). Individual force curves were collected at velocity of 16 μm/s. The maximum applied loading force was set to 1.8 nN.

Force displacement curves were corrected for tilt and tip-sample displacement as previously documented [7, 34].

Both Forward and Backward force-displacement (F-D) curves were recorded. Backward curves were adopted to extract average samples Young modulus adopted in FE simulations making use of the Oliver-Pharr model [35] to determine E values, as indicated to be suitable for hydrogels and soft materials.[10] An elastic modulus histogram was derived for each experimental group (Fig. 9a) and mean and standard deviation calculated.

As depicted in Fig. 9a the average E for 2% PEG gel only was 1.9 ± 0.53 kPa. Modulus histograms in mature constructs showed both an upward shift in the distribution centre and a wider values range attesting the deposition a cellular secreted matrix. After 14 days of static culture, areas with different mechanical properties were indeed registered along the constructs (Fig. 9b). An average E of 3.66 ± 4.16 kPa was determined for cartilaginous microconstructs and such average value adopted in the subsequent estimation of the effective strain field in the two chambers.

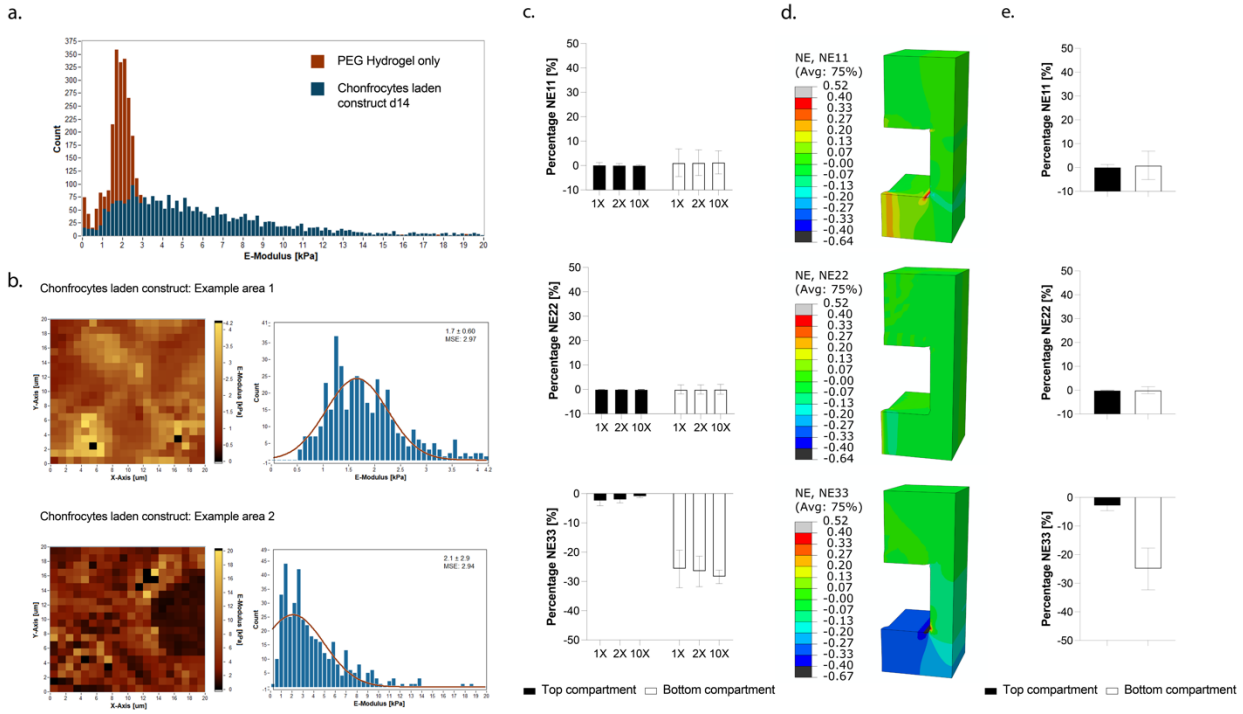

Figure 9: ***PEG gel and cartilaginous constructs modulus evaluation and compartment strain field determination****.* ***a,*** *CoC and 2% PEG hydrogels mechanical properties as determined by IT-AFM. Overall elastic modulus histograms refer to PEG hydrogels only (in red) or to hydrogels laden with hACs cultured statically for 14 days within microfluidic devices. (n= 3 biologically independent samples from 1 donor were measured for constructs, 3 independent samples were measured for PEG hydrogels only).* ***b,*** *Mature cartilaginous constructs properties varied along constructs depending on the indentation sites. Two indentation maps referring to different locations are reported as an example.* ***c,*** *Percentage strains along the principal direction X, Y, and Z, respectively NE11, NE22, and NE33, as a function of the top compartment Young's modulus. 1X, 2X, and 3X, refer to the modulus adopted for the hydrogel in the top compartment with respect to the one of the bottom compartment i.e. 1.9 KPa. The construct volume in correspondence of the VBV striction was considered as part of the top constructs in calculations.* ***d, e,*** *Strain deformation field in the principal directions. Strain distribution is reported as NE values along the principal directions. Lateral and longitudinal expansions are limited by the device geometry. A clear difference in the compression levels (i.e. NE33) in the top and bottom compartment is visible from the contour plots as well as from the mean values reported in f. Both top and bottom compartments were considered as filled with cartilaginous constructs. A young modulus of 3.66. kPa was adopted in simulations.*

5.5.3 Mature constructs strain field assessment and strains dependency on material properties

A conceptual experiment was performed to demonstrate the robustness of the designed device with respect to variations in the elastic modulus of the hosted hydrogels/constructs. The NDG configuration was employed. Constructs with a modulus of 1X, 2X and 10X with respect to the E of the 2% PEG gel in the compression chamber (i.e. 1.9 kPa, as detected by AFM indentation) were considered to be present in the

top culture chamber and the strain in both compartments was evaluated. Results are visible in Fig. 9c. Top and bottom constructs mean nominal strains in the Z direction (i.e. NE33) resulted respectively, equal to -2.5% ± 1.6% and -25.7% ± 6.4%, -2.1% ± 1.1% and -26.6% ± 5.2%, and -0.98% ± 0.36% and -28.4% ± 2.3%, respectively when the top construct had a Young's modulus E equal to 1X, 2X or 10X that of the bottom construct.

A more refined assessment of the strain field of mature cartilaginous constructs was performed using the LDG configuration and introducing the E value (i.e. 3.66 kPa) previously estimated by IT-AFM. As visible from the contour plot of NE11, NE22 and NE33 (Fig. 9d), the constructs assumed homogeneous and close to null strains in the X and Y directions and well-defined compression levels depending on the location in the Z direction. Specifically, the mean NE33 resulted equal to -2.9% ± 1.6% and -25% ± 7% in the top and bottom constructs, respectively (Fig. 9e).

Overall, these data indicate the achievement of defined and discrete compression levels in the two constructs, together with minimal lateral and longitudinal expansion. The platform was moreover capable of finely control the overall strain field with a minimal dependency on the constructs' properties determining its employability in a wide range of settings.

5.6 Effect of the discrete compression levels applied to cartilaginous constructs on mechanotransduction activation and assumption of a degradative inflammatory phenotype

Mature cartilaginous constructs were subjected to cyclic mechanical compression. The activation of a mechanotransduction signalling network and the assumption of a degradative and inflammatory signature was evaluated differentiating between top and bottom constructs.

5.6.1 Transduction of green fluorescent protein (GFP) in chondrocytes to sort constructs populations after culture

A GFP positive hACs population was developed to be able to dissect the compression effect on top and bottom constructs separating the respective cell populations after the culture.

GFP+ chondrocytes were obtained through lentiviral transduction. A previously introduced protocol demonstrated not to affect chondrocytes differentiation capacity was adopted [36]. Briefly, first passage hACs were seeded in Petri dishes (Sigma Aldrich; 60 mm x 15 mm polystyrene Petri dishes) at a density of 10^4 chondrocytes/cm^2 and transduced the following day with 2.8 x 10^6 transducing units (TU) of GFP lentivirus (Multiplicity of Infection, MOI, of 5) in presence of 5µg/ml of protamine sulphate. Cells were cultured for approximately 3 days post transduction before detachment and sorting. GFP+ cells were

selected through FACS (BD FACSAria III Cell sorter) (the gating strategy is reported in Fig. 10a), subsequently re-passaged, and used at passage 3.

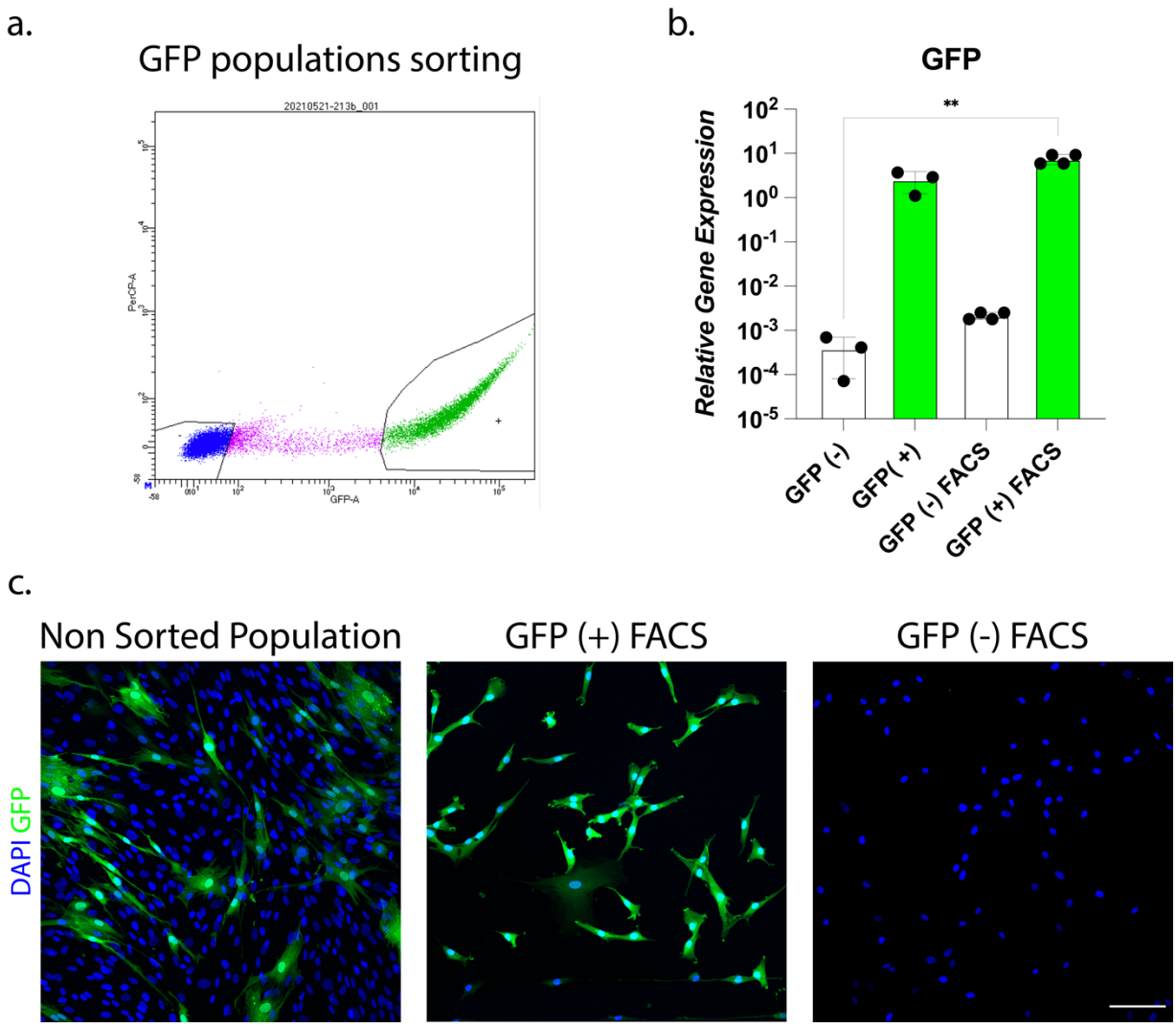

Figure 10: ***Compartments populations separation based on GFP expression: procedure efficacy****.* ***a****, example of populations selection during sorting.* ***b****, GFP gene expression quantification by RT-qPCR. Gene expression was normalized for GAPDH, values are log scaled. The pure populations i.e. populations which were never in contact are indicated as GFP (+) and GFP (-), populations sorted after culture and constructs enzymatic digestion are indicated as GFP (-) FACS and GFP (+) FACS. At least n=3 independent constructs, from n=1 donor for each population were considered for each condition. Populations' normality was assumed if both Shapiro-Wilk and Kolmogorov-Smirnov tests resulted positive. Kruskal-Wallis test with Dunn's multiple comparison test was adopted for non-normal populations. **P>0.001.* ***c****, Examples of cellular populations obtained after constructs digestion demonstrating successful population separation based on GFP. At least n=3 independent constructs, from n=1 donor for each population were considered for each condition. Constructs were digested and FACS sorted (or not) and cells plated in 2D on an IBIDI 8 well µ-plate. Cells were left to adhere for 48 hours then fixed and imaged. DAPI is represented in blue, GFP in green. Scale bar 100 µm.*

The feasibility of analyzing top and bottom constructs populations separately was assessed.

GFP transduced chondrocytes (i.e. GFP + hACs) were injected in one of the compartments and normal hACs in the remaining one (e.g. GFP+ hACs in the top compartment and GFP- in the bottom one). The

LDG configuration was adopted in this phase. Constructs were cultured statically for 3 weeks in chondrogenic medium as previously described.

At the end of the culture period constructs were digested enzymatically. Briefly, constructs were extracted from devices and incubated on an orbital shaker for 1 hour in a solution of 0.15% type II collagenase (Worthington Biochemical Corporation) in DMEM, 300 µl per construct. Cells were then centrifuged, rinsed in a solution of 1mM EDTA and 2% v/v FBS in PBS, incubated for five minutes in 0.05% trypsin/0.53 mM EDTA (37°C 5% CO2), washed twice in 1mM EDTA, 2% v/v FBS in PBS and held in ice prior to sorting. GFP positive and negative cellular populations were sorted (BD FACSAria III Cell sorter) and analysed performing RT-qPCR, as described in section 5.7, on separated populations. An example of populations selection during sorting is reported in Fig. 10a. RT-qPCR for GFP was performed on the sorted populations and on single GFP+ and non GFP starting populations as controls confirming the success of the sorting procedure (Fig. 10b). Sorted populations were also replated in 2D (IBIDI µ/slide 8 well) and left to adhere for 48 hours in DMEM containing 10% foetal bovine serum, 4.5 mg ml^{-1} d-glucose, 0.1 mM non-essential amino acids, 1 mM sodium pyruvate, 100 mM HEPES buffer, 100 U ml^{-1} penicillin, 100 µg ml^{-1} streptomycin and 0.29 mg ml^{-1} l-glutamine (complete medium). Non sorted population were used as controls. After 48 h samples were rinsed with PBS and fixed with a solution of 4% Formalin for 24 hours. Populations purity after sorting was confirmed through confocal immunofluorescent imaging (Nikon A1R Nala) as visible in Fig. 11c. At least three independent samples per condition were considered in analyses.

5.6.2 Compartments differentiated strains induce differential cellular mechanotransduction signalling activation

The effect of a differential compression applied in the two compartments was evaluated by assessing the activation of a gene expression signature associated with mechanotransduction signalling [37]. To this aim, GFP hACs and normal hACs embedded in 2% PEG gel were seeded in the LDG top culture chamber and compression chamber, respectively (Fig. 11a).

Fos Proto Oncogene (*FOS*), Prostaglandin-endoperoxide synthase 2 (*PTGS2*) and C-JUN (*C-JUN*), i.e., genes that were demonstrated to be downstream of the mechanotransduction signalling mediated by the ion channel TRPV4 [37] were considered in analyses. The modulation of these genes following cyclic compression in the two compartment was quantified through RT-qPCR.

An assessment of *FOS*, *PTGS2*, and *C-JUN* expression in construct cultured statically in the top culture chamber and in the compression chamber for 3 weeks was established to verify that constructs positioning did not present an offset in terms of selected gene expression. Construct cultured in the same way but not subjected to digestion and sorting were used as further controls to assess the effect of these procedure on

gene expression alteration. The LDG configuration was adopted. Results are depicted in Fig. 11b and c. Both paired and unpaired comparisons of the selected genes between top and bottom compartments of static controls revealed no differences (indicated statistic inFig. 11. b is referred to paired tests) but all three considered genes were significantly upregulated by the digestion-sorting procedure. The effect of differential compression on the two compartments was referred to expression of static controls which were also subjected to digestion and sorting. A schematization of the experimental setup and timeline is visible in Fig. 11d.

After 14 days of maturation constructs were subjected to mechanical loading for 7 further days. Loading was applied following a previously tested regimen demonstrated to induce OA traits in cartilage on chip constructs subjected to hyperphysiological compression [1]. Briefly two 2h stimulation cycles (1Hz, 50% duty cycle) were applicated each day with a 4h stop in-between. Mechanical stimulation was achieved connecting the devices to a pressure regulator (Comnhas), linked to a custom made electropneumatic controller able to apply the described loading regimen [1]. External connections were realized through tygon tubing (internal diameter = 0.5 mm, Qosina, Ny, USA). A pressure of 0.4 Atm was applied to the actuation chamber during cyclic loading. Culture medium was changed every second day and collected for analysis.

At the end of the culture period, constructs were enzymatically digested and sorted by flow cytometry based on GFP positivity as described above. The two sorted hAC populations were thus analysed by qRT-PCR as described in section 5.7 to qualify the expression of *FOS*, *PTGS2,* and *C-JUN*.

A statistically significant upregulation of *FOS*, with respect to static controls (also subjected to sorting), was registered for hACs isolated from both compartments. No statistically significant FOS regulation was however registered among the two compartments. Contrarywise, pairwise analyses of single constructs revealed a statistically significant decrease in the expression of *PTGS2*, even if limited in value, and a statistically significant increase in the expression of *C-JUN* in hACs from the bottom construct with respect to those from the top one, thus suggesting the achievement of a differential compression level within bi-layered construct. Notably, the fact that constructs digestion and sorting caused an overall increase of the selected genes (static controls were also subjected to sorting before comparisons with other groups), can possibly explain the fact that *PTGS2* and *C-JUN* did not show significant increases when hACs from mechanically stimulated top and bottom constructs were compared to static controls.

To determine if gene upregulation in one compartment could be the result of inter-compartments cross talk (i.e. if the differences in gene expression were more defined at earlier time points), constructs activation was assessed after 1, 3 and 7 days of compression (Fig. 11f). Results are reported in Fig. 11g. A significant increase in *FOS* expression in both top and bottom compartments was visible between 1 and 7 days of stimulation. *PTGS2* and *C-JUN* did not exhibit a clear time trend, with *C-JUN* upregulation tendency in the

bottom compartment being visible already from day 3 of stimulation. The data suggest therefore an overall increase of selected genes modulation in time, reflecting naturally occurring OA hallmarks manifestation rather than an overloading impulse-mediated response.

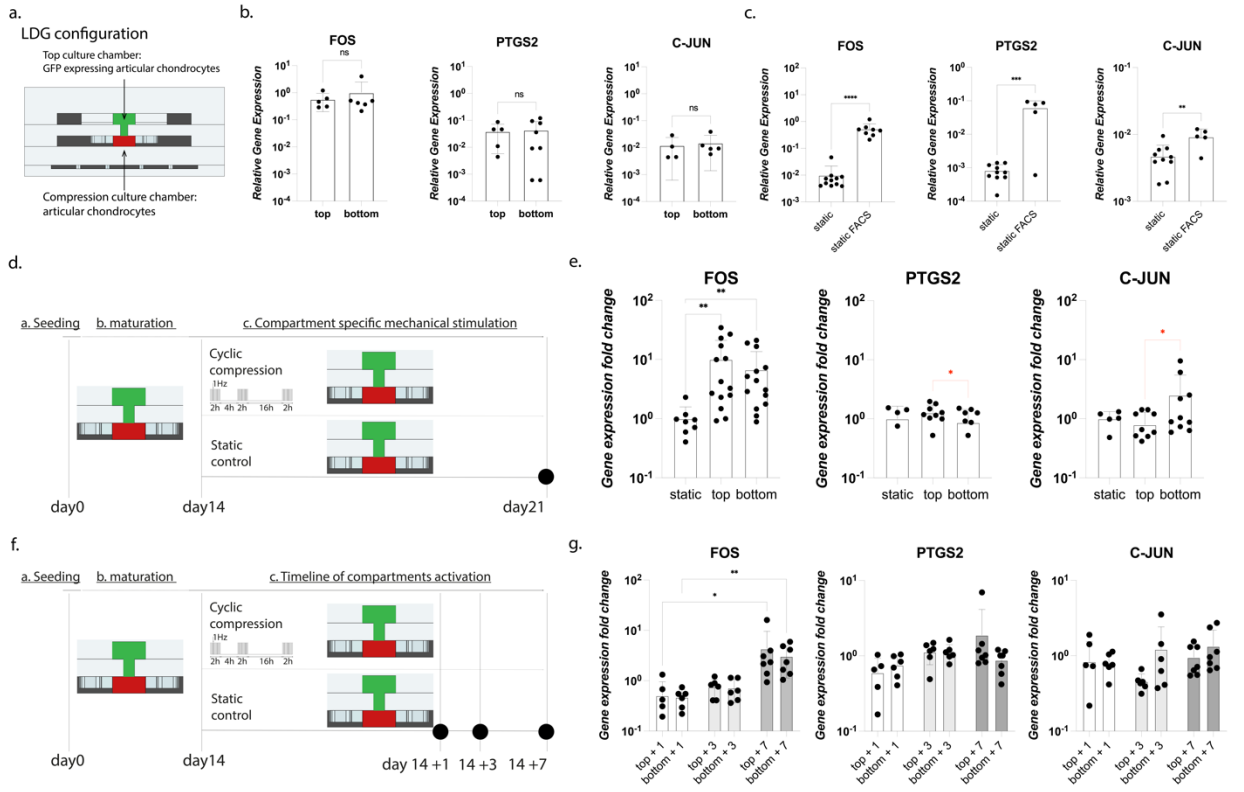

Figure 11: ***Determination of compartment specific compression levels on mechanotransduction activation****.* ***a*** *Experimental setup for the validation of the strain field. Either plain or GFP labelled hACs were seeded in the two compartments.* ***b, c*** *Determination of baselines in gene expression.* ***b,*** *Assessment of the difference between top culture chambers and compression chambers in static conditions. Gene expression was quantified through RT-qPCR. All genes were normalized for GAPDH, values are log scaled. Populations' normality was assumed if both Shapiro-Wilk and Kolmogorov-Smirnov tests resulted positive. Both paired and unpaired statistical tests were performed. Non-Paired double comparisons were performed using two tailed t-test for normal populations and Mann-Whitney test for non-Gaussian ones. Paired double comparison were performed using paired t-test and Wilcoxon test respectively. N≥4 independent samples were adopted from n≥2 different donors. ns statistically non-significant.* ***c****, Determination of the effect of constructs digestion and sorting on expression of genes of interest. Gene expression was quantified through RT-qPCR. All genes were normalized for GAPDH, values are log scaled. Populations' normality was assumed if both Shapiro-Wilk and Kolmogorov-Smirnov tests resulted positive. Statistics by two tailed t-test for normal populations and Mann-Whitney test for non-Gaussian ones. *P<0.05, **P<0.01, ***P<0.001, ****P>0.0001.* ***d,*** *Experimental timeline schematization. Constructs were cultured statically for 14 days and subjected to mechanical stimulation for 7 days. Static constructs were used as controls. After the culture constructs were digested and sorted to separate the populations in the two compartments.* ***e,*** *Constructs gene expression as quantified by RT-qPCR (n≥ 9 biologically independent samples from n=3 donors were evaluated for each condition). Al genes expression values are relative to GAPDH expression and were normalized for the expression level of static controls. Results are expressed as mean + s.d. Populations' normality was assumed if both Shapiro-Wilk and Kolmogorov-Smirnov tests resulted positive. Statistics refers to One way ANOVA with Tukey's multiple comparison test and Kruskal-Wallis test with Dunn's multiple comparison test populations to compare all experimental groups in the case of normal and non-normal distributions respectively (in black) or to paired t-test or Wilcoxon test for normal and non-normal populations applied to the pairwise comparison of top and bottom compartments (in red). * P<0.05, **P<0.01* ***f****, Experimental timeline for the determination of mechanotransduction signaling onset. Constructs were cultured statically for 14 days and subjected to mechanical stimulation for 1, 3, or 7 days with the pattern indicated in figure. Static constructs were used as controls. After the culture constructs were digested and sorted to separate the populations in the two compartments.* ***g****, Constructs gene expression as quantified by RT-qPCR (n≥5 biologically independent samples from n=2 donors were evaluated for each condition). All genes expression values are relative to GAPDH expression and were normalized for the expression level of static controls. Results are expressed as mean + s.d. Populations' normality was assumed if Shapiro-Wilk and Kolmogorov-Smirnov tests resulted positive. Statistics refers to One*

*way ANOVA with Tukey's multiple comparison test and Kruskal-Wallis test with Dunn's multiple comparison test to compare all experimental groups in the case of normal and non-normal distributions respectively * P<0.05, **P<0.01*

5.6.3 Inter-compartments differentiated strain elicits strain-dependent cartilage inflammation and degradation processes

Predicted compression levels for top and bottom constructs were reminiscent, respectively, to physiological compression levels experienced *in vivo* at the interface between cartilage and bone [5], and to the hyperphysiological compression of cartilage upper layers in "OA facilitating" conditions [38, 39]. A proof of concept on the strain-dependent selective activation of OA-like degradative and inflammatory processes in the bottom construct was thus introduced. As described before, hACs labelled or not with GFP were seeded respectively in the LDG top culture chamber and in the compression chamber (Fig. 11a) so that the two constructs could be sorted by flow cytometry at the end of the culture period. Constructs were cultured statically for 14 days and cyclic compression was applied as previously described for further 7 days (Fig. 11d). Assumption of a degradative and inflammatory phenotype in the two compartments was assessed by RT-qPCR quantification of gene expression (normalized for the expression of static constructs). The gene expression of MMP13, a metalloproteinase associated with cartilage breakdown in OA, was considered as a marker of catabolism. Top and bottom constructs exhibited opposite *MMP13* expression modulations trends with respect to static controls (Fig. 12a, dashed line), despite not in a statistically significant manner. Gene expression was specifically downregulated in the top constructs and upregulated in the bottom ones. The pairwise analysis of hACs isolated from the top and bottom constructs from the same device revealed a statistically significant difference in *MMP13* expression, with relative fold changes of respectively 0.3 ± 0.2 and 1.5 ± 1.1 in the top and bottom constructs. Experimental groups estimation plot depicts the variation in expression for single devices constructs and an overall assessment of the fold changes differences (Fig. 11b). Conversely, the gene expression of the pro inflammatory cytokine interleukin 8 (*IL8*) did not show differences between hACs isolated from the two constructs, with both expression levels lower than static controls.

Given the proven effect of cell sorting on IL8 gene expression modulation (Fig. 12c), that could pose as a confounding factor, onset of an inflammatory phenotype was also assessed through measurement of IL8 release in the culture medium. A statistically significant increase of this inflammatory cytokine was measured in the culture medium collected from the compression chamber as a result of exposure to hyper-physiological mechanical compression (Fig. 12d), while IL8 concentration in the top culture chamber showed intermediate levels between those of static devices and those of the compression chamber. Notably different trends in the cytokine concentration in the two chambers could be measured given the LDG adopted for the top culture chamber thus limiting solutes diffusion between compartments.

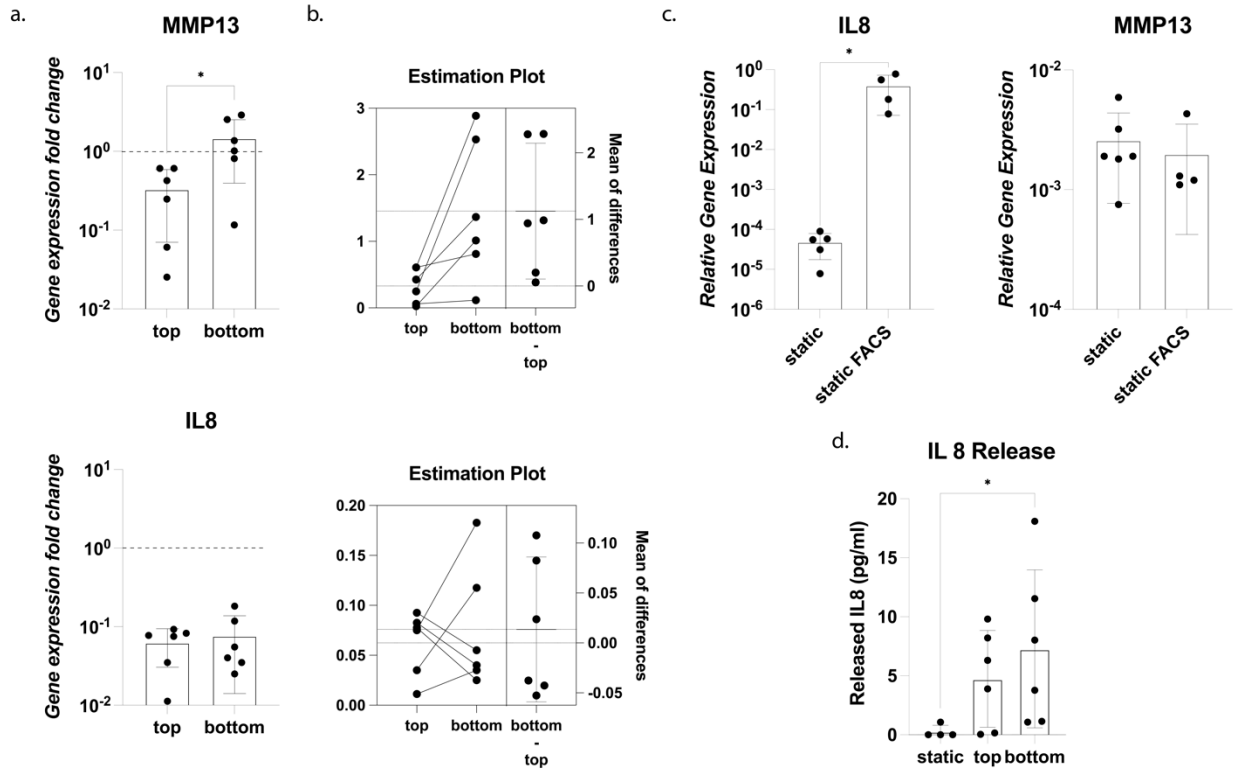

Figure 12: ***Compartments Catabolic and inflammatory response to cyclical loading****.* ***a****, gene expression quantification of the degradative enzyme MMP13 and the inflammatory cytokine IL8 by RT-qPCR. (n=6 biologically independent samples from n=2 donors). Gene expression was referred to GAPDH, values were normalized for the expression of static controls (dashed lines). Statistics by paired t test after having assessed populations normality (Shapiro-Wilk Test). * P<0.05.* ***b,*** *Estimations plots reporting the mean of differences from pairwise comparison of top and bottom construct gene expression.* ***c,*** *Determination of the effect of constructs digestion and sorting on the expression of genes of interest. Gene expression was quantified through RT-qPCR. All genes were normalized for GAPDH, values are log scaled. Populations' normality was assumed if both Shapiro-Wilk and Kolmogorov-Smirnov tests resulted positive. Statistics by two tailed t-test for normal populations and Mann-Whitney test for non-Gaussian ones. *P<0.05, **P<0.01, ***P<0.001, ****P>0.0001.* ***d****, IL8 secreted in the culture medium was quantified. A statistically significant higher release was detected between bottom compartment and static controls. (n=6 biologically independent samples from n=2 donors). Statistics by Kruskal-Wallis test with Dunn's multiple comparison test. Normality assessment by Shapiro-Wilk test.*

5.7 Alteration of subchondral layer local properties affect cartilaginous constructs response to loading

The proposed device was finally exploited to test the hypothesis that alterations and inhomogeneities in the local mechanical properties of subchondral layers may cause a different response to loading in the cartilage compartment. hACs were loaded in an enzymatically cross-linkable and degradable PEG based hydrogel formulation [23] as described above and injected in the compression chamber i.e. the bottom compartment of the device (Fig. 13a). The top culture chamber was injected with hydrogels loaded with either 0.1% or 5% in volume of polystyrene beads (diameter 10 um, Sigma-Aldrich). Mechanical properties of the beads-laden construct were calculated as described below.

5.7.1 Determination of the mechanical properties of polystyrene beads laden hydrogels.

The effective properties of the PEG hydrogels laden with different percentages of spherical polystyrene beads, namely 0.1% and 5% of the volumetric fraction, were determined starting from the properties of the constituents and adopting an averaging scheme.

Young modulus and Poisson's ratio of the PEG hydrogel matrix were assumed equal to 1.9 kPa and 0.33 as previously described. The added 10 μm polystyrene beads inhomogeneities were assumed to have a Young's modulus of 3250 x10^3 kPa and a Poisson ratio of 0.34 derived from material properties tables [40].

The effective properties of a composite material can be evaluated solving an inclusion problem, as formulated by Eshelby [41], for each of the phases, and then adopting an adequate averaging scheme. The solution of the inclusion problem requires, therefore, the determination of Eshelby's tensor components which depends in general on the properties of the materials and on the geometry of the inclusions. An explicit formulation of Eshelby's tensor is available for spherical inclusions in an isotropic material and the fourth order tensor components can be calculated as:

$$S_{ijkl} = \frac{5\nu - 1}{15(1-\nu)}\delta_{ij}\delta_{kl} + \frac{4 - 5\nu}{15(1-\nu)}\left(\delta_{ik}\delta_{jl} + \delta_{il}\delta_{jk}\right)$$

Where δ_{ij} is the Kroeneker delta, while ν is the Poisson's ratio of the matrix [42]. Mori-Tanaka averaging scheme [42, 43] was adopted to derive the homogenized stiffness tensor $\bar{L}$.

$$\bar{L} = L_0 + \sum_{r=1}^{N} c_r (L_r - L_0) T_r \left[c_0 I + \sum_{r=1}^{N} c_r T_r \right]^{-1}$$

With

$$T_r = [I + S_r L_0^{-1}(L_r - L_0)]^{-1}$$

Where S_r is the Eshelby tensor computed using the matrix material properties L_0 and the geometry of the *r-th* inhomogeneity, L_r is the stiffness matrix of the *r-th* inhomogeneity, and C_0 and C_r are the volume fractions of the matrix and of the *r-th* inhomogeneity. Effective properties were computed using a custom MATLAB script (MATLAB 2020 release, Mathworks), considering polystyrene beads as the sole present inclusion.

The estimation of the bulk properties of the beads laden PEG gels demonstrated a limited effect of introducing small volumetric fractions of a stiffer material on the overall properties of the PEG based

hydrogels. E values of 1,9 kPa and 2,1 kPa were calculated respectively for 0.1% PS and 5% PS hydrogels, with null or very limited variations of the global mechanical properties caused by beads incorporation.

5.7.2 Determination of the effect of stiff inhomogeneities incorporation in substrates on chondrocytes response to hyperphysiological loading.

The effect of introducing local alterations in the mechanical properties of the subchondral layer on chondrocytes response to compression was investigated.

The adopted experimental setup is depicted in Fig. 13a. hACs laden PEG gel (mimicking the cartilage compartment) and PEG gel only loaded with different percentages of polystyrene beads (diameter 10 μm) (mimicking the subchondral layer) were seeded in the compression chamber and in the top culture chamber, respectively. The stiffer inhomogeneities constituted by the beads introduced discontinuities in the top construct mechanical properties. After 14 days of static culture, necessary for cartilage like construct to mature, mechanical loading was applied for 7 days with the regimen indicated in Fig. 13b. Substrates with different grades of inhomogeneities were obtained employing an inclusion volumetric fraction of polystyrene beads of 0.1% (0.1% PS) and 5% (5% PS), respectively. Constructs cultured statically also during the stimulation period were adopted as controls. Both devices seeded with PEG gel only and with the 5% volumetric fraction gels in the top culture chamber were adopted as controls to exclude that observed results could be attributed to factors released by the polystyrene beads. Given the absence of biological material requiring culture medium supplementation in the top constructs the NDG configuration was exploited for the top chamber maximizing the control over the strain field. During the stimulation period the culture medium, changed every second day, was collected for analyses. At the end of the culture constructs were collected for RT-qPCR.

Application of loading to constructs with 0.1% PS and 5% PS substrates resulted in limited increases in the expression of the previously mentioned mechanotransduction related genes *FOS*, *PTGS2* and *C-JUN*. Exclusively FOS showed a statistically significant upregulation following the inclusion of the higher beads fraction. Bone Morphogenic Protein 6 (*BMP6*) gene expression, which had also previously been correlated with mechanotransduction [37], did not show a detectable increase (Fig. 13c). OA is also associated with the onset of a hypertrophic phenotype. Hypertrophy markers collagen type X (*COL10A1*) and Indian Hedgehog (*IHH*) did not show any modulation following cyclical loading. Conversely, *FRZB*, whose decrease had been correlated to load bearing areas in OA joint ([44]), showed a decrease with both substrates, and *GREM1,* correlated with load mediated OA induction [45], showed an upward trend exclusively top constructs with a higher inhomogeneities inclusion percentage (Fig. 13 d). Alterations of the expression of genes associated to catabolic and anabolic processes, and inflammation, two of the main features of OA, were also investigated. A clear trend was visible in the *COL2A1/COL1A1* mRNA ratio with

a decrease more pronounced with the 5% PS substrate. Conversely, the gene expression of *ACAN* demonstrated a very minimal downward tendency with compression and no statistical differences were detected. Moreover, both *MMP13* and *IL8* expressions increased in a statistically significant manner exclusively following stimulation with the 5% beads substrate (Fig. 13e). Release of inflammatory cytokines was also investigated. Significant differences in the release of IL8 were detected between constructs with 0.1% PS and 5% PS substrates (Fig. 13f.) An upregulation of IL6 was also registered with the 5% PS substrate (Fig. 13f), while culture medium resulted negative for TNFα and IL1β which could not be detected in any condition (data not shown). Overall, these data suggest that the introduction of stiffer localized inhomogeneities in subchondral layers can alter chondrocytes response to loading, exacerbating the assumption of a degradative and inflammatory phenotype in response to hyperphysiological compression.

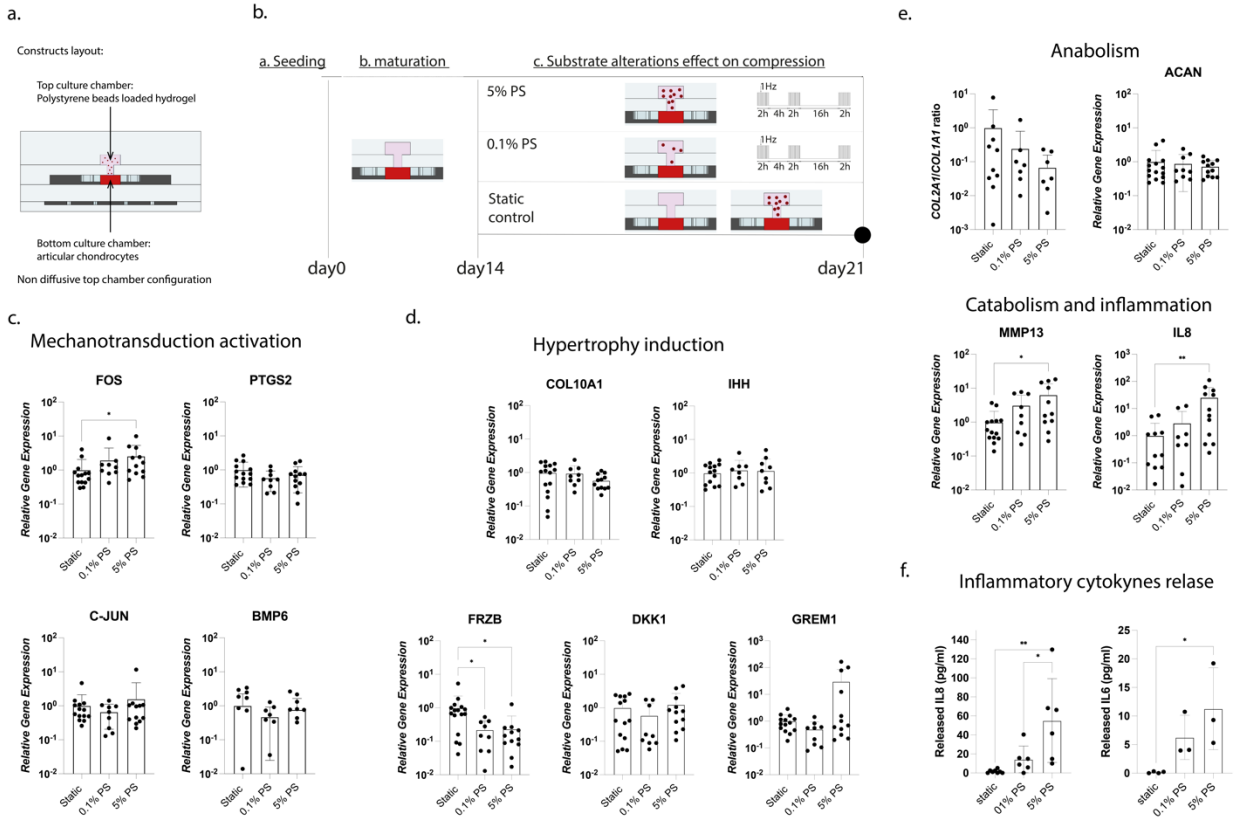

Figure 13: ***Subchondral layer local alterations induce different loading responses in chondrocytes, a proof of concept****.* ***a****, schematization of the two constructs loaded in the device. The NDG was adopted.* ***b****, Experimental timeline, constructs were cultured statically for 14 days before application of the indicated loading regimen.* ***c****,* ***d, e*** *Gene expression quantification through RT-qPCR. Genes correlated to mechanotransduction activation,* ***c****, induction of a hypertrophic phenotype,* ***d****, and anabolism (COL2A1/COL1A1 and ACAN), catabolism (MMP13), and inflammation (IL8) are represented. (n≥9 biologically independent samples from n=3 donors) All genes expression was referred to GAPDH and values were normalized for the expression of static controls. Results are expressed as mean + s.d. Statistics refers to one way ANOVA with Tukey's multiple comparison test for normal population and Kruskal-Wallis test with Dunn's multiple comparison for non-normal distributions. *P<0.05, *P<0.01.* ***f****, Quantification of cytokines release in the culture medium. IL8 release was determined by ELISA. Statistics by one way ANOVA*

*with Tukey's multiple comparison test. (n=6 biologically independent samples from n=2 donors were considered) Populations' normality was assessed with Shapiro-Wilk and Kolmogorov Smirnov tests. *P<0.05, *P<0.01. IL6 concentration was determined by Luminex analysis. n=3 biologically independent samples from n=1 donor were considered. Populations' normality was assessed by Shapiro-Wilk test. Statistics by Kruskal-Wallis test with Dunn's multiple comparison test. * P<0.05.*

5.8 Analyses procedures and methodologies

5.8.1 Gene expression analysis

Total RNA extraction by TRIzol, complementary DNA synthesis, and RT-qPCR were performed according to standard protocols (7300 AB; Applied Biosystems). The following gene of interests were quantified (Applied biosystems) to assess the level of cartilage maturation i.e.COL2A1 (Hs00264051_m1), COL1A1 (Hs00164004_m1), ACAN (Hs00153936_m1), PRG4 (Hs00981633_m1), GDF5 (Hs00167060_m1), FRZB (Hs00173503_m1), GREM1 (Hs01879841_s1); the mechanical actuation in the two compartments i.e. FOS (Hs99999140_m1), PTGS2 (Hs00153133_m1), JUN (Hs01103582_s1), BMP6 (Hs01099594_m1); the expression level of hypertrophy markers and hypertrophy regulators, i.e. FRZB (Hs00173503_m1), GREM1 (Hs01879841_s1), DKK1 (Hs00183740_m1), COL10A1 (Hs00166657_m1), IHH (Hs01081800_m1); and the onset of cartilage OA markers i.e. the ratio between COL2A1 and COL1A1, ACAN, MMP13 (Hs00233992_m1), and IL8 (Hs00174103_m1). GFP (Mr00660654_cn) was used to check populations purity.
Glyceraldehyde 3 phosphate dehydrogenase (GAPDH) was used as housekeeping gene (Hs02758991_g1).

5.8.2 Biochemical analyses

Release of biochemical factors in the supernatant was measured. Supernatants were collected every second day during the entire 7 days of mechanical stimulation and finally pooled together to measure solutes accumulation during the whole stimulation period. Thanks to the use of the LDG configuration culture medium from the top culture chamber and from the compression chamber was collected and analyzed separately to ascribe release of solutes to one of the two compartments only. IL8 concentration was measured using the Human IL-8 ELISA Set (BD Bioscience) following the manufacturer instructions. Measurements were acquired using a configurable multimode microplate reader (synergy H1, BioTek instruments). IL-1β, TNFα, and IL6 release was analyzed by a Luminex® Assay using the Human Premixed Multi-Analyte Kit (R&D Systems) according to manufacturer instructions and acquiring readings with a BioPlex MagPlex Magneti Beads system (Bio-Rad). At least six biologically independent samples from two different donors were adopted for analyses if not otherwise specified.

5.8.3 Statistical Analyses

Results of FE analyses and biochemical analyses were presented ad mean ± standard deviation. RT-qPCR results were presented as mean + standard deviation. Single data were plotted to account for non-normal distributions. Population normality was verified using Shapiro-Wilk and Kolmogorov-Smirnov tests. Non-Paired double comparisons were performed using two tailed t-test for normal populations and Mann-Whitney test for non-Gaussian ones. Paired double comparison were performed using paired t-test and Wilcoxon test respectively. Multiple comparisons were performed using ordinary one-way analysis of variance (ANOVA). Ordinary one-way ANOVA with Tukey's multiple comparison tests were adopted for normal distributions, Kruskal-Wallis test with Dunn's multiple comparison tests for non-normal distributions. Statistical significance was indicated by * $P<0.05$, ** $P<0.01$, *** $P<0.001$, **** $P<0.0001$, respectively.

5.9 Discussion

A multi-compartmental microfluidic device that allows the vertical superimposition of two directly interfaced 3D constructs and the stimulation of these constructs with well-defined discrete levels of confined compression limitedly dependent on the constructs' properties was presented. To achieve this aim, a new microfluidic concept, namely the VBV was conceived and a methodology for the achievement of required suspended PDMS structures introduced. A biological validation of the proposed device was performed demonstrating different levels of mechanotransduction signalling activation in cartilaginous tissues cultured in the two compartments of the device, and thus subjected to different compression levels. The device was finally exploited to demonstrate that local alterations in the composition of subchondral layers have an influence on the physio-pathological response of cartilaginous constructs to hyper-physiological mechanical loading.

OA has been characterized as a joint failure disease affecting all joint tissues and in particular the OCU constituted by superimposed layers of hyaline cartilage, calcified cartilage and subchondral bone [2, 46]. The order with which alterations appear in the various tissues is however still debated and a consensus on the pathological origin has not been reached yet. Some authors posited for instance that changes in the constitution and in the properties of subchondral bone precede OA traits induction in cartilage [47, 48].

The limited knowledge on the disease mechanism and the multiplicity of tissues and factors involved in OA onset and progression make urgent the demand for advanced *in vitro* models allowing to discern the causal relationship between observed phenomena in a controlled manner. Achievement of relevant OA representations should however include (i) multiple tissues organized with an OCU-like disposition, and (ii) physio-pathological stimuli reminiscent of the native articular environment.

Different OoCs permitting the co-culture of juxtaposed tissues had been designed and exploited for applications ranging from cancer research [15], to vascular permeability assessments [49], and to OA investigation itself [50]. The positioning of cells in adjacent constructs was rendered possible by various declination of the CBV concept [11]. However, no mechanical stimulation was included in such devices even when relevant in the native *milieu*. Indeed, joint abnormal loading was demonstrated as one of OA risk factors [4, 45]. Moreover, in load bearing diarthrodial joint such as knees, the OCU is constituted by tissues organized as mechanical springs in series and thus the correct recapitulation of the joint functional anatomy requires mechanical stimulation of superimposed and not juxtaposed constructs.

In Chapter 2 a procedure to subject 3D constructs within OoC devices to well defined and controlled levels of compression was reported. However, such approach was only compatible with single homogeneous constructs. Building on this technology in this Chapter it was proposed a new microfluidic concept that, integrating two compartments for the discrete injection of cell laden hydrogels (namely the VBV) and an actuation compartment, allows to apply discrete levels of compression to complex 3D bi-layer constructs.

Achievement of such a VBV-integrating device required a modular fabrication approach, consisting in the adoption of multiple master moulds and in the bonding of multiple (specifically four) layers of PDMS, increasing production time and complexity. Attempts at obtaining both top culture chamber and compression chamber from a monolithic master mould revealed indeed unsatisfactory geometrical features. Although the achievement of master moulds containing suspended structures was previously demonstrated [16], the underlying method relies on the use of multiple photomasks and a finely tailored polymerization of SU-8 layers, resulting in a complex, poorly reproducible, series of photolithography operations. Indeed, while a simple VBV hourglass profile geometry could be obtained with this technique, dosing the exposure energy required for both the VBV geometry and the suspended pillars in the compression chamber proved unfeasible. The functioning of the VBV, and of the CBV in general depends in fact on the variation of the contact angle formed between an advancing fluid and the channel wall. When an aperture is reached the angle variation causes an increment in the pressure necessary for the fluid to advance. The pinning interface depends therefore on the achievement of abrupt geometrical changes. Attempt at developing a monolithic mould resulted instead in rather smooth curvatures not suitable for a functional valve.

The multi-layer approach adopted, conversely, allowed the achievement of features with high geometrical fidelity to device schematizations, allowing successful injection of both hydrogels with a high (i.e. roughly 90%) success rate. Furthermore, the layers' alignment precision was assessed proving applicability of the technique in a laboratory setting.

By exploiting the described multi-layer approach a modular device construction was possible, as demonstrated in this study by designing three top chambers configurations with different purposes. A closed geometry simply constituted by a linear channel (NDG configuration) allows for instance the coupling of a

cartilaginous construct with artificial constructs with various mechanical properties. Conversely, the introduction of culture medium channels also in the top culture chamber (DG and LDG configurations) allows for two cellular constructs to be injected and cultured in the device. Upon sufficient maturation of the constructs, moreover, the LDG allows the independent chemical conditioning of the two compartments although limited in time, without requiring continuous flows to generate a media gradient. This latter concept was demonstrated by assessing the limited inter-compartmental diffusion of a compound (i.e.20 KDa dextran) with a molecular weight in the range of known morphogens [18] up to 12 hours. The time-based fluidic separation among the compartments allowed furthermore to measure separately the IL8 released in the top culture chamber and in the compression chamber. The same configuration could be applied to biochemically condition with different compounds the two constructs hosted in the top and bottom compartments, with the aim to observe possible short term (i.e. hours) crosstalk mediated effects.

In the native joint the OCU response to loading is mediated by tissues with a complex hierarchical organization [51] and with mechanical properties ranging from a few MPa to GPa [8]. Given the higher mechanical properties of calcified cartilage [9] and subchondral bone [6, 8], these tissues are reasonably subjected to strain levels which are at least one order of magnitude lower than those experienced by cartilage *in vivo*.

In vitro, at the microscale, 3D cellular tissues are obtained by the incorporation of cells in hydrogels thus not permitting to achieve elastic moduli similar to bone tissue (i.e. GPa). Moreover, since, OoC devices are largely constituted by PDMS characterized by E values of 1.32-2.97 KPa [52], adoption of materials with higher E would result in the deformation of PDMS structures rather than the material itself.

The geometry of the proposed device was conceived so that the construct hosted in the compression chamber would be subjected to a hyper-physiological compression level (i.e. 30%), while very limited compression (~-1% for the uppermost cells) was applied to the construct in the top culture chamber. Such values are, respectively, well in accordance with the hyper-physiological strain experienced by cartilage *in vivo* (in conditions associated with OA onset [4, 38, 39]), and with the low strain experienced by the immediately subchondral layers [3, 5]. An evaluation of the effective strain field in the bi-layered constructs was performed though FE modelling. Both preliminary PEG based simulations and simulations performed after the experimental measurement of mature cartilaginous constructs mechanical properties, revealed achievement of homogeneous and limited lateral and longitudinal expansions and discrete levels of compression in the two compartments. Limiting the lateral expansion (i.e. achieving confined compression) is instrumental in generating the compression associated fluid outflow that was correlated with chondrocytes mechanotransduction activation rather than direct cellular deformation [37]. Moreover, achieving of a homogeneous strain within the same construct avoids multiplying the complexity due to heterogeneous cellular responses and the adoption of different donor and tissue sources.

A different methodology to apply mechanical stimuli to three dimensional constructs from the side has been introduced [53]. However, the proposed platform could only host homogeneous single tissues; moreover, no control on the applied strain was devised with the consequence that mechanical stimuli were dependent of tissue properties, which vary during culture time due to tissue maturation. Instead, in the here presented device very limited variations in the top and bottom constructs strains were associated to the top construct Young's modulus varying up to one order of magnitude.

Admittedly, cartilage and subchondral bone *in vivo* are subjected to a wide variety of stimuli (comprehensive of compression but also shear stresses [54]) whose full recapitulation *in vitro* is highly complex and would introduce multiple confounding factors. The focus of this work was therefore centred exclusively on physiologically relevant compression levels.

The proposed device was exploited to recapitulate an *in vitro* model of cartilage on chip and, subsequently, to alter its mechanical microenvironment demonstrating that constructs hosted in the two compartments respond differently to the discrete compression levels applied (i.e. ~3% and ~25% respectively).

Constructs were cultured statically for 14 days, previously demonstrated to be sufficient to obtain cartilage like structures [1], revealing assumption of a gene profile reminiscent of stable articular cartilage with the increases expression of the *COL2A1/COL1A1* ratio, *ACAN* and *PRG4*, but also of the Wnt antagonist *FRZB* and the BMP agonist *GREM1,* recently characterized as hypertrophy breaks [44, 55], and of the cartilage development associated factor *GDF5* [56].

The gene regulatory network downstream of chondrocytes response to compression has recently been clarified [37]. Making use of GFP transfected chondrocytes filling one of the two compartment it was feasible, at the end of the culture, to separate cells which were hosted in the top culture chamber or in the compression chamber and verify if reported markers, namely *FOS*, *PTGS2,* and *C-JUN* were differently upregulated due to the distinctive imposed levels of mechanical stimulation. An upregulation of *FOS* expression with respect to static controls was registered for both compartments after 7 days of stimulation indicating an overall mechanical activation. Moreover, both *PTGS2* (downregulated) and *C-JUN* (upregulated) resulted to be differentially expressed in the bottom compartment with respect to the top one, indicating the effective application of different mechanical stimuli in the two zones. Notably, such strain dependent effect seemed to increase with the stimulation time, being negligible after one day of stimulation but evident after seven. Markedly, while upregulation of the selected genes was previously reported in response to the application of a ~10% compression level [37], their modulation varying the strain level was never directly assessed. Moreover different mechanotransduction pathways, e.g. those mediated by PIEZO1 and PIEZO2 channels, were related following higher over-physiological compression levels [57, 58]. Reported results are not therefore meant to indicate a correlation between the applied compression and gene modulation but exclusively as an indication, together with the FE estimate, that the proposed device is

effectively capable of providing superimposed construct with discrete compression levels. A drawback of the proposed platform is, nevertheless, the impossibility of determining the strain level in the two constructs by simple visual inspection under compression as done previously for other models [1].

Two of the hallmarks of OA onset in cartilage are represented by an increase in catabolic processes and cytokine mediated inflammation [1]. The expression of *MMP13* and *IL8* in the two compartments following discrete mechanical stimulation were therefore investigated. A difference was noticeable in *MMP13* expression in top and bottom compartments possibly suggesting a strain dependent effect.

Specifically, moderate compression (i.e. ~3% experienced by the top construct) limited matrix catabolic processes, which are instead stimulated, together with inflammation as demonstrated by increased IL8 released in the bottom compartment, upon hyperphysiological loading (i.e. ~25%).

Finally, the proposed device was adopted for a proof-of-concept verification that local alterations in the composition or in the mechanical properties of subchondral layers can induce different cartilage responses to loading.

A localized stiffening of the area immediately adjacent to the tidemark was correlated to increased stresses in cartilage low layers [59, 60]. Furthermore, an increased mineral content of calcified cartilage [61],[61] was reported in OA joints.

A complete osteochondral model would require the development of a cellular mineralized tissue layer on top of a cartilaginous one. An artificial introduction of stiffer inhomogeneities (i.e. polystyrene beads) in the top construct allowed to test the hypothesis that subchondral layer local mechanical inhomogeneities have an effect on cartilage response in a simplified (co-culture effects free) setup. The bulk properties of hydrogels were evaluated theoretically through an averaging scheme. Notably the increase in global Young's modulus due to beads incorporation was limited (from 1.9 KPa to 2.1 KPa) and preliminary simulations predicted a variation smaller than 1% in the compression level in the bottom construct when the Young's modulus of the top construct doubled. These results reflect changes occurring in OA joints. *In vivo*, in fact, despite both calcified cartilage and subchondral bone mechanical properties change due to OA, modulations are still 2-3 orders of magnitude lower with respect to the difference in stiffness between cartilage and subchondral tissues. Cartilage remains therefore the compartment experiencing macroscopic deformations upon loading. In the same way, in the proposed model, beads insertion had a reduced effect on the overall mechanical properties of PEG gels mimicking the subchondral compartment and, as previously demonstrated, the device geometry assured discrete and defined compressing strains in the two compartments.

The introduction of local alterations in the top culture chamber constructs produced very limited effects on mechanotransduction associated genes, thus confirming the overall negligible changes in the compression level experienced by the bottom constructs. *FOS* expression was statistically upregulated with the higher

percentage of incorporated beads but compression did not lead to the upregulation of *PTGS2*, *C-JUN* and *BMP6*.

OA was also associated with the onset of a hypertrophic phenotype [62]. While in the CoC model presented in Chapter 2 an increase of *COL10A1* and *IHH* expression was achieved [1], the same results could not be achieved in this case. The onset of hypertrophy in OA was associated with a decrease in the expression of Wnt inhibitors *FRZB* and *DKK1*, and of the BMP antagonist *GREM1*, with further decreases being indicative of more load bearing areas [55]. A decrease in the expression of *FRZB* was achieved with both substrates while *DKK1* was not modulated and *GREM1* was upregulated only using 5% PS substrates. A decrease of all three genes and a consequent upregulation of hypertrophy markers was obtained with the simple OA CoC [1], but other authors reported an increase in expression of these genes *in vitro* when mechanical actuation was applied instead of chemical conditioning [55]. These results seem therefore to indicate that assumption of a hypertrophic phenotype depends on BMP and Wnt regulation and that fine mechanical strain are necessary in replicating such phenotype.

Lastly, the assumption that degradative and inflammatory phenotypes acquired by cartilage in response to loading are enhanced by local alterations in mechanical properties of subchondral layers was assessed. COL2A1*/COL1A1* mRNA expression ratio decreased in hACs cultured with the higher beads concentration in the top construct. The same trend was observed for the expression of MMP13, and IL8 which increased with compression and increased more with 5% PS constructs. Moreover, modulation of substrate properties led to a statistical difference between IL8 release in the culture medium of mechanically stimulated constructs; the same trend was visible for IL6.

These results demonstrate that the inclusion of stiff inhomogeneities in the subchondral layer may modulate cartilaginous construct response to hyperphysiological compression, despite limited variations in construct bulk elastic properties and tissues strain levels. While more investigations are required, these results are in line with *in vivo* occurring phenomena.

Overall, a better understanding of the mechanisms by which cartilaginous constructs respond to loads and how the properties of subchondral layer affect their behaviour is necessary.

5.10 Conclusive remarks

Some of the peculiar characteristics of OA, like the formation of osteophytes, cannot be recapitulated in OoC settings owing to the dimensional scale of the phenomena. While the achievement of a full osteochondral model of OA was beyond the scope of the present work, the proposed device could help in tackling some of the most debated open questions in OA development. We indeed demonstrated the ability

to host two different cellular constructs, providing them with defined compression levels, and possibly conditioning them with separate factors for limited time spans.

Furthermore, the study provided a proof-of-concept that local alterations in subchondral layer properties, even in a simple artificial fashion, modify cartilaginous construct response to loading in terms of Wnt/BMP activation, alteration in anabolic and catabolic processes, and assumption of an inflammatory phenotype. These results therefore highlight how more refined models of OA are required to achieve a relevant representation of the pathology and, possibly, predict the behaviour of given promising anti OA compounds. Moreover, the proposed model could be adopted in a wider set of applications studying the effect of mechanical stimuli on models of cartilage but also of bone and vasculature with the ultimate broad field perspective of highlighting drug targets beyond inflammation reduction but acting on OA pathological causes.

5.11 References

1. Occhetta P, Mainardi A, Votta E, et al (2019) Hyperphysiological compression of articular cartilage induces an osteoarthritic phenotype in a cartilage-on-a-chip model. Nat Biomed Eng. https://doi.org/10.1038/s41551-019-0406-3
2. Loeser RF, Goldring SR, Scanzello CR, Goldring MB (2012) Osteoarthritis: A Disease of the Joint as an Organ. Arthritis Rheum 64:1697. https://doi.org/10.1002/ART.34453
3. Eckstein F, Lemberger B, Gratzke C, et al (2005) In vivo cartilage deformation after different types of activity and its dependence on physical training status. Ann Rheum Dis 64:291. https://doi.org/10.1136/ARD.2004.022400
4. Sanchez-Adams J, Leddy HA, McNulty AL, et al (2014) The Mechanobiology of Articular Cartilage: Bearing the Burden of Osteoarthritis. Curr Rheumatol Rep 16:451. https://doi.org/10.1007/S11926-014-0451-6
5. Zheng YP, Mak AFT, Lau KP, Qin L (2002) An ultrasonic measurement for in vitro depth-dependent equilibrium strains of articular cartilage in compression Related content An ultrasonic measurement for in vitro depth-dependent equilibrium strains of articular cartilage in compression. Med Biol Phys Med Biol 47:3165–3180
6. Korhonen RK, Laasanen MS, Töyräs J, et al (2002) Comparison of the equilibrium response of articular cartilage in unconfined compression, confined compression and indentation. J Biomech 35:903–909. https://doi.org/10.1016/S0021-9290(02)00052-0
7. M L, D W, AU D, et al (2010) Micro- and nanomechanical analysis of articular cartilage by indentation-type atomic force microscopy: validation with a gel-microfiber composite. Biophys J 98:2731–2740. https://doi.org/10.1016/J.BPJ.2010.02.013
8. Peters AE, Akhtar R, Comerford EJ, Bates KT (2018) The effect of ageing and osteoarthritis on the mechanical properties of cartilage and bone in the human knee joint. Sci Rep 8:. https://doi.org/10.1038/S41598-018-24258-6
9. Mente PL, Lewis JL (1994) Elastic modulus of calcified cartilage is an order of magnitude less than that of subchondral bone. J Orthop Res 12:637–647. https://doi.org/10.1002/JOR.1100120506
10. Norman MDA, Ferreira SA, Jowett GM, et al (2021) Measuring the elastic modulus of soft culture surfaces and three-dimensional hydrogels using atomic force microscopy. Nat Protoc 2021 165 16:2418–2449. https://doi.org/10.1038/s41596-021-00495-4
11. Cho H, Kim HY, Kang JY, Kim TS (2007) How the capillary burst microvalve works. J Colloid Interface Sci 306:379–385. https://doi.org/10.1016/j.jcis.2006.10.077
12. Yildirim E, Trietsch SJ, Joore J, et al (2014) Phaseguides as tunable passive microvalves for liquid routing in complex microfluidic networks. Lab Chip 14:3334. https://doi.org/10.1039/C4LC00261J
13. Vulto P, Podszun S, Meyer P, et al (2011) Phaseguides: a paradigm shift in microfluidic priming and emptying. Lab Chip 11:1596. https://doi.org/10.1039/c0lc00643b
14. Trietsch SJ, Israëls GD, Joore J, et al (2013) Microfluidic titer plate for stratified 3D cell culture. Lab Chip 13:3548. https://doi.org/10.1039/c3lc50210d
15. Huang CP, Lu J, Seon H, et al (2009) Engineering microscale cellular niches for three-dimensional multicellular co-cultures. Lab Chip 9:1740–1748. https://doi.org/10.1039/b818401a
16. Moser Y, Forti R, Jiguet S, et al (2011) Suspended SU-8 structures for monolithic microfluidic channels. Microfluid Nanofluidics 10:219–224. https://doi.org/10.1007/s10404-010-0657-5
17. Lienemann PS, Lutolf MP, Ehrbar M (2012) Biomimetic hydrogels for controlled biomolecule delivery to augment bone regeneration. Adv Drug Deliv Rev 64:1078–1089. https://doi.org/10.1016/J.ADDR.2012.03.010
18. Marsano A, Conficconi C, Lemme M, et al (2016) Beating heart on a chip: a novel microfluidic platform to generate functional 3D cardiac microtissues. Lab Chip 16:599–610
19. TGF-beta | C211H345N61O62S - PubChem. https://pubchem.ncbi.nlm.nih.gov/compound/TGF-beta. Accessed 1 Aug 2021
20. Bialy I El, Jiskoot W, Nejadnik MR (2017) Formulation, Delivery and Stability of Bone Morphogenetic Proteins for Effective Bone Regeneration. Pharm Res 34:1152. https://doi.org/10.1007/S11095-017-2147-X
21. Lienemann PS, Lutolf MP, Ehrbar M (2012) Biomimetic hydrogels for controlled biomolecule delivery to augment bone regeneration. Adv Drug Deliv Rev 64:1078–1089. https://doi.org/10.1016/J.ADDR.2012.03.010
22. Barbero A, Grogan S, Schäfer D, et al (2004) Age related changes in human articular chondrocyte yield, proliferation and post-expansion chondrogenic capacity. Osteoarthr Cartil 12:476–484. https://doi.org/10.1016/J.JOCA.2004.02.010
23. Ehrbar M, Rizzi SC, Schoenmakers RG, et al (2007) Biomolecular hydrogels formed and degraded via site-specific enzymatic reactions. Biomacromolecules 8:3000–3007. https://doi.org/10.1021/bm070228f
24. Caron MMJ, Emans PJ, Coolsen MME, et al (2012) Redifferentiation of dedifferentiated human articular chondrocytes: comparison of 2D and 3D cultures. Osteoarthr Cartil 20:1170–1178. https://doi.org/10.1016/J.JOCA.2012.06.016
25. Blum MM, Ovaert TC (2012) Experimental and numerical tribological studies of a boundary lubricant functionalized poro-viscoelastic PVA hydrogel in normal contact and sliding. J Mech Behav Biomed Mater 14:248–258. https://doi.org/10.1016/j.jmbbm.2012.06.009
26. DiSilvestro MR, Suh JKF (2001) A cross-validation of the biphasic poroviscoelastic model of articular cartilage in unconfined compression, indentation, and confined compression. J Biomech 34:519–525. https://doi.org/10.1016/S0021-9290(00)00224-4
27. DiSilvestro MR, Zhu Q, Wong M, et al (2001) Biphasic poroviscoelastic simulation of the unconfined compression of articular cartilage: I - Simultaneous prediction of reaction force and lateral displacement. J Biomech Eng 123:191–197. https://doi.org/10.1115/1.1351890
28. DiSilvestro MR, Suh JKF (2001) A cross-validation of the biphasic poroviscoelastic model of articular cartilage in unconfined compression, indentation, and confined compression. J Biomech 34:519–525. https://doi.org/10.1016/S0021-9290(00)00224-4
29. Hosmane S, Fournier A, Wright R, et al (2011) Valve-based microfluidic compression platform: single axon injury and regrowth. Lab Chip 11:3888–3895. https://doi.org/10.1039/C1LC20549H
30. Phelps DEA, Enemchukwu MNO, Fiore MVF, et al (2012) Maleimide cross-linked bioactive PEG hydrogel exhibits improved reaction kinetics and cross-linking for cell encapsulation and in-situ delivery. Adv Mater 24:64. https://doi.org/10.1002/ADMA.201103574
31. Fox AJS, Bedi A, Rodeo SA (2009) The Basic Science of Articular Cartilage: Structure, Composition, and Function. Sports Health 1:461. https://doi.org/10.1177/1941738109350438
32. Ehrbar M, Sala A, Lienemann P, et al (2011) Elucidating the Role of Matrix Stiffness in 3D Cell Migration and Remodeling. Biophys J 100:284–293. https://doi.org/10.1016/J.BPJ.2010.11.082
33. Sader JE, Chon JWM, Mulvaney P (1999) Calibration of rectangular atomic force microscope cantilevers. Rev Sci Instrum 70:3967. https://doi.org/10.1063/1.1150021
34. M P, M L, CA M, et al (2012) The nanomechanical signature of breast cancer. Nat Nanotechnol 7:757–765.

https://doi.org/10.1038/NNANO.2012.167
35. Oliver WC, Pharr GM (1992) An improved technique for determining hardness and elastic modulus using load and displacement sensing indentation experiments
36. Miot S, Gianni-Barrera R, Pelttari K, et al (2009) In Vitro and In Vivo Validation of Human and Goat Chondrocyte Labeling by Green Fluorescent Protein Lentivirus Transduction. https://home.liebertpub.com/tec 16:11–21. https://doi.org/10.1089/TEN.TEC.2008.0698
37. Nims RJ, Pferdehirt L, Ho NB, et al (2021) A synthetic mechanogenetic gene circuit for autonomous drug delivery in engineered tissues. Sci Adv 7:9858–9885. https://doi.org/10.1126/sciadv.abd9858
38. Greaves LL, Gilbart MK, Yung AC, et al (2010) Effect of acetabular labral tears, repair and resection on hip cartilage strain: A 7 T MR study. J Biomech 43:858–863. https://doi.org/10.1016/J.JBIOMECH.2009.11.016
39. Wong BL, Sah RL (2010) Effect of a Focal Articular Defect on Cartilage Deformation during Patello-Femoral Articulation. J Orthop Res 28:1554. https://doi.org/10.1002/JOR.21187
40. Physical properties of thermo plastic materials:Polystyrene. In: Des. D2 Mater. Repos.
41. Eshelby JD (1957) The Determination of the Elastic Field of an Ellipsoidal Inclusion, and Related Problems. Proc R Soc A Math Phys Eng Sci 241:376–396. https://doi.org/10.1098/RSPA.1957.0133
42. Mura T (1987) Micromechanics of Defects in Solids, Second, Re. Martinus Nijhoff publishers
43. Mori T, Tanaka K (1973) Average stress in matrix and average elastic energy of materials with misfitting inclusions. Acta Metall 21:571–574. https://doi.org/10.1016/0001-6160(73)90064-3
44. Leijten JCH, Emons J, Sticht C, et al (2012) Gremlin 1, Frizzled-related protein, and Dkk-1 are key regulators of human articular cartilage homeostasis. Arthritis Rheumatol 64:3302–3312
45. Chang SH, Mori D, Kobayashi H, et al Excessive mechanical loading promotes osteoarthritis through the gremlin-1-NF-κB pathway. https://doi.org/10.1038/s41467-019-09491-5
46. Goldring SR, Goldring MB (2016) Changes in the osteochondral unit during osteoarthritis: structure, function and cartilage–bone crosstalk. Nat Rev Rheumatol 12:632–644. https://doi.org/10.1038/nrrheum.2016.148
47. Boyd SK, Müller R, Zernicke RF (2002) Mechanical and Architectural Bone Adaptation in Early Stage Experimental Osteoarthritis. J Bone Miner Res 17:687–694. https://doi.org/10.1359/JBMR.2002.17.4.687
48. Chen Y, Hu Y, Yu YE, et al (2018) Subchondral Trabecular Rod Loss and Plate Thickening in the Development of Osteoarthritis. J Bone Miner Res 33:316–327. https://doi.org/10.1002/jbmr.3313
49. Van Duinen V, Van Den Heuvel A, Trietsch SJ, et al (2017) 96 perfusable blood vessels to study vascular permeability in vitro. Sci Rep 7:1–11. https://doi.org/10.1038/s41598-017-14716-y
50. Mondadori C, Palombella S, Salehi S, et al (2021) Recapitulating monocyte extravasation to the synovium in an organotypic microfluidic model of the articular joint. Biofabrication 13:045001. https://doi.org/10.1088/1758-5090/AC0C5E
51. Mow VC, Ratcliffe A, Robin Poole A (1992) Cartilage and diarthrodial joints as paradigms for hierarchical materials and structures. Biomaterials 13:67–97. https://doi.org/10.1016/0142-9612(92)90001-5
52. I D Johnston, D K McCluskey CKLT and MCT (2014) Mechanical characterization of bulk Sylgard 184 for microfluidics and microengineering Related content. https://doi.org/10.1088/0960-1317/24/3/035017
53. Paggi CA, Venzac B, Karperien M, et al (2020) Monolithic microfluidic platform for exerting gradients of compression on cell-laden hydrogels, and application to a model of the articular cartilage. Sensors Actuators, B Chem 315:. https://doi.org/10.1016/j.snb.2020.127917
54. Chan DD, Cai L, Butz KD, et al (2015) In vivo articular cartilage deformation: noninvasive quantification of intratissue strain during joint contact in the human knee. Nat Publ Gr. https://doi.org/10.1038/srep19220
55. Leijten JCH, Bos SD, Landman EBM, et al (2013) GREM1, FRZB and DKK1 mRNA levels correlate with osteoarthritis and are regulated by osteoarthritis-associated factors. Arthritis Res Ther 15:R126
56. Ray A, Singh PNP, Sohaskey ML, et al (2015) Precise spatial restriction of BMP signaling is essential for articular cartilage differentiation. Development 142:1169–1179
57. Lee W, Guilak F, Liedtke W Role of Piezo Channels in Joint Health and Injury. https://doi.org/10.1016/bs.ctm.2016.10.003
58. Lee W, Leddy HA, Chen Y, et al (2014) Synergy between Piezo1 and Piezo2 channels confers high-strain mechanosensitivity to articular cartilage. Proc Natl Acad Sci U S A 111:E5114–E5122. https://doi.org/10.1073/pnas.1414298111
59. TD B, EL R, RB M, DB B (1984) Finite element studies of some juxtarticular stress changes due to localized subchondral stiffening. J Biomech 17:. https://doi.org/10.1016/0021-9290(84)90075-7
60. Burr DB (2004) Anatomy and physiology of the mineralized tissues: Role in the pathogenesis of osteoarthrosis. Osteoarthr Cartil 12:20–30. https://doi.org/10.1016/J.JOCA.2003.09.016
61. Ferguson VL, Bushby AJ, Boyde A (2003) Nanomechanical properties and mineral concentration in articular calcified cartilage and subchondral bone. J Anat 203:191–202. https://doi.org/10.1046/j.1469-7580.2003.00193.x
62. Dreier R (2010) Hypertrophic differentiation of chondrocytes in osteoarthritis: the developmental aspect of degenerative joint disorders. Arthritis Res Ther 12:216. https://doi.org/10.1186/ar3117

6 Towards an osteochondral unit on a chip: engineering of complex bilayer constructs as possible tools for the study of mechanically-driven OA traits in chondral and subchondral tissues

The work described in this chapter was carried out in the framework of a collaboration between the Microfluidic and Biomimetic Microsystems Laboratory of Politecnico di Milano, (Milan, Italy) and the Tissue Engineering Laboratory of the University Hospital of Basel (Basel, Switzerland).

6.1 Introduction

Collocated at the epiphysis of diarthrodial joints, the cartilage-bone interface is a multi-layer composite comprising hyaline cartilage deep zone, the basophilic tidemark, calcified cartilage, the cement line, and subchondral bone plate [1]. The close physical association between layers leads to a deep connection between compartments in both joint homeostasis and disease [2].

In osteoarthritis (OA) the normal state of cartilage-bone cross-talks is altered by vasculature and innervation invading the normally avascular cartilage deep zone [5], and by an increase in the number of subchondral bone microcracks, factors which are all posited to act as transport conduits facilitating molecular passage among tissues [3]. OA was also associated with calcified cartilage hyper-mineralization, that possibly exacerbates the catabolic processes responsible for hyaline cartilage erosion [4], and with subchondral bone marrow replacement by a fibrovascular tissue [5] demonstrating a deep pathological involvement of all subchondral structures.

An evaluation of specific modifications undergone by the osteochondral unit (OCU) tissues during OA evolution was performed in Chapter 4. The present knowledge of the causal relationship of OCU tissues alterations is however very limited [2]. Some authors hypothesized, for instance, that changes in architecture and composition of subchondral bone precede cartilage degradation, functioning as a trigger for catabolic processes due to altered loading patterns [12].

The study of these causal links could be helped by *in vitro* OCU models balancing relevance to the clinical conditions with a strict control over the environmental parameters and a sufficient operational ease.

A promising OoC based device to provide multiple microtissues with compression levels similar to those experienced in the OCU was described in Chapter 5. The development of cellular constructs representative the different OCU layers (i.e. cartilage, calcified cartilage, and vascularized subchondral bone) remains however a challenge.

During development, joint formation is mediated by a strict temporal and spatial control of bone morphogenic protein (BMP) and wingless/integrated (Wnt) pathways [6]. OCU models based on the provision of BMP2 gradients to mesenchymal stromal cells (MSCs) allowed to develop biphasic constructs mimicking cartilage and mineralized tissues [1]. Strategies to deliver morphogens gradients ranged from fluid flow [1], to BMP2-conjugated particles distributed by buoyancy and magnetic fields [7, 8]. While bone marrow derived MSCs are a relatively easy to procure cellular source, MSCs were demonstrated to spontaneously assume an hypertrophic phenotype upon chondrogenic differentiation [9], a trait which is typical of chondrocytes following OA onset [10].The use of MSCs to engineer hyaline cartilage constructs could thus lead to the introduction of confounding factors, attributing to a given OA trigger a phenotype which is due to the cellular commitment.

Conversely, MSCs could represent a valuable cell source to model calcified cartilage. While this tissue has a pivotal role in OCU load transfer [13], it is however often neglected in *in vitro* osteochondral models.
As regards vascularization, instead, different *in vitro* vascular bone models have been presented, but the main research focus was typically cancer metastases rather than joint pathologies [15]. However, a recent study addressed the interaction between cartilage and the vascular compartment correlating the presence of endothelial cells to an enhanced expression of osteogenic genes by hypertrophic chondrocytes [14].
Finally, an osteochondral model featuring both a cartilaginous and a vascularized bone compartment was recently reported demonstrating how incorporation of vascular cells modifies the differentiative potential of MSCs [16]. Further investigations are however necessary.
In this scenario, in the present chapter different OoCs platforms and cell culture models were exploited to provide a proof-of-concept recapitulation of specific aspects of the OCU, namely coupling of hyaline cartilage with calcified cartilage and vascular subchondral tissues, and mimicry of the mechanically active joint environment. Specifically, primary human articular chondrocytes (hACs) and MSCs were differentiated, respectively, in hyaline cartilage and calcified cartilage first in macroscale 3D aggregates and then in on-chip microconstructs. A biphasic construct integrating the two tissues was then achieved through a specifically designed OoC platform allowing a direct interface between two adjacent cell-laden hydrogels. The model was furthermore integrated with a vascular compartment preliminary assessing how endothelial cells influence MSCs differentiation. Finally, through an OoC platform capable of providing spatially discrete mechanical compression to biphasic constructs (as described in Chapter 5), a preliminary evaluation of the effect of loading on the obtained biphasic constructs was performed.

6.2 Addition of beta glycerophosphate to chondrogenic medium allows formation of a mineralized chondrogenic tissues by mesenchymal stromal cells while not impairing the chondrogenic potential of articular chondrocytes

hACs were adopted in the development of a hyaline cartilage model. Achievement of a mineralized tissue was pursued by differentiation of MSCs. In joints, hyaline cartilage is directly interfaced with a layer of calcified cartilage persisting after bone plate closure through endochondral ossification [21]. MSCs were, therefore, differentiated following a protocol aimed at obtaining a hypertrophic mineralized tissue through a development inspired endochondral process [22] rather than direct intramembranous ossification.

With the final aim of obtaining a complex bi-layer construct, comprehensive of both hACs and MSCs, the formulation of a single culture medium to differentiate the abovementioned cellular sources, respectively, in hyaline cartilage and calcified cartilage was investigated. An initial assessment of the differentiation capacity of the proposed medium formulation was performed with a previously established scaffold-free macroscale 3D cellular aggregate (i.e. pellet) model [9] focusing on detecting possible changes in hACs chondrogenicity. A more detailed analysis of the phenotype assumed by both hACs and MSCs was then performed in microfluidic devices.

6.2.1 Human MSCs collection, isolation and expansion

Human MSCs were isolated from bone marrow aspirates and processed as previously described [23]. Briefly, marrow aspirates (20 mL volume) were harvested from healthy donors (two males and two females, 35 ± 15 years old) during routine orthopaedic procedures involving exposure of the iliac crest. Bone marrow harvesting was performed after informed consent and in accordance with the local ethics committee (University Hospital Basel, Switzerland). A bone-marrow biopsy needle (Argon medical devices) was inserted through the cortical bone, and the aspirate was immediately transferred into plastic tubes containing 15,000 IU heparin. Isolated MSCs were counted using Crystal violet, plated in tissue culture flasks and expanded in a humidified 37°C/5% CO_2 incubator in minimum essential medium eagle - Alpha modification (α-MEM), containing 10% foetal bovine serum (FBS), 4.5 mg/mL D-glucose, 0.1 mM nonessential amino acids, 1 mM sodium pyruvate, 100 mM Hepes buffer, 100 Ul/mL penicillin, 100 µg/mL streptomycin, and 0.29 mg/mL L-glutamate, further supplemented with 5 ng/mL of fibroblast growth factor-2 (FGF-2, R&D Systems). Medium was changed twice a week. After approximately 10 days, when they were about 80% confluent, cells were rinsed with phosphate buffered saline (PBS), detached using 0.05% trypsin/0.53 mM EDTA and replated at 5×10^3cells/cm^2. MSCs were used at passage 3 for subsequent experiments.

6.2.2 Healthy human articular chondrocytes collection, isolation and expansion

Macroscopically normal human articular cartilage was obtained from the knee joints of a total of 4 patients with unknown clinical history of joint disorders (four males, 56 ± 6 years old), and collected as previously described after informed consent by relatives and in accordance with the local ethics committee (University Hospital Basel, Switzerland). Cartilage biopsies were minced and digested enzymatically. Briefly hACs were isolated using 0.15% type II collagenase (10 ml solution/g tissue, 300 U/mg, Worthington Biochemical Corporation, Lakewood, NJ) for 22 h and resuspended in Dulbecco's modified Eagle's medium (DMEM) containing 10% foetal bovine serum, 4.5 mg/ml D-Glucose, 0.1 mM nonessential amino acids, 1 mM sodium pyruvate, 100 mM HEPES buffer, 100 U/ml penicillin, 100 µg/ml streptomycin, and 0.29 mg/ml L-glutamine (i.e. complete medium). Isolated chondrocytes were counted using Trypan blue, plated in tissue culture flasks at a density of 10^4 cells/cm^2 and cultured in complete medium with the supplementation of 1 ng/ml of transforming growth factor-β1 (TGF-β1) and 5 ng/ml of FGF-2 in a humidified 37°C/5% CO_2 incubator. The growth factor combination was selected based on its previously reported ability to increase human chondrocyte proliferation and capability to re-differentiate, even upon an initial dedifferentiating culture [24, 25]. At an approximate 80% confluency, first passage cells (P1) were rinsed with phosphate buffered saline (PBS), detached using 0.05% trypsin/0.53 mM EDTA and replated at 5×10^3cells/cm^2. hACs were used at passage 3 for following experiments.

6.2.3 Differentiation of hACs and MSCs towards hyaline cartilage and calcified cartilage in macroscale 3D scaffold-free aggregates.

hACs and MSCs isolated and expanded as described above were cultured in 3D pellets for 14 days in either chondrogenic medium (CM) or mineralizing medium (MM). Briefly, P3 cells were detached using 0.05% trypsin/0.53 mM EDTA and counted with Trypan blue. 2.5 x 10^5 cells were adopted for each pellet. Cellular aggregation was obtained via centrifugation (1300 RPM, 3 min), in screw top microtubes (Thermo-fisher). CM was constituted by DMEM (Sigma–Aldrich) containing, 4.5 mg ml^{-1} d-glucose, 0.1 mM non-essential amino acids, 1 mM sodium pyruvate, 100 mM HEPES buffer,100 U ml^{-1} penicillin, 100 µg ml^{-1} streptomycin, 0.29 mg ml^{-1} l-glutamine, 1.0 mg/ml bovine insulin, 0.55 mg/ml human transferrin, 0.5 µg/ml sodium selenite, 50 mg/ml bovine serum albumin, 470 µg/ml linoleic acid, and 1.25 % of human serum albumin and supplemented with 0.1 mM ascorbic acid 2-phosphate, 10^{-4} mM Ddexamethasone and 10 ng ml^{-1} TGF-β3. MM was obtained by addition to the CM of 10 mM beta-Glycerophosphate (β-Gly, Sigma Aldrich), previously demonstrated to induce mineralization [26]. Culture medium was changed thrice a week for 2 weeks.

At the end of the culture period, constructs were harvested for histological analyses. Briefly, pellets were fixed with 4% paraformaldehyde for 24 hours at 4 °C, and subsequently dehydrated and embedded in

paraffin. A 5 μm thickness was used to section samples. Safranin-O (Saf-O)/fast green staining (Fluka) was performed to visualise the glycosaminoglycan (GAG) content, mineralization was determined through alizarin red staining (Sigma Aldrich).

hACs maintenance of a hyaline cartilage phenotype upon exposure to the MM was also investigated by quantification of pellets GAG accumulation and DNA content, and gene expression.

Samples for biochemical analyses were digested in 300 mL of proteinase-K (1 mg/mL proteinase-K in 50 mM Tris with 1 mM EDTA, 1 mM iodoacetamide, and 10 μg/mL pepstatin-A) overnight at 56°C. GAG amounts were measured spectrophotometrically after reaction with dimethylmethylene blue using chondroitin sulphate as a standard [27]. The amount of DNA was measured spectrophotometrically using the CyQuant cell proliferation assay Kit (Molecular Probes, Eugene, OR), according to manufacturer's instructions. The ratio GAG/DNA was calculated.

Gene expression was quantified through real-time quantitative polymerase chain reaction (RT-qPCR) as further detailed in section 6.7.2. Results of histological and gene expression analyses, of both hACs and MSCs are, reported in Fig. 1.

The MM formulation allowed differentiation of MSCs in mineralized and GAG rich constructs reminiscent of calcified cartilage. With respect to pellets cultured in CM, those supplemented with β-Gly remained positive for Saf-O staining, demonstrating retention of GAG deposition, but exhibited MSCs with an enlarged, hypertrophic morphology (Fig. 1a), and were positive for alizarin red staining of calcium deposits (Fig. 1b). Notably, no mineralization was registered with the CM formulation.

Conversely, supplementation with MM did not alter hACs chondrogenic potential, nor induced mineralization or hypertrophic traits in hACs pellets. Saf-O stainings revealed no differences between CM and MM conditioning (Fig. 1c). Furthermore, no traces of mineralization were indicated by the alizarin red staining, independently from the adopted medium formulation.

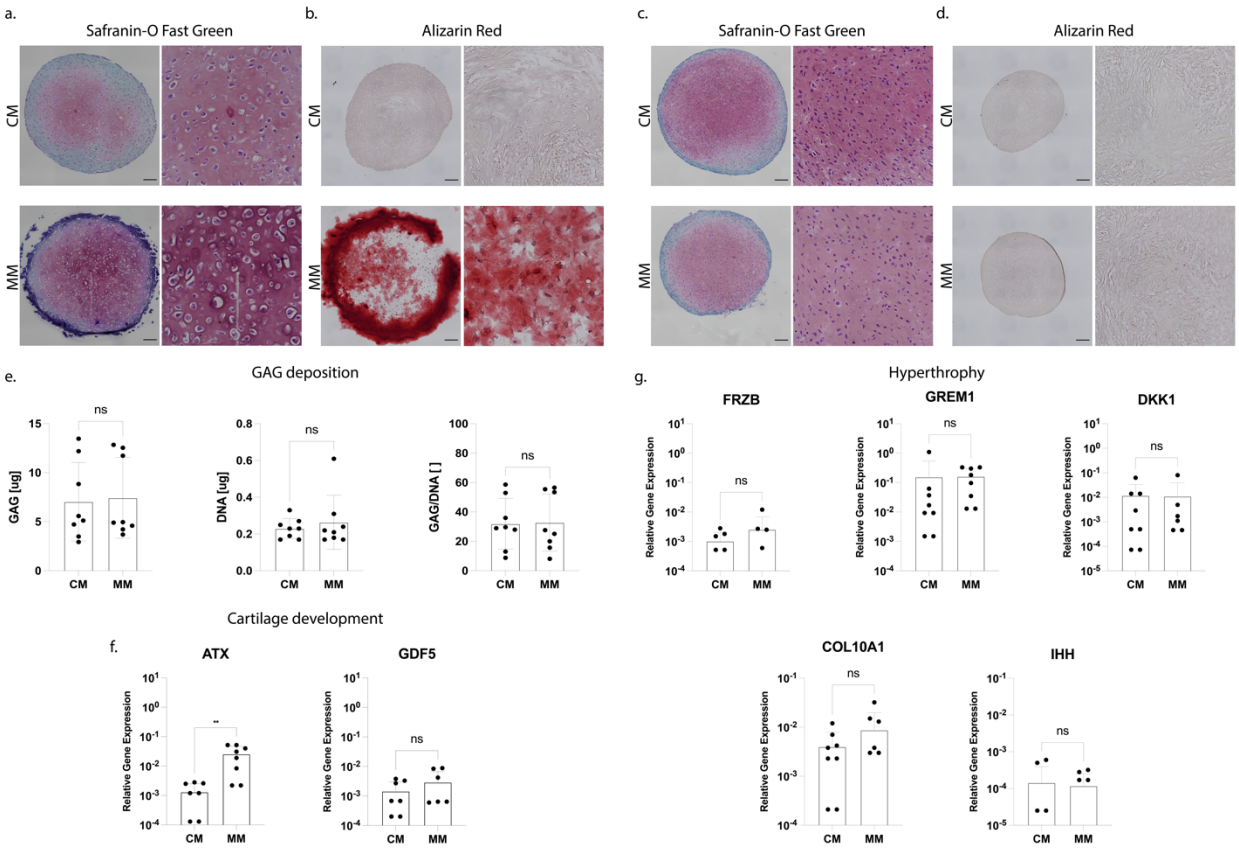

Figure 1: ***Effect of β-Gly addition to CM on hACs and MSCs differentiation in hyaline and mineralized cartilage. a,*** *Safranin-O / fast green staining of MSCs after 14 days of culture in CM or MM. MM had no impact on GAG deposition as evidenced by the Safranin-O positive staining in the constructs. Upon culture with MM, MSCs presented however an enlarged hypertrophic morphology as visible in the insets. Scale bar 100 µm.* ***b,*** *Alizarin red staining of MSCs cultured with CM or MM. No mineralisation was present in the former case while deposition of a calcium deposit rich matrix was present in the latter. a, b, n≥2 biologically independent samples from n=3 donors were considered in analyses. Scale bar 100 µm.* ***c,*** *Safranin-O / Fast green staining of hACs after 14 days of culture in CM or MM. MM had no impact on GAG deposition as evidenced by the Safranin-O positive staining in the constructs. Differently than MSCs, hACs did not display an enlarged hypertrophic morphology upon MM supplementation.* ***d,*** *Alizarin red staining of hACs cultured with CM or MM. No mineralisation was present regardless of the adopted medium formulation. c,d n≥2 biologically independent samples from n=4 donors were considered in analyses. Scale bar 100 µm.* ***e,*** *GAG and DNA quantification of hACs derived constructs exposed to CM or MM. n≥2 biologically independent samples from n=3 donors were considered in analyses. Statistics by unpaired t test or Mann-Whitney test, respectively, for normal and non-gaussian populations. Populations' normality was assessed by Shapiro-Wilk and Kolmogorov-Smirnov tests.* ***f, g,*** *Expression of genes correlated with hyaline cartilage formation during embryonic development (f) and assumption of hypertrophic traits (g) in hACs. Gene expression was measured by RT-qPCR. Statistics by unpaired t test or Mann-Whitney test, respectively, for normal and non-gaussian populations. Population normality was assessed by Shapiro-Wilk and Kolmogorov-Smirnov tests. n≥2 biologically independent samples from n=3 donors were considered in analyses. All gene expression values are normalized relative to GAPDH expression and values are log scale. ns = non significant, ** P< 0.01.*

hACs constructs had a donor-dependent chondrogenic potential (data not shown). To highlight possibly medium-dependent alterations, the GAGs deposition was quantified. Both absolute GAG values and the ratio between GAG and DNA per construct did not vary between experimental conditions, signifying that addition of β-Gly to CM does not alter hACs GAG deposition capacity.

Furthermore, gene expression of growth differentiation factor 5 (*GDF5*) and autotaxin (*ATX*), associated with joint interzone embryonic development [28] and regulation of cartilage formation [29], were respectively not influenced and increased by MM supplementation with respect to CM controls (Fig. 1f). Finally, expressions of wingless-type MMTV integration site (Wnt) antagonist frizzled-related protein (*FRZB*), *BMP* antagonist Gremlin-1 (GREM1), and dickkopf 1 homolog *(DKK1),* characterized as hypertrophy brakes in adults human cartilage, were not modulated by the medium formulation in hACs [30] (Fig. 1g). The same was true for the expression of the direct hypertrophy markers collagen type X (*COL10A1*) and Indian hedgehog (IHH) [31] (Fig. 1g). Overall, presented data demonstrated that addition of β-Gly to CM (i.e. MM) allows differentiation of MSCs into calcified cartilage, while it does not affect hACs chondrogenic potential.

6.3 Addition of β-Gly to chondrogenic medium allows development of cartilage and calcified cartilage on chip

The possibility of obtaining separate hyaline and calcified cartilage microconstructs on chip (respectively from hACs and MSCs) through conditioning with the described MM formulation was investigated.

A previously described OoC platform employed for the development of a cartilage on chip model was adopted [19]. The platform is constituted by a culture chamber composed of a central gel channel divided by two rows of overhanging T shaped pillars from lateral culture medium channels (an accurate description of the device was provided in Chapter 2).

hACs or MSCs were embedded into an enzymatically cross-linkable and degradable polyethylene-glycol (PEG) based hydrogel [32] and injected into microdevices at a density of $5x10^4$ cells μl^{-1}. Hydrogels with a final dry mass content of 2% were prepared, as previously described, by stoichiometrically balanced ([Lys]/[Gln] = 1) precursor solutions of 8-PEG-Gln and 8-PEG-MMPsensitive-Lys in Tris-Buffer (TBS, 50 mM, pH 7.6) containing 50 mM calcium chloride. The cell-laden PEG pre-polymer solution was manually injected into the culture channel of the microscale device and incubated for 15 minutes (5% CO_2 and 37 °C) before filling the lateral channels with either CM or MM. Culture medium was changed every second day. Images of the constructs were acquired through a brightfield microscope with an embedded camera (EVOS XL Core, Life Technologies) to assess tissues maturation during the culture period. Upon 14 days of static differentiation, constructs were collected for immunofluorescence and RT-qPCR as described in section 6.7.2. Results are reported in Fig. 2.

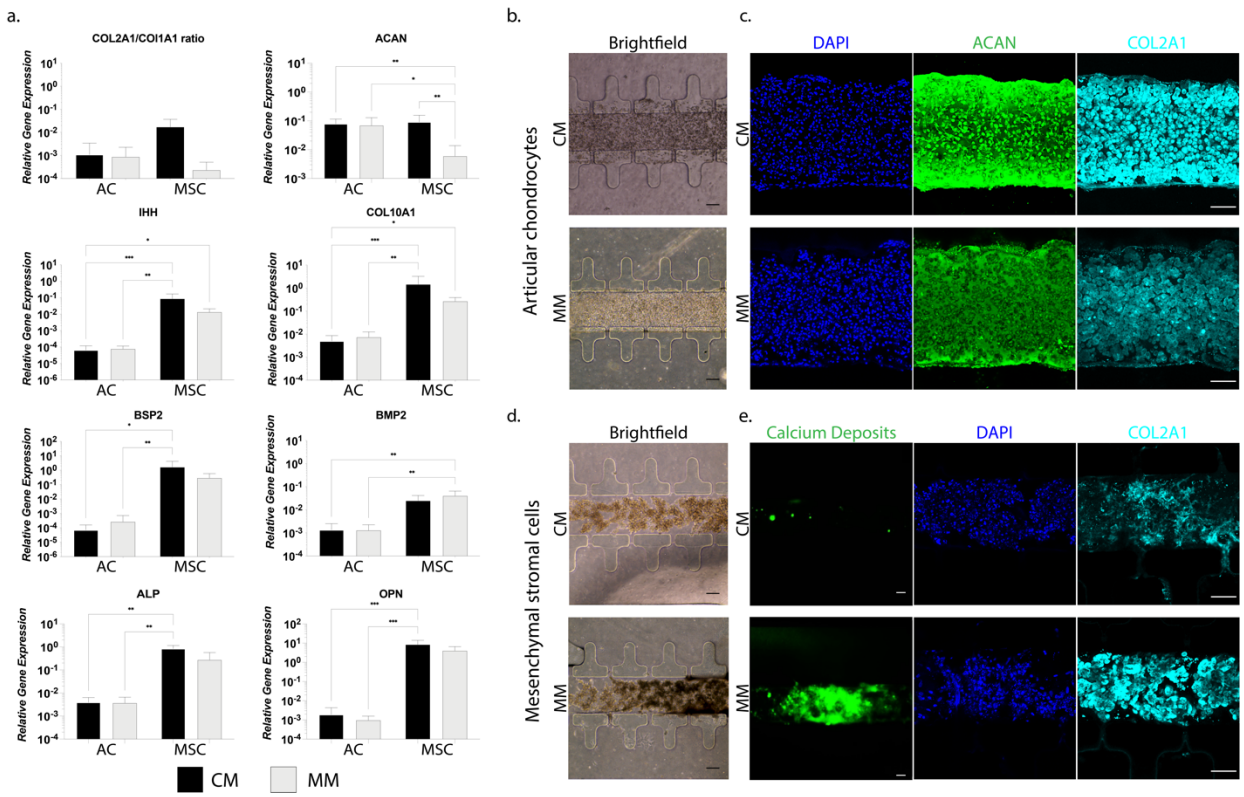

Figure 2: ***Establishment of hyaline and calcified cartilage models on chip. a,*** *Expression of genes correlated with cartilage anabolysm (COL2A1/COL1A1 and ACAN) hyperthrophy (COL10A1, IHH), and bone matrix formation (BMP2, BSP2, ALP, OPN) following hACs and MSCs constructs conditioning with CM or MM. Gene expression was measured by RT-qPCR. Statistics by ordinary one way Anova or Mann-Whitney tests, respectively, for normal and non-gaussian populations. Population normality was assessed by Shapiro-Wilk and Kolmogorov-Smirnov tests. n=3 biologically independent samples from n≥2 donors were considered in analyses. All gene expression values are normalized relative to GAPDH expression and values are log scale. * P<0.05,** P< 0.01, *** P<0.001.* ***b,*** *Representative brightfield images of hACs based microconstructs after 14 days of culture with either CM or MM.* ***c,*** *Immunofluorescence images of hACs based constructs after 14 days of culture confirming achievement of a hyaline cartilage like constructs with administration of both media. DAPI is represented in blue, ACAN in green and COL2A1 in cyan.* ***d,*** *Representative brightfield images of MSCs based microconstructs after 14 days of culture with either CM or MM. MM but not CM supplementation determined deposition of dark mineral deposits.* ***e,*** *Immunofluorescence images of MSCs based constructs after 14 days of culture. DAPI is represented in blue, calcium deposits in green, and COL2A1 in cyan. Both medium formulations determined COL2A1 accumulation; mineral deposition was specific of MM supplementation. b, c, d, e Scale bar 100 µm.*

Supplementation of MM to hACs in microdevices did not hinder the formation of cartilaginous like constructs while allowed MSCs to differentiate into calcified cartilage like microtissues.

Specifically, the addition of β-Gly had no effect on the expression of anabolic genes in hACs (i.e. *COL2A1/COL1A1* ratio and *ACAN*), confirming maintenance of the chondrogenic potential. Conversely, β-Gly supplementation led to a diminished expression of *ACAN* (statistically significant) and *COL2A1* (non-statistically significant) in MSCs (Fig. 2a).

With the aim of achieving well distinguished hyaline cartilage and hypertrophic calcified cartilage constructs, the expression of the hypertrophy markers *COL10A1* and *IHH* was determined. Culture medium variation did not affect *COL10A1* and *IHH* expression in hACs nor in MSCs (Fig. 2a). Notably, distinctly

higher levels of both markers were expressed by MSCs as compared to hACs, demonstrating their tendency in assuming an hypertrophic phenotype.

Given the deposition of a mineralized matrix by MSCs pellets upon exposure to β-Gly (Fig. 1b), the expression of genes associated with a bone related signature was determined [34]. Specifically, the expression of bone morphogenic protein-2 (*BMP2*), bone sialoprotein-2 (*BSP2*), alkaline phosphatase (*ALP*), and osteopontin (*OPN*) genes was quantified. For both cell types, no differences in expression were detected between CM and MM cultured constructs, while statistically significant higher levels of all genes were expressed by MSCs with respect to hACs.

Gene expression results were confirmed by constructs characterization by imaging.

No differences were detectable upon brightfield visual inspection of CM and MM conditioned hACs constructs after 14 days of culture (Fig. 2b). Similarly aggrecan (ACAN), the most prominent proteoglycan in cartilage matrix [33], and COL2A1 were positive in both conditions (Fig. 2c). Independently from the adopted medium, hACs based constructs were negative for calcium mineral deposition (data not shown).

The MM allowed instead accumulation of a mineralized matrix by MSCs. After 14 days, MSCs constructs displayed deposition of dark matrix regions as evident from the brightfield images (Fig. 2d). Dark regions, which were more prominent following hypertrophic maturation induced by MM, were found to correspond to calcium deposits areas (Fig. 2e). No differences were detected in COL2A1 accumulation between experimental conditions (Fig. 3d) despite the detected decrease in gene expression following MM conditioning.

Overall, these data demonstrate that distinct hyaline like and calcified cartilage constructs can be achieved on chip through the proposed MM composition and cellular sources.

6.3.1 Characterization of MSCs based calcified cartilage constructs on chip

While a cartilage on chip model had previously been developed ([19], Chapter 2), no previous reports of calcified cartilage on chip were available. A characterization of MSCs constructs maturation in time upon MM differentiation was thus performed. As described above, both *COL2A1/COL1A1* ratio and *ACAN* expression was upregulated during maturation (Fig. 3a). Notably, furthermore a statistically significant increase in cartilage anabolic genes expression (*COL2A1/COL1A1* ratio and *ACAN*) was already present after 7 days of static culture (Fig. 3a). The same trend was detected for *COL10A1* and *IHH*. Congruently with the increase in *COL10A1* and *IHH* expression, constructs maturation did not led to upregulation of the hypertrophy brake *FRZB*, conversely from what previously demonstrated for hACs derived cartilage microconstructs [19].

An upregulated gene expression in time was also detected in the bone markers *BSP2* and *ALP*, confirming, furthermore, the achievement of higher gene expression levels already after 7 days of static maturation.

Notably, instead, the expression of the bone marker osteocalcin (*OCN*) did not show a statistically significant increase despite constructs being positive for OCN deposition, similarly to ALP and OPN, after 14 days of maturation (as depicted in Fig. 3b).

Presented data give an overall indication that MSCs can undergo a developmental reminiscent on-chip differentiation into calcified cartilage constructs thus mimicking the thin layer of mineralized tissue at the interface between cartilage and bone in joints. Analysis of the maturation timeline, furthermore, proved the acquisition of a mature gene expression signature already after 7 days of culture.

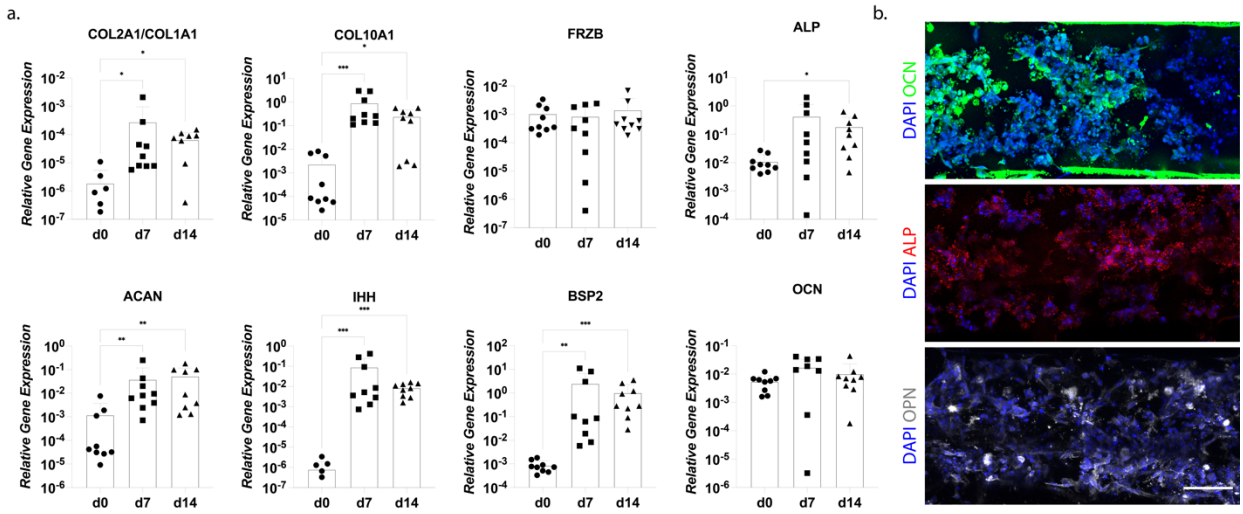

Figure 3: ***Calcified cartilage on chip maturation assessment. a,*** *Maturation in time of MSCs based constructs upon MM supplementation. Gene expression was measured by RT-qPCR. Statistics by ordinary one way Anova or Mann-Whitney tests, respectively, for normal and non-gaussian populations. Population normality was assessed by Shapiro-Wilk and Kolmogorov-Smirnov tests. n=3 biologically independent samples from n=3 donors were considered in analyses. All gene expression values are normalized relative to GAPDH expression and values are log scale. * P<0.05,** P< 0.01, *** P<0.001.* ***b,*** *Characterization of bone related matrix component depostion of MSCs based constructs after 14 days of culture. DAPI is represented in blue, OCN in green, ALP in red, and OPN in grey. Scale bar 100 µm.*

6.4 A bi-chamber device allows to co-culture directly interfaced hyaline cartilage and calcified cartilage microconstructs on chip

A biphasic bi-layer construct composed of both hyaline cartilage and calcified cartilage was developed aiming at modelling the organization of the two tissues in the OCU. A dedicated OoC device designed to host both constructs and provide them with a direct (and visible) interface was developed.

6.4.1 Device concept: a microscale platform allowing co-culture of directly interfaced tissues and tissue-tissue interface direct visualization.

An *ad hoc* microfluidic based platform was developed to host two directly interfaced constructs, with the aim to optimize and assess the maturation of hACs- and MSCs-based microtissues upon co-culture. As compared to the device described in Chapter 5 (which enables to host two vertically superimposed

constructs mimicking OCU tissues configuration in *in vivo*), the here introduced device was designed disposing the constructs one next to the other with the aim of permitting a direct visualization of the two tissues and their interface.

The device, depicted in Fig. 4a, is constituted by a culture chamber composed by two central hydrogel channels separated by two rows of overhanging T shaped pillars from lateral culture medium channels. A third row of hexagonal shaped pillars was introduced to divide the two central hydrogel chambers. A thin membrane constitutes the culture chamber bottom surface. While no compression was applied in the maturation phase, the devices was designed introducing a gap between the bottom surface of the pillars and the culture chamber floor (both external and central pillar rows) to keep constant the gel-medium interface area with respect to previously presented devices (as described in chapter 2, 3 and 5). Pillars and gap heights were respectively 100 µm and 43 µm, reflecting the previously introduced aspect ratio of both single culture devices (Chapter 2) and complex co-culture devices (Chapter 5). Both hydrogel channels were 300 µm wide and 143 µm thick. 30 µm windows were introduced between pillars. The central hexagonal shaped pillars were designed to allow separate injection of the two hydrogels while maximising the available contact interface. Pillars' hexagonal cross-sections had a width of 50 µm and a length of 90 µm. The distance between two subsequent pillars was set to 50 µm.

6.4.2 Device fabrication procedure

Devices were produces as previously specified. Briefly, chambers features were designed through Computer Aided Design (CAD) Software (AutoCAD 2020, Autodesk). Master moulds were fabricated in a cleanroom environment (Class ISO6) using multilayer direct laser writing (Heidelberg MLA100) of SU-8 2035 or SU-8 2100 (MicroChem) onto 102 mm silicon wafer substrates. Microscale systems were realized by replica moulding of master moulds features in polydimethylsiloxane (PDMS, Sylgard 184; Dow Corning), polymerized with defined casts at a 10:1 weight ratio of base to curing agent. All PDMS parts were cured for at least 2 hours at 65°C. Final features had a cross section of 2175.5 µm (width) by 143 µm (height). Appropriate holes for culture medium reservoirs (diameter 5 mm) and hydrogels channels inlets and outlets (diameter 1mm) were bored with biopsy punchers. Device layers were bonded treating surfaces to be united with air plasma (Harrick plasma) and bringing them in conformal contact for at least 30 min at 80°C to achieve irreversible adhesion.

Three device chambers were introduced in the same platform. A picture of an assembled device is reported in Fig. 4b. A cross section of the culture chamber is depicted in Fig. 4c highlighting the lateral and the central pillars rows.

6.4.3 Assessment of co-culture effects on hACs and MSCs maturation on chip

Complex biphasic hyaline cartilage and calcified cartilage constructs were obtained co-culturing hACs and MSCs in the described device. Cells were embedded in the previously defined enzymatically cross-linked and degradable PEG based hydrogel formulation [32] at a density of 5 x 10^4 cells/µl. Complex constructs were obtained by subsequent injections of hACs and MSCs laden hydrogels in the respective compartments (Fig. 4a). Complete polymerization of the first hydrogel was necessary before injection of the second formulation.

Constructs were cultured statically for 14 days in MM. Culture medium was changed every second day. Brightfield pictures were acquired to evaluate constructs maturation in time. After 14 days, constructs were collected for immunofluorescent analyses. Alizarin red staining were also performed directly on chip to quantify the amount of calcium deposits in the culture medium chambers.

Confirming the results obtained in single culture, co-culture maturation in MM led to accumulation of a mineralized matrix exclusively in MSCs based microtissues. In the MSC compartment, an increase in the presence of constructs dark areas, previously demonstrated to correspond to mineralized matrix, was directly visible from brightfield images (Fig. 4d). Furthermore, only the MSCs compartment resulted positive for a hydroxyapatite specific staining (OsteoImage mineralization assay, Lonza), demonstrating deposition of a bone reminisced mineral matrix, while both compartments were positive for ACAN staining (Fig. 4e).

It was also possible to quantify the amount of calcium deposits in the culture medium channels of hACs and MSCs compartments respectively. Alizarin red staining was performed directly on chip (Fig. 4f). While a direct distinction in mineral deposition between the two cellular constructs could not be performed due to the strong alizarin red background (hydrogels alone without cells resulted positive for the staining, data not shown), a difference was noticeable between culture medium channels, the one adjacent to the MSCs construct resulting positive for alizarin red (Fig. 4f). A quantification of the calcium deposits in the lateral channels was performed as follows.

After removal of the constructs from the devices, these were cut along the longitudinal axis so to separate the MSCs and hACs lateral channels. Alizarin red positive calcium deposits were then dissolved incubating PDMS slabs in 10% acetic acid (30 mins, at 37 °C on an orbital shaker, followed by gentle manual scraping). The amounts of deposits were quantified correlating the quantities with alizarin red standards of known concentrations. Alizarin red concentration was determined measuring absorbance at 405 nm trough a configurable multimode microplate reader (synergy H1, BioTek instruments). Three independent devices from one donor per cellular type were considered in analyses.

Quantifications are reported in Fig. 4g. Results demonstrated release of calcium deposits in the culture medium channels adjacent to the MSCs construct. Conversely no deposition was detected for hACs, confirming their capacity of resisting mineralization in healthy conditions.

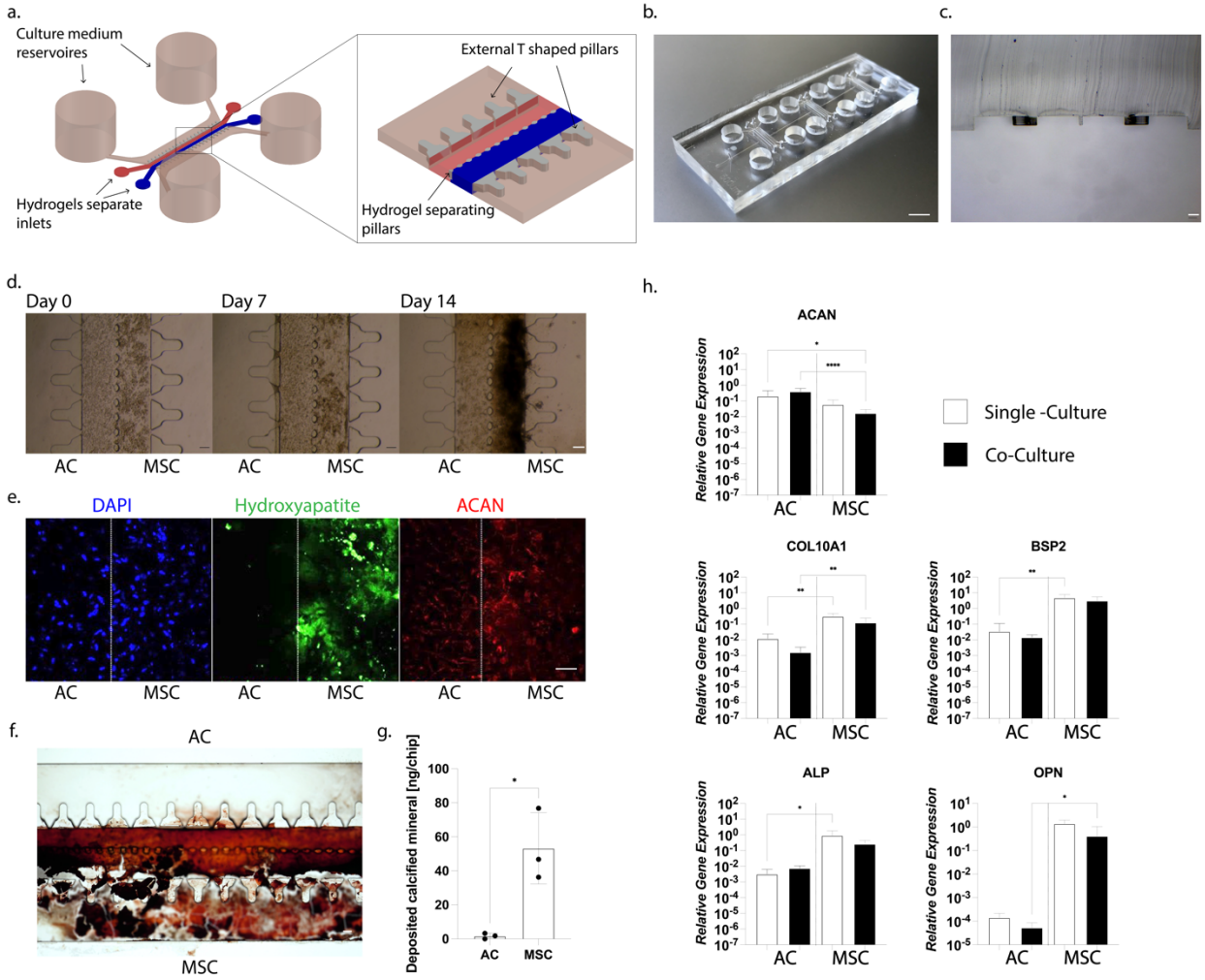

*Figure 4: **Assessment of hACs and MSCs co-culture on complex tissues maturation. a,** Schematization of the device. The two hydrogels hosted in the central gel channels are represented, respectively, in red and blue. Culture medium channels and reservoirs are represented in pink. A zoom in of the central section of the culture camber highlights the geometry of the T shaped lateral pillars and of the hexagonal central pillars. **b,** Photograph of an assembled PDMS device. Scale bar, 5 mm. **c,** Device culture chamber cross section; the three pillar rows are visible. Scale bar 100 µm. **d,** Brightfield images of hACs and MSCs constructs cultured in MM over time. Deposition of a mineralized matrix was peculiar of MSCs constructs. n≥2 biologically independent samples from n=2 donors for each cellular type were considered in analyses. Scale bar 100 µm. **e,** Immunofluorescence images of hACs (left) and MSCs (right) co-culture constructs after 14 days of static differentiation. DAPI is represented in blue, hydroxyapatite in green and ACAN in red. Scale bar 100 µm. **f, g,** Quantification of the calcium deposits in the medium channels next to ACs and MSCs constructs respectively. A representative alizarin red staining is reported in (f). A direct assessment of calcium deposition in the constructs could not be performed with alizarin red given the strong background signal of the hydrogels alone. Calcium deposits were however visible in the medium channels next to the MSCs constructs. A quantification of calcium deposits in lateral channels was performed after removal of the constructs. Results are reported in (g). n=3 biologically independent samples from n=1 donor per each cellular type were considered in analyses. Statistics by unpaired t test. Populations' normality was assessed through Shapiro-Wilk normality test. **h,** Effect of co-culture on constructs gene expression measured by RT-qPCR. GFP labelled chondrocytes were used to generate hACs constructs. At the end of the culture hACS and MSCs populations were sorted and the expression of relevant genes confronted with that of single culture respective controls. Statistics by ordinary one way Anova or Mann-Whitney tests, respectively, for normal and non-gaussian populations. Population normality*

*was assessed by Shapiro-Wilk and Kolmogorov-Smirnov tests. n≥6 biologically independent samples from n=1 hACs donor, and n=3 biologically independent samples from n≥2 MSCs donors were considered in analyses. All gene expression values are normalized relative to GAPDH expression and values are log scale. * P<0.05,** P< 0.01, **** P<0.0001*

Co-culturing hACs and MSCs did not affect their capacity to acquire distinct hyaline and calcified cartilage gene expression signatures. To correlate the co-culture with possible alterations in the gene expression profile, hACs were transduced to express green fluorescent protein (GFP). At the end of the 14 days maturation period, constructs were digested and cellular populations separated through fluorescent activated cellular sorting (FACS) flow cytometry (GFP transduction, construct digestion and sorting procedure were described in Chapter 5). Gene expression in the sorted populations was quantified by RT-qPCR. Separate hACs and MSCs constructs cultured in single channel devices were adopted as controls. At least three biologically independent devices for each experimental condition and each donor were considered. Cells from a single GFP positive hACs donor were cocultured with cells from n = 3 MSCs donors.

Gene expression quantification results are reported in Fig. 4h. No differences in expression of genes related to cartilage matrix deposition (*ACAN*), hypertrophy (*COL10A1*) and bone matrix deposition (*BSP2*, *ALP*, and *OPN*) between single culture and co-culture conditions were observed. Moreover, both hypertrophy related and bone related genes exhibited clearly higher expression levels in MSCs constructs, demonstrating that co-culture did not induce alterations in cells gene expression.

Notably, while similar ACAN deposition in both constructs was detected by immunofluorescence, a statistically significant lower expression of ACAN was found for MSCs in co-culture.

6.5 Coupling of cartilage constructs with a vascularized compartment

One of OA hallmarks is the vascular invasion of calcified cartilage and cartilage deep zone [5]. With the final aim of possibly replicating this feature in a complex OoC based *in vitro* model of OA OCU, a vascular component was introduced.

6.5.1 Incorporation of a vascular component in MSCs constructs

Achievement of a vascularized construct reminiscent of the subchondral layers in the OCU was aimed for by co-culturing MSCs and red fluorescent protein (RFP) expressing human umbilical vein endothelial cells (HUVECs) in the same construct.

A preliminary assessment of HUVECs effect on tissues maturation was performed adopting the previously presented single channel devices ([19], Chapter 2).

MSCs were isolated and expanded as previously described, RFP HUVECs at passage 0 (P0) were purchased (ANGIO-PROTEOMIE,cAP-0001RFP), and expanded in flask up to P3 using Endothelial Cell Growth Medium-2 BulletKit (EGM-2,LONZA). P4 RFP HUVECs were adopted in subsequent experiments.

MSCs and HUVECs were laden in the previously described PEG gel formulation at a respective density of $3x10^4$ cells μl^{-1} and $2x10^4$ cells μl^{-1}, maintaining constant the overall cellular density with respect to MSCs only constructs adopted as controls. Constructs (namely MSCs+HU) were cultured statically for 7 or 14 days. MSCs only constructs were conditioned with the previously described MM. MSCs+HU constructs were conditioned with a 1:2 dilution of MM and EGM-2. The final concentration of differentiating growth factors was kept constant with respect to the MM formulation (0.1 mM ascorbic acid 2-phospate, 10^{-4} mM Dexamethasone and 10 ng ml^{-1} TGF-β3, and 10 mM β-Gly). Constructs were collected for immunofluorescence analyses at day 7, and for both immunofluorescence and RT-qPCR at day 14. Brightfield images were acquired during the maturation period. Results are presented in Fig. 5.

HUVECs introduction in constructs resulted in formation of vascular like reticules after 7 days of culture (Fig. 5a). 3D confocal reconstructions of MSCs+HU constructs at day 7 are represented in Fig. 5b. Constructs resulted positive for the bone markers BSP2. Through 3D reconstructions it was moreover possible to visualize that HUVECs organised in reticules with capillary-like structures and with an internal lumen as indicated by the white asterisks in Fig. 5b. HUVECs co-culture with MSCs, however, hindered both mineralization (Fig. 5a brightfield images) and deposition of COL2A1. The phenomenon, incipient at day 7, was more evident at day 14 where co-culture constructs displayed a diminished presence of dark mineral areas and were negative for COL2A1. HUVECs reticules seemed moreover to start degrading at day 14 with cells acquiring an aberrant morphology and detaching form the main vessel bodies. Similar results were obtained by quantification of the gene expression by RT-qPCR performed on MSCs+HU and MSCs only constructs after 14 day of maturation (Fig. 5c). Aside from an increase in expression of the bone matrix marker *COL1A1* which was significantly upregulated in the MSCs+HU group, cartilage matrix markers (*COL2A1*), hypertrophy markers (*COL10A1* and *IHH*) and bone mineralization markers (*BSP2* and *OCN*) all exhibited downward trends with HUVECs addition.

Conclusively, these results indicate that coculture of MSCs and HUVECs (i) led to formation of a vascularized tissue but (ii) caused a decrease in expression of markers reminiscent of both calcified and hyaline cartilage. Furthermore, the presented data suggested that (iii) HUVECs culture was sustainable for shorter time frames than those indicated for the deposition of a cartilaginous matrix (i.e. 14 days). Further analyses are however required for a complete assessment of the intra-cellular effects on constructs maturation.

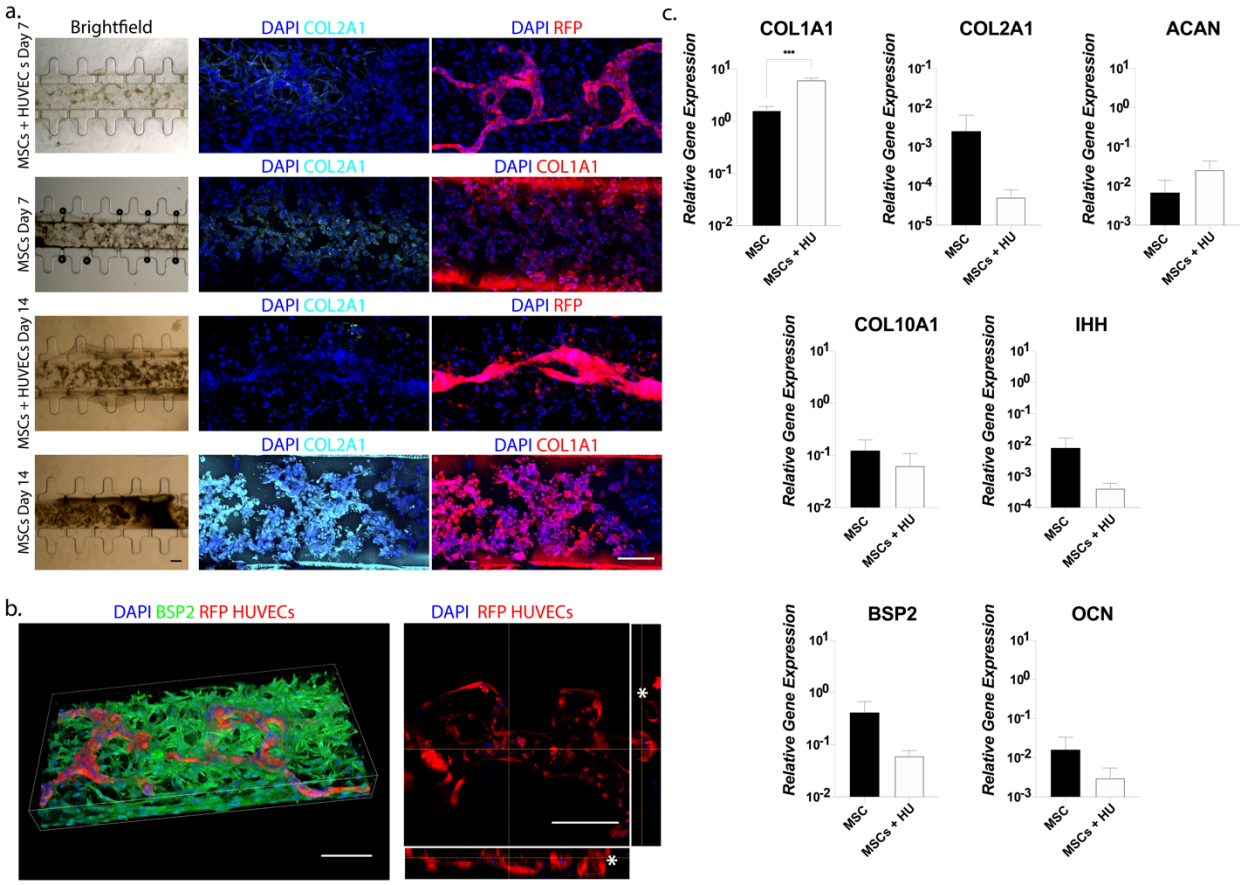

Figure 5: ***Introduction of the vascular component. a,*** *Brightfield and fluorescent images of MSCs and HUVECs co-cultures, or of MSCs alone, after 7 or 14 days of static maturation. DAPI is represented in blue, COL2A1 in cyan. Red represents RFP HUVECs or COL1A1 in co-culture and single constructs images respectively. Scale bar 100 µm.* ***b,*** *3D confocal reconstruction of MSCs-HUVECs co-culture constructs after 7 days of maturation. DAPI is represented in blue, BSP2 in greed, and RFP HUVECs in red. A detail of a tubular structure is represented on the right depicting both top view and side views. Capillary-like structures with an open lumen are highlighted by white asterisks. Scale bar 100 µm* ***c,*** *Gene expression of MSCs-HU and MSCs only constructs after 14 days of static maturation measured by RT-qPCR. Statistics by unpaired t test or Mann-Whitney test, respectively, for normal and non-gaussian populations. Population normality was assessed by Shapiro-Wilk test. n=3 biologically independent samples from n=1 donor were considered in analyses. All gene expression values are normalized relative to GAPDH expression and values are log scale.*

6.5.2 Coupling of vascular MSCs constructs with a hyaline cartilage layer

The possibility to couple the vascularized tissue with a hyaline cartilage layer was assessed. Based on the achieved results, the culture time was limited to 7 days, with the aim to investigate the cellular cross-talk between HUVEC and hACs, while being conscious that the formation of a complete cartilaginous tissues could not be achieved (requiring 14 days of maturation as demonstrated). Specifically, the following cross-talk / effects were hypothesized: i) a possible negative effect of chondrocytes on HUVECs reticule formation capabilities, or ii) HUVECs tendency to invade the hACs compartment even in the absence of OA like stimuli.

hACs and MSCs+HU were seeded in PEG hydrogels as indicated before. Composite tissues were obtained making use of the platform described in section 6.4 to allow an immediate visualization of the interface between constructs (GFP hACs and RFP HUVECs were adopted to facilitated the distinction of relevant structures). The described 1:2 dilution of MM and EGM-2 was used during the differentiation period. Devices seeded with MSCs+HU (or MSCs alone) on one side and empty PEG hydrogels on the other were used as controls.

At the end of the culture period biphasic constructs were harvested for immunofluorescence analyses. Results are depicted in Fig. 6. Flanking of hACs and MSCs+HU constructs did not inhibit formation of a HUVEC based reticule which was still well visible and formed (as evident from the RFP signals in Fig. 6a). Interestingly, moreover, no MSCs or HU migration was visible when GFP hACs were present in the adjacent compartment, while a cellular invasion was detected towards the cell-free hydrogel in the control condition. As visible in the insets in Fig.6a, in fact, no GFP negative and RFP positive (i.e. HUVECs) or GFP negative and RFP negative (i.e. MSCs) cells could be detected in the hACs compartment. This data demonstrates hACs capacity of resisting cellular invasion in healthy condition. Of note, when no hACs were present not only RFP positive HUVECs, but also RFP negative MSCs invaded the neighbouring compartment. MSCs seemed moreover to express vascular endothelial growth factor (VEGF) contrariwise to hACs (as visible in Fig. 6a in the insets)

To better investigate the role of HUVECs in enhancing MSCs tendency to invade the adjacent compartment, MSCs were seeded with or without HUVECs in one compartment, while the other was filled with acellular PEG gel. When HUVECs were not present, MM only or the MM-EGM-2 mix was used. As visible in Fig. 6b, when MSCs were co-cultured with HUVECs, cellular invasion was visible in the adjacent compartment after 7 days; MSCs alone instead invaded or not the empty neighbouring compartment after 7 days depending on the use of MM-EGM-2 mix or MM alone, respectively. These data suggested that the invading phenotype demonstrated by MSCs was not only mediated by HUVECs secreted factors, but was also dependent on growth factors contained in the EGM-2 medium formulation (e.g. VEGF).

Although presented data on the integration of cartilaginous and vascular compartment are preliminary, the performed initial assessment allowed to demonstrate that it is feasible to obtain the integration of 3D hACs and vascular tissue compartments on chip while providing a direct intra-constructs interface.

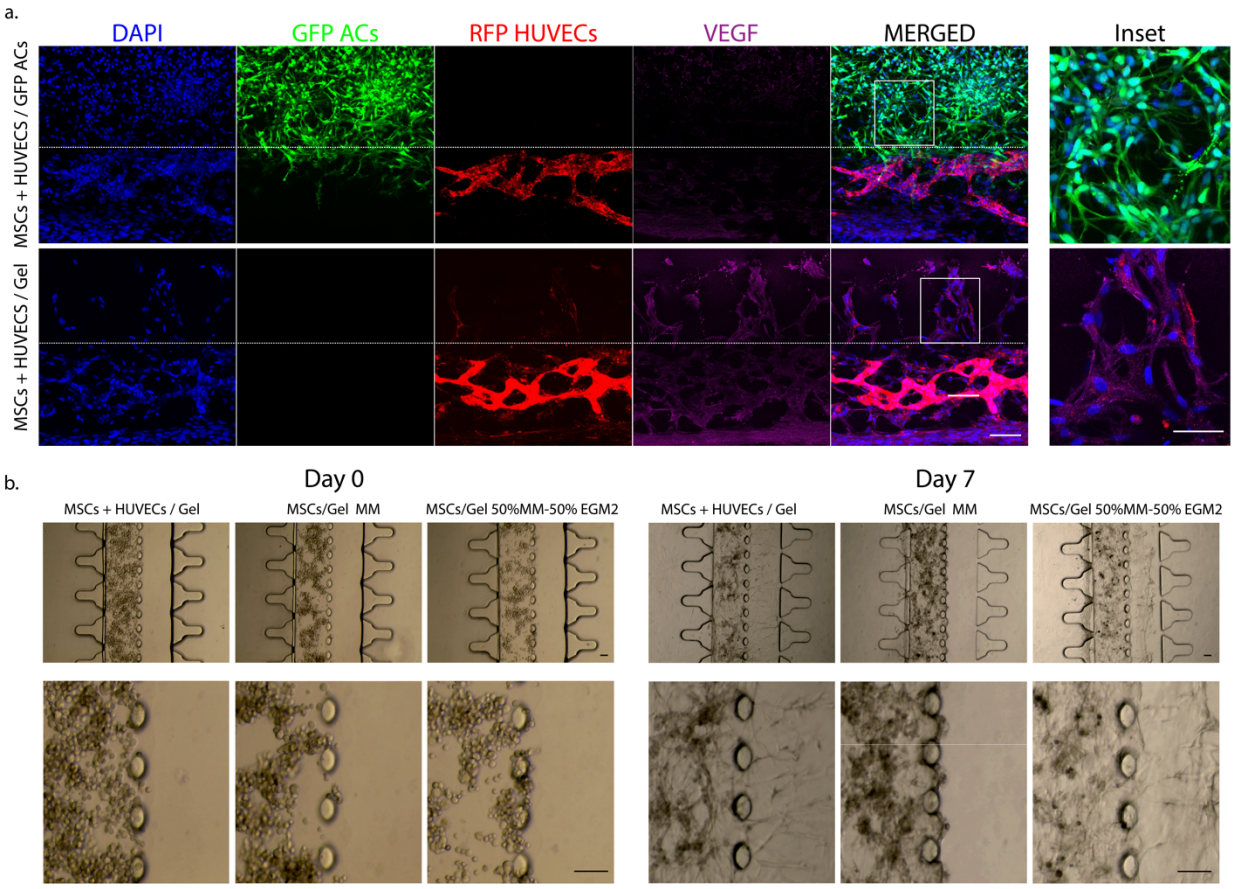

Figure 6: ***Coupling of hACs and vascular constructs****.* ***a,*** *Immunofluorescent images of biphasic constructs comprehensive of a cartilage compartment and of a vascularized tissue compartment after 7 days of maturation. DAPI is represented in blue, GFP hACs in green, VEGF in magenta, and RFP HUVECs in red. Insets focused on the area at the interface between the two constructs are reported on the right. No GFP negative cells were detected on the hACs side. Scale bar 100 µm.* ***b,*** *Brightfield images of various co-culture conditions at day 0 and at day 7. Scale bar 100 µm.*

6.6 Preliminary evaluation of the effect of hyperphysiological compression on complex osteochondral constructs on chip.

OA was characterized as a whole joint disease leading to pathological modifications in all OCU tissues; vascular invasion of the normally avascular cartilage tissue being, in particular, one of the disease features [5]

As a conclusion, a pilot evaluation of the effects of mechanical loading on biphasic constructs was performed. Tissues in the OCU (e.g. in knees) are superimposed and aligned to the load direction. Therefore, while a side-by-side organization of the constructs was preferred in determining their maturation given the associated ease in visualisation, the effect of loading was assessed making use of the OoC platform described in Chapter 5 coupling the vertical burst valve (VBV) concept with a compression compartment.

Biphasic constructs constituted by hyaline cartilage and vascularized tissue were translated to a superimposed configuration through the VBV compressive device described in Chapter 5, so that tailored hyperphysiological and physiological compressive levels could be applied to the two layers.

The disposition of hACs and MSCs+HU constructs in the device is depicted in Fig. 7a. GFP chondrocytes were seeded in the compression chamber to ease tissues distinguishment. After 7 days of static culture in the 1:2 dilution of MM and EGM-2, HUVECs based vascular structures were detectable in the top culture chamber (Fig. 7b). Sections of the devices showed, moreover, that highlighted structures had an empty lumen (Fig. 7c). It was hence feasible to replicate the organization of layers obtained through the horizontal disposition in the devices.

hACs response to loading *in vitro* was demonstrated to depend on tissues maturation levels. Differentiation of hACs based construct in a mature cartilage layer (i.e. a differentiation time of 14 days) was therefore required to properly assess the effect of hyperphysiological compression. HUVECs networks were however demonstrated to degrade with excessive culture time (section 6.5.1), thus precluding the adoption of a 14 days differentiation period before the additional culture time required for the cyclical loading phase. To solve this problem, the low diffusive geometry (LDG) of the top culture chamber described in Chapter 5 was exploited to obtain hACs maturation for 14 days before coupling with the MSCs+HU layer. Experimental setup and adopted timeline are depicted in Fig. 7d. hACs-laden PEG hydrogels were seeded in the compression chamber of VBV devices at day 0. The top culture chamber was filled with culture medium together with the lateral channels. Constructs were conditioned with the previously described CM for 14 days.

Given the contentive LDG configuration, it was feasible to inject MSCs+HU laded PEG hydrogel into the top culture chamber on day 14. Devices were carefully emptied from all culture medium before injection of the cellular solution. Notably, while PDMS was hydrophilic after 14 days in culture, the limited dimension of the channels connecting central gel channel and medium channels (10 μm in width, 50 μm in height) allowed to confine the cell-laden hydrogel formulation in the central gel chamber.

Biphasic constructs were cultured for further 8 days in the 1:2 dilution of MM and EGM-2. After one day of static culture, mechanical compression was applied for 7 days with the regimen indicated in Fig. 7d. Controls cultured statically for 22 days were introduced.

hACs pre-culture allowed to reach, after 22 days of static culture, deposition of COL2A1 in the cartilaginous compartment (Fig. 7e) (with sparse COL2A1 positive areas also in the vascular compartment), but also a spatially differentiated expression of LECT1 (i.e. chondromodulin) a protein known to counteract vascular invasion on healthy cartilage [37] (Fig. 5m). These data demonstrate the achievement of biphasic constructs suitable to investigate the effect of hyperphysiological loading on the assumption of various OA traits.

Representative immunofluorescence stainings of static and dynamic constructs are reported in Fig. 7g. Dynamic loading seemed to determine a reduction in hACs constructs positivity for COL2A1. Furthermore, traces of RFP positive HUVECs were detected above the constructs' midlines, possibly indicating an approximation to the hACs compartment following cyclic loading.

Further analyses are however necessary to confirm presented results and effectively determine which load induced changes are provoked respectively in the two layers.

Reported results, nevertheless, provide a proof-of-concept of the usability of the proposed model to investigated aspects of OA evolution (e.g. vascular invasion) not otherwise determinable in an *in vitro* setting.

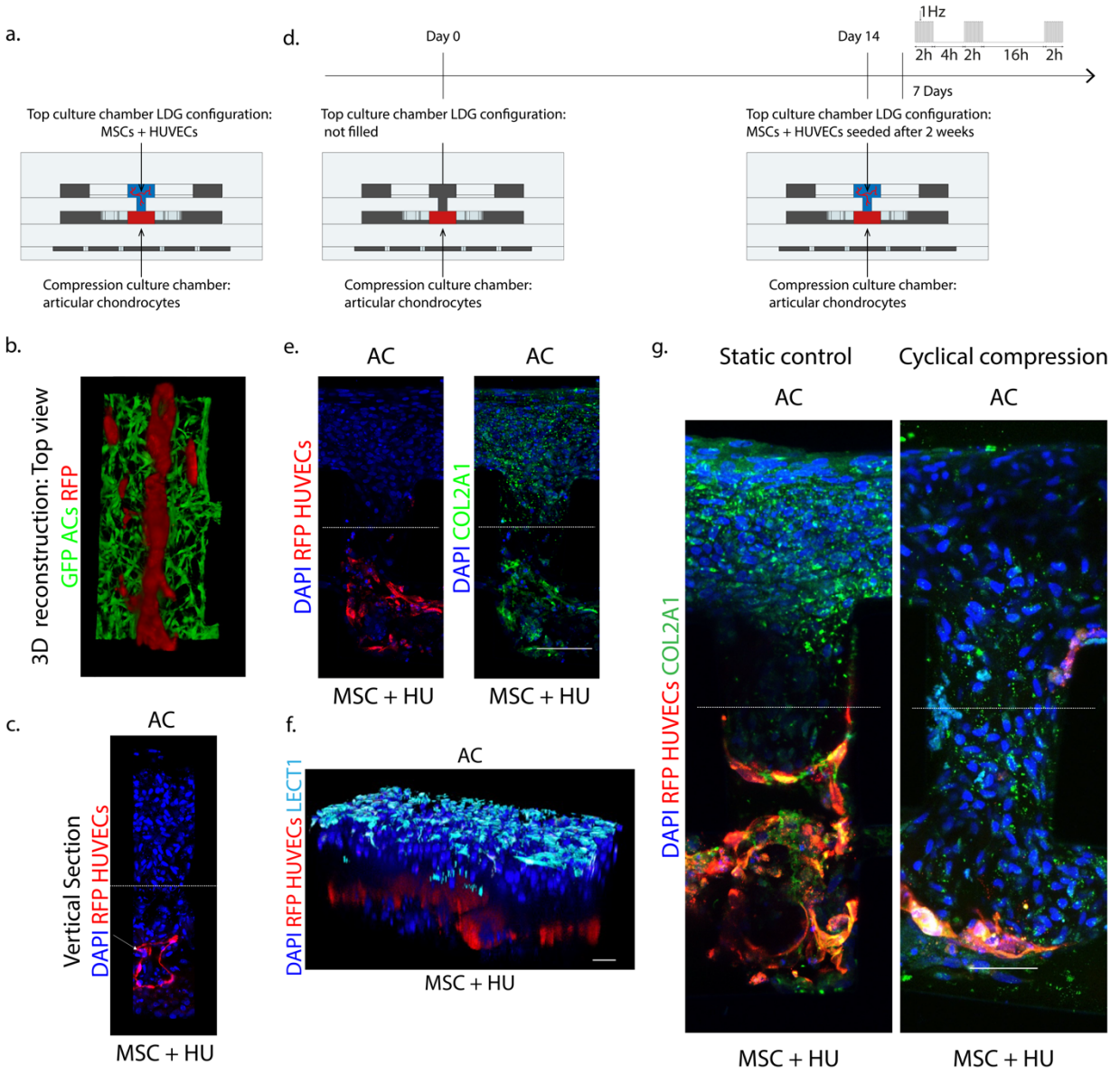

Figure 7: ***Effect of mechanical compression on complex biphasic constructs, a preliminary evaluation. a,*** *Schematization of the constructs disposition in the device adopted to determine if hACs constructs (in the compression chamber) could be coupled with*

vascularized MSCs+HU constructs (in the top culture chamber) in this vertical tissue disposition. Two examples of obtained constructs after 7 days of maturation, are reported in ***b,*** *and* ***c****, Images depict, respectively, a confocal 3D reconstruction of the biphasic construct viewed from top (RFP HUVECs are represented in red, GFP chondrocytes in green) and a section of the device highlighting the tubular structure formed by HUVECs (white arrow). DAPI is represented in blue. Scale bar 100 µm. The lowly diffusive geometry (LDG) configuration presented in Chapter 5 was adopted in experiments.* ***d,*** *Schematization of the experimental setup and timeline adopted to determine if compression had an effect on biphasic cartilaginous and vascular constructs. Adoption of the LDG configuration for the top culture chamber allowed to seed hACs on day 0, culture constructs for the 14 days previously determined to be sufficient for maturation in hyaline cartilage like tissues, and seed MSCs+HU constructs on day 14. A further week of culture was then carried on subjecting biphasic constructs with the stimulation regimen indicated in the figure.* ***e, f*** *Immunofluorescence images of construct after 21 days of total static culture. DAPI is represented in blue, RFP HUVECs in red, COL2A1 in green and LECT1 (chondromodulin) in cyan. n=2 biologically independent samples from n= 2 donors for each cellular type were considered in analyses. Scale bar 100 µm.* ***g,*** *Comparison of static and dynamic constructs after 2 weeks of maturation and a week of hyperphysiological loading or 3 weeks of static maturation. DAPI is represented in blue, RFP HUVECs in red, COL2A1 in green. n=2 biologically independent samples from n= 1 donors for each cellular type were considered in analyses. Scale bar 100 µm.*

6.7 Analyses techniques and procedures.

6.7.1 Immunofluorescence analysis.

Immunofluorescence analyses were performed, as described before, directly within the microscale device at day 7, 14 and day 21. Samples were fixed in 4% paraformaldehyde (PFA) overnight at 4°C. Cells were permeabilized with 0.3% Tween (Sigma) PBS solution for 10 minutes. A 3% bovine serum albumin (BSA), 0.5% Triton (Sigma) in PBS blocking solution was applied for 1 hour at room temperature to block nonspecific bindings. Samples were incubated overnight at 4°C with primary antibodies. Rabbit anti-human aggrecan (dilution 1:200, Abcam), mouse anti-human collagen type-II (dilution 1:200, Abcam), rabbit anti-human osteocalcin (dilution 1:200 MILLIPORE), mouse anti-human alkaline phosphatase (dilution 1:200, Abcam), and rabbit anti-human osteopontin (dilution 1:200, Abcam) antibodies were used to evaluate constructs maturation at day14.

Constructs maturation at day 7 was assessed with mouse anti-human collagen type-II (dilution 1:200, Abcam), mouse anti-human collagen type-I (dilution 1:200, Abcam), rabbit anti-human bone sialoprotein (dilution 1:200, Abcam), and mouse anti-human vascular endothelial growth factor (dilution 1:200, Abcam) antibodies. At day 21, constructs maturation and differences between static controls and cyclically loaded constructs were assessed with mouse anti-human collagen type-I (dilution 1:200, Abcam) and rabbit anti-human chondromodulin (dilution 1:200, Abcam) antibodies.

Mineralization stainings were performed through binding of FITC Calceine (Sigma-Aldrich). Calceine was added to the culture medium (1 µg/ml) during culture and incubated for two days before image acquisition. Specific hydroxyapatite stainings were performed with OsteoImage mineralization assay (Lonza), according to manufacturer instructions.

DAPI staining was used to identify the cell nuclei. As appropriate, secondary antibodies labelled with Alexa Fluor 488, Alexa Fluor 546, and Alexa Fluor 647 (Invitrogen) were used at 1:200 for 45 minutes at room temperature.

Representative images of constructs regions were acquired with 20x and 40x objectives with a fluorescence Nikon A1R Nala Confocal microscope (Nikon, Tokyo, Japan), and analysed by using ImageJ software.

6.7.2 Quantitative real-time reverse transcriptase polymerase chain reaction (RT-PCR).

Total RNA extraction by Trizol, cDNA synthesis and real-time reverse transcriptase-polymerase chain reaction (RT-PCR; 7300 AB Applied Biosystem) were performed according to standard protocol to quantitate expression levels of the following genes of interest (Applied Biosystems): *COL2A1* (Hs00264051_m1), *COL1A1* (Hs00164004_m1), *ACAN* (Hs00153936_m1), *GDF5* (Hs00167060_m1), *ATX* (Hs00905117_m1), *FRZB* (Hs00173503_m1), *GREM1* (Hs01879841_s1), *MMP13* (Hs00233992_m1), *IL8* (Hs00174103_m1), *COL10A1* (Hs00166657_m1), *IHH* (Hs01081800_m1), *DKK-1* (Hs00183740_m1), *BMP2* (Hs00154192_m1), *BSP2* (Hs00173720_m1), *ALP* (Hs01029144_m1), *OCN* (Hs01587814_g1), and *OPN* (Hs00959010_m1).
The house-keeping gene Glyceraldehyde 3-phosphate dehydrogenase (*GAPDH*) was used as reference (Hs02758991_g1).

6.7.3 Biochemical analyses.

Samples were digested in 500 µl of proteinase-K (1 mg/mL proteinase-K in 50 mM Tris with 1 mM EDTA, 1 mM iodoacetamide, and 10 µg/mL pepstatin-A) overnight at 56°C. GAG amounts were measured spectrophotometrically after reaction with dimethylmethylene blue using chondroitin sulphate as a standard [27]. The amount of DNA was measured spectrophotometrically using the CyQuant cell proliferation assay Kit (Molecular Probes, Eugene, OR), according to manufacturer's instructions. GAG contents were reported as GAG/DNA. At least eight biologically independent samples from three different donors were considered for each condition.

6.7.4 Statistical analysis.

Results of biochemical analyses are represented as mean ± SD. Results of quantitative RT-qPCR, as mean + SD. Statistical analysis was performed using GraphPad Prism 9.0. Data Populations normal distribution was assessed through D'Agostino-Pearson, Shapiro-Wilk and/or Kolmogorov-Smirnov tests. Two tailed Student's T-test (normal distributions) and Mann-Whitney test (non-normal distributions) were used when comparing two populations. Multiple comparisons were performed using ordinary one-way analysis of variance (ANOVA). Ordinary one-way ANOVA with Tukey's multiple comparison tests were adopted for normal distributions, Kruskal-Wallis test with Dunn's multiple comparison tests for non-normal

distributions. Statistical significance was indicated by * P<0.05, **P<0.01, ***P<0.001, ****P<0.0001, respectively.

6.8 Discussion

In this chapter, different strategies for engineering complex multi-layer tissues were proposed to recapitulate specific aspects of the OCU.

Starting from 3D macroscale pellets culture, a medium formulation, namely the MM, suitable to drive MSCs differentiation into hypertrophic calcified cartilage, while not altering hACs chondrogenic potential was obtained. The suggested MM was adopted to achieve a co-culture model on chip of hyaline cartilage and calcified cartilage. These constructs were coupled through an *ad hoc* OoC designed platform to achieve a direct inter-tissue interface reminiscent of the OCU *in vivo*. The same platform was exploited to couple hyaline cartilage reminiscent constructs with a vascularized compartment. Finally, hyperphysiological compressive cyclical loading, which demonstrated to induce OA traits *in vitro* [19], was applied to the complex biphasic hyaline cartilage + vascular compartment constructs in a pilot demonstration of their suitability as tools to investigate OA mechanisms (e.g. the imbalance of catabolic and anabolic processes, or vascular invasion). While more in-depth investigations with higher experimental numerosity are needed on these matters, the presented work provided (i) a proof of concept of the potentiality of developed OoC platforms and (ii) differentiation strategies to obtain complex multi-tissues models for the *in vitro* investigation of chondral and subchondral tissues related OA hallmarks.

OA is a multifactorial disorder affecting the joint as a whole [2]. Calcified cartilage, at the interface between hyaline cartilage and bone, expands into the deep cartilage layer and exhibits an hyper-mineralized phenotype [4]; osteoarthritic joints are furthermore subjected to angiogenesis at the osteochondral interface [5]. A limited number of *in vitro* OA models incorporate, however, tissues other than cartilage [38].

Available models defined as osteochondral (e.g. [1, 7, 8]) were based on differentiation of MSCs towards cartilage or bone through the provision of morphogens gradient (e.g. BMP2). Differentiation in positionally defined tissues through provision of concentration gradients recapitulates limb developmental process during embryogenesis [6]. MSCs were however demonstrated as committed to differentiation into hypertrophic rather than hyaline cartilage [9]. Chondrocyte hypertrophy being one of OA hallmarks [36], MSCs could thus not be the ideal cellular source to investigate the effect of given stimuli (e.g. loading or cytokine administration) on assumption of OA traits. A solution to this issue could be the adoption of induced pluripotent stem cells (iPSCs) [34].

On the other hand, the adoption of different cellular sources allows an increased freedom in controlling the various model components. Starting from these considerations, in the present chapter differentiation into hyaline and hypertrophic cartilage was achieved through the use of hACS and MSCs, while vascularization was obtained incorporating HUVECs.

OoCs purpose was defined as “not to build a whole living organ but rather to synthesize minimal functional units that recapitulate tissue- and organ-level functions’’ [17]. This concept, together with the complexity

of OA, gives the rational for developing OCU OA models recapitulating specific and well-defined disease aspects. With the aim of investigating the effect of mechanical overloading on joints, we developed a biphasic construct constituted by cartilage and hypertrophic cartilage rather than bone, given the tissues disposition *in vivo*. Moreover, vasculature incorporation allowed to replicate the development-reminiscent OA hypertrophic cartilage vascular invasion.

Organophosphates, such as glycerophosphate, were proven to induce mineralization in cell culture systems serving as a source of inorganic phosphate hydrolysed by alkaline phosphatase [26]. In this work it was demonstrated how addition of β-Gly to a chondrogenic medium formulation allowed MSCs to deposit a matrix rich in GAG but also positive for mineralization thus mimicking *in vivo* calcified cartilage extracellular matrix. It was also determined that β-Gly does not impair hACs chondrogenic potential nor causes them to assume a mineralizing phenotype (as evidenced by the negative alizarin red staining), or a hypertrophic gene expression (not modulating for instance the expression of *FRZB*, *GREM1* and *DKK1* which were defined as hypertrophy brakes [39], or the direct hypertrophy markers *COL10A1* and *IHH*). Interestingly, moreover, the β-Gly supplemented MM formulation increased hACs expression of *ATX,* marking the interzone during joint development [6].

A first assessment of hACs and MSCs differentiation in MM was determined through macroscale pellet cultures. The reduction in scale of OoCs makes them ill-suited for classic immunohistochemistry stainings such as safranin-O or Alizarin red, making alternative culture methods necessary if such assays need to be performed. The results obtained at the macroscale were however confirmed on chip. The adopted MM formulation allowed, for the first time, on chip differentiation of MSCs in calcified cartilage microconstructs rich in COL2A1 but also ALP, OCN, OPN, and expressing high levels of *COL10A1* and *IHH*. Furthermore, as in pellet culture, the same MM formulation did not alter hACs capacity of differentiate into hyaline cartilage microconstructs rich in COL2A1 and ACAN.

Through a purposefully designed OoC platform it was possible to coculture hACs and MSCs based constructs reaching an interface similar to that of cartilage deep zone and calcified cartilage *in vivo,* demonstrating that co-culture does not alter the expression profile of both populations.

As previously discussed, the OCU is configured as a multi-layer bio-composite with layers stacked in the load direction. If one's aim is the recapitulation of joint reminiscent mechanical loading into layered constructs it is therefore necessary to recapitulate this tissue organization (as presented in Chapter 5).

To optimize the differentiation phase however, a horizontal tissue patterning was preferable given (i) the simpler device fabrication limited to a single culture chamber and (ii) the easier visualization of both tissues and their interface. Making use of the platform proposed in this chapter it was possible to directly visualize the difference in constructs matrix through brightfield images, and the deposition of hydroxyapatite exclusively in one of the two compartments through immunofluorescence.

One of the hallmarks of OA is cartilage vascular invasion from the neighbouring subchondral bone [2]. Interactions between vascularized and cartilage tissues are however seldom considered in *in vitro* models. Preliminarily, an on-chip model of vascularized, hypertrophic tissue was developed. Through the co-culture of MSCs and HUVECs, constructs which exhibited well-defined vascular structures were obtained on chip. Congruently with previously reported results [41], however, HUVECs networks started to degrade after 7 days in culture. This behaviour limited vascular tissues maximum differentiation time, preventing the achievement of microconstructs featuring a vascular network together with the characteristics of mineralized or cartilaginous mature tissues. Alternative strategies (based for instance on the adoption of the stromal vascular fraction, previously demonstrated to be suitable for the *in vitro* formation of vascular networks supported by an ECM backbone [42]) could be considered in the future to overcome this issue.

Notably, while the limited matrix deposition at 7 days could simply be due to an insufficient culture time, MSCs+HU constructs gene expression at day 14 demonstrated an overall decrease of genes related to cartilage ECM, hypertrophy, and bone differentiation (i.e. respectively *COL2A1*, *COL10A1* and *IHH*, and *BSP2* and *OCN*), and an upregulation of *COL1A1* expression possibly indicating a HUVECs (or HUVECs related factors) dependent effect on MSCs differentiation.

Through the proposed multi tissues platform it was possible to give a proof of concept of the achievement of complex biphasic constructs coupling a cartilaginous and a vascular layer (with tissues both juxtaposed and superimposed). It was moreover demonstrated that healthy hACs prevent HUVECs and MSCs from expanding into neighbouring tissues and that the invading phenotype assumed by MSCs is likely dependent on factors contained in EGM-2. Further investigations on this matter need, however, to be performed (e.g. an assessment of the gene expression in the separated populations or investigations of the specific factors inducing the invading phenotype). Interestingly, moreover, MSCs+HU constructs resulted positive for VEGF. These results, while needing confirmation with a higher sample numerosity, correlate with observations of subchondral tissues in OA joints. Osteochondral angiogenesis was in fact characterized precisely by formation of a fibrovascular tissue expressing VEGF [5] similar to the obtained MSCs+HU constructs.

Finally, a proof-of-concept application of hyperphysiological loading to biphasic cartilage-vascular tissue constructs was performed. Notably, it was feasible to subject the bi-layer tissues to discrete precise levels of confined compression not depending on the mechanical properties of the tissues themselves (as per the technology described in Chapter 5). In particular the cartilaginous compartment was subjected to a hyperphysiological compression level (i.e. 25-30%) reminiscent of OA originating strains [43–45], while the subchondral compartment (calcified cartilage or vascular tissue), was subjected to minimal compressive strains (i.e. 1-3%) thus recapitulating the deformation experienced *in vivo* by tissues at the osteochondral interface [46, 47]. Application of such stimuli to biphasic osteochondral reminiscent constructs could help

in recapitulating OA traits not otherwise representable *in vitro.* Through the proposed cartilage-calcified cartilage model for instance it could be studied how variations in the mineral content of calcified cartilage (i.e. through loading of MSCs constructs with different quantities of hydroxyapatite) affect hyaline cartilage response to loading.

Moreover, exploiting a particular device design (i.e. the LDG) it was possible to obtain mature cartilaginous constructs before coupling of this layer with the vascular compartment solving the issue of the limited culture time of HUVECs. Such a strategy permitted, for instance, to obtain tissues with a hyaline cartilage layer specific expression of chondromodulin which was demonstrated to be involved in cartilage resistance to vascular invasion [37]. Assessing how chondromodulin expression varies following loading or other OA stimuli (i.e. administration of given inflammatory cytokines) could help to understand which factors are governing cartilage vascular invasion in OA.

Through the proposed differentiation strategies, it could, therefore, be feasible to study OA traits ranging from cartilage altered anabolic/catabolic balance and inflammation, to calcified cartilage matrix and mineral content variations, to subchondral layers vasculature behaviour.

6.9 Conclusive remarks

Making use of different microscale OoCs and macroscale models various differentiation strategies aimed at obtaining disease relevant multi-tissue OA models were presented. Models of hyaline cartilage, calcified cartilage and vascularized subchondral-like tissues could be established on chip. While the biological implications of the present chapter are preliminary, it was demonstrated how the incorporation of subchondral layers aimed at representing different and specific OCU tissues and OA traits could be introduced in OoC devices. These differentiation strategies could possibly be adopted in relevant preclinical osteochondral models allowing to increment our comprehension of OA evolution by dissecting which compartments are responsible for a given phenotype in a highly controlled *in vitro* microenvironment.

6.10 References

1. H L, TP L, PG A, et al (2014) Stem cell-based microphysiological osteochondral system to model tissue response to interleukin-1β. Mol Pharm 11:2203–2212. https://doi.org/10.1021/MP500136B
2. Goldring SR, Goldring MB (2016) Changes in the osteochondral unit during osteoarthritis: structure, function and cartilage–bone crosstalk. Nat Rev Rheumatol 12:632–644. https://doi.org/10.1038/nrrheum.2016.148
3. Yuan XL, Meng HY, Wang YC, et al (2014) Bone-cartilage interface crosstalk in osteoarthritis: potential pathways and future therapeutic strategies. Osteoarthr Cartil 22:1077–89. https://doi.org/10.1016/j.joca.2014.05.023
4. Ferguson VL, Bushby AJ, Boyde A (2003) Nanomechanical properties and mineral concentration in articular calcified cartilage and subchondral bone. J Anat 203:191–202. https://doi.org/10.1046/j.1469-7580.2003.00193.x
5. Walsh DA, McWilliams DF, Turley MJ, et al (2010) Angiogenesis and nerve growth factor at the osteochondral junction in rheumatoid arthritis and osteoarthritis. Rheumatology 49:1852–1861. https://doi.org/10.1093/rheumatology/keq188
6. Ray A, Singh PNP, Sohaskey ML, et al (2015) Precise spatial restriction of BMP signaling is essential for articular cartilage differentiation. Development 142:1169–79. https://doi.org/10.1242/dev.110940
7. Li C, Ouyang L, Pence IJ, et al (2019) Buoyancy-Driven Gradients for Biomaterial Fabrication and Tissue Engineering. Adv Mater 31:1900291. https://doi.org/10.1002/adma.201900291
8. Li C, Armstrong JP, Pence IJ, et al (2018) Glycosylated superparamagnetic nanoparticle gradients for osteochondral tissue engineering. Biomaterials 176:24–33. https://doi.org/10.1016/J.BIOMATERIALS.2018.05.029
9. Occhetta P, Pigeot S, Rasponi M, et al (2018) Developmentally inspired programming of adult human mesenchymal stromal cells toward stable chondrogenesis. Proc Natl Acad Sci U S A 115:4625–4630. https://doi.org/10.1073/pnas.1720658115
10. Dreier R (2010) Hypertrophic differentiation of chondrocytes in osteoarthritis: the developmental aspect of degenerative joint disorders. Arthritis Res Ther 12:216. https://doi.org/10.1186/ar3117
11. CI J, DJ A, DN C (2016) In vitro models for the study of osteoarthritis. Vet J 209:40–49. https://doi.org/10.1016/J.TVJL.2015.07.011
12. Chen Y, Hu Y, Yu YE, et al (2018) Subchondral Trabecular Rod Loss and Plate Thickening in the Development of Osteoarthritis. J Bone Miner Res 33:316–327. https://doi.org/10.1002/jbmr.3313
13. Wang F, Ying Z, Duan X, et al (2009) Histomorphometric analysis of adult articular calcified cartilage zone. J Struct Biol 168:359–365. https://doi.org/10.1016/J.JSB.2009.08.010
14. SA W, KO R, T M, et al (2018) Microenvironmental Regulation of Chondrocyte Plasticity in Endochondral Repair-A New Frontier for Developmental Engineering. Front Bioeng Biotechnol 6:. https://doi.org/10.3389/FBIOE.2018.00058
15. Jeon JS, Bersini S, Gilardi M, et al (2015) Human 3D vascularized organotypic microfluidic assays to study breast cancer cell extravasation. Proc Natl Acad Sci 112:214–219. https://doi.org/10.1073/PNAS.1417115112
16. Pirosa A, Gottardi R, Alexander PG, et al (2021) An in vitro chondro-osteo-vascular triphasic model of the osteochondral complex. Biomaterials 272:120773. https://doi.org/10.1016/J.BIOMATERIALS.2021.120773
17. Bhatia SN, Ingber DE (2014) Microfluidic organs-on-chips. Nat Biotechnol 2014 328 32:760–772. https://doi.org/10.1038/nbt.2989
18. Marsano A, Conficconi C, Lemme M, et al (2016) Beating heart on a chip: a novel microfluidic platform to generate functional 3D cardiac microtissues. Lab Chip 16:599–610
19. Occhetta P, Mainardi A, Votta E, et al (2019) Hyperphysiological compression of articular cartilage induces an osteoarthritic phenotype in a cartilage-on-a-chip model. Nat Biomed Eng. https://doi.org/10.1038/s41551-019-0406-3
20. Huang CP, Lu J, Seon H, et al (2009) Engineering microscale cellular niches for three-dimensional multicellular co-cultures. Lab Chip 9:1740–1748. https://doi.org/10.1039/b818401a
21. Baumann CA, Hinckel BB, Bozynski CC, Farr J (2019) Articular Cartilage: Structure and Restoration. Jt Preserv Knee A Clin Caseb 3–24. https://doi.org/10.1007/978-3-030-01491-9_1
22. Decker RS, Koyama E, Pacifici M (2014) Genesis and morphogenesis of limb synovial joints and articular cartilage. Matrix Biol 39:5–10. https://doi.org/10.1016/j.matbio.2014.08.006
23. Martin I, Muraglia A, Campanile G, et al (1997) Fibroblast Growth Factor-2 Supports ex Vivo Expansion and Maintenance of Osteogenic Precursors from Human Bone Marrow. Endocrinology 138:4456–4462. https://doi.org/10.1210/ENDO.138.10.5425
24. Braddock M, Quinn A (2004) Targeting IL-1 in inflammatory disease: new opportunities for therapeutic intervention. Nat Rev Drug Discov 3:330
25. Caron MMJ, Emans PJ, Coolsen MME, et al (2012) Redifferentiation of dedifferentiated human articular chondrocytes: comparison of 2D and 3D cultures. Osteoarthr Cartil 20:1170–1178. https://doi.org/10.1016/J.JOCA.2012.06.016
26. Chang Y-L, Stanford CM, Keller JC (2000) Calcium and phosphate supplementation promotes bone cell mineralization: Implications for hydroxyapatite (HA)-enhanced bone formation. J Biomed Mater Res 52:270–278. https://doi.org/10.1002/1097-4636(200011)52:2<270::AID-JBM5>3.0.CO;2-1
27. Farndale RW, Buttle DJ, Barrett AJ (1986) Improved quantitation and discrimination of sulphated glycosaminoglycans by use of dimethylmethylene blue. Biochim Biophys Acta (BBA)-General Subj 883:173–177
28. Ray A, Singh PNP, Sohaskey ML, et al (2015) Precise spatial restriction of BMP signaling is essential for articular cartilage differentiation. Development 142:1169–1179
29. Nishioka T, Arima N, Kano K, et al (2016) ATX-LPA1 axis contributes to proliferation of chondrocytes by regulating fibronectin assembly leading to proper cartilage formation. Sci Rep 6:23433
30. Leijten JCH, Emons J, Sticht C, et al (2012) Gremlin 1, Frizzled-related protein, and Dkk-1 are key regulators of human articular cartilage homeostasis. Arthritis Rheumatol 64:3302–3312
31. Kronenberg HM (2003) Developmental regulation of the growth plate. Nature 423:332–336
32. Ehrbar M, Rizzi SC, Schoenmakers RG, et al (2007) Biomolecular hydrogels formed and degraded via site-specific enzymatic reactions. Biomacromolecules 8:3000–3007. https://doi.org/10.1021/bm070228f
33. Fox AJS, Bedi A, Rodeo SA (2009) The Basic Science of Articular Cartilage: Structure, Composition, and Function. Sports Health 1:461. https://doi.org/10.1177/1941738109350438
34. Lin Z, Li Z, Li EN, et al (2019) Osteochondral Tissue Chip Derived From iPSCs: Modeling OA Pathologies and Testing Drugs. Front Bioeng Biotechnol 0:411. https://doi.org/10.3389/FBIOE.2019.00411
35. Grodzinsky AJ, Wang Y, Kakar S, et al (2017) Intra-articular dexamethasone to inhibit the development of post-traumatic

osteoarthritis. J Orthop Res 35:406–411
36. Pesesse L, Sanchez C, Walsh DA, et al (2014) Bone sialoprotein as a potential key factor implicated in the pathophysiology of osteoarthritis. Osteoarthr Cartil 22:547–556. https://doi.org/10.1016/j.joca.2014.01.010
37. Deng B, Chen C, Gong X, et al (2017) Chondromodulin-I expression and correlation with angiogenesis in human osteoarthritic cartilage. Mol Med Rep 16:2142–2148. https://doi.org/10.3892/mmr.2017.6775
38. Johnson CI, Argyle DJ, Clements DN (2016) In vitro models for the study of osteoarthritis. Vet J 209:40–49. https://doi.org/10.1016/j.tvjl.2015.07.011
39. Leijten JCH, Bos SD, Landman EBM, et al (2013) GREM1, FRZB and DKK1 mRNA levels correlate with osteoarthritis and are regulated by osteoarthritis-associated factors. Arthritis Res Ther 15:R126
40. Bourgine PE, Scotti C, Pigeot S, et al (2014) Osteoinductivity of engineered cartilaginous templates devitalized by inducible apoptosis. Proc Natl Acad Sci 111:17426–17431. https://doi.org/10.1073/PNAS.1411975111
41. Kim S, Lee H, Chung M, Jeon NL (2013) Engineering of functional, perfusable 3D microvascular networks on a chip. Lab Chip 13:1489–1500. https://doi.org/10.1039/C3LC41320A
42. Cerino G, Gaudiello E, Muraro MG, et al (2017) Engineering of an angiogenic niche by perfusion culture of adipose-derived stromal vascular fraction cells. Sci Reports 2017 71 7:1–14. https://doi.org/10.1038/s41598-017-13882-3
43. Sanchez-Adams J, Leddy HA, McNulty AL, et al (2014) The Mechanobiology of Articular Cartilage: Bearing the Burden of Osteoarthritis. Curr Rheumatol Rep 16:451. https://doi.org/10.1007/S11926-014-0451-6
44. Wong BL, Sah RL (2010) Effect of a Focal Articular Defect on Cartilage Deformation during Patello-Femoral Articulation. J Orthop Res 28:1554. https://doi.org/10.1002/JOR.21187
45. Greaves LL, Gilbart MK, Yung AC, et al (2010) Effect of acetabular labral tears, repair and resection on hip cartilage strain: A 7 T MR study. J Biomech 43:858–863. https://doi.org/10.1016/J.JBIOMECH.2009.11.016
46. Eckstein F, Lemberger B, Gratzke C, et al (2005) In vivo cartilage deformation after different types of activity and its dependence on physical training status. Ann Rheum Dis 64:291. https://doi.org/10.1136/ARD.2004.022400
47. Zheng YP, Mak AFT, Lau KP, Qin L (2002) An ultrasonic measurement for in vitro depth-dependent equilibrium strains of articular cartilage in compression Related content An ultrasonic measurement for in vitro depth-dependent equilibrium strains of articular cartilage in compression. Med Biol Phys Med Biol 47:3165–3180

7 General conclusions

Current drug discovery and development processes suffer from limitations in terms of efficiency and required time thus calling for new compound assaying methodologies to discriminate early, during the testing phases, if a drug is passible of clinical translation.

Relevant *in vitro* models precisely recapitulating key aspects of diseases and organs physiology would function as powerful tools in dissecting the causes and the mechanisms underlying different pathological states.

The advent of microfabrication techniques and Organs-on-Chip (OoCs) allowed to engineer *in vitro* relevant human models with an enhanced mimicry of the *in vivo* physiology (i.e. tissues structure and functionality) and an increased control of the cellular microenvironment.

The achievement of significant models of given body districts such as the heart muscle or of musculoskeletal diseases remains however a challenge due to the particularly demanding requirement of a trade-off between accurate replication of the organs function (e.g. the necessity to incorporate multiple tissues or to provide mechanical stimuli) and attainment of a sufficient throughput and ease of use for drug discovery campaigns.

Case in point, osteoarthritis (OA) is a joint multifactorial disorder involving multiple tissues and with an unknown pathological origin correlated with mechanical risk factors. A proper *in vivo* representation would require therefore (i) a suitable three-dimensional environment, (ii) a device capable of providing mechanical stimulation, and (ii) the possibility of studying the interactions among the multiple tissues affected by the pathology. The same features would, nevertheless, be useful to study a multiplicity of diseases (e.g. cardiac pathologies) where a mechanically active environment is part of the physiological environment and/or is a contributing factor in the pathological onset.

The present PhD project focused on developing micro-platforms and/or biological models and techniques to increase our *in vitro* modelling capabilities of diseases involving mechanically active districts with a specific focus on OA. All advancements were done with the precise aim of testing a defined hypothesis or addressing a technological need. Each platform was conceived applying (or introducing) key principles of microfluidics and microfabrication to supply biological cues at a cellular relevant scale. Performed activities ranged from platforms conception and design, to their realization and functional validation, to their biological validation and exploitation.

Specifically, a mechanically active OoC platform that allowed to provide cartilaginous microconstructs with defined levels of confined physiological or hyperphysiological compression allowed to determined that (i) a cartilage model could be achieved on chip, and that (ii) hyperphysiological compression can, alone, elicit OA cartilage hallmarks (i.e. imbalanced catabolic/ anabolic processes, inflammation and

hypertrophy). The suitability of the developed OA cartilage on chip model to screen the effects of known and innovative anti OA compounds was also demonstrated.

Addressing the need for an increased experimental throughput, a second platform capable of mechanical stimulation of multiple independent chambers was introduced. The device was validated proving that multiple chambers, filled with a single operation, remain independent experimental replicates despite being subject to mechanical stimulation. As a proof of concept, the device was used to study the effects of different cardiomyocytes and fibroblasts co-culture ratios on the assumption of a cardiac fibrosis phenotype.

The establishment of a direct relationship between clinical data and OoCs-based biological readouts would increase their reliability as disease models and drug screening tools. As an effort in this direction, indentation type atomic-force microscopy (IT-AFM) was adopted to investigate which mechanical properties alterations occur in the osteochondral unit of OA patients knee joints. Given the sub-micrometric resolution of the technique, measurements were performed distinguishing between osteochondral unit layers, namely cartilage transitional and deep zones, and calcified cartilage and subchondral bone. On top of gaining additional information directly from patients' samples, the technique was translated to the assessment of the mechanical properties of on-chip developed cartilaginous microconstructs. Evaluating tissues mechanical properties at an organizational scale that could be recapitulated *in vitro* provides new readouts to determine the relevance of a given model but also to evaluate the possible structural effects of a drug treatment.

Subsequently, a new microfluidic concept, namely the vertical burst valve (VBV) was introduced and embedded in a device capable of providing discrete and defined levels of compression to biphasic layered cellular constructs. The platform was validated demonstrating the feasibility to vertically superimpose two cellular constructs so that they could be exposed to mechanical stimuli with a direction similar to that of joints *in vivo*. Finite element modelling was used to estimate the strain field in the two constructs. A biological validation of the platform was carried out proving that different activation levels of mechanotransduction signalling can be achieved in the two constructs, and that alterations in the local properties of an artificial subchondral layer are sufficient to modulate chondrocytes response to loading exacerbating the assumption of a degradative and inflammatory phenotype. The platform provided therefore a technological advancement that could allow the development of a complete osteochondral unit on a chip model.

Finally, a tissue engineering approach was adopted to obtain OoC models of complex biphasic constructs composed either by a hyaline cartilage and a calcified cartilage layer or by a hyaline cartilage and a vascular subchondral layer. An *ad hoc* microfluidic platform was developed to visualize the layers interface during maturation; subsequently, the VBV mechanically active platform was employed in a proof-of-concept application of hyperphysiological, tissues-specific, compressive strains to the constructs.

In summary, the proposed techniques and solutions were aimed at achieving relevant OA Organ-on-Chip models providing pathophysiological compression levels, initially to simple cartilaginous constructs, and later to complex osteochondral unit reminiscent tissues. Both technological and biological advancements were introduced to reach the final goal. Solutions to increase the throughput of the proposed platforms and to establish possible direct comparison methods between *in vitro* models and patients' samples were also established.

The set of proposed models and techniques could therefore function as an important starting point for the study of mechanical induction of pathological traits in both musculoskeletal (e.g. osteoarthritis) or cardiac (e.g. cardiac fibrosis) tissues. Specifically referring to OA, as the main focus of thiss PhD project, the models here presented could be used in applications ranging from mechanistic studies of the mechanotransduction signalling involved in the pathological onset, to the understanding of intra tissue cross talks. The incorporation of multiple tissues, in particular, could suggest innovative therapeutic targets and help the dissection of the temporal evolution and the causal effects of OA traits presentation in the different compartments.

All proposed platforms were based on replica moulding of polydimethylsiloxane (PDMS). The adoption of PDMS allowed to translate microfabrication techniques to biological and biomedical fields; the material is however known to adsorb small lipophilic compounds, possibly altering their concentration. Adequate compensation strategies or alternative materials should be therefore put in place for the widespread diffusion of the proposed technologies as common *in vitro* testing tools.

On the same note, a true dissemination of similar techniques in both pharma companies and basic research laboratories would require the transition to production methodologies passible of scaleup and industrial realization. Integration of the platforms with additional instrumentation to standardise for example medium changes or analyses procedures (e.g. stainings or PCR) could also be considered to ease the adoption of OoC based models from unskilled users.

Primary human donor cells were adopted in all proposed models. The usage of donors' material is necessary when validating a model to maximise the mimicry of physiological cells behaviour (as compared for instance to the use of cell lines). Results are however affected by donor - donor variability and the amount of available material (despite the microscale allows a reduction in required cell numbers) is limited. Furthermore, chondrocytes were demonstrated to dedifferentiate towards a fibroblastic phenotype when expanded *in vitro*. While in the presented models it was feasible to re-differentiate chondrocytes obtaining constructs rich in cartilage specific extracellular matrix components, they still exhibited an uncharacteristic spread morphology. The use of appropriately differentiated induced pluripotent stem cells (iPSCs) could provide a, theoretically infinitely expandable, attractive source for high throughput screenings.

All proposed devices were designed to provide 3D constructs with a precise level of confined compression (or stretching in the case of the model presented in Chapter 3). *In vivo*, however, osteochondral tissues, and mainly cartilage, are exposed to a wide range of mechanical stimuli. Considering the knee, compression is combined with (shear stresses inducing) rotation of the distal femoral condyles on the tibial plateau and relative articular motion (i.e. gliding or respective articular surfaces). Moreover, beside an increased compressive load (e.g. due to obesity) also an augmented joint instability with the relative increased articular motion (e.g. as associated with anterior cruciate ligament injuries) and high levels of adduction moment of the knee were correlated to OA.

Motion derived shear stresses were introduced (and coupled with compression) in different macroscale bioreactors resulting in an overall more physiological experimental environment (and usually into a higher expression of lubricin on engineered cartilage surfaces). The introduction of complex stimuli in OoC devices is however difficult. As mentioned in the discussion of Chapter 5 [ref 53], an OoC devices providing a more complex strain field has been proposed. The suggested solution does not allow, however, to control the compression (and shear) level applied depending these on the constructs' properties. In this thesis the focus was therefore posed only on compression as a main driver of OA hallmarks. Further advances will be needed to achieve alternative stimulation modalities and assess how these impact the microconstructs phenotypes.

Finally, specifically regarding the study of OA, while tissues of the whole osteochondral unit were considered in this project, other compartments should also be integrated. Synovial inflammation is one of the key aspects of the pathology and an active crosstalk between cartilage, subchondral bone, and synovial membrane has been demonstrated. Coupling of the proposed models with an OA mimicking synovial compartment would increase models' relevance and possible readouts.

Controversy still exists regarding the timing and the causal effects of inter-tissue interplays in OA development; we are not capable of inferring which is the principal disease cause and which observations are dependent on previous phenomena. New light shed on these matters could provide novel targets for effective disease modifying drugs.

On this note, as per its aim, the present PhD project provided new tools (i.e. technological instruments and cellular models) to study the pathophysiology of OA development in a controlled microenvironment. Further studies are, however, required to understand the interaction between chondral and subchondral compartments. Possible refined assessments could regard in which compartments OA traits are elicited first, protracting the adopted hyperphysiological mechanical compression (or the supplementation of cytokines mimicking OA synovial fluid) for different extents of time and analysing the compartments separately.

Furthermore, while probed alterations and genetic signature were based on a large-base investigation of currently known OA traits, the introduction of techniques able to provide a wider assessment of the genetic alterations caused by selected OA triggers (e.g. transcriptomic analyses) and an assessment of alterations on a single cell level could enormously advance our knowledge of the disease.

About the author

Articles in this thesis

Occhetta P $, **Mainardi A $**, Votta E, Vallmajo-Martin Q, Ehrbar M, Martin I, Barbero I, Rasponi M. *Hyperphysiological compression of articular cartilage induces an osteoarthritic phenotype in a cartilage-on-a-chip model* Nature Biomedical Engineering volume 3, pages 545–557 (2019). DOI: 10.1038/s41551-019-0406-3
$ Equally contributing authors

Mainardi A, Carminati C, Ugolini G.S, Occhetta P, Isu G, Diaz D.R, Reid G, Visone R, Rasponi M, Marsano A. *A dynamic microscale mid-throughput fibrosis model to investigate the effects of different ratios of cardiomyocytes and fibroblasts.* Lab on a Chip, 21 September 2021 (Online ahead of print), DOI: 10.1039/D1LC00092F

Mainardi A, Occhetta P, Ehrbar M, Loparic M, Oertle P, Egloff C. Martin I, Barbero A and Rasponi M. *Provision of discrete level of compression to complex bi-layered 3 dimensional cartilaginous constructs via a newly designed Vertical Capillary burst valve enables to recapitulate compression-dependent Osteoarthritic degradative and inflammatory phenotypes.* Science Advances (manuscript under submission)

Statement of own contribution to the PhD project
The PhD student was personally responsible for the ideation and realization of all described devices, together with the computations required to optimize and validate the platforms. The PhD student was also the sole responsible for the planning, the execution, and the analyses of all mentioned experimental procedures. Experimental results were discussed with the supervisors.

Reason for shared first authorship:
In the framework of the work for the co-authored publication the role of the PhD student consisted in ideating, engineering and realizing the microuidic platform, performing the computational simulations, performing cell culture experiments and associated analyses, summarizing the results, writing the manuscript with the realization of the images, and responding to reviewers during the revision process. The Role of the other co- first author, namely Paola Occhetta, as a post doc, was to provide direct supervision in the experimental planning (particularly in the drug validation process) and in the manuscript drafting phases. The supervision was rendered necessary given the complexity of the work encompassing phases going from the ideation of a new platform to a drug screening validation.
Given the high impact factor of the target journal and the extremely high number of experiments and controls requested both in the original planning and in the revision process the authorship was therefore equally attributed to the PhD student and to the direct supervisor.

Other articles

Pirosa A, Tankus E.B $, **Mainardi A** $, Occhetta P, Dönges L, Baum C, Rasponi M, Martin I, Barbero A. *Modeling in vitro osteoarthritis phenotypes in a vascularized bone model based on a bone-marrow derived mesenchymal cell line and endothelial cells* International Journal of Molecular Sciences. 2021 Sep 3;22(17):9581. DOI: 10.3390/ijms22179581. **$ Equally contributing authors**

Book chapters

Ugolini G.S, Visone R, Cruz-Moreira C.D, **Mainardi A**, Rasponi M. *Generation of functional cardiac microtissues in a beating heart-on-a- chip.* Methods in Cell Biology. 2018; 146: 69-84. DOI: 10.1016/bs.mcb.2018.05.005.

Mainardi A, Occhetta P, Rasponi M. *Mechanical induction of osteoarthritis traits in a cartilage on chip model.* Methods in Molecular Biology 2022, 2373, pp. 231–251 DOI: 10.1007/978-1-0716-1693-2_14

Ballerini M, Jouybar M, **Mainardi A**, Rasponi M, Ugolini G.S. *Organ-on-Chips for Studying Tissue Barriers: Standard Techniques and a Novel Method for Including Porous Membranes Within Microfluidic Devices.* Methods in Molecular Biology 2022, 2373, pp. 21–38 DOI: 10.1007/978-1-0716-1693-2_2

International conferences contributions

Mainardi A, Occhetta P, Votta E, Rasponi M. *Towards the knee on a chip : development of a microfluidic platform for the mechanical stimulation of three dimensional cartilaginous constructs.* VII Annual Meeting of the Italian chapter of the European society of biomechanics. Rome 28-29 September 2017

Mainardi A, Occhetta P, Votta E, Ehrbar M, Martin I, Barbero A, Rasponi M. *Cartilage-on-chip model: triggering osteoarthritis traits through mechanical compression*. 6th Congresso del gruppo nazionale di Bioingegneria. Milan 25-27 June 2018

Andrea Mainardi, Paola Occhetta, Emiliano Votta, Martin Ehrbar, Ivan Martin, Andrea Barbero, Marco Rasponi. *Cartilage on chip: Hyper-Physiological Compression in a microscale platform triggers osteoarthritic traits in a cartilage model.* 8th World Congress of Biomechanics. Dublin 8-12 July 2018

Carminati F, Isu G, Diaz D.R, Occhetta P, **Mainardi A**, Reid G, Ugolini G.S, Rasponi M, Marsano A. *A microfluidic model to study the interaction between cardiomyocytes and fibroblast in cardiac scar formation.* Wiener klinische wochenschrift 2019. Volume: 131, Supplement: 2 Pages: 254-254

Mainardi A, Occhetta P, Ugolini G.S, Ehrbar M, Martin I, Barbero A, Rasponi M. *Towards the joint on a chip: a microfluidic osteochondral model.* TERMIS European Chapter Meeting 2019. 27th-31st May 2019, Rhodes, Greece

Mainardi A, Occhetta P, Ehrbar M, Martin I, Barbero A, Rasponi M. *Cartilage on chip: Hyper-Physiological Compression in a microscale platform triggers osteoarthritic traits in a cartilage model.* 1st annual conference of the European Organ-on-Chip Society. Graz, Austria on 2-3 July 2019

Visone R, **Mainardi A**, Occhetta P, Rasponi M. *Beating organs-on-chip as advanced tools in drug screening: Engineered in vitro models of human organs and diseases.* ALTEC Proceedings Springer Spectrum volume 8, Page 497 EUSAAT 2019, Linz 12-13 October 2019

Mainardi A, Occhetta P, Votta E, Vallmajo-Martin Q, Ehrbar M, Martin I, Barbero A, Rasponi M. *Cartilage on chip: Hyper-Physiological Compression in a microscale platform triggers osteoarthritic traits in a cartilage model.* 2nd Shenzen summit: international forum on autoimmunity. Shenzen 25-27 October 2019. Invited speaker.

Mainardi A, Occhetta P, Ugolini G.S, Martin I, Barbero A, Rasponi M.*Towards the joint on a chip: double layered directly interfaced tissues to mimic the Osteoarthritic cartilage-subchondral interface* 2nd Annual conference of the European Organ-on-Chip Society. Online meeting 8-9 July 2020

Mainardi A, Occhetta P, Ugolini G.S, Isu G, Visone R, Carminati F, Diaz D.R, Marsano A, Rasponi M. *Modelling cardiac fibrosis through a mechanically active multi-chamber organ on chip device.* 2nd Annual conference of the European Organ-on-Chip Society. Online meeting 8-9 July 2020

Occhetta P, Visone R, **Mainardi A**, Piazza S, Barbero A, Rasponi M. *Beating organs-on-chips as advanced preclinical tools for drug screening and disease modelling.* 2nd Annual conference of the European Organ-on-Chip Society. Online meeting 8-9 July 2020

Pirosa A, **Mainardi A**, Occhetta P, Tankus E.B, Erhbar M, Martin I, Rasponi M, Barbero A. *Modeling in vitro osteoarthritis phenotypes in a human vascularized bone construct based on a bone-marrow derived mesenchymal cell line and endothelial cells* OARSI CONNECT 21 Virtual world congress on Osteoarthritis. Online meeting April 29-May 21 2021

Visone R; **Mainardi A,** Redaelli A, Marsano A, Occhetta P, Rasponi M. *Modeling the pathophysiology of the heart through a beating organ-on-chip platform.* 26th Congress of the European Society of Biomechanics. Online meeting July 11-14 2021

Mainardi A, Occhetta P, Martin I, Barbero A, Rasponi M. *Modelling the joint on a chip: a Vertical Burst Valve allows for mechanically active, 3D, multi-layer vascularized osteochondral compartment OoC representations.* Selected presentation. 3rd Annual conference of the European Organ-on-Chip Society. Online meeting 1-2 July 2021.

Awards and grants

Finalist at Premio Gaetano Marzotto 2017: Dall'idea all'impresa. Occhetta P, Ugolini S, Visone R, **Mainardi A**, Rasponi M.

Ex-Equo Best Evaluated paper on "Track 2- Biomaterials and Tissue Engineering" 6th Congresso del gruppo nazionale di Bioingegneria, Milan 25-27 June 2018

ESB student award runner-up prize, 8th World Congress of Biomechanics, Dublin 8-12 July 2018

Cotutelles de thèse" und Promotionspartnerschaften 2020 zwischen schweizerischen Hochschulen und Partnerhochschulen in Europa und Israel- Mobility Swissuniversities grant